Mixed-ligand diruthenium complexes: Theoretical modelling and interpretation of electronic absorption spectra

A dissertation submitted to the

University of Cape Town

in fulfilment of the requirements for the degree of

Master of Science

By

Jean-Luc Mutomb

(BSc Hons. University of Cape Town)

Supervisor: Dr. Siyabonga Ngubane

Co-supervisor: Dr. Gerhard Venter

Department of Chemistry

University of Cape Town

June 27, 2025

Acknowledgements

The research was carried out at the University of Cape Town (UCT) under the supervision of Dr GA Venter and Dr SP Ngubane, with funding provided by the National Research Foundation (NRF) Thuthuka grant and the UCT Internal Refugee Scholarship.

First and foremost, I want to express my heartfelt gratitude to Dr Ngubane and Dr Venter for their invaluable support and supervision throughout my research, for paring me much of their time to read and re-reading this work and for providing me with valuable feedback, and for showing me great patient when the project was not going according to expectations.

My gratitude also extends to everyone I have worked with, to mention a few: Dr S Siangwata, who assisted me with experiments in the organometallic synthetic laboratory, and Thato Medupe, who provided me with previous compounds and data as well as Dr William for his constructive advice on both science and life.

I would also like to take this opportunity to thank all the colleagues in the research groups of Dr Ngubane and Prof. G Smith who jointly participated in oral presentations and shared pleasant moments with me outside of the university setting.

The people in my life—my parents (Felicien and Josephine Mutomb), siblings, and friends—who have supported me no matter how far away they are and who have given me the motivation to do this task will always have my undying gratitude.

Most significantly, I am grateful to God Almighty for providing me with the fantastic individuals and possibilities I have experienced during my studies.

Table of Contents

ACKNOWLEDGEMENTS 1

TABLE OF CONTENTS 2

LIST OF ABBREVIATIONS 5

LIST OF FIGURES 8

LIST OF TABLES 11

ABSTRACT 12

CHAPTER 1 INTRODUCTION 13

1.1 Ru_2^{5+} Complexes: Structure, Properties and Applications 13

1.1.1 Effect of O,O'-donor bridging ligands on $[Ru_2(\mu\text{-}O_2CCH_3)_4]^+$ 13

1.1.2 Effect of axial chloride ligand on $Ru_2(\mu\text{-}O_2CCH_3)_4Cl$ 17

1.1.3 From O,O'- to O,N- or N,N'-donor bridging ligands 18

1.2 UV-Vis of absorption spectra of Ru_2^{5+} compounds 20

1.2.1 Absorption spectroscopy of $Ru_2(\mu\text{-carboxylate})_4Cl$ derivatives 20

1.2.2 Absorption spectroscopy of mixed-ligands $Ru_2(\mu\text{-}O_2CR)_{4-n}(Rap)_nX$ derivatives 24

1.3 Aim 27

CHAPTER 2 THEORETICAL BACKGROUND 29

2.1 Wavefunction-based methods 29

2.1.1 *Ab initio* Hartree-Fock methods 29

2.2 Density functional theory 34

2.2.1 Density-dependent Hamiltonian 34

2.2.2 The Hohenberg and Kohn theorems 35

2.2.3 Kohn-Sham Equations 37

2.2.4 Ladder of XC functionals 40

2.2.4.1 Local density approximation 41

2.2.4.2 Generalized gradient approximation 42

2.2.4.3 Meta-generalized gradient approximation 43

2.2.4.4 Global hybrid functionals and range-separated correction 43

2.2.4.5 Double hybrid functionals 45

2.3 Basis sets 46
2.3.1 Atom-localized basis sets 46
2.3.1.1 Contracted Gaussian-type orbitals 46
2.3.1.2 Single- , multiple-ζ and split-valence basis sets 47
2.3.1.3 Augmentation with polarization and diffuse functions 48
2.3.2 Effective core potential basis sets 49
2.3.3 Def2-, LANL2-, and D95-type basis sets and ECPs 50

2.4 Time-dependent density functional theory 52
2.4.1 Time-dependent Hamiltonian and density 52
2.4.2 Rung and Gross theorem 53
2.4.3 Time-dependent Kohn-Sham equations 54
2.4.4 Linear response TD-DFT 55
2.4.5 How to characterize the experimental and TD-DFT UV-Vis absorption spectrum 58
2.4.5.1 Natural transition orbitals 58
2.4.5.2 Convolution of modelled UV-Vis spectrum 61
2.4.5.3 Deconvolution of experimental UV-Vis spectrum 63

2.5 Chemical solvent models 64
2.5.1 Solvent effect on DFT potential energy surface 64
2.5.2 Explicit models 65
2.5.3 Implicit models 66
2.5.3.1 Polarizable Continuum Models vs Solvent Model based on Density 67
2.5.4 Solvatochromism 69
CHAPTER 3 EXPERIMENTAL DETAILS 71

3.1 General procedures and physical measurements 71
3.1.1 Synthesis of $Ru_2(\mu\text{-}O_2CCH_3)_3(2\text{-Fap})I$ 71

3.2 Computational methods 71
3.2.1 General ground state calculations set up 71
3.2.2 Excited state calculations and UV-Vis spectra analysis 72
3.2.3 Natural transition orbitals calculations and charge contributions 74
CHAPTER 4 RESULTS AND DISCUSSION 75

4.1 Strategy for choosing the best TD-DFT level of theory for predicting the UV-Vis-NIR electronic absorption spectra of diruthenium(II,III) complexes 75
4.1.1 Benchmarking LANL2- and Def2-type basis set in gas and solvated phase 75
4.1.2 Benchmarking GGA, hybrid GGA, hybrid meta-GGA and RSH functionals 82

4.1.3 Comparing natural transition orbitals and canonical molecular orbitals 90

4.2 Analysis of UV-Vis-NIR electronic absorption spectra of $Ru_2(\mu\text{-}O_2CCH_3)_3(\mu\text{-}2\text{-}Fap)X$ (X=Cl, Br, I) 98

4.2.1 Characterization of absorption bands of $Ru_2(\mu\text{-}O_2CCH_3)_3(\mu\text{-}2\text{-}Fap)Cl$ 98

4.2.2 Comparison of neutral, cationic, and anionic species 110

4.2.3 Nature of halogen ligand 122

4.2.4 Solvatochromism 132

CHAPTER 5 CONCLUSIONS AND FUTURE WORK 141

REFERENCES 143

List of abbreviations

1-TDM	One-electron transition density matrix
A-LR-TD-DFT	Adiabatic LR-TD-DFT
AO	Atomic orbital
ap	Anilinopyridinate
ASA	Analytic Surface Area
B3LYP	Three parameter hybrid exchange functional of Becke with correlation functional of Lee, Yang and Parr
B88	Becke 1988 exchange functional
BP86	Becke and Perdew's 1986 exchange-correlation functional
CAM-B3LYP	Couloumb-attenuated B3LYP exchange-correlation functional
CBS	Complete basis set
CDS	Cavity-dispersion-solvent-structure (a component of SMD solvent model)
CGTO	Contracted GTO
CI	Configuration interaction
CPCM	conductor-like PCM
CPU	Central processing unit
CT	Charge transfer
D95	Double-zeta basis set of Dunning and Huzinaga
DCM	Dichloromethane
Def-	Earlier Def-type basis sets by Karlsruhe group of Ahlrichs *et al*.
Def2-SVP	Def2 basis sets of the Karlsruhe group of Ahlrichs *et al.*, with split valence double-ζ and polarization functions
Def2-TZVP	Def2 basis sets of the Karlsruhe group of Ahlrichs *et al*., with triple-ζ valence and polarization functions
DFT	Density functional theory
DH	Double hybrid
DMSO	Dimethyl sulfoxide
DN	Donor number
ECP	Effective core potential
EDA	Electron donating ability
EES	Electronic excited state
ENP	Electronic-nuclear-polarization (a component of SMD solvent model)
EX	HF exact exchange
Fap	2-(2-fluoroanilino)pyridinate
GGA	Generalized gradient approximation
GH-GGA	Global hybrid generalized gradient approximation
GH-mGGA	Global hybrid meta-generalized gradient approximation
GS	Ground state
GTO	Gaussian-type orbital
HF	Hartree-Fock
HK	Hohenberg-Kohn
HOMO	Highest occupied molecular orbital

HOTO	Highest occupied transition orbital
IEF-PCM	Integral equation formalism PCM
KS	Kohn-sham
LANL2DZ	The Los Alamos National Laboratory split valence-double-ζ basis set
LANL2-ECP	LANL2 ECP developed by Hay and Wadt
LCAO	Linear combination of atomic orbitals
LCECP	Large-core ECP
LDA	Local density approximation
LHS	Left-hand side
LLCT	Ligand-to-ligand charge transfer
LMCT	Ligand-to-metal charge transfer
LR	Long-range
LRC	Long-range corrected hybrid exchange-correlation functional
LR-TD-DFT	Linear response time-dependent density functional theory
LS1DH	Linear-scaled one-parameter double-hybrid
LSDA	Local spin density approximation
LUMO	Lowest unoccupied molecular orbital
LUTO	Lowest unoccupied transition orbital
AD	Absolute Deviation
MB	Mega magnetic induction
mGGA	Meta-generalized gradient approximation
MLCT	Metal-to-ligand charge transfer
MMCT	Metal-to-metal charge transfer
MO	Molecular orbital
MPn	N-th order Moller-Plesset perturbation theory
NCI	Non-covalent interaction
NIR	Near-infrared region
NTO	Natural transition orbital
PBE	Perdew, Burke and Ernzerhof Exchange-correlation functional
PBE0	Perdew, Burke and Ernzerhof Exchange-correlation hybrid functional
PBE0-DH	Double hybrid version of PBE
PCM	Polarizable continuum model
PES	Potential energy surface
PGTO	Primitive Gaussian-type orbital
QM	Quantum mechanics
RHS	Right-hand side
RSH	Range-seperated hybrid
Ru_2	Diruthenium
R_{VDW}	Van Der Waals Radius
SAS	Solvent-accessible surface
SASA	Solvent-accessible surface area
SCECP	Small-core ECP

SCF	Self-consistent field
SCF-αX-SW	Self-consistent field αX scattered wave
SCRF	Self-consistent reaction field
SE	Signed Error/deviation from experiment
SMD	Solvent model based on density
SOMO	Singly occupied MO
SR	Short-range
STO	Slater-type orbital
STO-nG	Slater-type orbital approximated by n Gaussian functions
TD	Time-dependent
TDA-LR-TD-DFT	Tamm-Dancoff approximation LR-TD-DFT
TD-DFT	Time-dependent DFT
TO	Transition orbital
TPSS	Tao, Perdew, Staroverov and Scuseria non-hybrid mGGA functional
TPSSh	Tao, Perdew, Staroverov and Scuseria hybrid GGA functional
UEG	Uniform electron gas
UV	Ultraviolet
UV-Vis	Ultraviolet-visible
UV-Vis-NIR	Ultraviolet-visible-near-infrared
Vis	Visible
VTE	Vertical transition energies
XC	Exchange-correlation

List of Figures

Figure 1.1 Comparison of the spin-restricted MO diagram and electronic configuration of (a) ligand-free $[Ru_2^{5+}]$ barycenter and (b) $[Ru_2(\mu\text{-}O_2CR)_4]^+$ complex. Effect of bridging ligands indicated by the dashed lines. 14

Figure 1.2 General (A) paddlewheel with axial ligand (red ball) and (B) bi-octahedral molecular structures.....15

Figure 1.3 General molecular structure of the four possible arrangement of unsymmetrical bridging ligands around the Ru_2 center. 15

Figure 1.4 Molecular arrangement observed in $Ru_2(m\text{-}O_2CR)_4Cl$ complexes: polymeric (A)linear and (B) zigzag, (C) discrete molecules or (D) ion pair. Axial anionic (X, red) or solvent (Solv, blue) ligands. 16

Figure 1.5 Comparison of the spin-restricted MO diagram and electronic configuration of $[Ru_2(\mu\text{-}O_2CR)_4]^+$, $[Ru_2(\mu\text{-}O_2CR)_4]$---X and $[Ru_2(\mu\text{-}O_2CR)_4]X$ species. Effect of axial ligand indicated by the dashed lines. 18

Figure 1.6 Comparison of the spin-restricted MO diagram and electronic configuration of (A) $[Ru_2(\mu\text{-}O_2CR)_4]^+$, (B) $[Ru_2(\mu\text{-}NOCR)_4]^+$ and (C) $[Ru_2(\mu\text{-}NN'CR)_4]^+$ complexes. Effect of bridging ligands indicated by the dashed lines. 19

Figure 1.7 (a) Experimental UV-Vis spectra of $[Ru_2(\mu\text{-}O_2CCH_3)X_2]^-$ (X = Cl, Br, I) in acetonitrile and (b) the corresponding TD-DFT spectra simulated in acetonitrile at the B3LYP/LANL2DZ-IEPCM. Adapted from Ref.[21] 21

Figure 1.8 (a) Experimental UV-Vis spectra of $Ru_2(\mu\text{-}OC_2CH_3)_x(\mu\text{-}2\text{-}Fap)_{4-x}Cl$ in neat DCM and (b) UV-Vis spectra of $Ru_2(\mu\text{-}O_2CCH_3)_3(\mu\text{-}2\text{-}Fap)Cl$ in DCM before (-) and after (…) adding 0.1 M TBACl. Adapted from Ref.[43] 25

Figure 2.1 Schema summarizing the KS SCF procedure.....39

Figure 2.2 Classification of DFT XC functionals according to the Jacob's Ladder of J.P Perdew. 40

Figure 2.3 Most used DFT functionals in geometry optimization (a) and reaction energy (b) calculations in 2013-2014. Adapted from ref.[98] 43

Figure 2.4 A STO of 1s AO modeled by a linear combination of three GTOs (STO-3G). Adapted from Ref.[80] 47

Figure 2.5 Interaction between the symmetry combination of two hydrogen 1s AOs and one oxygen AO to form an H_2O MO. Bonding interactions are enhanced by mixing a small amount of oxygen d character into the MO.[77] 48

Figure 2.6 Most used basis sets in geometry optimization (a) and reaction energy (b) calculations involving Pd, Ni, Rh, and Ir metals. Adapted from Ref.[98].....51

Figure 2.7 Simplified Jablonski diagram representing only two singlet states free of interaction(s). Adapted from Ref. [192].....58

Figure 2.8 (a) The hole and electron coordinates $\boldsymbol{r}H$ and $\boldsymbol{r}E$, the center-of-mass coordinate R, and the separation $\boldsymbol{r}HE$, and (b) an exemplary exciton wavefunction $\Omega(\boldsymbol{r}h, \boldsymbol{r}e)$ (c) Deconstruction of $\Omega(\boldsymbol{r}h, \boldsymbol{r}e)$ into separate hole $\rho H(\boldsymbol{r}H)$ and particle $\rho E(\boldsymbol{r}E)$ densities, using an $n\pi*$ excited state (S1) in pyridine as example. (d) NTOs for the pyridine molecule for this excited state. Adapted from Ref.[194] 59

Figure 2.9 A three-dimensional gas-phase PES (black) and the PES derived from adding the free energy of solvation (blue). The chemical reaction proceed from one minimum-energy structure to another (thick line). 65

Figure 2.10 An acetonitrile molecule immersed in an explicit (a) solvated phase (pink) and implicit (b) solvated phase. 66

Figure 2.11 A two-dimensional gas-phase, solvated phase GS PESs and the corresponding EES PESs. 69

Figure 4.1 Comparison of experimental (Expt.) UV-Vis spectra of anionic $[Ru_2(O_2CCH_3)_4X_2]^-$ complexes, where X = Cl **(a)**, Br **(b)** or I **(c)**, recorded in acetonitrile (AN) and the corresponding TDDFT UV-Vis-NIR spectra predicted at B3LYP/LANL2DZ//B3LYP/LANL2DZ, B3LYP/LANL2DZ-IEFPCM(AN)//B3LYP/LANL2DZ and B3LYP/LANL2DZ-IEFPCM(AN)//B3LYP/LANL2DZ-IEFPCM(AN) levels of theory. 77

Figure 4.2 Comparison of experimental (Expt.) UV-Vis spectra of anionic $[Ru_2(O_2CCH_3)_4X_2]^-$ complexes, where X = Cl **(a)**, Br **(b)** or I **(c)**, recorded in acetonitrile (AN) and the corresponding TDDFT UV-Vis-NIR spectra predicted using Def-SVP-IEFPCM(AN), Def-TZVP-IEFPCM(AN), LANL2DZ-IEFPCM(AN) and LANL2DZ+D95-IEFPCM(AN) in conjunction with the B3LYP 80

Figure 4.3 Accuracy plots for TD-DFT calculated wavelength of maximum absorption for (a) LAN2DZ (b) Def2-SVP and (c) Def2-TZVP in conjunction with B3LYP and IEF-PCM in Acetonitrile. Points above the line indicate positive errors while points below the line indicate negative errors. 82
Figure 4.4 Comparison of experimental (Expt.) UV-Vis spectra of anionic $[Ru_2(O_2CCH_3)_4X_2]^-$ complexes, where X = Cl **(a)**, Br **(b)** or I **(c)**, recorded in acetonitrile (AN) and the corresponding TDDFT UV-Vis-NIR spectra predicted at the PBE/LANL2DZ-IEFPCM(AN) and BP86/LANL2DZ-IEFPCM(AN) levels of theory. 83
Figure 4.5 Comparison of experimental (Expt.) UV-Vis spectra of anionic $[Ru_2(O_2CCH_3)_4X_2]^-$ complexes, where X = Cl **(a)**, Br **(b)** or I **(c)**, recorded in acetonitrile (AN) and the corresponding TDDFT UV-Vis-NIR spectra predicted at the B3LYP/LANL2DZ-IEFPCM(AN), PBE0/LANL2DZ-IEFPCM(AN) and TPSSH/LANL2DZ-IEFPCM(AN) levels of theory. 85
Figure 4.6 Comparison of experimental (Expt.) UV-Vis spectra of anionic $[Ru_2(O_2CCH_3)_4X_2]^-$ complex, where X = Cl **(a)**, Br **(b)** or I **(c)**, recorded in acetonitrile (AN) and the corresponding TDDFT UV-Vis-NIR spectra predicted at the B3LYP/LANL2DZ-IEFPCM(AN), PBE0/LANL2DZ-IEFPCM(AN) and TPSSH/LANL2DZ-IEFPCM(AN) levels of theory. 87
Figure 4.7 Accuracy plots for TD-DFT calculated wavelength of maximum absorption for (a) PBE (b) TPSSH (c) BP86 (d) LC-ωHPBE, (e) B3LYP, (f) PBE0, and (g) CAM-B3LYP, for the $[Ru_2(O_2CCH_3)_4X_2]^-$ complexes, where X =Cl, Br, I. The red line represents the y=x line. Points above and below the line indicate positive or negative errors, respectively. 88
Figure 4.8 Comparison of density functional mean absolute deviations for UV-Vis absorption band 1, 2 and 3 of the $[Ru_2(O_2CCH_3)_4X_2]^-$ complexes, where X = Cl, Br, I. LANL2DZ and IEFPCM(Acetonitrile) was used in all cases. 89
Figure 4.9 (a) Experimental curve (black), TD-DFT (green) of the electronic absorption spectrum of $[Ru_2(O_2CCH_3)_4Cl_2]^-$ in water. Numbers annotate the re-numbered excited states for clarity. (b)Experimental curve (data), fit peaks I - VII, cumulative fit curve (Model) obtained from Gaussian deconvolution of the electronic absorption spectrum of $[Ru_2(O_2CCH_3)_4Cl_2]^-$ in Acetonitrile. 94
Figure 4.10 A portion (-2.35 eV to -7.00 eV) of spin unrestricted MOs of $Ru_2(\mu\text{-}O_2CCH_3)_3(\mu\text{-}2\text{-}Fap)Cl$, partitioned into percentage contributions from (blue) two Ru atoms, (green) one Cl atom, four acetate groups and one Fap group. Orbital pairing (blue dashed). Calculated using PBE/LANL2DZ-IEPCM in water 100
Figure 4.11 The difference between the α-spin (orange) and β-spin (blue) density in $Ru_2(\mu\text{-}O_2CCH_3)_3(\mu\text{-}2\text{-}Fap)Cl$. Obtained with PBE/LANL2DZ-IEFPCM. 101
Figure 4.12 (a) Experimental curve (black), TD-DFT (green) of the electronic absorption spectrum of $Ru_2(\mu\text{-}O_2CCH_3)_3(\mu\text{-}2\text{-}Fap)Cl$ in water. (b) Experimental band (Expt), fit curves I - X, cumulative fitted curve (Model) obtained from Gaussian deconvolution of the electronic absorption spectrum of $Ru_2(\mu\text{-}O_2CCH_3)_3(\mu\text{-}2\text{-}Fap)Cl$ in Water. TD-DFT employed the PBE/LANL2DZ-IEFPCM (water) level of theory. 105
Figure 4.13 Comparison of π(O) and π(Ru-N) orbital character in (a) $Ru_2(OCCH_3)_4Cl$ and (b) $Ru_2(OCCH_3)_3(2\text{-}Fap)Cl$, respectively. 109
Figure 4.14 Neutral (a), cationic (b) and anionic (c) complexes used for the UV-Vis simulation 110
Figure 4.15 (a) Experimental curve (black), TD-DFT absorption curve of the neutral (green) $Ru_2(\mu\text{-}O_2CCH_3)_3(\mu\text{-}2\text{-}Fap)Cl$ and cationic (blue) $[Ru_2(\mu\text{-}O_2CCH_3)_3(\mu\text{-}2\text{-}Fap)(H_2O)]^+$ in water. (b) The experimental curve (Black), and cumulative fit curve (Red) were obtained from the sum of green and blue fit curves. PBE/LANL2DZ-IEFPCM was used. 111
Figure 4.16 Experimental curve (black), TD-DFT absorption curve of the neutral (green) $Ru_2(\mu\text{-}O_2CCH_3)_3(\mu\text{-}2\text{-}Fap)Cl$ and anionic (blue) $[Ru_2(\mu\text{-}O_2CCH_3)_3(\mu\text{-}2\text{-}Fap)Cl_2]^-$ complexes in water. TD-DFT employed the PBE/LANL2DZ-IEFPCM(water) level of theory. 114
Figure 4.17 Electronic structure calculations of the cationic (black), neutral (green) and anionic (dark-green) complexes in water obtained at the PBE/LANL2DZ-IEFPCM level of theory. 119
Figure 4.18 The single electron excitations and the δ-δ^* gap energies for band 4 of the cationic (black), neutral (green) and anionic (dark-green) complexes in water obtained at the PBE/LANL2DZ-IEFPCM level of theory. 121

Figure 4.19 (a) Experimental (solid) and TD-DFT (dashed) curves of $Ru_2(\mu\text{-}O_2CCH_3)_3(\mu\text{-}2\text{-}Fap)X$ where X=Cl (green), Br(red) or I (purple) complexes in water. (b) Experimental (solid) and cumulative fit curves obtained from the sum of the TD-DFT curve of $[Ru_2(\mu\text{-}O_2CCH_3)_3(\mu\text{-}2\text{-}Fap)]^+$ with the TD-DFT curve of $Ru_2(\mu\text{-}O_2CCH_3)_3(\mu\text{-}2\text{-}Fap)Cl$ (green) or $Ru_2(\mu\text{-}O_2CCH_3)_3(\mu\text{-}2\text{-}Fap)I$ (purple). TD-DFT employed the PBE/LANL2DZ-IEFPCM(water) level of theory. 123
Figure 4.20 Electronic structure calculations of the $Ru_2(\mu\text{-}O_2CCH_3)_3(\mu\text{-}2\text{-}Fap)X$ where X is Cl (green), Br (brown) and I (pink) complexes in water obtained at the PBE/LANL2DZ-IEFPCM level of theory. 128
Figure 4.21 Electronic structure calculations of the $[Ru_2(\mu\text{-}O_2CCH_3)_3(\mu\text{-}2\text{-}Fap)X_2]^-$ where X is Cl (green), Br (brown) and I (pink) complexes in water obtained at the PBE/LANL2DZ-IEFPCM level of theory. 130
Figure 4.22 The $\delta \rightarrow \delta^*$ charge(CT) and the most intense CT (MICT) excitation wavelength of the $Ru_2(\mu\text{-}O_2CCH_3)_3(\mu\text{-}2\text{-}Fap)X$, $[Ru_2(\mu\text{-}O_2CCH_3)_3(\mu\text{-}2\text{-}Fap)X_2]^-$ and $[Ru_2(\mu\text{-}O_2CCH_3)_4X_2]^-$ complexes (X = Cl, Br, I) computed using the PBE/LANL2DZ-IEFPCM in water, as a function of R_{VDW} of X.[263] 132
Figure 4.23 Comparison of the simulated (dashed) UV-Vis-NIR curves of $Ru_2(\mu\text{-}O_2CCH_3)_3(\mu\text{-}2\text{-}Fap)Cl$ obtained in DCM (green), DMSO (green) and water (red). Computed at the PBE/LANL2DZ-IEFPCM level of theory 133
Figure 4.24 The solvent dielectric constant (ε) as a function of the simulated λ_{max}(nm) of band 3 of $Ru_2(\mu\text{-}O_2CCH_3)_3(\mu\text{-}2\text{-}Fap)Cl$. 134
Figure 4.25 Electronic structure calculations of the neutral complex in the water, DCM and DMSO, obtained at the PBE/LANL2DZ-IEFPCM level of theory. 134
Figure 4.26 Comparison of TD-DFT absorption curve of the solvent-coordinated $Ru_2(\mu\text{-}O_2CCH_3)_3(\mu\text{-}2\text{-}Fap)(Solv)Cl$ (—) and non-coordinated $Ru_2(\mu\text{-}O_2CCH_3)_3(\mu\text{-}2\text{-}Fap)Cl$ (- - -) complexes in DCM (green), water (blue) and DMSO(red). 136
Figure 4.27 The solvent donor number (DN) as a function of the simulated λ_{max}(nm) of band 3 of $Ru_2(\mu\text{-}O_2CCH_3)_3(\mu\text{-}2\text{-}Fap)Cl$. 137
Figure 4.28 Comparison of the simulated (dashed) UV-Vis-NIR curves of $Ru_2(\mu\text{-}O_2CCH_3)_3(\mu\text{-}2\text{-}Fap)Cl$ obtained in DCM (green), DMSO (green) and water (red). Computed at the PBE/LANL2DZ-IEFPCM level of theory 137
Figure 4.29 Electronic structure calculations of the neutral complex in explicitly bound water, DCM and DMSO solvent obtained at the PBE/LANL2DZ-IEFPCM level of theory. 139
Figure 4.30 Comparison of the simulated (dashed) UV-Vis spectrum of $Ru_2(\mu\text{-}O_2CCH_3)_3(\mu\text{-}2\text{-}Fap)Cl(Solv)$ and experimentally obtained in DCM (green), DMSO (green) and water (red). Computed at the PBE/LANL2DZ. (See Figure 4.12 for Higher wavelengths band and peak) 140

List of tables

Table 1.1 Literature Assignment of electronic absorption transitions in Ru_2(μ-carboxylate)$_4$ compounds 22
Table 1.2 Literature Assignment of electronic absorption transitions in Ru_2(μ-Rap)$_n$(μ-O_2CR')$_{4-n}$Cl compounds 26
Table 2.1 Number of core electrons described the SDD ECP for various heavy elements 51
Table 4.1 Comparison of environmental effect UV-Vis wavelength of maximum absorption (λ_{max}) of anionic $[Ru_2(O_2CCH_3)_4X_2]^-$ complexes, where X = Cl, Br, or I, recorded experimentally (Expt.) in acetonitrile (AN) and predicted using TDDFT UV-Vis-NIR ($i-iii$) at B3LYP/LANL2DZ//B3LYP/LANL2DZ, B3LYP/LANL2DZ-IEFPCM(AN)//B3LYP/LANL2DZ and B3LYP/LANL2DZ-IEFPCM(AN)//B3LYP/LANL2DZ-IEFPCM(AN) levels of theory. 78
Table 4.2 Comparison of basis set effect on the UV-Vis wavelength of maximum absorption (λ_{max}) of anionic $[Ru_2(O_2CCH_3)_4X_2]^-$ complexes, where X = Cl, Br, or I, recorded experimentally (Expt.) in acetonitrile (AN) and predicted using TDDFT UV-Vis-NIR at the B3LYP/Def2-SVP-IEFPCM(AN), B3LYP/Def2-TZVP-IEFPCM(AN), and B3LYP/LANL2DZ-IEFPCM(AN) levels of theory. 81
Table 4.3 Comparison of DFT functional effect on the UV-Vis wavelength (nm) of maximum absorption (λ) of anionic $[Ru_2(O_2CCH_3)_4X_2]^-$ complexes, where X = Cl, Br, or I, recorded experimentally (Expt.) in acetonitrile (AN) and predicted using TDDFT UV-Vis-NIR the BP86, PBE, B3LYP, PBE0, TPSSH, CAM-B3LYP and LC-ωHPBE functionals in conjunction with the LANL2DZ basis set and IEFPCM(AN) solvation. 84
Table 4.4 Comparison of TD-DFT UV-Vis MO and NTO transitions for $[Ru_2(O_2CCH_3)_4Cl_2]^-$ complexes in acetonitrile (AN), calculated at the B3LYP/LANL2DZ-IEFPCM(AN) level of theory was used in all cases. 91
Table 4.5 Comparison of TD-DFT UV-Vis wavelength (λ)of electronic transition (State) of the anionic $[Ru_2(O_2CCH_3)_4Cl_2]^-$ complex, and the experimentally recorded band maxima (Expt.) in acetonitrile (AN). The B3LYP/LANL2DZ-IEFPCM(AN) level of theory was used in all cases. 97
Table 4.6 NTO transitions for Ru_2(μ-O_2CCH_3)$_3$(μ-2-Fap)Cl complex in water, calculated at the PBE/LANL2DZ-IEFPCM(water) level of theory was used in all cases. 102
Table 4.7 Percentage contribution of fragmented Mulliken charges to the NTOs of Ru_2(μ-O_2CCH_3)(μ-2-Fap)Cl calculated with PBE/LANL2DZ-IEFPCM in water. 105
Table 4.8 Summarized comparison of TD-DFT UV-Vis characterization in this study and previously reported assignments. TD-DFT employed the PBE/LANL2DZ-IEFPCM(water) level of theory. 106
Table 4.9 Percentage contribution of fragmented Mulliken charges to the NTOs of $[Ru_2$(μ-O_2CCH_3)(μ-2-Fap)$(H_2O)]^+$ calculated with PBE/LANL2DZ-IEFPCM in water. 112
Table 4.10 Percentage contribution of fragmented Mulliken charges to the NTOs of $[Ru_2$(μ-O_2CCH_3)(μ-2-Fap)$(Cl_2)]^-$ calculated with PBE/LANL2DZ-IEFPCM in water. 114
Table 4.11 Comparison of NTO transitions neutral Ru_2(μ-O_2CCH_3)$_3$(μ-2-Fap)Cl, cationic $[Ru_2$(μ-O_2CCH_3)$_3$(μ-2-Fap)$]^+$ and anionic $[Ru_2$(μ-O_2CCH_3)$_3$(μ-2-Fap)$Cl_2]^-$ complexes in water, calculated at the PBE/LANL2DZ-IEFPCM(water) level of theory 116
Table 4.12 Comparison of NTO transitions the neutral Ru_2(μ-O_2CCH_3)$_3$(μ-2-Fap)X (X = Cl, Br and I) complexes in water, calculated at the PBE/LANL2DZ-IEFPCM(water) level of theory. 124
Table 4.13 The δ → δ* charge transfer (CT) and the most intense CT (MICT) excitation wavelength of the Ru_2(μ-O_2CCH_3)$_3$(μ-2-Fap)X, $[Ru_2$(μ-O_2CCH_3)$_3$(μ-2-Fap)$X_2]^-$ and $[Ru_2$(μ-O_2CCH_3)$_4X_2]^-$ complexes (X = Cl, Br, I) computed using the PBE/LANL2DZ-IEFPCM in water. 131

Abstract

The speciation and improved solubility of $Ru_2(\mu\text{-}O_2CCH_3)_3(\mu\text{-}2\text{-}Fap)X$ complexes, where 2-Fap is 2-(2-fluoroanilino)pyridinate, and X represents Cl, Br or I, are influenced by the axial ligand (X) lability and solvent coordination at the axial site. These complexes have Ru(II) and Ru(III) metal centers that can be written as Ru_2^{5+}. Researchers have observed distinctive spectroscopic and electrochemical characteristics of these Ru_2^{5+} complexes but lack an established theoretical framework to fully understand specific characteristic traits, such as a shoulder band in the visible range of the ultraviolet-visible (UV-Vis) spectrum in aqueous solutions, the absence thereof in solutions containing excess chloride ions, as well as the solvatochromic shifts of the UV-Vis bands in aqueous and non-aqueous solvents. This study therefore investigates the characteristics of $Ru_2(\mu\text{-}O_2CCH_3)_3(\mu\text{-}2\text{-}Fap)X$ complexes using time-dependent density functional theory (TD-DFT) calculations that utilize the PBE/LANL2DZ level of theory and an Integral Equation Formalism Polarizable Continuum (IEF-PCM) solvent model using water, DCM and DMSO. Calculation of natural transition orbitals (NTOs) and spectrum deconvolution methods have aided in characterizing the electronic transitions of the prominent UV band at 250-350 nm as a combination of $\delta(Ru_2) \rightarrow \pi^*(N_p,C)$, $\pi(Cl) \rightarrow \pi^*(C_p,N_p)$ and $\pi(Cl) \rightarrow \pi^*(C_a)$ transitions, where the subscript “a” and “p” represents the aniline and pyridine moieties, respectively. On the other hand, the weak band at the 400-450 nm visible region is ascribed to the $\pi(C_a,N_a)/\delta^*(Ru_2) \rightarrow \pi^*(C_p,N_p)$ transition, whereas the broad band at 450-750 nm has been characterized as a combination of $\pi(Cl,Ru_2) \rightarrow \delta^*(Ru_2)$, $\delta(Ru_2) \rightarrow \delta^*(Ru_2)$, $\pi(Cl,Ru_2) \rightarrow \pi^*(Ru_2)$, $\pi(F,C_a\text{-}C_a) \rightarrow \pi^*(Ru_2)$, $\pi(Cl) \rightarrow \pi^*(Ru_2)$ and $\pi(Cl,F,C_a\text{-}C_a) \rightarrow \pi^*(Ru_2)$ transitions. The near-infrared (NIR) region is characterized by a weak band at 900-1000 nm, which mainly consists of a $\delta(Ru_2) \rightarrow \delta^*(Ru_2)$ transition. The equilibria, involving the cationic, neutral and anionic species in solution and corresponding spectroscopic changes are interpreted for $Ru_2(\mu\text{-}O_2CCH_3)_3(\mu\text{-}2\text{-}Fap)X$, along with the solvatochromic shift.

Chapter 1 Introduction

1.1 Ru_2^{5+} Complexes: Structure, Properties and Applications

The search for novel anti-cancer agents remains a crucial and pressing challenge for medicinal chemistry and metal-containing compounds have emerged as a promising avenue of exploration in this pursuit.[1-3] In our laboratory, prior investigations centered on dirhodium (Rh_2) complexes has produced potential anti-cancer agents,[4] and our laboratory has expanded its research for anti-cancer agents to encompass diruthenium (Ru_2) mixed-ligand complexes[5, 6] that exhibit enhanced solubility and contain biologically active ligands, making them particularly attractive from the viewpoint of therapeutic efficacy. An important goal of the investigations conducted in our laboratory has been to gain a deeper understanding of the molecular structure and paramagneticity of these metal complexes and how these factors relate to biological activity. In the sections that follow, some key electronic properties pertaining a majority of Ru_2 complexes are discussed.

1.1.1 Effect of O,O'-donor bridging ligands on $[Ru_2(\mu\text{-}O_2CCH_3)_4]^+$

Each Ru atom possesses five valence d orbitals, namely, d_{z^2}, d_{xz}, d_{yz}, d_{xy} and $d_{x^2-y^2}$ (Figure 1.1.A). In a Ru_2 system, five positive and five negative overlaps are symmetrically allowed between the d orbitals. The positive overlap of the two d_{z^2} orbitals, $d_{z^2}^{(1)} + d_{z^2}^{(2)}$, produces a σ bonding molecular orbital (MO) (Figure 1.1.A). Negative overlap forms the analogous antibonding σ^* MO. The overlaps $d_{xz}^{(1)} + d_{xz}^{(2)}$ and $d_{yz}^{(1)} + d_{yz}^{(2)}$ can each give birth to two degenerate but orthogonal $\pi(\mathrm{Ru_2})$ bonding MOs. Again, the negative overlaps result in the matching π^* anti-bonding MOs. Finally, the bonding and antibonding MOs δ and δ^* combinations of the d_{xy} orbitals. The remaining pair of d-orbitals on each metal atom, $d_{x^2-y^2}$, can overlap to produce bonding and antibonding combinations, but calculations[7] indicated that each of them interacts strongly with a maximum of four ligands on its own metal atom along

the x,y-axis. In this sense, they contribute significantly to metal-ligand interaction while having little to do with Ru-Ru bonding.[7] Based on the Hückel concept, which states that MO energies are proportional to overlap integrals and noting that these overlaps must increase in the order $\delta < \pi < \sigma$, the orbitals energy order beginning with the most stable is expected to be $\sigma < \pi < \delta < \delta^* < \pi^* < \sigma^*$ (Figure 1.1.A).[8] For Ru_2^{5+} complexes, the Ru atoms have a 2.5 fractional formal oxidation state, which means that each Ru atom has 8 - 2.5 = 5.5 electrons and thus eleven electrons can be positioned in valence d-orbitals.[8]

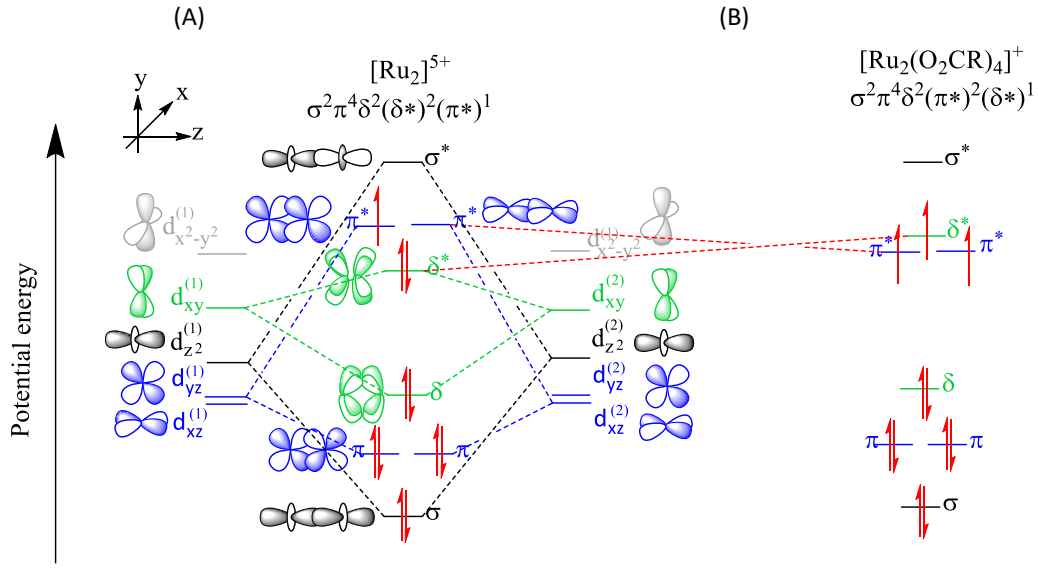

Figure 1.1 Comparison of the spin-restricted MO diagram and electronic configuration of (a) ligand-free [Ru_2^{5+}] barycenter and (b) [$Ru_2(\mu\text{-}O_2CR)_4]^+$ complex. Effect of bridging ligands indicated by the dashed lines.

Eight out of the eleven electrons would occupy the four bonding MOs, while the remaining three electrons fill the antibonding MOs, resulting in the configuration $\sigma^2\pi^4\delta^2(\delta^*\pi^*)^3$ (Figure 1.1.A). The intuitive electronic structure based on energy grounds is the low-spin S = 1/2 ground state (GS) with electronic configuration $\sigma^2\pi^4\delta^2(\delta^*)^2\pi^*$, including four pairs of bonding electrons, a pair of electrons in the antibonding δ^* MO, a single unpaired electron in either one of the antibonding π^* MOs and the $\delta^* < \pi^*$ ordering of MOs.[9-11] However, surprisingly, there are three unpaired antibonding electrons in the π^* and δ^* MOs. The antibonding MOs are very close in energy (Figure 1.1.B), and the high-spin S=3/2 GS with $\sigma^2\pi^4\delta^2(\pi^*\delta^*)^3$ configuration and $\delta^* > \pi^*$ ordering has been found or Ru_2^{5+} complexes. [7, 11] According to Eq. (1.1) from MO theory, which defines bond order as the number of electrons occupying the bonding and

antibonding MOs, the Ru_2^{5+} bond order is 2.5, which means Ru_2^{5+} complexes consist of a peculiar double and half bond.[8, 12]

$$BO = \frac{n_{bonding} - n_{antibonding}}{2} \qquad (1.1)$$

The $Ru_2(\mu\text{-}L)_4$ complexes containing four bridging ligands (L) can adopt either the paddlewheel (Figure 1.2A) or the face-sharing bi-octahedral (Figure 1.2B) structural framework.[8] However, the paddlewheel structure is prominent for Ru_2^{5+} complexes and it is characterized by four strongly bound monoanionic, three-atom, donor bridging ligands, which by connecting the two bonding Ru atoms favours shorter Ru-Ru bond lengths than in the bi-octahedral equivalent.[8]

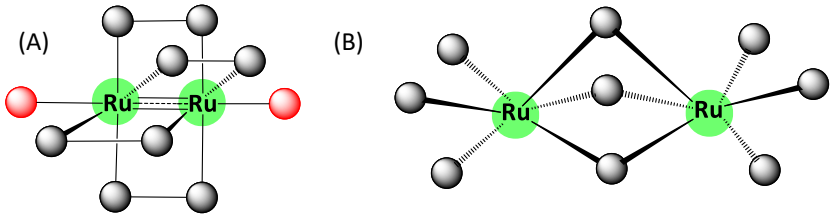

Figure 1.2 General (A) paddlewheel with axial ligand (red ball) and (B) bi-octahedral molecular structures

The Ru-Ru bond lengths in paddlewheel Ru_2^{5+} complexes lie in the narrow range of 2.248-2.310 Å.[8] A paddlewheel Ru_2^{5+} complexes may have zero or one axially coordinating ligands (Figure 1.2A), which are characterized by long Ru-axial ligand bonds.[13] Asymmetrical bridging ligands make up a majority of the significant bridging ligands found among paddlewheel Ru_2^{5+} complexes. This asymmetry can yield four possible regioisomers, namely, (4:0), (3:1), trans-(2:2), or cis-(2:2) isomers (Figure 1.3).[8, 14-17]

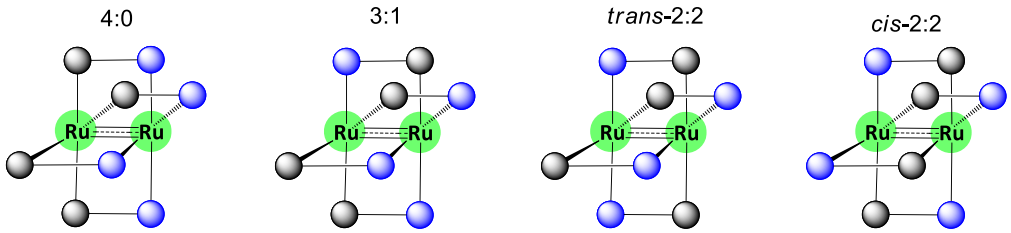

Figure 1.3 General molecular structure of the four possible arrangement of unsymmetrical bridging ligands around the Ru_2 center.

The characteristics of most other paddlewheel complexes are present in $Ru_2(\mu\text{-}O_2CR)_4Cl$ (where O_2CR = carboxylic ligand), which consist of four O,O'-donor bridging ligands coordinating to the Ru_2^{5+} core through two oxygen (O) donor atoms. Therefore, a consideration of the O,O'-donor-bridged class of Ru_2^{5+} serves as a reasonable foundation for all others. Wilkinson and

Stephenson[12] reported the first synthesis of $Ru_2(\mu\text{-}O_2CPr^n)_4Cl$ in 1966, and its crystal structure was determined as a polymeric $[\text{-Ru-Ru-Cl-Ru-Ru-Cl-}]_n$ configuration with four bridging butyrate and a D_{4h} symmetry per Ru_2^{5+} unit. Whilst a 125.4° Ru-Cl-Ru angle between adjacent Ru_2^{5+} units was initially found for $Ru_2(\mu\text{-}O_2CPr^n)_4Cl$,[18] it can significantly vary for polymeric $Ru_2(\mu\text{-}O_2CR)_4Cl$ due to a trade-off between micro-segregation, orbital overlap, or lattice packing.[19, 20,21, 22] Such variation is a critical factor in tuning the antiferromagnetic interaction between adjacent Ru_2^{5+} units,[19, 23] for $Ru_2(\mu\text{-}O_2CR)_4Cl$ which has been of interest in the development of polymeric $Ru_2(\mu\text{-}O_2CR)_4Cl$ complexes with antiferromagnetic properties.[19, 21, 23-25] Furthermore, the Ru-Cl-Ru angle variation enables $Ru_2(\mu\text{-}O_2CR)_4Cl$ complexes to adopt either a linear[26-29] (Figure 1.4A) or zigzag[18, 30-34] (Figure 1.4B) polymeric chain.

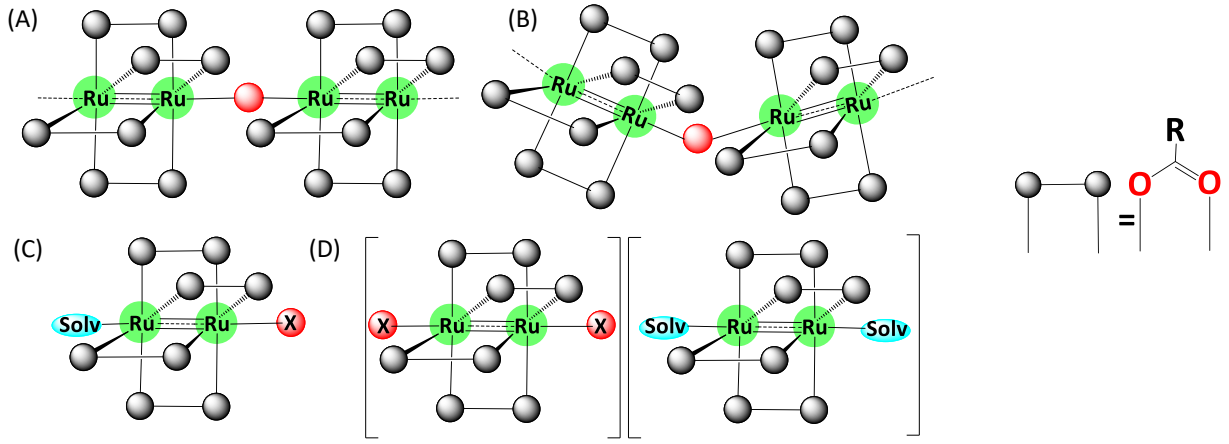

Figure 1.4 Molecular arrangement observed in $Ru_2(m\text{-}O_2CR)_4Cl$ complexes: polymeric (A)linear and (B) zigzag, (C) discrete molecules or (D) ion pair. Axial anionic (X, red) or solvent (Solv, blue) ligands.

Despite their lack of antiferromagnetic properties, non-polymeric $Ru_2(\mu\text{-}O_2CR)_4Cl$ are more prominent than polymeric ones and consist of either a neutral[26, 29, 34, 35] $Ru_2(\mu\text{-}O_2CR)_4(Solv)X$ complexes (where X = anionic ligand, Solv = neutral solvent ligand) (Figure 1.4C) or paired cationic $[Ru_2(\mu\text{-}O_2CR)_4(Solv)_2]^+$ and anionic $[Ru_2(\mu\text{-}O_2CR)_4X_2]^-$ ions (Figure 1.4D).[29] Uncertainty persists regarding the variables that affect whether a given molecule will adopt a polymeric structure or be a discrete molecule.[26-28, 36] However, it has been suggested that the interplay between the axial ligand ability to bind two $[Ru_2(\mu\text{-}O_2CR)_4]^+$ units simultaneously and the destabilizing forces of steric interactions between branched chains of the carboxylic bridging

ligands in $[Ru_2(\mu\text{-}O_2CR)_4]^+$ affects the possibility of forming a monomeric or polymeric structure.[22, 29]

Prior research has concentrated on isolating $Ru_2(\mu\text{-}O_2CR)_4Cl$ having Ru_2^{n+} units (n = 3, 4 or 6),[7] but the Ru_2^{5+} core is the most common owing to its excellent stability in air and magnetic characteristic.[20] The almost degenerate half-filled π^* and δ^* MOs are responsible for the Ru_2^{5+} oxidation state stability due to the stabilizing exchanging energy of the three unpaired electrons that accounts for almost two-thirds of the stability.[7] Magnetic susceptibility studies of $Ru_2(\mu\text{-}O_2CR)_4Cl$ showed magnetic moments of ~4.00 BM per Ru_2^{5+} unit due to the existence of three unpaired electrons delocalized across the Ru_2^{5+} core (c.f. 1.1.1).[12, 37] The two Ru atoms are magnetically equivalent in $Ru_2(\mu\text{-}O_2CR)_4Cl$. Hence, referring to the unit as Ru_2^{5+} is more appropriate than the mixed-valent designations of Ru^{2+}–Ru^{3+}, or Ru$_2$(II,III).

The theoretical analysis on $Ru_2(\mu\text{-}O_2CR)_4Cl$, $[Ru_2(\mu\text{-}O_2CR)_4]^+$, and $[Ru_2(\mu\text{-}O_2CR)_4Cl_2]^-$ using the self-consistent field Xα scattered wave (SCF-Xα-SW), published by Norman and colleagues in 1979,[38] demonstrated that regardless of axial ligands nature or the use of a spin-restricted or spin-unrestricted model, the π^* and δ^* MO levels are very close, with 0.0097 Ha (0.026 eV) and 0.001 Ha (0.0026 eV) for the cationic and anionic species, respectively. Furthermore, Norman[38] theoretically demonstrated that the ligands present have a considerable influence on the relative π^* and δ^* MOs ordering as well as their precise separation. The calculations indicated that the δ^* orbital interacts much more than the π^* orbitals with lower lying carboxylate orbitals due to symmetry-allowed negative overlap of Ru-based d_{xy} orbitals with carboxylate-based $d_{x^2-y^2}$ along the x, y −axis and destabilizes the Ru-based δ^* relative to the π^* MOs. Consequently, the Ru-based δ^* MO energy does not drop as much the Ru-based π^* MOs (Figure 1.1.B) during overlap and thus the $\pi^* < \delta^*$ ordering calculated for these O,O'-donor-bridged Ru_2^{5+} complexes.[34, 38-41]

1.1.2 Effect of axial chloride ligand on $Ru_2(\mu\text{-}O_2CCH_3)_4Cl$

An axial σ(Ru-Cl) bond in $Ru_2(\mu\text{-}O_2CR)_4Cl$ is formed between an empty Ru-based d_{z^2} orbital and an occupied ligand orbital along the z-axis.[38] An additional axial Ru-Cl bond is possible due to

the Cl-based lone pair orbitals.[38] The axial Cl influence on the Ru_2^{5+} is antagonistic to that of the bridging ligands (c.f. 1.1.1 and 1.1.3), such that the axial ligand contributes some charge[38] to and destabilizes the π* MOs but not the δ* MO due to the fact (c.f. 1.1.1) that the Ru-based π* MOs formed by the negative overlap of Ru-based d_{xz} or d_{yz} orbitals are symmetrically aligned to overlap with the Cl lone pair-based p-orbitals interacting along the z-axis in an antibonding manner, whereas the Ru-based d_{xy} for the δ* orbitals lack the proper symmetry to overlap with the Cl-based p-orbitals. Therefore, the negative overlap of the Cl-based p-orbital with Ru-based d_{xz} or d_{yz} orbitals destabilizes the Ru-based π* MOs and lowers the π*-δ* splitting energy.[34, 38-41] This Ru-based π* MOs destabilization upon interacting with axial Cl-based p-orbitals MOs results in a Ru-based π*-δ* energy gap decrease, which becomes more substantial as the axial ligand π*-donation increases (Figure 1.5).

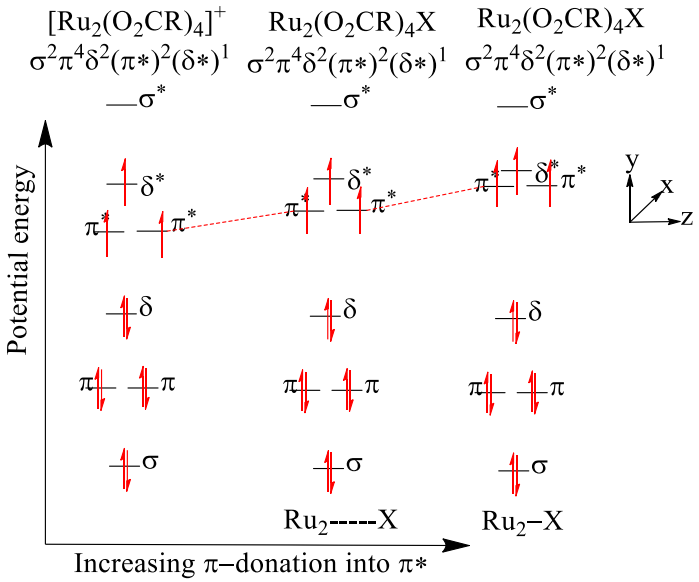

Figure 1.5 Comparison of the spin-restricted MO diagram and electronic configuration of $[Ru_2(\mu\text{-}O_2CR)_4]^+$, $[Ru_2(\mu\text{-}O_2CR)_4]$---X and $[Ru_2(\mu\text{-}O_2CR)_4]X$ species. Effect of axial ligand indicated by the dashed lines.

1.1.3 From O,O'- to O,N- or N,N'-donor bridging ligands

A bridging ligand containing of a nitrogen (N) donor-atom is a stronger π-donor than a bridging ligand with only oxygen (O) donor atoms because N is less electronegative than O. Consequently, a substitution of a more labile O,O'-donor bridging ligands with O,N-donor (e.g., oxypyridinates)[42] or N,N'-donor (e.g., aminopyridinates)[17, 43-46] bridging ligands under

appropriate conditions is possible and can afford complexes with more strongly bound bridging ligands than the initial O,O-donor ligand.[8, 17, 43-47] For instance, the first known mixed-ligands Ru_2^{5+} complex, *viz.* $Ru_2(mhp)_2(\mu\text{-}O_2CCH_3)_2Cl$ (mhp = 6-methyl-2-hydroxypyridinate anion), was derived from $Ru_2(\mu\text{-}O_2CCH_3)_4Cl$.[45] The N,O- and N,N'-donor bridging ligands can be symmetric or asymmetric ligands, which unlike the typical linear O,O'-donor ligands, can more favorably protect the Ru_2^{5+} core, which could lead to useful properties like selective axial ligand coordination.

In contrast to Ru_2 with O,O'-donor-bridge Ru_2^{5+} complexes, N,O' or N,N'-donor-bridged Ru_2^{5+} only present non-polymeric structures,[48-52] possibly due to the greater steric demand of the prominent aryl-containing N,O' or N,N'-donor bridging ligands. Furthermore, despite the high steric requirements of asymmetric aryl-containing N,N'-donor-bridged (4,0) and (3,1) Ru_2^{5+} isomerism (c.f. Figure 1.3) that even results in an paddlewheel eclipsed geometry, these regioisomers (4,0) and (3,1) are more prominent than the (2,2) isomers.[15, 16, 44]

Substituents on a N,O' or N,N'-donor bridging ligands ring can modulate the electron density on the Ru_2^{5+} core, as demonstrated by the linear free energy relationships between the Hammett substituent constants (Σσ) of N,N'-donor bridging ligands and the wavenumber of an absorption band or the $Ru_2^{5+/4+}$ reduction half-wave potentials.[43, 44, 47]

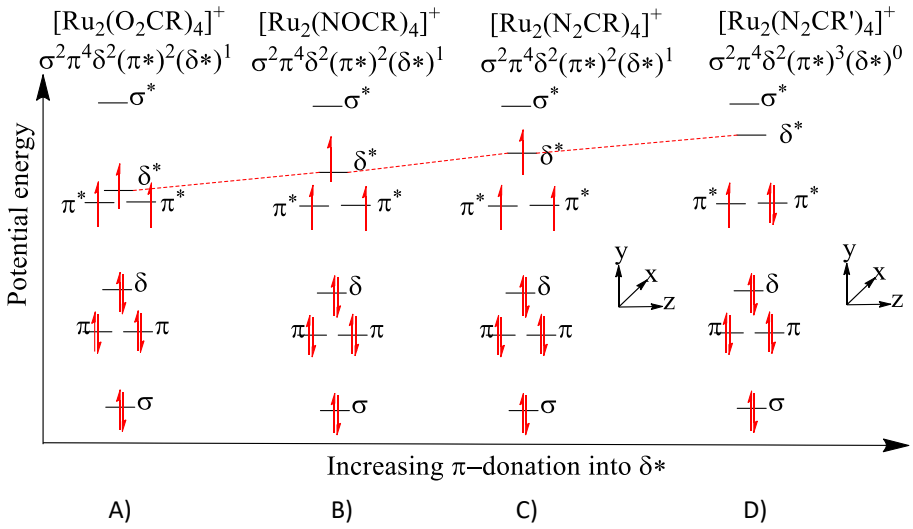

Figure 1.6 Comparison of the spin-restricted MO diagram and electronic configuration of (A) $[Ru_2(\mu\text{-}O_2CR)_4]^+$, (B) $[Ru_2(\mu\text{-}NOCR)_4]^+$ and (C) $[Ru_2(\mu\text{-}NN'CR)_4]^+$ complexes. Effect of bridging ligands indicated by the dashed lines.

It is anticipated that a Ru-based δ* MO will interacts more substantially with a lower lying N,N'- or N,O-donor-based $d_{x^2-y^2}$ than with O,O-donor $d_{x^2-y^2}$ orbital. Thus, a Ru-based δ* would be more destabilize as the π-donation increase from O,O'-donors to N,O-donors to N,N'-donors (Figure 1.6 A-C). Highly basic N,N'- or N,O-donor-bridging ligands can even produce a S=1/2 low-spin state by destabilizing the Ru-based δ* MO enough to break the δ*-π* degeneracy and present an unoccupied δ* MO (Figure 1.6 D) [39, 41, 53, 54]

1.2 UV-Vis of absorption spectra of Ru_2^{5+} compounds

The electronic absorption spectra of paddlewheel Ru_2^{5+} compounds have revealed some interesting and unexpected challenges. $Ru_2(\mu\text{-}O_2CR)_3(\mu\text{-}Rap)Cl$ have spectral properties that are different from those of $Ru_2(\mu\text{-}O_2CR)_4Cl$, where many interpretation techniques that rely on the survival of this axis of symmetry can be used. For unsymmetrical $Ru_2(\mu\text{-}O_2CR)_3(\mu\text{-}Rap)Cl$, the simplifications and approximations that result from an axis of symmetry do not exist, a more rigorous theoretical investigation is required.

1.2.1 Absorption spectroscopy of $Ru_2(\mu\text{-carboxylate})_4Cl$ derivatives

The electronic configuration of paddlewheel Ru_2^{5+} complexes (c.f. 1.1.1) is $\sigma^2\pi^4\delta^2(\delta^*\pi^*)^3$. Norman *et al.*[38] proposed band assignments in the electronic[12, 55] and resonance Raman spectra[56] based on this electronic structure. Regardless of the alkyl substituent, these compounds exhibit three groups of bands in solution, labeled band 1, band 2, and band 3 (Figure 1.7A). Two strong UV band 1 and 2 at ~230 nm and ~330 nm, respectively, and a weak visible band 3 at ~425 nm, as well as a very weak NIR band at ~961 nm,[21, 34, 55-57] which is sometimes not visible.[21] In this case the wavelength is only being shown up to 700nm and even if it were to be extended one would probably not see this very weak band.

The more intense and high-energy UV Band 1 was then assigned[21, 57] to an LMCT $\sigma(\mathrm{Cl}) \rightarrow \sigma^*(\mathrm{Ru_2})$ transition, whereas band 2 was assigned[57] to a ligand to metal charge transfer (LMCT)

$\pi(\mathrm{Cl}) \rightarrow \pi^*(\mathrm{Ru_2})$ (Table 1.1) transition after considering by analogy with experimentally characterized LMCT in Rh_2^0 complexes.

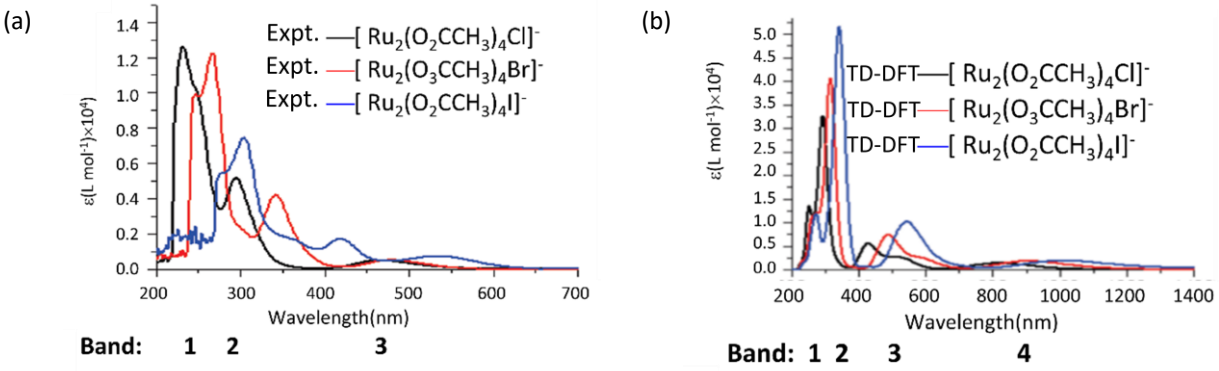

Figure 1.7 (a) Experimental UV-Vis spectra of $[Ru_2(\mu\text{-}O_2CCH_3)X_2]^-$ (X = Cl, Br, I) in acetonitrile and (b) the corresponding TD-DFT spectra simulated in acetonitrile at the B3LYP/LANL2DZ-IEPCM. Adapted from Ref.[21]

Although the attribution of the UV bands to LMCT is logical on energy grounds, calculations have shown numerous allowed transitions in the UV range in question,[21, 38] as responsible for the very high molar absorptivity (reaching $\epsilon > 2000$)[21] and the ill-defined maxima in the range 392-200 nm.[56] Furthermore, the attribution of band 2 to the $\pi(\mathrm{Cl}) \rightarrow \pi^*(\mathrm{Ru_2})$ transition was not confirmed by calculations.[21, 38] In contrast, a weak ($f \cong 0.015$) $\mathrm{p(O)} \rightarrow \pi^*(\mathrm{Ru_2})$ transition at ~330 nm was predicted. The UV band assignment is thus unclear, and in principle, the intense absorption in the UV range could be the net result of a large number of overlapping transitions simulated with various characters that are not accounted for in the proposed UV band assignment, and thus the latter could well be in error by such a large amount. It has been shown that band 1 of $[Ru_2(\mu\text{-}O_2CR)_4X_2]^-$ (X = Cl, Br, or I) substantially red-shifts when changing the axial ligand from Cl to Br to I (Figure 1.7A), from 230 nm to 280 nm to 310 nm, respectively (Table 1.1).[21, 22, 57] Similarly, band 2 moves from 330 nm to 375 nm to 430 nm upon changing from Cl to Br to I. The redshift was consistent with the axial ligand character of the $\sigma(\mathrm{X}) \rightarrow \sigma^*(\mathrm{Ru_2})$ and $\pi(\mathrm{X}) \rightarrow \pi^*(\mathrm{Ru_2})$ LMCT (Table 1.1) proposed to be responsible for these UV bands and the anticipated reduction in MO overlap along the Ru-Cl to Ru-I bond, which would result in a decrease of the $\sigma(\mathrm{X}) - \sigma^*(\mathrm{Ru_2})$ and $\pi(\mathrm{X}) - \pi^*(\mathrm{Ru_2})$ energy gaps. Additionally, the $\pi^*(\mathrm{Ru_2}) - \delta^*(\mathrm{Ru_2})$ is anticipated to increase due to the lower binding of the axial ligands (c.f. 1.1.1), which would also decrease the $\pi(\mathrm{X}) - \pi^*(\mathrm{Ru_2})$ energy gap.

The visible band 3 at 425 nm, which was first allocated incorrectly[18] to $\delta(\mathrm{Ru_2}) \rightarrow \sigma_n(\mathrm{Ru_2})$ and/or $\delta(\mathrm{Ru_2}) \rightarrow \sigma_n'(\mathrm{Ru_2})$[55] and $\delta(\mathrm{Ru_2}) \rightarrow \delta^*(\mathrm{Ru_2})$[56] transitions, has been definitively reassigned to a charge transfer $\pi(\mathrm{Ru-O,Ru_2}) \rightarrow \pi^*(\mathrm{Ru_2})$ transition, containing ~75% $\mathrm{Ru-O}\pi$ and ~24% $\mathrm{Ru-Ru}\ \pi$ bonding orbitals, could only be established by calculations.[21, 27, 38, 57] This assignment was validated by the fact that resonance Raman experiments have shown that the band corresponds to a dipole allowed z-polarized $\pi \rightarrow \pi^*$ transition in D_{4h} symmetry.[27, 56-58]

Table 1.1 Literature Assignment of electronic absorption transitions in Ru_2(μ-carboxylate)$_4$ compounds

Assignment	Intensity	$\nu_{max}(\mu\mathrm{m}^{-1})$	$\lambda_{max}(\mathrm{nm})$
	Band 1		
$\sigma(\mathrm{Cl}) \rightarrow \sigma^*(\mathrm{Ru_2})$[e]	vs	~4.35	~230[e]
	Band 2		
$\pi(\mathrm{Cl}) \rightarrow \pi^*(\mathrm{Ru_2})$[d]	s	~3.03	~330[d]
	Band 3		
$\pi(\mathrm{Ru-O,Ru_2}) \rightarrow \pi^*(\mathrm{Ru_2})$ [a][e][f][g]	w	~2.35[b](~2.16[c])	~425(~463)
$\pi(\mathrm{Cl}) \rightarrow \pi^*(\mathrm{Ru_2})$[a] or $\sigma(\mathrm{Ru_2}) \rightarrow \sigma^*(\mathrm{Ru_2})$[e] or $\delta(\mathrm{Ru_2}) \rightarrow \pi^*(\mathrm{Ru_2})$[f] or $\sigma(\mathrm{Cl}) \rightarrow \pi^*(\mathrm{Ru_2})$[d]	sh	(~1.76)[c]	~568
	Band 4		
$\delta(\mathrm{Ru_2}) \rightarrow \delta^*(\mathrm{Ru_2})$[a][f][g]	vw	~1.04[b]	~961
$\delta(\mathrm{Ru_2}) \rightarrow \pi^*(\mathrm{Ru_2})$[a]	vw	~0.92[b]	~1087

[a]From Ref.[38]. [b]Molar absorptivity in solution from Ref.[55] [c]Band maxima in solid state from Ref.[56]. [d]Band maxima in solution[34] [e]Band maxima from Ref.[21]. [f]From Ref.[57]. [g]From Ref.[27]. $\sigma/\pi/\delta/\delta^*/\sigma^*/\delta^*(\mathrm{Ru_2})$ denote the $\mathrm{Ru-Ru}$ character of mainly Ru orbitals. $\pi(\mathrm{Ru-O,Ru_2})$ is a predominantly Ru-O orbital, but with significant (24%) Ru-Ru character. $\pi(\mathrm{X})$ denote Axial halide ligand. $\pi(\mathrm{Cl})$ denote predominantly Cl lone pairs orbitals with π overlap. $\sigma(\mathrm{Cl})$ denote predominantly Cl lone pairs orbitals with σ overlap. Used convention from Ref.[27][56] for intensities: w (weak), vw (very weak), s s(strong), vs (very strong), sh(shoulder). "or" implies ambiguously assigned.

The incorrect assignment were ruled out because $\delta(\mathrm{Ru_2}) \rightarrow \sigma_n(\mathrm{Ru_2})$ and $\delta(\mathrm{Ru_2}) \rightarrow \sigma_n'(\mathrm{Ru_2})$ are not dipole allowed, the $\sigma_n(\mathrm{Ru_2})$ MO was predicted at much higher energy and the $\delta(\mathrm{Ru_2}) \rightarrow \delta^*(\mathrm{Ru_2})$ transition, which should be accurately simulated for systems of $(\delta)^2(\delta^*)^1$ configuration,[10, 38, 56, 59] lied at much lower energy. Band 3 has been reported to occur in two components: a primary maximum at ~463 nm (analogous to the band at ~425 nm in solution) and a shoulder/secondary maximum at ~568 nm.[28, 34, 56, 57] This has sparked discussion about the reason for this feature. On the one hand, prior to the development of DFT, Norman *et al.*[38] calculated using SCF-Xα-SW, proposed that the splitting into two components (primary and shoulder band) in the solid phase could be due to the lifting of the removal of the δ^* and π^* orbital degeneracies in crystal of low symmetry, and it was proposed that the calculated maximum (502 nm) was essentially the average energy of the two experimental maxima (510 nm), implying that the optimized geometry corresponds to the average structure between the highly symmetric and modestly symmetric structures.

Another hypothesis suggested by Norman was that the shoulder could be due to $\pi(\mathrm{Cl}) \rightarrow \pi^*(\mathrm{Ru_2})$ LMCT at 535 nm, therefore the assignment.[38] The latter assignment was accepted by some[28] and ignored by others[57] who advocated for the $\delta(\mathrm{Ru_2}) \rightarrow \pi^*(\mathrm{Ru_2})$ metal-based transition (Table 1.1). Notably, the pioneering characterization should considered with caution because it was based on the archaic density-based method SCF-Xα-SW, which was proposed by John Slater in 1950 to as brilliant replacement of HF,[60] but in current DFT classification it is equivalent to an exchange-only LSDA functional in the gas phase. Such a functional is of relatively mediocre quality, which leads to the consideration based on more sophisticated DFT functionals. Indeed, Castro *et al.* using advanced DFT functionals, recently yielded different data.[21] Although Castro *et al.* did not specifically mention the shoulder band issue, their TD-DFT results predicted a $\sigma(\mathrm{Ru_2}) \rightarrow \sigma^*(\mathrm{Ru_2})$ (Table 1.1) transition at 529.5 nm in the gas phase. This was the closer transition to the experimental shoulder in question and contradictory to the characterization by Norman. The $\pi(\mathrm{Cl}) \rightarrow \pi^*(\mathrm{Ru_2})$ LMCT was predicted in the solvent phase but it was at 680 nm, which was much lower energy than that of Norman, but was in good agreement with the spectrum recorded by Barral *et al*.[34] The latter, whose work produced the

spectra of a cohort $Ru_2(\mu\text{-}O_2CR)X$ (X=Cl, Br, or I) compounds in various solvents, attributed the $\sigma(\mathrm{Cl}) \rightarrow \pi^*(\mathrm{Ru_2})$ LMCT to band 3 on the basis of its sensitivity to the type of axial ligands.[34] Band 3 was only marginally impacted by the change from Cl to Br, whereas a large red-shift is observed for $[Ru_2(\mu\text{-}O_2CR)_4I_2]^-$ (Figure 1.7A).[22] Unlike the experimentally measured spectrum, the TD-DFT simulated spectrum (Figure 1.7B) showed a large shift even when switching from Cl to Br. This stark difference left unexplained. According to the ascribed transition of band 3, *viz.* $\pi(\mathrm{Ru-O,Ru_2}) \rightarrow \pi^*(\mathrm{Ru_2})$, it should virtually unaffected variation of axial ligand. Therefore, it was proposed that it is possible that some axial ligand CT contributes to the transition.[22]

The very weak NIR band 4 at ~961 nm was initially $\delta(\mathrm{Ru_2}) \rightarrow \delta^*(\mathrm{Ru_2})$, [38] by analogy with similar band of Mo_2 complexes.[28] Later, detailed single crystal polarized optical spectroscopy and vibrational studies confirmed that indeed the band is a *z*-polarized $\delta(\mathrm{Ru_2}) \rightarrow \delta^*(\mathrm{Ru_2})$ transition.[27] However, some studies have reported an additional maximum at ~1087 nm,[38, 55, 57] which was assigned to vibronically allowed but spin-forbidden $\delta(\mathrm{Ru_2}) \rightarrow \pi^*(\mathrm{Ru_2})$ transition[38] because it was characterized by a weak oscillator strength. According to Miskowski *et al.,*[57] such a transition would occur in the visible shoulder band (~630 nm) region, owing to repulsive forces within the molecule that elevate the $\Delta[\delta(\mathrm{Ru_2}) - \pi^*(\mathrm{Ru_2})]$ energy gap. However, this transition was sensitive to the type of axial ligand, possibly because it mixed with some ligand character, but the Miskowski did not intend on explaining this observation and uncertainty still lurks whether the transition should be part of the visible shoulder band or the NIR ($\delta(\mathrm{Ru_2}) \rightarrow \delta^*(\mathrm{Ru_2})$) band.[57] Band 4 in the measured spectrum is virtually unaffected[22, 27, 57] by the change of axial ligand coordination, which was consistent with the predominantly metal character of this band (Table 1.1). The simulated TD-DFT spectrum did, however, demonstrate the red-shift of band 4 (Figure 1.7B) when changing from Cl, Br, to I. The disparity is still a mystery.[21]

1.2.2 Absorption spectroscopy of mixed-ligands $Ru_2(\mu\text{-}O_2CR)_{4-n}(Rap)_nX$ derivatives

Complexes with the formula $Ru_2(\mu\text{-}Rap)_n(\mu\text{-}O_2CR')_{4-n}Cl$ (n=1-4) exhibit quite similar UV-Vis spectroscopic behavior characterized by four absorption bands (Figure 1.8A): a very strong UV

band below ~400 nm (band 1), a weak band in the 400 nm-500 nm (band 2A and 2B) visible range, a strong band in the visible range (band 3A and 3B) and a NIR band ~990 nm (band 4). The electronic transition assignments were not included in the initial report by Cotton *et al.* of $Ru_2(\mu\text{-ap})_4Cl$, which was the first reported Ru_2 incorporating an ap ligand.[61]

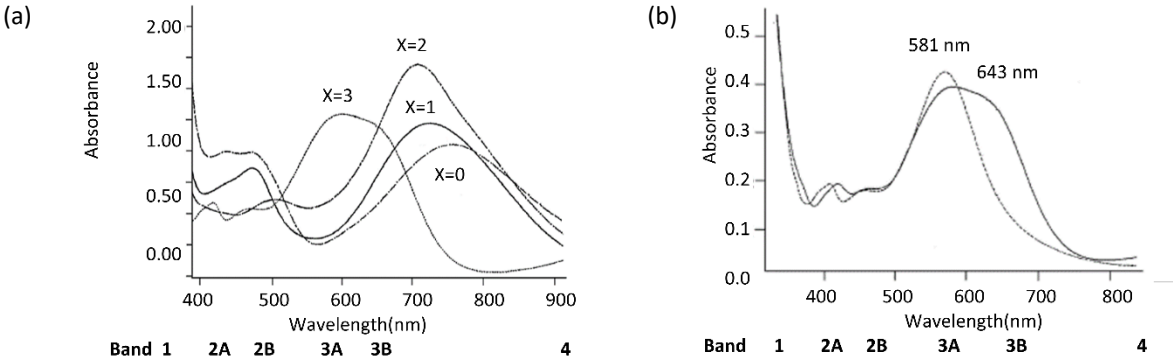

Figure 1.8 (a) Experimental UV-Vis spectra of $Ru_2(\mu\text{-}OC_2CH_3)_X(\mu\text{-2-Fap})_{4-X}Cl$ in neat DCM and (b) UV-Vis spectra of $Ru_2(\mu\text{-}O_2CCH_3)_3(\mu\text{-2-Fap})Cl$ in DCM before (-) and after (...) adding 0.1 M TBACl. Adapted from Ref.[43]

Subsequently, Chakravarty and Cotton[62] attempted to characterize the spectrum and proposed that band 2 and band 3 could be caused by transitions in $\pi(\mathrm{Cl}) \rightarrow \pi^*/\delta^*(\mathrm{Ru_2})$ and $\pi(\mathrm{N}) \rightarrow \pi^*(\mathrm{Ru_2})$, respectively, but admitted that "a more definite assignment would require a thorough MO calculation on the system".

To date, only the $Ru_2(\mu\text{-ap})_4Cl$ has been characterized theoretically. On one hand, the groups of Ren *et al.* thoroughly characterized the UV-Vis spectra of $Ru_2(\mu\text{-ap})_4X$,[64-70] but the axial ligands X were generally covalently coordinated carbon-based axial ligands, instead of labile halogen ligands that are of interest herein. On the other hand, the group of Berry *et al.*[63] fully characterized the spectrum of $Ru_2(\mu\text{-ap})_4Cl$, which lack, however, the shoulder band of $Ru_2(\mu\text{-Rap})_n(\mu\text{-}O_2CR')Cl$, which the unique feature associated with the mixed-ligand mono-ap complexes (Figure 1.8A) and has been a hot topic of discussion to be squared off herein.

Although, Kadish *et al.*[14-17, 43, 44, 47, 71, 72] extensively investigated $Ru_2(\mu\text{-Rap})(\mu\text{-}O_2CR')_3Cl$, their spectroscopic UV-Vis spectrum interpretation of these complexes was not based on definitive calculation, but solely relied on the UV-Vis spectrum of $Ru_2(\mu\text{-}O_2CR)_4Cl$ (Figure 1.8A) or on the work of Berry *et al.*,[63] both which clearly do not paint the full picture regarding the peculiar nature of $Ru_2(\mu\text{-Rap})(\mu\text{-}O_2CR')_3Cl$.

For the $Ru_2(\mu\text{-Rap})(\mu\text{-}O_2CR')_3Cl$ complex, band 1 has not yet been assigned. Bands 2 and 3 can be separated into 2A, 2B and 3A, 3B, respectively (Table 1.2). Band 2A has been attributed to $\pi(\mathrm{N/aryl}) \rightarrow \sigma^*/\pi^*/\delta^*(\mathrm{Ru_2})$ LCMT.[63] Interestingly, Band 2A (λ_{max}) was revealed to linearly increase with the Hammett substituent constant ($\Sigma\sigma$) of Rap,[47] which was attributed to possible stabilization of MOs by analogy with Mo_2 complexes,[73] and a change in the $\pi(\mathrm{N})$-donation (c.f. 1.1.3) by its close proximity the EDG or EWG on the Rap.

Table 1.2 Literature Assignment of electronic absorption transitions in $Ru_2(\mu\text{-Rap})_n(\mu\text{-}O_2CR')_{4-n}Cl$ compounds

Assignment	Intensity	$\lambda_{max}(\mathrm{nm})^{[a]}\ (\mu - \mathrm{Rap})_n$			
		$n=1$	$n=2$	$n=3$	$n=4$
	Band 2A				
$\pi(\mathrm{N/aryl}) \rightarrow \sigma^*/\pi^*/\delta^*(\mathrm{Ru_2})$[b]	w	415	431	429	428
	Band 2B				
$\sigma/\pi/\delta(\mathrm{Ru_2}) \rightarrow \delta^*(\mathrm{Ru_2})$[b]	w	464	513	469	463
	Band 3A				
$\pi(\mathrm{Ru-O/N, Ru_2}) \rightarrow \pi^*(\mathrm{Ru_2})$[a][b] and $\delta(\mathrm{Ru_2})/\pi(\mathrm{N}) \rightarrow \pi^*(\mathrm{Ru_2})$[b]	s	581	682	728	750
	Band 3B				
$\pi(\mathrm{Cl}) \rightarrow \pi^*(\mathrm{Ru_2})$[c] or $\delta(\mathrm{Ru_2}) \rightarrow \pi^*(\mathrm{Ru_2})$[b]	sh	643			
	Band 4				
$\delta(\mathrm{Ru_2}) \rightarrow \delta^*(\mathrm{Ru_2})$[a][b] or $\delta(\mathrm{Ru_2}) \rightarrow \pi^*(\mathrm{Ru_2})$[c]	vw	990			

[a]From Ref.[43, 63]. [b]From Ref.[63]. [c]From Ref.[47]. $\sigma/\pi/\delta/\delta^*/\sigma^*/\delta^*(\mathrm{Ru_2})$ denote the $\mathrm{Ru-Ru}$ character of mainly Ru orbitals. $\pi(\mathrm{Ru-O, Ru_2})$ is a predominantly Ru-O orbital, but with significant (24%) Ru-Ru character. L denote axial halide ligand. $\pi(\mathrm{L})$ denote predominantly L lone pairs orbitals with π overlap. Used convention[27, 56] for intensities: w (weak), vw (very weak), s (strong), vs (very strong), sh(shoulder). "or" implies ambiguously assigned; "and" or "/" imply multiple contributing transitions.

Multiple $\mathrm{Ru_2} \rightarrow \mathrm{Ru_2}$ excitations, notably the $\sigma/\pi/\delta(\mathrm{Ru_2}) \rightarrow \delta^*(\mathrm{Ru_2})$ transitions, were proposed to cause band 2B,[47, 63] which is a common feature of complexes with strong EWG on Rap.[43, 47]

The $\pi(\mathrm{Ru}-\mathrm{N},\mathrm{Ru}_2) \rightarrow \pi^*(\mathrm{Ru}_2)$ LMCT and the $\pi(\mathrm{N}) \rightarrow \pi^*(\mathrm{Ru}_2)$ and $\delta(\mathrm{Ru}_2) \rightarrow \pi^*(\mathrm{Ru}_2)$ Ru-based transitions, were proposed for band 3A, by analogy with $Ru_2(\mu\text{-}O_2CR)_4Cl$ and $Ru_2(\mu\text{-}Rap)_4Cl$ complexes[47] (Table 1.2). This is consistent with observed sensitivity of band 3A to the number of coordinating Rap (Table 1.2), which was linearly red-shifting upon changing from $Ru_2(\mu\text{-}Fap)(\mu\text{-}O_2CR)_3Cl$ to $Ru_2(\mu\text{-}Fap)_4Cl$[43] and sensitive to the change in EWG or EDG on Rap.[47] The $\pi(\mathrm{Cl}) \rightarrow \pi^*(\mathrm{Ru}_2)$ LMCT has been attributed to the shoulder band, *viz.* band 3B.[47] The equilibrium between the chloride and solvent molecule in solution has been proposed to be the reason for the shoulder band. This has been supported by a linear correlation between the number ap ligand and band 3B,[43, 47] the disappearance of band 3B (Figure 1.8B) and of one of the cyclic voltammogram single-electron reduction peaks in excess chloride. However, none of the experimental evidence seems to explain why this feature is unique to the $Ru_2(\mu\text{-}Rap)(\mu\text{-}O_2CR)_3Cl$ and why it is observable in and sensitive to both coordinating and non-coordinating solvents.[43, 47] Band 4 has been tentatively assigned to the allowed $\delta(\mathrm{Ru}_2) \rightarrow \delta^*(\mathrm{Ru}_2)$ or $\delta(\mathrm{Ru}_2) \rightarrow \pi^*$ by analogy with similar weak NIR band in other Ru_2 complexes.[43, 47]

1.3 Aim

The objective of this research is to simulate the UV-Vis spectroscopic behavior of $Ru_2(\mu\text{-}2\text{-}Fap)(\mu\text{-}O_2CH_3)_3X$ species (where X = Cl, Br, or I), through TD-DFT calculations and reconcile the predicted and observed spectroscopic properties. The UV-Vis spectrum of neutral $Ru_2(\mu\text{-}2\text{-}Fap)(\mu\text{-}O_2CH_3)_3Cl$ will be calculated and fully characterized as to the electronic transitions responsible for the four experimentally observable absorption bands. The UV-Vis spectra of the cationic and anionic derivates will be simulated in water and the experimental spectrum will be deconvoluted in order to assess the previously postulated existence of an equilibrium between the neutral species, $Ru_2(\mu\text{-}2\text{-}Fap)(\mu\text{-}O_2CH_3)_3Cl$, and the cationic species, $Ru_2(\mu\text{-}2\text{-}Fap)(\mu\text{-}O_2CH_3)_3Cl$, in aqueous solution.

The UV-Vis spectra of the bromo, and iodo derivative will be simulated in order to assess the viability of methods that make use of band shifts to determine axial ligand coordination. Furthermore, the UV-Vis spectra of neutral species will also be calculated in DCM and DMSO to

investigate the experimentally observed solvatochromic shifts. The basic ideas are that the balance between the different cationic and neutral species that may be controlled by the choice of the solvent and that the UV-Vis spectra are highly sensitive to species in solution.

Chapter 2 Theoretical background

2.1 Wavefunction-based methods

2.1.1 *Ab initio* Hartree-Fock methods

In 1925, Erwin Schrödinger proposed the Schrödinger equation.[74] He was inspired by the work of Louis de Broglie[75] on the wave-particle duality. The Schrodinger equation (*2.1*) is a non-relativistic wave equation that governs the behaviour of a quantum mechanical system in a potential field:

$$\hat{\mathcal{H}}\Psi(\boldsymbol{r}) = E\Psi(\boldsymbol{r}) \qquad (2.1)$$

Notable is the energy, E, of the particle, which is associated with the eigenfunction, $\Psi(\boldsymbol{r})$ and the Hamiltonian operator, $\hat{\mathcal{H}}$, describing the system. When applied to a chemical system made up of N electrons and N_n nuclei, the Hamiltonian Eq. (*2.2*) [76, 77] can be constructed as:

$$\hat{\mathcal{H}} = \sum_{i=1}^{N}\left(-\frac{1}{2}\nabla_{\boldsymbol{r}_i}^2\right) + \sum_{\alpha=1}^{N_n}\left(-\frac{1}{2}\nabla_{\boldsymbol{R}_\alpha}^2\right) + \sum_{\alpha=1}^{N_n-1}\sum_{\beta=\alpha+1}^{N_n}\frac{Z_\alpha Z_\beta}{|\boldsymbol{R}_\alpha - \boldsymbol{R}_\beta|} - \sum_{i=1}^{N}\sum_{\beta=1}^{N_n}\frac{Z_\beta}{|\boldsymbol{r}_i - \boldsymbol{R}_\beta|} + \sum_{i=1}^{N-1}\sum_{j=i+1}^{N}\frac{1}{|\boldsymbol{r}_i - \boldsymbol{r}_j|} \qquad (2.2)$$

The above equation and other subsequent equations, henceforth, are written in atomic units,[‡] which means that known physical constants such as the mass and charge of an electron are set to 1. The first and second terms, containing the Laplacian operator, ($\nabla^2 = \frac{\partial^2}{\partial x^2} + \frac{\partial^2}{\partial y^2} + \frac{\partial^2}{\partial z^2}$), describes the energy of motion of the N electrons and N_n nuclei. The third term accounts for nuclei-nuclei repulsions between nuclei α and β, associated with nuclear charges Z_α and Z_β, respectively, and which are a distance $|\mathbf{R}_\alpha - \mathbf{R}_\beta|$ away from each other. The fourth term is the electron-nucleus attraction operator, which describes the interaction between an electron i and the N_n nuclei. The last term is the electronic self-repulsion, which describes how two electrons i and j, at a distance $|\mathbf{r}_i - \mathbf{r}_j|$, repel each other.

Since the mass of a nucleus is approximately 1800 times greater than that of an electron, the adiabatic or Born-Oppenheimer approximation,[78] developed by Born and Oppenheimer in

[‡] Expressed in atomic units (value in SI unit): Planck's reduced constant = 1 (1.055×10^{-34} J), the mass m = 1 (9.109×10^{-34} kg), and the charge e = 1 (1.602×10^{14} C), vacuum permittivity $4\pi\epsilon_0$ = 1 (1.113×10^{-10}) F.m^{-1}

1927, assumes that the velocity of nuclei and electrons are independent and that the nuclei are fixed relative to the electrons. As such, the nuclear kinetic energy can be neglected and the nucleus-nucleus repulsion is constant. Omitting the nuclear coordinate reduces the Schrödinger equation to:

$$\widehat{\mathcal{H}}_e \Psi_e(\boldsymbol{r}) = E_e \Psi_e(\boldsymbol{r}) \tag{2.3}$$

where $\widehat{\mathcal{H}}_e$, Ψ_e and E_e represent the electronic Hamiltonian, wavefunction and energy, all of which depend explicitly only on the coordinates of the electrons, under the adiabatic approximation. This approximation reduces the Hamiltonian in Eq.(*2.2*) to:

$$\widehat{\mathcal{H}}_e = \sum_{i=1}^{N} \left(-\frac{1}{2}\nabla_{r_i}^2\right) - \sum_{i=1}^{N}\sum_{\beta=1}^{N_n} \frac{Z_\beta}{|\boldsymbol{r}_i - \boldsymbol{R}_\beta|} + \sum_{i=1}^{N-1}\sum_{j=i+1}^{N} \frac{1}{|\boldsymbol{r}_i - \boldsymbol{r}_j|} \tag{2.4}$$

Despite this approximation, it is impossible to solve Eq. (2.3) analytically for a multi-electron chemical system. Therefore, the Hartree-Fock (HF) method involves simplifying assumptions or approximations to obtain solutions for an N-electron system as a polyelectronic wavefunction. One of those required approximations is that, given that electrons are fermion, they obey the Pauli exclusion principle, the polyelectronic wavefunction. Therefore, this wavefunction is required to be constructed from a Slater determinant,[79] Φ_{SD}, which is an anti-symmetric wavefunction of fictitious monoelectronic wavefunctions ϕ_i, which are in turn constructed from a product of a spatial orbital and an α (or β) electron spin function, which is also called spin orbital:

$$\Phi_{SD}(\boldsymbol{r}) = \frac{1}{\sqrt{N!}} \begin{vmatrix} \phi_1(\boldsymbol{r}_1) & \cdots & \phi_N(\boldsymbol{r}_1) \\ \vdots & \ddots & \vdots \\ \phi_1(\boldsymbol{r}_N) & \cdots & \phi_N(\boldsymbol{r}_N) \end{vmatrix} \tag{2.5}$$

Each monoelectronic wavefunction describes an occupied molecular orbital (MO) of the multi-electron chemical system. The spin orbitals are orthogonal:

$$\int \phi_i^* \phi_j d\boldsymbol{r} = \delta_{ij} = \begin{cases} 0 \; if \; i = j \\ 1 \; if \; i \neq j \end{cases} \tag{2.6}$$

where δ_{ij} the Kronecker delta. Another approximation is that a single determinant is used. This implies that the effect of dynamic correlation between electrons is completely excluded and the electron-electron repulsion effect is described as the average repulsive potential, which qualifies the HF theory as a mean-field approximation. The single Slater determinant, Φ_{SD}, can

also be expressed in terms of an antisymmetry operator $\hat{\mathrm{A}}$ acting on the diagonal elements of the determinant to enforce the required antisymmetry property:

$$\Phi_{SD}(\boldsymbol{r}) = \hat{A}[\phi_1(\boldsymbol{r}_1) \dots \phi_N(\boldsymbol{r}_N)] = \hat{A}\Pi$$

$$\hat{A} = \frac{1}{\sqrt{N!}} \sum_{p=0}^{N-1} (-\hat{1})^p \hat{P} = \frac{1}{\sqrt{N!}} \left[\mathbf{1} - \sum_{ij} \hat{P}_{ij} + \sum_{ijk} \hat{P}_{ijk} - \cdots \right] \tag{2.7}$$

The diagonal products, the permutation of electron coordinates and the identity operator are denoted as Π, $\hat{1}$, and $\hat{\mathrm{P}}$, respectively. The sum of $\hat{\mathrm{P}}_{ij}$ yields all possible permutations of two-electron coordinates, the sum of $\hat{\mathrm{P}}_{ijk}$ yields all possible permutations of three electron coordinates and so on. $\hat{\mathrm{A}}$ and $\hat{\mathcal{H}}_e$ are commutive and $\hat{\mathrm{A}}$ acting twice is equivalent to multiplying by $\sqrt{N!}$.[77]

Neglecting the constant nuclear-nuclear repulsion under the adiabatic approximation, the total energy of the single Slater determinant can be written as:

$$E = \sum_{i=1}^{N} h_i + \frac{1}{2} \sum_{i=1}^{N} \sum_{j=1}^{N} (J_{ij} - K_{ij}) \tag{2.8}$$

The energy consists of a one-electron operator h_i describing the motion of electron i in the presence of all the nuclei, and the two-electron Coulomb and exact exchange[80] integrals J_{ij} and K_{ij} that represent the classical and quantum mechanical electron-electron interaction, respectively. These operators can be expressed as follows:[77]

$$h_i = \int \phi_i^*(\boldsymbol{r}_1) \left[\sum_{i=1}^{N} \left(-\frac{1}{2} \nabla_{\boldsymbol{r}_i}^2 \right) - \sum_{\beta=1}^{N_n} \frac{Z_\beta}{|\boldsymbol{r}_i - \boldsymbol{R}_\beta|} \right] \phi_i(\boldsymbol{r}_1) d\boldsymbol{r}_1 = \langle \phi_i | \hat{h}_i | \phi_i \rangle \tag{2.9}$$

$$J_{ij} = \int \phi_i^*(\boldsymbol{r}_1) \phi_j^*(\boldsymbol{r}_2) \frac{1}{|\boldsymbol{r}_1 - \boldsymbol{r}_2|} \phi_i(\boldsymbol{r}_1) \phi_j(\boldsymbol{r}_2) d\boldsymbol{r}_1 d\boldsymbol{r}_2 = \langle \phi_i \phi_j | \hat{g}_{12} | \phi_i \phi_j \rangle \tag{2.10}$$

$$K_{ij} = \int \phi_i^*(\boldsymbol{r}_1) \phi_j^*(\boldsymbol{r}_2) \frac{1}{|\boldsymbol{r}_1 - \boldsymbol{r}_2|} \phi_i(\boldsymbol{r}_2) \phi_j(\boldsymbol{r}_1) d\boldsymbol{r}_1 d\boldsymbol{r}_2 = \langle \phi_i \phi_j | \hat{g}_{12} | \phi_j \phi_i \rangle \tag{2.11}$$

where $\hat{g}_{12} = \frac{1}{|\boldsymbol{r}_1 - \boldsymbol{r}_2|}$. The angle brackets in Eq(*2.9*) to Eq (*2.11*) denote the integral of a wavefunction "ket" or $|\phi\rangle$, with its complex conjugate "bra",$\langle\phi|$, that is, $\int \phi_i^*(\hat{x}\phi_j) d\boldsymbol{r} = \langle \phi_\mathrm{i} | \hat{x} | \phi_\mathrm{i} \rangle$. The classical self-interaction or self-repulsion errors in Eq(2.8) given by $J_{ii} = \langle \phi_i \phi_i | \hat{g}_{12} | \phi_i \phi_i \rangle$, is corrected by the numerically equivalent $K_{ii} = \langle \phi_i \phi_i | \hat{g}_{12} | \phi_i \phi_i \rangle$ term.

To determine a set of MOs that generates the lowest total energy, the energy is varied in such a way that the MOs remain orthonormal. An elegant way of enforcing orthonormality is through the method of Lagrange multipliers, such that, the variation in the Lagrange function, δL, must be zero with respect to a change in MOs:

$$\delta L = \delta E - \sum_{ij}^{N} \lambda_{ij}\left(\langle \delta\phi_i | \phi_j \rangle - \langle \phi_i | \delta\phi_j \rangle\right) = 0 \qquad (2.12)$$

$$\delta E = \sum_{i}^{N} \left(\langle \delta\phi_i | \hat{F}_i | \phi_i \rangle + \langle \phi_i | \hat{F}_i | \delta\phi_j \rangle\right) \qquad (2.13)$$

where λ_{ij} denotes a Lagrange multiplier and $\hat{F}_{\mathrm{i}}$ is the effective energy Fock operator. The Fock operator is applied to every electron in the Slater determinant, describing their kinetic energy and attraction to all the nuclei, as well as the mean repulsive potential (via $\hat{J}_j$ and $\widehat{K}_j$) of each electron toward the other *N-1* electrons:[77]

$$\hat{F}_i = \hat{h}_i + \sum_{j}^{N} \left(\hat{J}_j - \widehat{K}_j\right) \qquad (2.14)$$

The variational principle states that the desired orbitals are those that make $\delta L = 0$ with respect to the MOs. This yields the following HF equations:

$$\hat{F}_i \phi_i = \lambda_{ij} \phi_i \qquad (2.15)$$

The HF equations can be simplified by using a unitary transformation that makes the matrix of Lagrange multipliers diagonal, that is, $\lambda_{ij} = 0$ and $\lambda_{ii} = \varepsilon_i$. The transformation results in a set of pseudo-eigenvalue equations with a new set of eigenfunctions (ϕ'), called canonical MOs:

$$\hat{F}_i \phi_i' = \varepsilon_i \phi_i' \qquad (2.16)$$

where ε_i is a canonical MO energy. Hence, by dropping the prime notation and letting ϕ be a canonical MO, the Lagrange multipliers become equivalent to the MO energies. The mathematical functions for the MOs required to compute MO energies from the HF equations are unknown and the HF equations do not prescribe a way of obtaining them. Thus, one way of approximating the MOs is as a Linear Combination of Atomic Orbitals (LCAO), belonging to what is termed a basis set:

$$\phi_i = \sum_{\mu}^{k.basis} c_{i\mu} \varphi_\mu \qquad (2.17)$$

where, the φ_μ and $c_{i\mu}$ denote atomic orbitals and their associated coefficient MO i, respectively. Although a basis set is generally not a solution to the multielectron atomic HF equation, the approximated energy becomes better as the basis set size (or k_{basis}) increases. Each atomic orbital in LCAO is itself a linear combination of functions (typically Gaussian functions). Hence, the MOs in the equation (*2.16*) can be written in terms of a basis set, which leads to the Roothaan-Hall equations:

$$\boldsymbol{FC} = \boldsymbol{SC\varepsilon}$$

$$F_{\mu v} = \langle\varphi_\mu|\hat{h}_i|\varphi_v\rangle + \sum_{\gamma\sigma}^{kbasis} D_{\gamma\sigma}\left[\langle\varphi_\mu\varphi_\gamma|\hat{g}_{ij}|\varphi_v\varphi_\sigma\rangle - \langle\varphi_\mu\varphi_\gamma|\hat{g}|\varphi_\sigma\varphi_v\rangle\right];\ S_{\mu v} = \langle\varphi_\mu|\varphi_v\rangle \qquad (2.18)$$

$$D_{\gamma\sigma} = \sum_{j}^{occ.MO} c_{j\gamma}c_{j\sigma}$$

where $\mathbf{F}$, $\mathbf{C}$, $\mathbf{S}$ and $\boldsymbol{\varepsilon}$ are the matrices of Fock elements, MO coefficient of basis functions, overlap elements between basis functions and MO energies, respectively. Each $F_{\mu v}$ Fock element consists of integrals involving the one-electron operators and a sum over occupied orbitals of electron repulsion integrals multiplied by the density matrix $D_{\gamma\sigma}$, which is a sum of products of MO coefficients as shown in Eq. (2.18). In practical applications, the Roothaan-Hall equations is utilized to compute the eigenvalues of the Fock matrix. The diagonalization of the Fock matrix is necessary to establish the values of the unknown MO coefficients. However, acquiring knowledge of all MO coefficients is a prerequisite for the evaluation of the total Fock matrix. Hence, an estimation of the coefficients is initially made, following which the Fock matrix is constructed and diagonalized. Thereafter, the new coefficient set is incorporated to compute a new Fock matrix, and the process is iterated until the coefficient set used to generate the Fock matrix is consistent with the diagonalization results (within a stipulated threshold). Subsequently, this coefficient set enables the determination of a self-consistent field solution. This iterative process is called the Hartree-Fock Self-Consistent Field (HF-SCF) approach.

Every Fock matrix element is comprised of four independent basis functions in the two-electron integrals, which leads to the four-center two-electron computational bottleneck, making the calculations grow by $O(\mu^4)$.[77] However, the primary flaw in HF theory is that it ignores the

dynamic correlation in electronic motion that exists between electrons with different spins, leading to a larger HF energy than exact energy.

2.2 Density functional theory

2.2.1 Density-dependent Hamiltonian

The electron density can be defined as the probability of finding any one of N electrons, with arbitrary spin within a volume element $d\boldsymbol{r}_1$, while all other N-1 electrons can be located anywhere. This can be mathematically expressed as follows:[81]

$$\rho(\boldsymbol{r}) = N \int \dots \int |\Psi(\boldsymbol{x}_1, \boldsymbol{x}_2, \dots, \boldsymbol{x}_N)|^2 d\boldsymbol{s}_1 d\boldsymbol{x}_2 \dots d\boldsymbol{x}_N \qquad (2.19)$$

where $\boldsymbol{r}$ and $\boldsymbol{s}$ are spatial and spin coordinates of an electron respectively, whereas $\boldsymbol{x}$ represents both spatial and spin coordinates.

The probability of jointly finding two electrons with spin $\boldsymbol{s}_1$ and $\boldsymbol{s}_2$, each within its own volume elements $d\boldsymbol{r}_1$ and $d\boldsymbol{r}_2$, is described by the pair density:[81]

$$\rho(\boldsymbol{x}_1, \boldsymbol{x}_2) = N(N-1) \int \dots \int |\Psi(\boldsymbol{x}_1, \boldsymbol{x}_2, \dots, \boldsymbol{x}_N)|^2 d\boldsymbol{x}_3 \dots d\boldsymbol{x}_N \qquad (2.20)$$

The pair density accounts for electron correlation and can be thought of as the electron density produced by two isolated electrons interacting with a remnant, called the exchange-correlation hole,[82] defined to accommodate for the energy errors imposed by assuming classical behavior:

$$h_{XC}(\boldsymbol{x}_1, \boldsymbol{x}_2) = \frac{\rho(\boldsymbol{x}_1, \boldsymbol{x}_2)}{\rho(\boldsymbol{x}_1)} - \rho(\boldsymbol{x}_2) \qquad (2.21)$$

The hole function $h_{XC}(\boldsymbol{x}_1, \boldsymbol{x}_2)$ notation implies that the evaluation of the function on an electron located at $\boldsymbol{r}_1$ depends on all other electrons located at $\boldsymbol{r}_2$. This makes it difficult to define an exact non-classical expression for $h_{XC}(\boldsymbol{x}_1, \boldsymbol{x}_2)$.[83, 84] Consequently, for a system of interacting electrons and nuclei, the kinetic energy

(*2.22*), the electron-nucleus (2.23), and electron-electron (2.24) potential energies composing the Hamiltonian (c.f. (2.4)) can be re-formulated in terms of the density as follows:

$$T[\rho(r)] = -\frac{1}{2} \int_{\tilde{r}=r} \nabla_r^2 \rho(r, \tilde{r}) dr \qquad (2.22)$$

$$V_{ne}[\rho(r)] = \int_r v(r)\rho(r,r')\,dr \tag{2.23}$$

$$V_{ee}[\rho(r_1,r_2)] = \frac{1}{2}\int_{r_1}\int_{r_2}\frac{\rho(r_1,r_2)}{|r_1-r_2|}dr_1dr_2 \tag{2.24}$$

Substituting Eqs. (2.21) and (2.23) into (2.24) gives:

$$V_{ee}[\rho(\boldsymbol{r}_1,\boldsymbol{r}_2)] = \underbrace{\frac{1}{2}\int_{\boldsymbol{r}_1}\int_{\boldsymbol{r}_2}\frac{\rho(\boldsymbol{r}_1)\rho(\boldsymbol{r}_2)}{|\boldsymbol{r}_1-\boldsymbol{r}_2|}d\boldsymbol{r}_1d\boldsymbol{r}_2}_{J(\rho)} + \underbrace{\frac{1}{2}\int_{\boldsymbol{r}_1}\int_{\boldsymbol{r}_2}\frac{\rho(\boldsymbol{r}_1)h_{XC}(\boldsymbol{r}_1,\boldsymbol{r}_2)}{|\boldsymbol{r}_1-\boldsymbol{r}_2|}d\boldsymbol{r}_1d\boldsymbol{r}_2}_{E_{nc}(\rho)} \tag{2.25}$$

The classical Coulomb and non-classical interactions between two electrons, are denoted $\mathrm{J}(\rho)$ and $\mathrm{E}_{nc}(\rho)$, respectively. The latter accounts for the exchange, correlation, and a correction for self-interaction, which corrects the errors in $\mathrm{J}(\rho)$ due to the classical mechanics approximation.

2.2.2 The Hohenberg and Kohn theorems

Two basic theorems proved by P. Hohenberg and W. Kohn[85] in 1964 supported the use of electron density $\rho(\mathbf{r})$ as a variable for describing the electronic structure of a system (Eq. (2.3)):

Theorem 1: The first Hohenberg-Kohn[85] (HK) theorem is an existence theorem, which states that the total GS energy, E_0, of an electronic system in an external potential, $v(\mathbf{r})$, is a unique functional of its $\rho(\mathbf{r})$; since $v(\mathbf{r})$ determines $\widehat{\mathcal{H}}$, the GS of the system is entirely determined by $\rho(\mathbf{r})$.The proof of theorem 1 was accomplished via *reductio ad absurdum*: Assume the contrary, *viz.* $\rho(\mathbf{r})$ give rise to two different external potentials $v(\mathbf{r})$ and $v'(\mathbf{r})$, each associated with different $\widehat{\mathcal{H}}$ and $\widehat{\mathcal{H}}'$, respectively, such that the Schrödinger equation yields two different normalized wavefunction Ψ and Ψ', and two different eigenvalues E_0 and E'_0, respectively. The variational theorem of molecular orbital (MO) theory requires that the expectation value of $\widehat{\mathcal{H}}$ over Ψ' be greater than the energy E_0:

$$E_0 < \langle\Psi'|\widehat{\mathcal{H}}|\Psi'\rangle = \langle\Psi'|\widehat{\mathcal{H}} - \widehat{\mathcal{H}}' + \widehat{\mathcal{H}}'|\Psi'\rangle \tag{2.26}$$

$$= \langle\Psi'|\widehat{\mathcal{H}} - \widehat{\mathcal{H}}'|\Psi'\rangle + \langle\Psi'|\widehat{\mathcal{H}}'|\Psi'\rangle$$

$$= \int_r [v(\boldsymbol{r}) - v'(\boldsymbol{r})]\rho(\boldsymbol{r})\,d\boldsymbol{r} + E'_0 \tag{2.27}$$

Because the primitive variables were not differentiated, their indices in the inequality Eq. (*2.27*) can be switched to obtain the equally valid result:

$$E'_0 < \int_{\boldsymbol{r}} [v'(\boldsymbol{r}) - v(\boldsymbol{r})]\rho(\boldsymbol{r})\, d\boldsymbol{r} + E_0 \tag{2.28}$$

Since it was initially assumed that $\rho(\boldsymbol{r})$ is associated with both $v'(\boldsymbol{r})$ and $v(\boldsymbol{r})$, summing Eq. (2.27) and Eq. (2.28) eliminates the integrals and results in:

$$E_0 + E'_0 < E'_0 + E_0 \tag{2.29}$$

This indetermination (2.29) indicates that the initial assumption was incorrect. Hence, the non-degenerate $\rho(\boldsymbol{r})$, must uniquely determine $v(\boldsymbol{r})$, and thus $\widehat{\mathcal{H}}$ and Ψ. Consequently, $\rho(\boldsymbol{r})$ uniquely determines all the GS properties, including the number of electrons N and the total GS energy E, which can be written as:

$$N[\rho(\boldsymbol{r})] = \int_{\boldsymbol{r}} \rho(\boldsymbol{r})\, d\boldsymbol{r} \tag{2.30}$$

$$E[\rho(\boldsymbol{r})] = V_{ne}[\rho(\boldsymbol{r})] + T[\rho(\boldsymbol{r})] + V_{ee}[\rho(\boldsymbol{r})] = \int_{\boldsymbol{r}} v(\boldsymbol{r})\rho(\boldsymbol{r})\, d\boldsymbol{r} + F_{HK}[\rho(\boldsymbol{r})] \tag{2.31}$$

$$F_{HK}[\rho(\boldsymbol{r})] = T[\rho(\boldsymbol{r})] + V_{ee}[\rho(\boldsymbol{r})] \tag{2.32}$$

The energy of the electronic system can be computed exactly, if the functional, $\mathrm{F_{HK}}[\rho(\mathbf{r})]$, is known. Unfortunately, the exact formulation of the functionals $T[\rho(\mathbf{r})]$ and $V_{ee}[\rho(\mathbf{r})]$ and consequently $F_{\mathrm{HK}}[\rho(\mathbf{r})]$ is not known.

Theorem 2: The second theorem of HK[85] states that $F_{\mathrm{HK}}[\rho(\mathbf{r})]$ yields the exact GS energy if and only if ($\Leftrightarrow$) $\rho(\mathbf{r})$ is the exact GS electronic density. The proof of this theorem was accomplished via the variational theorem: Let $E(\psi)$ and $\tilde{E}(\tilde{\psi})$ be the GS and variational energy, respectively, of a system of N electrons. The variational principle ensures the existence of an energy minimum when $\tilde{\psi}$ tends to ψ:

$$E(\psi) = \min_{\tilde{\psi} \to \psi} \tilde{E}(\tilde{\psi}) \tag{2.33}$$

From this statement, one can deduce that:

$$\begin{gathered} E(\psi) \leq \tilde{E}(\tilde{\psi}) \\ \langle\psi|\widehat{\mathcal{H}}|\psi\rangle \leq \langle\tilde{\psi}|\widehat{\mathcal{H}}|\tilde{\psi}\rangle \\ \int \rho(\boldsymbol{r})\, v(\boldsymbol{r}) d\boldsymbol{r} + F_{HK}[\rho(\boldsymbol{r})] \leq \int \tilde{\rho}(\boldsymbol{r})\, v(\boldsymbol{r}) d\boldsymbol{r} + F_{HK}[\tilde{\rho}(\boldsymbol{r})] \\ E[\rho(\boldsymbol{r})] \leq \tilde{E}[\tilde{\rho}(\boldsymbol{r})] \end{gathered} \tag{2.34}$$

The first HK theorem and inequality (2.34), then gives:

$$E[\rho(\mathbf{r})] = \tilde{E}[\tilde{\rho}(\mathbf{r})] \Leftrightarrow \rho(\mathbf{r}) = \tilde{\rho}(\mathbf{r}) \tag{2.35}$$

Consequently, only by knowing the exact GS $\rho(\mathbf{r})$ will $F_{\mathrm{HK}}[\rho(\mathbf{r})]$ yield the exact GS $E[\rho(\mathbf{r})]$. The HK theorems are still rather insufficient because they do not prescribe a procedure of choosing $\tilde{\rho}(\mathbf{r})$ and even if $\rho(\mathbf{r})$ is known, the theorems do not guarantee the correct treatment of the

EES. In addition, computing $E[\rho(\mathbf{r})]$ as an expectation value of Ψ mapped is similar to wave mechanics, which is being avoided in DFT.

2.2.3 Kohn-Sham Equations

The functional $\mathrm{F_{HK}}[\rho(\mathbf{r})]$ (2.32) can be further separated into the kinetic energy ($T[\rho(\mathbf{r})]$), the classical Coulomb-repulsion ($J[\rho(\mathbf{r})]$) and a non-classical component $\mathrm{E}_{nc}[\rho(\mathbf{r})]$ consisting of XC and a correction for self-interaction:

$$F_{HK}[\rho(\boldsymbol{r})] = T[\rho(\boldsymbol{r})] + J[\rho(\boldsymbol{r})] + E_{nc}[\rho(\boldsymbol{r})] \tag{2.36}$$

The classical Coulomb repulsion is given by Eq.(2.25); however, expressions for the kinetic energy and non-classical contributions as a functional of the electron density are not known. Hence, in 1965 Kohn and Sham[86] suggested an approach that provides an estimate of the largest part of the kinetic energy, with the error due to the remaining part merged with the non-classical energy, which is the smaller term of $\mathrm{E}_{nc}[\rho(\mathbf{r})]$. The Kohn-Sham (KS) technique considers a *fictitious* system of non-interacting electrons where $\rho(\mathbf{r})$ equals the exact density of the real system of interacting electrons. In such a case, the exact kinetic energy of the fictitious system, T_{ft}, can be written using wave mechanics and one-electron orbitals as:

$$T_{ft}[\rho(\mathbf{r})] = \sum_{i=1}^{N} \langle \chi_i \left| -\frac{1}{2}\nabla_{\mathrm{r}}^{2} \right| \chi_i \rangle \tag{2.37}$$

$$\rho(\mathbf{r}) = \sum_{i=1}^{N}\sum_{s=1}^{N} |\chi_i(\mathbf{r}, s)|^2 \tag{2.38}$$

The KS orbitals, χ_i, are orthonormal wavefunctions of non-interacting electrons built from the basis set approximation of LCAO. The fictitious system avoids calculating the kinetic energy of the interacting electrons, making DFT feasible. Since T_{ft} is not equivalent to T, Kohn and Sham sugegsted the following separation of F_{HK}:

$$F_{HK}[\rho(\boldsymbol{r})] = T_{ft}[\rho(\boldsymbol{r})] + J[\rho(\boldsymbol{r})] + E_{XC}[\rho(\boldsymbol{r})] \tag{2.39}$$

The XC energy $E_{xc}[\rho(\mathbf{r})]$ is the potential and kinetic energy, ΔV and ΔT, respectively, missing in the fictitious system due to the neglect of electron-electron interactions and the error of self-interaction, which must be added to achieve the true energy of the interacting system:

$$E_{XC}[\rho(\boldsymbol{r})] = \underbrace{\left(T[\rho(\boldsymbol{r})] - T_{ft}[\rho(\boldsymbol{r})]\right)}_{\Delta T} + \underbrace{\left(V_{ee}[\rho(\boldsymbol{r})] - J[\rho(\boldsymbol{r})]\right)}_{\Delta V} \tag{2.40}$$

The total energy E is then the sum of the interacting and non-interacting components, which can be written in terms of the KS χ_i as follows:[81]

$$\begin{aligned} E[\rho(\boldsymbol{r})] &= T_{ft}[\rho(\boldsymbol{r})] + V_{ne}[\rho(\boldsymbol{r})] + J[\rho(\boldsymbol{r})] + E_{XC}[\rho(\boldsymbol{r})] \\ &= -\frac{1}{2}\int \nabla_{\boldsymbol{r}}^2 \rho(\boldsymbol{r},\tilde{\boldsymbol{r}})d\boldsymbol{r} + \frac{1}{2}\iint \frac{\rho(\boldsymbol{r}_1)\rho(\boldsymbol{r}_2)}{|\boldsymbol{r}_1-\boldsymbol{r}_2|}d\boldsymbol{r}_1 d\boldsymbol{r}_2 + \int \rho(\boldsymbol{r})\, v(\boldsymbol{r})d\boldsymbol{r} + E_{XC}[\rho(\boldsymbol{r})] \\ &= \sum_{i=1}^{N}\langle\chi_i(\boldsymbol{r})\left|-\frac{1}{2}\nabla_{r_i}^2\right|\chi_i(\boldsymbol{r})\rangle + \frac{1}{2}\sum_{i=1}^{N-1}\sum_{j=i+1}^{N}\iint \frac{|\chi_i(\boldsymbol{r}_1)|^2|\chi_j(\boldsymbol{r}_2)|^2}{|\boldsymbol{r}_1-\boldsymbol{r}_2|}d\boldsymbol{r}_1 d\boldsymbol{r}_2 \\ &\quad + \sum_{i=1}^{N}\int\sum_{\beta=1}^{M}|\chi_i(\boldsymbol{r})|^2\frac{Z_\beta}{|\boldsymbol{r}_i-\boldsymbol{r}_\beta|}d\boldsymbol{r} + E_{XC}[\rho(\boldsymbol{r})] \end{aligned} \tag{2.41}$$

Applying the variational principle to find the set of $\{\chi_i\}$ that would minimize E , similar to what is done in HF theory, results in the analogous KS equations:[81]

$$\underbrace{\left(-\frac{1}{2}\nabla_i^2 + \left[\int\frac{\rho(\boldsymbol{r}_2)}{|\boldsymbol{r}_1-\boldsymbol{r}_2|}d\boldsymbol{r}_2 - \sum_{\beta=1}^{M}\frac{Z_\beta}{|\boldsymbol{r}_i-\boldsymbol{r}_\beta|}d\boldsymbol{r} + V_{XC}(\boldsymbol{r})\right]\right)}_{\hat{h}_i^{KS}}\chi_i(\boldsymbol{r}) = \varepsilon_i\chi_i(\boldsymbol{r}) \tag{2.42}$$

where the terms in square brackets can be grouped to give the effective potential experienced by an electron in a KS orbital:

$$V_{eff}(\boldsymbol{r}) = \int\frac{\rho(\boldsymbol{r}_2)}{|\boldsymbol{r}_1-\boldsymbol{r}_2|}d\boldsymbol{r}_2 + V_{XC}(\boldsymbol{r}) - \sum_{\beta=1}^{M}\frac{Z_\beta}{|\boldsymbol{r}_i-\boldsymbol{r}_\beta|}d\boldsymbol{r} \tag{2.43}$$

The XC potential is defined as the functional derivative of the XC energy:

$$V_{XC}(\boldsymbol{r}) = \frac{\delta E_{XC}[\rho(\boldsymbol{r})]}{\delta\rho(\boldsymbol{r})} \tag{2.44}$$

It is worth noting that if the exact form of E_{XC} were known, the KS technique would yield the exact energy. Hence, DFT is an exact theory, unlike HF that is based on approximating the wavefunction as a Slater determinant of independent one-electron orbitals, which cannot yield the exact energy.

Two different spin orbitals with equal spatial parts have equal energies, they should however be different due to possessing different spin parts:

$$\begin{aligned} \chi_i(\mathbf{x}) &= \varphi_i(\mathbf{r})\alpha_i(\mathrm{s}) \\ \chi_j(\mathbf{x}) &= \varphi_i(\mathbf{r})\beta_i(\mathrm{s}) \end{aligned} \tag{2.45}$$

The KS operator $\hat{h}_i^{KS}$ (2.42) only has a spatial part and does not operate on spin functions. Consequently, for a closed shell system, to correct this anomaly $\rho(\mathbf{r})$ is redefined as:

$$\rho(\mathbf{r}) = 2\sum_{i=1}^{N/2}|\varphi_i(\mathbf{r})|^2 \qquad (2.46)$$

Since the density is required to solve the KS equations (Eq. (2.42)), but the density is also determined by solving these equations, the KS self-consistent field (SCF) approach (Figure 2.1) is used in practice to iteratively solve the KS equations. The initial density $\rho_0(\mathbf{r})$ is usually guessed in non-variational way, generally using the Harris functional.[87]

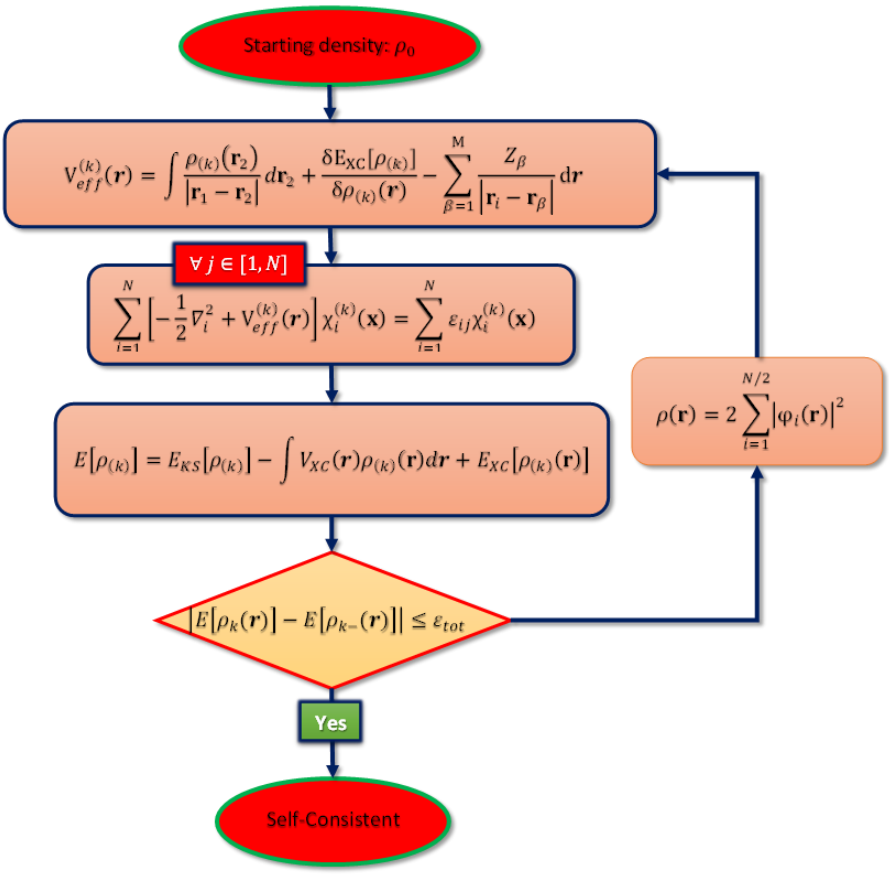

Figure 2.1 Schema summarizing the KS SCF procedure

This $\rho_0(\mathbf{r})$ is then used to calculate V_{eff} (2.43), which is subsequently used to solve the N expectation values ε_{ij} Eq (2.47) by multiplying from the LHS of Eq. (2.42) by $\chi_i{}^*$ and integrating over the space variables:

$$\varepsilon_{ij} = \langle \chi_i^*(\boldsymbol{r}) \left| \hat{h}_{ij}^{KS} \right| \chi_j(\mathbf{r}) \rangle \qquad (2.47)$$

The resulting $N \times N$ matrix of ε_{ij} is diagonalized and the total electronic energy of the system $E[\rho(\mathbf{r})]$ is then obtained from Eq.(2.41). The newly produced KS orbitals are re-circulated into

Eq. (2.46) to obtain $\rho(\mathbf{r})$, which is in turn used to re-evaluate V_{eff} (2.43). In practice, the cycle continues until $E[\rho(\mathbf{r})]$ is self-consistent, which means that its variation drops below a predefined threshold. This is called reaching self-consistency in k cycles (Figure 2.1). Determining the explicit exact form of $E_{XC}[\rho(\mathbf{r})]$ would be equivalent to finding the exact energy. This task is still impossible for now but numerous approximations exist, which leads to the various classes of DFT XC functionals discussed in the next section.

2.2.4 Ladder of XC functionals

Perdew proposed[88, 89] categorizing the approximations made when developing XC functionals by referring to the biblical account of "Jacob's dream" in which Jacob sees a ladder with one foot on Earth and the other end extending to heaven (Figure 2.2). The earth represents non-correlated HF whereas heaven is a reference to the exact XC functional. This ladder contains five rungs, and the idea is that as one climbs the ladder, the sophistication (and presumably accuracy) increases as each consecutive approximation builds on those before; however, at the expense of evaluation speed.

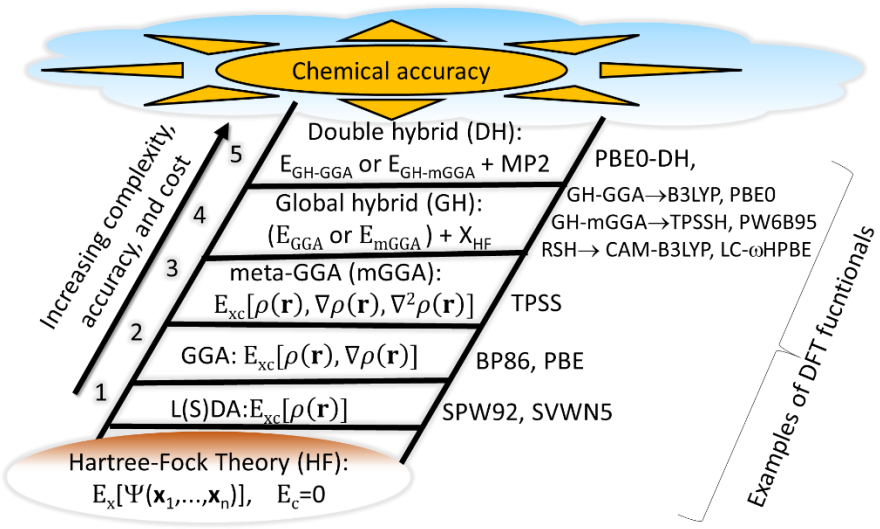

Figure 2.2 Classification of DFT XC functionals according to the Jacob's Ladder of J.P Perdew.

2.2.4.1 Local density approximation

The first rung is built on the local density approximation (LDA) and the local spin density approximation (LSDA), which depends only on the value of the electron density $\rho(\boldsymbol{r})$. The LDA assumes the system to be a uniform electron gas (UEG) having a locally constant or slowly varying $\rho(\boldsymbol{r})$. Every position $\boldsymbol{r}$ in space is associated with the XC energy per particle, $\varepsilon_{XC}^{LDA}[\rho(\boldsymbol{r})]$, that a UEG would have. The individual energy per particle integrated over the entire volume of space, gives the XC energy of the system:

$$E_{XC}^{LDA}[\rho(\boldsymbol{r})] = \int \varepsilon_{XC}^{LDA}[\rho(\boldsymbol{r})]\rho(\boldsymbol{r})d\boldsymbol{r} \tag{2.48}$$

In this approximation, the XC potential $\mathrm{V_{XC}}(\boldsymbol{r})$ (2.44) required for the resolution of the KS equations can be written as follows:

$$V_{XC}^{LDA}(\boldsymbol{r}) = E_{XC}^{LDA} + \frac{\rho(\boldsymbol{r})\delta E_{XC}^{LDA}[\rho(\boldsymbol{r})]}{\delta\rho(\boldsymbol{r})} \tag{2.49}$$

Approximations for the contributions of exchange and correlation can be explored separately. The Slater-Dirac (S) exchange, developed from the Thomas-Fermi model, is an accurate mathematical expression of the exchange energy density of a uniform electron gas:[90]

$$\varepsilon_X^{LDA}[\rho(\boldsymbol{r})] = -\frac{3}{4\pi}k_F(\boldsymbol{r}), \quad k_F(\boldsymbol{r}) = \sqrt[3]{3\pi^2\rho(\boldsymbol{r})} \tag{2.50}$$

The Fermi wavevector being $k_F(\boldsymbol{r})$. By contrast, the correlation part does not have an exact formula because it depends on the solution to the ground state wavefunction of the UEG.[91, 92] The VWN5,[92] PZ81,[93] and PW92 functionals[94] are the three most common approximations, which were created by fitting data for the UEG determined using quantum Monte Carlo simulations.[91] The LSDA accounts for magnetic or spin-polarized systems, using the two spin densities $\rho^{\alpha}(\boldsymbol{r})$ and $\rho^{\beta}(\boldsymbol{r})$ as the central inputs instead of $\rho(\boldsymbol{r})$:

$$E_{XC}^{LDA}[\rho^{\alpha}(\boldsymbol{r}), \rho^{\beta}(\boldsymbol{r})] = \int \varepsilon_{XC}^{LDA}[\rho^{\alpha}(\boldsymbol{r}), \rho^{\beta}(\boldsymbol{r})]\rho(\boldsymbol{r})d\boldsymbol{r} \tag{2.51}$$

By combining the Slater exchange and one of these correlation functionals, L(S)DA functionals like SVWN5, SPW92 can be built, which are exact for the UEG and well-performing for semiconductor and alloy systems, but are highly inaccurate for molecular properties[95-97]

2.2.4.2 Generalized gradient approximation

In order to address the inaccuracies of the L(S)DA and increase the scope of the applicability of DFT, the generalized gradient approximation (GGA), which makes up the second rung, was introduced. [98, 99] The GGA treats the system as a non-UEG and accounts for non-local effects by incorporating both $\rho(\boldsymbol{r})$ and its gradient $\nabla_{\mathbf{r}}\rho(\boldsymbol{r})$ into the expression for the energy density, as follows:

$$E_{XC}^{GGA}[\rho(\boldsymbol{r})] = \int \varepsilon_{XC}^{GGA}[\rho(\boldsymbol{r}), \nabla_{\boldsymbol{r}}\rho(\boldsymbol{r})]d\boldsymbol{r} \tag{2.52}$$

The exchange energy E_X^{GGA} can then be written as a sum of L(S)DA exchange E_X^{LDA} and a function $\mathcal{F}_X(\sigma)$ of the reduced gradient $|\nabla_{\mathbf{r}}\rho(\boldsymbol{r})|$:

$$E_X^{GGA}[\rho(\boldsymbol{r})] = E_X^{LDA}[\rho(\boldsymbol{r})] + \int \Delta\varepsilon[\rho]\, \mathcal{F}_X(\sigma)d\boldsymbol{r}\,, \quad \sigma[\rho(\boldsymbol{r})] = \frac{|\nabla_{\boldsymbol{r}}\rho(\boldsymbol{r})|}{\rho(\boldsymbol{r})^{\frac{4}{3}}} \tag{2.53}$$

The literature has suggested a number of expressions for $\mathcal{F}_X(\sigma)$,[100-105] such as that of the Perdew, Burke, and Ernzerhof (PBE) functional (2.54), which is a functional meant to replace[103] the complex 1991 Perdew Wang (PW91)[106] functional with the simpler expression:

$$\mathcal{F}_X^{PBE}(\sigma) = 1 + \lambda - \frac{\lambda}{1 + \frac{\mu}{\lambda}\sigma^2} \tag{2.54}$$

where μ is derived from the asymptotic behavior of the UEG approximation,[107, 108] while λ is derived from the asymptotic limit imposed by Lieb and Oxford.[109] PBE is a theoretical and non-empirical functional because it is only based on the UEG and fundamental physics constants. This functional is popular in the solid-state physics community and in geometry optimization and energy calculations.[98, 110] The BP86 functional,[101, 111] which is also widely used for geometry optimization and energy calculations (Figure 2.3),[98] is generated using the B88[111] exchange functional and the P86[101] correlation functional. Unlike PBE, the B88 exchange is empirically parameterized against the exchange energy of noble gas atoms.

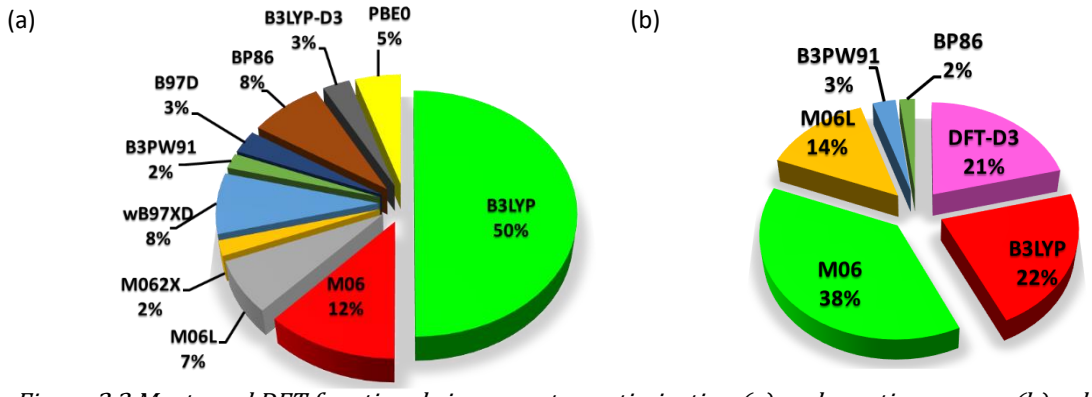

Figure 2.3 Most used DFT functionals in geometry optimization (a) and reaction energy (b) calculations in 2013-2014. Adapted from ref.[98]

2.2.4.3 Meta-generalized gradient approximation

GGA can be further improved through meta-GGA (mGGA) functionals, which add the Laplacian of the electronic density $\nabla^2_{\mathbf{r}}\rho(\boldsymbol{r})$ or the kinetic energy density $\tau(\boldsymbol{r})$ of the KS orbitals (2.55). The latter is identical to the von Weizsäcker kinetic energy[112] $\tau_W(\boldsymbol{r})$(2.56):

$$\tau(\mathbf{r}) = \frac{1}{2}\sum_{i}^{occupied} |\nabla_{\mathbf{r}}\varphi_i(\mathbf{r})|^2 \qquad (2.55)$$

$$\tau_W(\mathbf{r}) = \frac{|\nabla_{\mathbf{r}}\rho(\boldsymbol{r})|^2}{8\rho(\boldsymbol{r})} \qquad (2.56)$$

The orbital kinetic energy density and the Laplacian are related by the KS orbitals and effective potential V_{eff} (2.43):[80]

$$\tau(\mathbf{r}) = \frac{1}{2}\sum_{i}^{occupied} \varepsilon_i|\nabla_{\mathbf{r}}\varphi_i(\mathbf{r})|^2 - V_{eff} + \frac{1}{2}\nabla^2_{\mathbf{r}}\rho(\mathbf{r}) \qquad (2.57)$$

One of the most widely utilized m-GGA functionals is the non-empirical TPSS created by Tao, Perdew, Staroverov, and Scuseria[113] as an improvement over the PBE functional

.

2.2.4.4 Global hybrid functionals and range-separated correction

The exchange energy of GGA and m-GGA is approximate and therefore does not fully correct the classical self-interaction error because when the exchange energy is treated exactly, the self-interaction Jii is cancelled out by the equivalent exchange energy contribution Kii, as in the

HF method (c.f. Eqs (2.10)-(2.11)). To mitigate this, hybrid functionals combine exact HF and DFT exchange energies:

$$E_{XC}[\rho(\boldsymbol{r})] = E_C^{DFT}[\rho(\boldsymbol{r})] + E_X^{HF}[\rho(\boldsymbol{r})] \quad (2.58)$$

Perdew, Burke and Ernzerhof[103] formulated an XC functional using a polynomial of degree $n-1$ and parameter λ, derived from the adiabatic connection:[114]

$$E_{XC}^{\lambda}[\rho(\boldsymbol{r})] = E_{XC,\lambda}^{DFT}[\rho(\boldsymbol{r})] + (E_X^{HF}[\rho(\boldsymbol{r})] - E_X^{DFT}[\rho(\boldsymbol{r})])(1-\lambda)^{n-1} \quad (2.59)$$

Integrating Eq. (*2.59*) over the interval $\lambda \in [1,0]$ then gives:

$$E_{XC}^{\lambda}[\rho(\boldsymbol{r})] = E_{XC,\lambda}^{DFT}[\rho(\boldsymbol{r})] + \frac{1}{n}(E_X^{HF}[\rho(\boldsymbol{r})] - E_X^{DFT}[\rho(\boldsymbol{r})]) \quad (2.60)$$

Adamo and Barone, and Ernzerhof and Scuseria[115, 116] imposed using $n = 4$, and with the PBE functional, which defined the PBE0 hybrid functional:

$$E_{XC}^{PBE0}[\rho(\boldsymbol{r})] = E_{XC,\lambda}^{PBE}[\rho(\boldsymbol{r})] + \frac{1}{4}(E_X^{HF}[\rho(\boldsymbol{r})] - E_X^{PBE}[\rho(\boldsymbol{r})]) \quad (2.61)$$

Like PBE, the PBE0 functional is a theorical functional, with 25% HF exchange and 75% PBE XC energy. PBE0 is frequently used (Figure 2.3)[98] because it performs brilliantly across many applications, outperforming the most trustworthy, empirically parameterized functionals.[115]

The B3LYP functional, [117, 118] is the *de facto* standard functional in chemistry and it is arguably the most commonly used (Figure 2.3)[98] hybrid functional to date, demonstrating good performance in many chemical applications.[81] It has three empirical parameters a, b and c, which are set to 0.20, 0.72 and 0.81, to best replicate the proton affinities, atomization and ionization energies in the G2 database.[117, 118] B3LYP is formed by combining the B88 exchange, Lee-Yang-Parr (LYP) correlation, LSDA exchange and GGA $E_{XC}^{\lambda=0}$ XC energy:

$$E_{XC}^{B3LYP} = (1-a)E_X^{LSDA} + aE_{XC}^{\lambda=0} + bE_X^{B88} + cE_C^{LYP} + (1-c)E_C^{LSDA} \quad (2.62)$$

TPSSh[119] is a global hybrid m-GGA (GH-mGGA) functional that combines 10% HF exchange with 90% TPSS m-GGA XC energy using a single empirical parameter:

$$E_{XC}^{TPSSh}[\rho(\boldsymbol{r})] = aE_{XC}^{HF}[\rho(\boldsymbol{r})] + (1-a)E_X^{TPSS}[\rho(\boldsymbol{r})] + E_C^{TPSS}[\rho(\boldsymbol{r})], \qquad a = 0.10 \quad (2.63)$$

Another parameterized GH-mGGA that performed excellently is the PW6B95 functional developed by Truhlar[120], which has six parameters and combine 28 % HF exchange, 72 % optimized PW91 GGA exchange, and a re-optimized B95 m-GGA correlation.

Range separated hybrid (RSH) functionals are more recently developed methods of adding HF exchange by dividing the inverse distance operator into a short-range (SR) and long-range (LR) component, using the error function f_{erf} of and its complement $f_{erfc} = 1 - f_{erf}$:[121]

$$\frac{1}{|\boldsymbol{r}_2-\boldsymbol{r}_1|}=\frac{f_{erf}(\omega)}{\underbrace{|\boldsymbol{r}_2-\boldsymbol{r}_1|}_{SR}}+\frac{f_{erfc}(\omega)}{\underbrace{|\boldsymbol{r}_2-\boldsymbol{r}_1|}_{LR}},\quad f_{erf}(\omega)=\frac{2}{\sqrt{\pi}}\int_0^{\omega}e^{-(\omega)^2}d\omega\,,\quad \omega=c\mathbf{r_{12}} \tag{2.64}$$

Handy and coworkers[122] reformulated the error function to what is currently implemented in the CAM-B3LYP functional:

$$\frac{1}{|\boldsymbol{r}_2-\boldsymbol{r}_1|}=\underbrace{\frac{1-\left[\alpha+\beta\cdot f_{erf}(\omega)\right]}{|\boldsymbol{r}_2-\boldsymbol{r}_1|}}_{SR}+\underbrace{\frac{\alpha+\beta\cdot f_{erf}(\omega)}{|\boldsymbol{r}_2-\boldsymbol{r}_1|}}_{LR}, \tag{2.65}$$

In CAM-B3LYP (α=0.19, β=0.46, ω=0.33 au^{-1}), the SR exchange is described 25% DFT exchange and the LR part by 19% exact HF exchange. A RSH functional can be expressed generically as:

$$E_{XC}^{RSH}=a_X^{SR}E_{X,SR}^{HF}+a_X^{LR}E_{X,LR}^{HF}+(1-a_X^{SR})E_{X,SR}^{DFT}+(1-a_X^{LR})E_{X,LR}^{DFT}+E_C^{DFT} \tag{2.66}$$

The SR and LR Coulomb operator of the HF exchange energies are $E_{X,SR}^{HF}$ and $E_{X,LR}^{HF}$, respectively. To construct long-range corrected (LRC) RSH functionals a_X^{LR} is set close to 1, while a_X^{SR} is obtained either using least-squares fitting, adiabatic connection, or just set to zero.

The LC-HPBE (α=0, β=1, ω=0.4 au^{-1}) functional consists of 20% SR HF exchange, 100% LR HF exchange, 80% ωPBE exchange.[123] RSH functionals are designed to improve the description of CT at least in the limit of large donor-acceptor distance, as demonstrated by the RSH m-GGA ωB97M-V functional, which achieved the most accurate results across many applications.

2.2.4.5 Double hybrid functionals

So far, the highest level of sophistication in the development of DFT functionals is the double hybrid (DH) or extended hybrid functionals,[110, 124-127] which explicitly include both occupied and virtual KS MOs through MP2 perturbation theory.[128] DH functionals can be formulated as:

$$E_{XC}^{DH}[\rho]=\lambda_X E_X^{HF}[\rho]+(1-\lambda_X)E_X^{DFT}[\rho]+(1-\lambda_C)E_C^{DFT}[\rho]+\lambda_C E_C^{MP2}[\rho] \tag{2.67}$$

The analytical approximation upon which the DH functional PBE0-DH[129] is built on, is called the linear-scaled one-parameter DH (LS1DH)[130] approximation, and is given by:

$$E_{XC,\lambda}^{LS1DH}[\rho]=\lambda E_X^{HF}[\rho]+(1-\lambda)E_X^{DFT}[\rho]+(1-\lambda^3)E_C^{DFT}[\rho]+\lambda^3 E_C^{GL2}[\rho] \tag{2.68}$$

with the single parameter λ and the Görling-Levy (GL2) correlation energy[131] E_C^{GL2}, which is based on perturbation theory. Bremond and Adamo[129] imposed using $\lambda=4$ for PBE0-DH, with 50% HF exchange, 50% and 87.5% PBE exchange and correlation, respectively, and 12.5% GL2 correlation:

$$E_{XC}^{PBE0-DH}[\rho] = E_{XC}^{PBE}[\rho] + \frac{1}{2}(E_X^{HF}[\rho] - E_X^{PBE}[\rho]) + \frac{1}{8}(E_X^{GL2}[\rho] - E_C^{PBE}[\rho]) \quad (2.69)$$

When compared to global hybrids, DH functionals produce significantly better results. However, because virtual MOs are included, the cost of DH calculations is formally O(N^5), as in conventional MP2, which diminishes the advantage of the lower computational cost afforded by DFT in general.

2.3 Basis sets

In both wave function-based and DFT methods, the molecular orbitals MOs yielded as solutions to the Schrödinger equation are expressed as a LCAOs (c.f. Eq (2.17)), in addition, each atomic orbital is itself represented in terms of a group of functions called basis set. Basis sets are classified into several groups.

2.3.1 Atom-localized basis sets

2.3.1.1 Contracted Gaussian-type orbitals

The simplest way to approximate atomic orbitals is using Slater-type orbitals (STOs), which have the following form:[80]

$$\chi_{\zeta,n,l,m}^{STO}(r,\theta,\phi) = NY_{l,m}(\theta,\phi)r^{n-1}e^{-\zeta r} \quad (2.70)$$

where the angular momentum factor $\mathrm{Y_{l,m}}$, the normalization constant N, spherical coordinates r, θ and ϕ, the characteristic exponent ζ, the principal quantum number n, the angular quantum number l, and the magnetic quantum number m. STOs decay reasonably at larger as $r \rightarrow \infty$ and have a cusp at $r = 0$ (Figure 2.4). Hence, STOs resemble hydrogenic AOs to a high degree.[132] However, using STOs for many-electron systems would be impracticable because the two-electron four-index integral cannot be solved analytically when the basic functions are STOs. To bypass this issue, the STO radial decay $e^{-\zeta r}$ is converted into Gaussian-type orbital (GTO) radial decay $e^{-\zeta r^2}$:

$$\chi_{\zeta,l_x,l_y,l_z}^{GTO}(x,y,z) = Nx^{l_x}y^{l_y}z^{l_z}e^{-\zeta r^2} \quad (2.71)$$

where the Cartesian coordinates x, y, and z, and the normalization factor N. The sum of the l_x, l_y, and l_z (2.71) determines the type of AO. Although GTOs are more computationally economical than STOs, they do not contain a cusp at r = 0 and decay more rapidly as $r \rightarrow \infty$, hence the radial structure of some AOs cannot be correctly described.

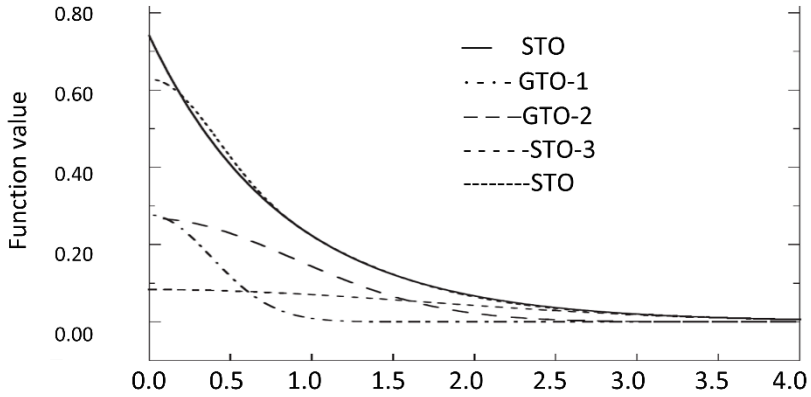

Figure 2.4 A STO of 1s AO modeled by a linear combination of three GTOs (STO-3G). Adapted from Ref.[80]

Basis sets constructed with GTOs employ them as linear combination fits to duplicate a STO as exactly as possible (Figure 2.4), which results in the concept of contracted GTO (CGTO)

(2.72), where the individual GTO are now called primitive GTOs (PGTOs):[80]

$$\chi^{CGTO} = \sum_{i}^{n} a_i \, \chi_i^{PGTO} \qquad (2.72)$$

where the contraction coefficients a_i and the degree of contraction n, which is the total number of GTOs utilized. The speed and accuracy decreases and increases with n, respectively. The STO approximated by n Gaussians (STO-nG)[133] basis set with $n = 3$ (Figure 2.4), was discovered to achieve the optimum combination of speed and accuracy.[80]

2.3.1.2 Single- , multiple-ζ and split-valence basis sets

A minimal basis set or single-ζ basis set is the most basic but least accurate expansion of AOs, in which every AO is specified by a single basis function or one set CGTO. The 'ζ' refers to when STOs with the exponent '-ζ' were used. Consider the STO-3G basis set (c.f. 2.3.1.1), which

combines three PGTOs into a single CGTO. For carbon, this fundamental set consists of five CGTOs, each of which describes the 1s, 2s, $2p_x$, $2p_y$, and $2p_z$ AO; hence, a total of 15 PGTOs are required. Double-ζ basis set consist of two functions for each AO, which allows for a non-isotropic description of electron distribution.[80] In general, the process of decontraction produces higher multiple-ζ or uncontracted basis sets from lower counterparts. Decontraction enhances flexibility, allowing one to get closer to the complete basis set (CBS) limit.

Split-valence or valence-multiple-ζ basis sets differentiate between the core and valence orbitals. For computational efficiency, the core AOs are represented by a single CGTO, whereas the valence AOs are described by an arbitrary number of CGTOs. Split-valence basis sets differ by the number and size of CGTOs utilized for the valence region. The Pople *et al.* basis sets, such as 6-31G or 6-311G,[134] indicates the number of PGTOs used in the core or valence CGTOs before or after the hyphen, respectively. If there are two such numbers after the hyphen, it is a valence-double-ζ basis. If there are three, it is a valence-triple-ζ.[80]

2.3.1.3 Augmentation with polarization and diffuse functions

Since MO are composed of multiple nuclei, greater mathematical flexibility than using just the occupied AOs of each atom is often required, which can be achieved through adding polarization and/or diffuse functions.[135, 136] Polarized basis set add a set of (un-)contracted functions with angular momenta greater than the highest occupied AOs valence shell. For instance, to improve the description of the O-H bonds in H_2O (Figure 2.5), the 6-31G(d, p)[134] polarized basis set can be used. 6-31G(d) shows that all non-hydrogen atoms, oxygen atoms in this case, have been augmented with d-type polarization functions. 6-31G(d, p) shows that in addition to that, all hydrogen atoms now have p-type polarization functions added.[77]

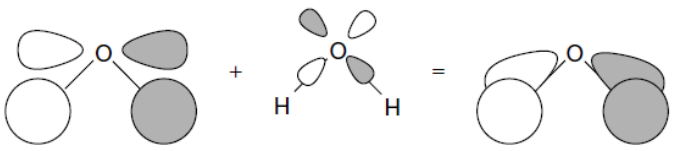

Figure 2.5 Interaction between the symmetry combination of two hydrogen 1s AOs and one oxygen AO to form an H_2O MO. Bonding interactions are enhanced by mixing a small amount of oxygen d character into the MO.[77]

On the other hand, with diffuse functions a full shell of AOs is added with similar angular momenta than the valence region. Diffused functions are variationally optimized functions with small exponents to characterize MOs with weakly bound electrons, such as electrons in anionic HOMOs or highly electronic excited state (EES) MOs, which are substantially spatially diffused. For example, in the basis set 6 31+G, the '+' signifies that heavy atoms have been enhanced with additional s- and p-type diffuse functions.[80] So that for carbon with s and p orbitals occupied in the valence shell, a full additional shell of s and p orbitals, but with much lower exponents so that they extend further into space, is added.

2.3.2 Effective core potential basis sets

In heavy atoms, relativistic effects are generally not negligible,[137-139] in addition, chemical properties are determined by the few valence electrons rather than the core electrons. The effective core potential (ECP) or pseudopotential approximation, simplifies computation by replacing the basis functions needed to describe each of the many core electrons with fewer functions that effectively model the core region. ECP functions precisely and efficiently characterize the combined nuclear-electronic core effects subject to the frozen core approximation and can be parameterized to reproduce relativistic effects in the core, which would otherwise require an explicit relativistic treatment of the Schrodinger equation. The valence electrons are described by pseudo-functions,[140] whereas contributions from the core orbitals are taken into account via an efficient one-electron potential operator $\hat{V}^{core}$ (2.73), which is a function of the atomic radius r. This operator is added to the one-electron Hamiltonian operator, substituting the interactions between core and valence electrons and accounting for self-repulsion.[141]

$$\hat{V}^{core}(r) = V_L(r) + \sum_{l=0}^{L-1} \sum_{m=-l}^{l} \left|Y_{l,m}\right\rangle [V_l(r) - V_L(r)] \left\langle Y_{l,m}\right|, \qquad L = l_{max}^{atom} + 1 \tag{2.73}$$

where the spherical harmonic angular momentum angular (l) projectors $\sum_m \left|\mathrm{Y}_{l,m}\right\rangle \left\langle \mathrm{Y}_{l,m}\right|$, the maximum angular momentum potential $\mathrm{V_L(r)}$ and the maximum value of the angular

momentum L. The radial parts of the operator $\hat{V}^{core}$ can be expressed as a linear combination of CGTOs:

$$V_l(r) = \sum_{k=1}^{K_l} D_{kl} r^{n_{kl}} e^{-\alpha_{kl} r^2} \ , \qquad n_{kl} \in \{-2, -1, 0\} \tag{2.74}$$

Several authors have published the parameters n_{kl}, α_{kl}, and D_{kl} required to assess the ECP integrals, including the Los Alamos ECP (LANL2-ECP) by Hay-Wadt[142] and Stuttgart Dresden ECP (SDD) (2.3.3).[143] When $\hat{V}^{core}$ is introduced into the electronic Hamiltonian, it produces two types of ECP integrals: local or type-1 integrals caused by $V_L(r)$ and semi-local or type-2 integrals caused by the $|Y_{l,m}\rangle$. The evaluation of these integrals follows the Flores-Moreno *et al.* scheme.[144] Large-core ECPs (LCECPs) comprise everything except the valence shell, hence LCECPs replace [Ar], [Kr], and [Xe] cores for the elements Sc-Zn, Y-Cd, and La-Hg, respectively. Small-core ECPs (SCECPs) scale back to the next lower sub-shell and so replace [Ne], [Ar], and [Kr] cores for the elements Sc-Zn, Y-Cd, and La-Hg, respectively. SCECP have higher computational cost, but this is often worth it because polarization of the explicitly handled sub-valence shell can improve accuracy.[77]

2.3.3 Def2-, LANL2-, and D95-type basis sets and ECPs

Ahlrichs *et al*.[145] developed the "Def2" split-valence double-ζ, triple-ζ, and quadruple-ζ with improved polarization functions formalized as Def2-SVP, Def2-TZVP, and Def2-QZVPP, respectively, to address some of the shortcomings, such as poor quality of polarization functions, of earlier "Def" basis sets.[146] Def2 basis sets are commonly used (Figure 2.6)[98] due to their computational efficiency and availability for almost all the elements in the periodic table.[98] For atomization energies, typical errors per atom are roughly 10-30 kJ mol^{-1}, ~5 kJ mol^{-1} and ~1 kJ mol^{-1} for Def2-SVP, Def2-TZVP and Def2-QZVPP, respectively.[145]

The Def2-SVP basis set is the smallest and most computationally efficient, which adds p-polarization functions on hydrogen, d-polarization functions on main group elements, as well as diffused functions.[145]

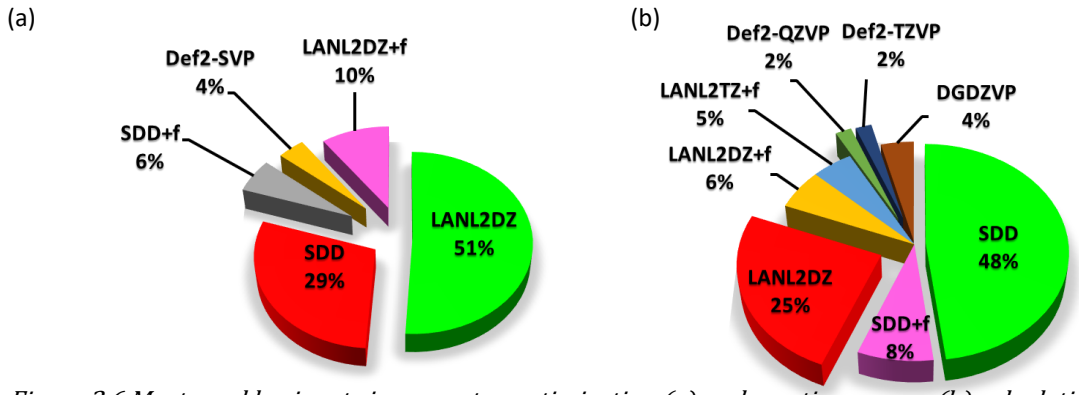

Figure 2.6 Most used basis sets in geometry optimization (a) and reaction energy (b) calculations involving Pd, Ni, Rh, and Ir metals. Adapted from Ref.[98]

Def2-TZVP has more basis functions than Def2-SVP and achieves a better balance of accuracy and computing efficiency. Def2-TZVP adds p-polarization functions on hydrogen, a 2d1f-polarization functions on main group elements, and much more complete polarization functions set for transition metals. If Def2-TZVP is not feasible, then Def2-TZVP(-f), which omits f-polarization functions can be used.[145] Def2 basis sets evaluate all the electrons in a relativistic manner for the elements H-Kr but automatically load the SDD ECP[143] for the heavier elements Rb-Rn with, various core sizes (Table 2.1).

Table 2.1 Number of core electrons described the SDD ECP for various heavy elements

Elements	Core size
Rb – Xe	28
Cs – La	46
Ce – Lu	28
Hf – Rn	60

Despite being a smaller basis set compared to the Karlsruhe basis sets, the Los Alamos National Laboratory double-ζ (LANL2DZ) basis set[142] is typically used in DFT and TD-DFT calculations involving transition metals (Figure 2.3.4.1).[98, 147-155] LANL2DZ combines valence GTO basis functions with the Hay-Wadt-developed LANL2-ECP, which is automatically applied to post-third-row elements.[142] Hitherto, LANL2 ECPs have not been established for elements H through Ne. In lieu of this, all-electron valence double zeta basis sets created by Dunning and Huzinaga are utilized. ECP parameters for elements Na through Kr are derived from atomic

wavefunctions obtained through all-electron non-relativistic Hartree-Fock calculations, whereas relativistic Hartree-Fock calculations have been employed for heavier elements Rb through Bi. The D95-type basis set such as Dunning and Huzinaga's D95 double-zeta basis set [156] and D95V split valence do not use EPC in their definition, and therefore explicitly includes the effect of all the electrons. However, the D95 basis set is often used for lighter non-metal elements when LANL2DZ is specified to avoid applying an ECP on such atoms.

2.4 Time-dependent density functional theory

The most extensively used tool for modelling the electronic spectra of organic and inorganic compounds is TD-DFT. This popularity can be attributed to the simplicity of this single-reference method,[157] the efficiency of computation,[158, 159] the availability of analytical first[160-162] and second[163, 164] derivatives in DFT functionals, and the flexibility to add environmental influences.[162, 165-175] This section present the TD-DFT principles.

2.4.1 Time-dependent Hamiltonian and density

When a quantum particle evolves over time in a potential field V(**r**,t), it is no longer sufficient to approximate the standing wave Schrödinger equation. Instead, it must be treated completely, including the time component. In the context of an isolated system composed of N electrons and N_n nuclei, the TD Hamiltonian (2.75)[80, 176, 177] takes the form:

$$\hat{\mathcal{H}}(\boldsymbol{r},t) = \hat{T} + \hat{V}_{nn}(\boldsymbol{r}) + \hat{V}_{ne}(\boldsymbol{r}) + \hat{V}_{ee}(\boldsymbol{r}) + \hat{V}_{pert}(\boldsymbol{r},t) \qquad (2.75)$$

The extra operator perturbation potential operator $\hat{V}_{pert}(\boldsymbol{r},t)$ is a TD term that describes external perturbations to the system such as a laser beam in UV-Vis spectroscopy:

$$\hat{V}_{pert}(\boldsymbol{r},t) = \sum_{i}^{N} v_{pert}(\boldsymbol{r}_i,t) \qquad (2.76)$$

The potential $v_{pert}(\boldsymbol{r}_i,t)$ describes the perturbation experienced by electron i at position $\boldsymbol{r}_i$:

$$v_{pert}(\boldsymbol{r}_i,t) = E_{el}(t)\boldsymbol{\alpha}\cdot\boldsymbol{r}_i \qquad (2.77)$$

where the TD periodic electric field E_{el}, and the polarization vector $\boldsymbol{\alpha}$ associated with it.

The net external potential experienced by electron i is the sum of $v_{pert}(\boldsymbol{r}_i, t)$ and the external potential electron i experiences due the nuclei $v(\boldsymbol{r}_i)$:

$$v_{ext}(\boldsymbol{r}_i, t) = v(\boldsymbol{r}_i) + v_{pert}(\boldsymbol{r}_i, t) \tag{2.78}$$

TD KS orbitals (and hence the density) of a non-interacting fictitious system can be written as products of TD and spatial orbitals integrated over spin orbitals:

$$\int_s \chi_i(\boldsymbol{r}, t) = \varphi_i(\boldsymbol{r})\phi_i(t) \tag{2.79}$$

Similar to time-independent KS theory, the exact TD density[80] $\rho(\boldsymbol{r}, t)$ can be expanded from χ_i orbitals and also integrate to the number of electrons N:

$$\rho(\boldsymbol{r}, t) = \sum_{i=1}^{N} \chi_i(\boldsymbol{r}, t)\chi_i^*(\boldsymbol{r}, t) \tag{2.80}$$

$$\int \rho(\boldsymbol{r}, t)d\boldsymbol{r} = N \tag{2.81}$$

2.4.2 Rung and Gross theorem

TD-DFT is grounded on two theorems developed by Runge and Gross in 1984[178] that extend the Hohenberg-Kohn theorems to problems needing TD external potentials: [85]

Theorem 1: There is a one-to-one mapping (2.82) between $\rho(\boldsymbol{r}, t)$ and $v_{ext}(\mathbf{r}, t)$ up to an additive time function $\psi(t)$:

$$\rho(\boldsymbol{r}, t) \overset{j(\boldsymbol{r}, t)}{\longleftrightarrow} v_{ext}(\boldsymbol{r}, t) + \psi(t) \tag{2.82}$$

The TD current densities $j(\boldsymbol{r}, t)$ is the sum of the imaginary parts over the TD KS orbitals $\chi_k(\boldsymbol{r}, t)$:

$$j(\boldsymbol{r}, t) = \sum_{k=1}^{N} \frac{\chi_k^*(\boldsymbol{r}, t)\nabla_{\mathbf{r}}\chi_k(\boldsymbol{r}, t) - [\nabla_{\mathbf{r}}\chi_k^*(\boldsymbol{r}, t)\chi_k(\boldsymbol{r}, t)]}{2i} \tag{2.83}$$

Theorem 2: The exact $\rho(\boldsymbol{r}, t)$ can be found by applying the least action principle to the Frenkel-Dirac action $\mathcal{A}[\psi(t)]$:

$$\mathcal{A}[\rho(t)] = \int_{t_0}^{t_f} \langle \psi[\rho(t)] \left| i\hbar \frac{\partial}{\partial t} - \hat{\mathcal{H}}(t) \right| \psi[\rho(t)] \rangle \, \mathrm{d}t - \langle \psi[\rho(t_f)] | \delta\psi[\rho(t_f)] \rangle \tag{2.84}$$

where the exact TD wave functional of the TD density $\psi[\rho(t)]$, the first-order differential of the wave function $\delta\psi[\rho(t_f)]$, the TD Hamiltonian $\hat{\mathcal{H}}(t)$, and the initial t_0 and final t_f time.

2.4.3 Time-dependent Kohn-Sham equations

Similar to GS KS DFT,[86] a TD non-interacting system can be constructed that will evolve as the real interacting TD system having exact $\rho(\boldsymbol{r},t)$:[176]

$$\rho(\boldsymbol{r},t)=\sum_{i=1}^{N} f_i|\chi_i(\boldsymbol{r},t)|^2 \tag{2.85}$$

where the orbital occupation f_i and the TD KS spin orbitals $\chi_i(\boldsymbol{r},t)$, which must satisfy the TD KS equation:

$$i\hbar\frac{\partial\chi_i(\boldsymbol{r},t)}{\partial t}=\hat{h}^{KS}[\rho(t,\mathbf{r})]\chi_i(\boldsymbol{r},t) \tag{2.86}$$

The TD KS Hamiltonian $\hat{h}^{KS}[\rho(t,\mathbf{r})]$ is defined as the sum of two operators, the kinetic energy of the fictitious non-interacting system $\hat{t}_{ft}$ and the effective potential operator $\hat{v}_{eff}[\rho(t,\mathbf{r})]$:

$$\hat{h}^{KS}[\rho(t,\mathbf{r})]=\hat{t}_{ft}+\underbrace{\hat{v}_{ext}[\rho(t)]+\hat{v}_H[\rho(t,\mathbf{r})]+\hat{v}_{xc}[\rho(t,\mathbf{r})]}_{\hat{v}_{eff}[\rho(t,\mathbf{r})]} \tag{2.87}$$

where the TD external potential operator $\hat{v}_{ext}$ is given in Eq. (2.78) and the non-interacting kinetic energy operator $\hat{t}_{ft}$ (2.88) and the TD Hartree electron-electron Coulomb repulsion potential operator $\hat{v}_H$ (2.89) are:

$$\hat{t}_{ft}=-\frac{1}{2}\nabla_{\mathbf{r}}^2 \tag{2.88}$$

$$\hat{v}_H[\rho(t,\mathbf{r})]=\int\frac{\rho(\mathbf{r}',t)}{|\mathbf{r}-\mathbf{r}'|}\mathrm{d}\mathbf{r}' \tag{2.89}$$

Van Leeuwen[179] showed that the XC potential $\hat{v}_{xc}$ is the differential of the XC action $\mathcal{A}_{XC}[\rho(t,\mathbf{r})]$:

$$\hat{v}_{xc}[\rho(t,\mathbf{r})]=\frac{\delta\mathcal{A}_{XC}[\rho(t,\mathbf{r})]}{\delta\rho(\tau,\mathbf{r})},\quad \mathcal{A}_{XC}[\rho(t,\mathbf{r})]=\int_0^1 v_{XC}[\rho(t,\mathbf{r})]\,dt \tag{2.90}$$

where the pseudo-time τ defined by Keldysh[180] and the XC potential energy v_{XC}. When solving the KS equations, several fundamental issues emerge. The first is that there is no analytical expression for v_{XC} (2.90), hence an approximation must be devised. The second challenge is how to solve the differential of $\mathcal{A}_{XC}$ (2.90). The first strategy is based on solving the time-independent KS equations (Eq. (2.42),[147] which are then propagated over time as a function of

the perturbation $v_{pert}(\mathbf{r},t)$ (2.76). However, in terms of processing time, this approach to the problem remains extremely greedy. To circumvent this, most quantum computation software employs response theory.[177]

2.4.4 Linear response TD-DFT

Response theory[177] makes it easy to formulate TD-DFT in the frequency domain. The essential quantity to build is the density response function, which connects fluctuations in the actual TD density to variations in the TD external potential. Response theory is a powerful technique[181] that allows various types of information to be extracted from the density response, not only in the linear regime, but also in higher order responses[182] or using special classes of excitation operators such as spin-flip[183] or spin-adapted excitation operators for open-shell systems.[184, 185] Linear-response TD-DFT (LR-TD-DFT), first derived by Casida in 1995[186] and reformulated by Petersilka *et al.* a year later, [187] solves the TD KS equation at time t_0 and then propagates the perturbation over time $t > t_0$. This allows a UV-Vis absorption spectrum to be obtained. LR-TD-DFT works with frequency ω rather than time t and a Fourier transform $\mathcal{F}$ is used to map between ω and t:

$$\mathcal{F}[f(t)] = \frac{1}{\sqrt{2\pi}}\int_{-\infty}^{+\infty} f(t)e^{-i\omega t}\,dt \qquad (2.91)$$

where $f(t)$ is a continuous function of the time variable. The first linear response $\delta\rho(\mathbf{r},t)$ depends on the first order change in external potential $\delta\hat{v}_{ext}(\mathbf{r},t)$:[176]

$$\delta\rho(\mathbf{r},t) = \int_{-\infty}^{t}\int_{\mathbf{r}'} \mathcal{R}(\mathbf{r},\mathbf{r}',t-t')\delta\hat{v}_{ext}(\mathbf{r}',t')\,d\mathbf{r}'\,dt' \qquad (2.92)$$

where the first-order changes in density and external potential, $\delta\rho(\mathbf{r},t)$, and $\delta v_{ext}(\mathbf{r},t)$, respectively, are:

$$\delta\rho(\mathbf{r},t) = \rho(\mathbf{r},t) - \rho_0(\mathbf{r}) \qquad (2.93)$$

$$\delta v_{ext}(\mathbf{r},t) = v_{ext}(\mathbf{r},t) - v_{ext,0}(\mathbf{r}) \qquad (2.94)$$

Applying the Fourier transform to Eq. (2.92), the response function of the real system of interacting electrons, $\mathcal{R}$, can be written as:

$$\mathcal{R}(\omega) = \lim_{\eta\to 0^+}\sum_{k=1}^{\infty}\frac{\langle\Psi^0|\hat{\rho}|\Psi^k\rangle\langle\Psi^k|\hat{\rho}|\Psi^0\rangle}{\omega-\Omega_k+i\eta} - \frac{\langle\Psi^0|\hat{\rho}|\Psi^k\rangle\langle\Psi^k|\hat{\rho}|\Psi^0\rangle}{\omega+\Omega_k-i\eta} \qquad (2.95)$$

where Ψ^0, Ψ^k are the wavefunctions of the GS and excited state k, respectively, and Ω_k is the true excitation energy of state k. Unfortunately, evaluating $\mathcal{R}$ is impractical. Therefore, $\delta\rho$ can be reformulated in terms of the system of non-interacting electrons:

$$\delta\rho(\mathbf{r},t) = \int_{-\infty}^{t}\int_{\mathbf{r}'} \mathcal{R}_{KS}(\mathbf{r},\mathbf{r}',t-t')\delta v_{eff}(\mathbf{r}',t')\,d\mathbf{r}'\,dt \qquad (2.96)$$

where the TD KS effective potential δv_{eff} (2.87):

$$\delta v_{eff}(\mathbf{r}',t) = \delta v_{ext}[\rho(t)] + \delta v_H[\rho(\mathbf{r},t)] + \delta v_{xc}[\rho(\mathbf{r},t)] \qquad (2.97)$$

Applying the Fourier transform to Eq. (2.96), the response function of a system of non-interacting electrons $\mathcal{R}_{KS}$ can be represented[§] as the Lehmann (or sum-over-state) representation of the response functions:[176]

$$\mathcal{R}_{KS}(\omega) = \lim_{\eta\to 0^+}\sum_{p=1}^{\infty}\sum_{q=1}^{\infty}(f_p - f_q)\frac{\hat{\chi}_p\hat{\chi}_q\hat{\chi}_p^*\hat{\chi}_q^*}{\omega - \omega_{p\to q} + i\eta}, \qquad \omega_{p\to q} = \varepsilon_q - \varepsilon_p \qquad (2.98)$$

where the occupation numbers f_p and f_q of KS spin orbitals χ_p and χ_q, and the associated KS eigenvalues ε_p and ε_q, respectively and the frequency $\omega_{p\to q}$ of an electronic excitation between χ_p, and χ_q. When ω is equal to $\omega_{p\to q}$ (or Ω_k), then $\mathcal{R}_{KS}$ (or $\mathcal{R}$) have poles, that is $\mathcal{R}_{KS}(\omega_{p\to q}) = \pm\infty$ (or $\mathcal{R}(\Omega_k) = \pm\infty$), which is the relationship that is exploited to obtain the excitation energy of the interacting system from the non-interacting system. The Dyson equation (2.99) for LR-TD-DFT is obtained from Eq. (2.92) and Eq. (2.96), and performing the Fourier transformation:

$$[\hat{1} - \hat{\mathcal{R}}_{KS}(\omega)f_{Hxc}(\omega)]\hat{\mathcal{R}}(\omega) = \hat{\mathcal{R}}_{KS}(\omega) \qquad (2.99)$$

The Hartree XC kernel f_{Hxc} is:

$$f_{Hxc}(\omega) = \frac{\delta v_H(\omega)}{\delta\rho(\omega)} + \frac{\delta v_{xc}(\omega)}{\delta\rho(\omega)} \qquad (2.100)$$

When $\omega = \Omega_k$, the LHS of Eq. (2.99) tends to infinity, while the RHS is finite. This indetermination implies that the first term in the LHS must be 0 when $\omega = \Omega_k$, which is when the following LR-TD-DFT eigenvalue equation is true:

$$[\hat{1} - \hat{\mathcal{R}}_{KS}(\omega)f_{Hxc}(\omega)]\hat{\mathcal{R}}(\omega) = \omega\hat{\mathcal{R}}_{KS}(\omega) \qquad (2.101)$$

This LR-TD-DFT equation can be reformulated into the recognizable Casida format:[186, 188]

$$\begin{bmatrix}\mathbf{A}(\omega) & \mathbf{B}(\omega)\\ \mathbf{B}^*(\omega) & \mathbf{A}^*(\omega)\end{bmatrix}\begin{bmatrix}\mathbf{X}(\omega)\\ \mathbf{Y}(\omega)\end{bmatrix} = \omega\begin{pmatrix}1 & 0\\ 0 & -1\end{pmatrix}\begin{bmatrix}\mathbf{X}(\omega)\\ \mathbf{Y}(\omega)\end{bmatrix} \qquad (2.102)$$

The matrices **A** and **B** are defined as:

[§] The space integrations and variables are omitted for simplicity.

$$\mathbf{A}_{ia,jb}(\omega) = \delta_{ij}\delta_{ab}(\varepsilon_a - \varepsilon_i) + \left(ia\middle|\hat{f}_{Hxc}(\omega)\middle|bj\right) \quad (2.103)$$

$$\mathbf{B}_{ia,jb}(\omega) = \left(ia\middle|\hat{f}_{Hxc}(\omega)\middle|jb\right) \quad (2.104)$$

In Mulliken notation, the two-electrons integrals are defined as:

$$\left(pq\middle|\hat{f}_{Hxc}(\omega)\middle|rs\right) = \iint \chi_p^*(\mathbf{r})\chi_q(\mathbf{r})\left[\frac{\mathbf{1}}{|\mathbf{r}-\mathbf{r}'|} + f_{xc}(\mathbf{r},\mathbf{r}',\omega)\right]\chi_r^*(\mathbf{r}')\chi_s(\mathbf{r}')\, d\mathbf{r}d\boldsymbol{r}' \quad (2.105)$$

The Hartree XC kernel operator $\hat{f}_{Hxc}$, is the first-order correction to the orbital energy difference, that relates the electron created in orbital i and the hole in orbital a, accounting for the relaxation that modulates the orbital gap, i.e., $(\varepsilon_a - \varepsilon_i)$:[189]

$$f_{xc}(\omega) = \frac{\delta v_{xc}(\omega)}{\delta\rho(\omega)} \quad (2.106)$$

KS orbitals from GS DFT are used to evaluate the matrices **A** and **B**. The matrix **A** describes the GS, while the **B** matrix, which is the same size as **A**, describes a single excitation or a single de-excitation. The excitation energy ω, the excitation (**X**) and de-excitation (**Y**) amplitudes are obtained by solving the eigenvalue Eq. (2.102), which involves finding the poles of $\mathcal{R}$ by first performing the KS-SCF to find the time-independent KS solution, then using the obtained eigenfunctions $\{\chi_i\}_{i\in[1,N]}$ and eigenvalues $\{\varepsilon_i\}_{i\in[1,N]}$ to solve for $\mathcal{R}$. Since there is no analytical equation for v_{xc} (2.106), f_{xc} need to be approximated. By default, LR-TD-DFT algorithms currently use the adiabatic LR-TD-DFT (A-LR-TD-DFT)[178] approximation, which uses GS DFT functionals for TD-DFT calculations.[161] The instantaneous XC kernel evaluated in A-LR-TD-DFT can be written as:

$$f_{xc}^A(\mathbf{r},t,\mathbf{r}',t') = \frac{\delta v_{xc}(\mathbf{r})}{\delta\rho(\mathbf{r}')}\delta(t-t') \quad (2.107)$$

The absorption energies in A-LR-DFT are computed as ideal vertical excitations $\Delta E^{\text{vert-abs}}$ with respect to a GS reference state of a chromophore at the GS geometry (Figure 2.7):

$$\Delta E^{vert-abs} = E^{EES}(\mathbf{R}^{\text{GS}}) - E^{GS}(\mathbf{R}^{\text{GS}}) \quad (2.108)$$

with $E^{GS}(\mathbf{R}^{GS})$ and $E^{EES}(\mathbf{R}^{GS})$ the ground state and excited state energies at the GS geometry ($\mathbf{R}^{GS}$). However, it should be noted that comparing A-LR-TD-DFT with a measured absorption spectrum is an approximate procedure. Since **A** and **B** are one-electron excitations, $\Delta E^{\text{vert-abs}}$ is ignorant of the EES density and energy gradient, and double and higher electronic excitations are lost, which lowers the quality of higher energy EES predictions. Furthermore, $\Delta E^{\text{vert-abs}}$ is affected by the quality of the GS DFT method. Nonetheless, A-LR-TD-DFT has produced many excellent results.[157, 190, 191]

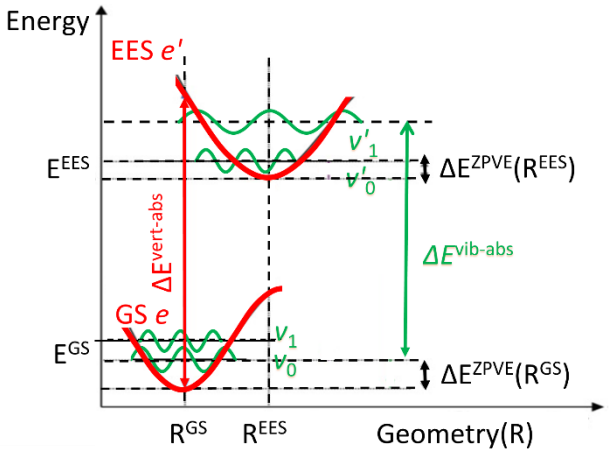

Figure 2.7 Simplified Jablonski diagram representing only two singlet states free of interaction(s). Adapted from Ref. [192]

Solving Casida's equation (2.102) iteratively for many excitation energies is computationally demanding and may not be feasible. An alternative approach is the Tamm-Dancoff approximation[193] (TDA-LR-TD-DFT), which neglects de-excitation amplitudes **Y**(ω). **B**(ω) is set to zero and Eq. (2.102) results in a simpler Hermitian eigenvalue equation:

$$[\mathbf{A}(\omega)][\mathbf{X}(\omega)] = \omega[\mathbf{X}(\omega)] \qquad (2.109)$$

TDA-LR-TD-DFT assumes excitations and de-excitations are independent, which is usually a good approximation that speeds up calculations.[159]

2.4.5 How to characterize the experimental and TD-DFT UV-Vis absorption spectrum

2.4.5.1 Natural transition orbitals

A TD-DFT absorption calculation yields a transition energy and an oscillator strength, which are related to the measured position and molar absorption coefficients of the bands. The chemical interpretation of a transition is an electron travelling from a *hole* to an *electron/particle*. The hole and electron/particle can be represented in a variety of ways.[194]

If an excitation can be completely described by a single *hole* → *electron* transition, then the hole and electron can be simply represented independently by a single pair of occupied and virtual canonical MOs. However, in most practical cases, several MO transitions may occur

within a narrow frequency range, resulting in multiple MO pairs having non-negligible contributions to the excitation. In such cases, the excitation must be represented as a transition of numerous MO pairs with associated weighting coefficients. This property makes determining electron excitation character solely based on MOs tedious and prone to mistakes.

Natural transition orbitals (NTOs) are transformed canonical MOs that confine a particular excitation to only one or two pairs of *hole* and *particle* transition orbitals (TOs).[195] NTOs are able to circumvent the necessity of inspecting several MOs. Consider a system with a MO hole and electron at $\mathbf{r}_H$ and $\mathbf{r}_E$, respectively (Figure 2.8A) in a system consisting of n_{occ} occupied $\{\Psi_i\}_{i\in[1,n_{occ}]}$ and n_{vir} virtual $\{\Psi'_j\}_{j\in[1,n_{vir}]}$ MOs, such that $n_{occ} \leq n_{vir}$ as is typically the case. Then, the one-electron transition density matrix (1-TDM) in an MO basis, [194, 195] $\mathbf{T}$, is a $n_{occ} \times n_{vir}$ matrix connecting the GS wavefunction, Ψ_{GS}, and EES Ψ_{EES}, and describing a vertical transition. Its (i,j) element can be written as:

$$T_{ij} = \sum_{\sigma} \langle \Psi_{EES} \left| \hat{c}^T_{i\sigma} \hat{c}_{j\sigma} \right| \Psi_{GS} \rangle \qquad (2.110)$$

where σ is the spin index. Associated with $\mathbf{T}$ is the exciton wavefunction $\Omega(\mathbf{r}_h, \mathbf{r}_e)$ or amplitude of the hole-electron amplitude of the polarization propagator (2.111), which describes the hole-particle motion (Figure 2.8B) during excitation and links the MOs with NTO. [194, 196]

$$\Omega(\mathbf{r}_h, \mathbf{r}_e) = \sum_{\sigma} T_{ij} \varphi^*_i(\mathbf{r}_H) \varphi'_j(\mathbf{r}_E) \qquad (2.111)$$

It is derived from the electron-hole response function, which is governed by the Bethe-Salpeter equation.[197, 198] The operators $\hat{c}^T_{i\sigma}$ and $\hat{c}_{j\sigma}$ create a hole and an electron in NTO φ_i and φ'_j, respectively.[176] The shape of the hole and electron (Figure 2.8C) can be generated from the density associated with φ_i and φ'_j.

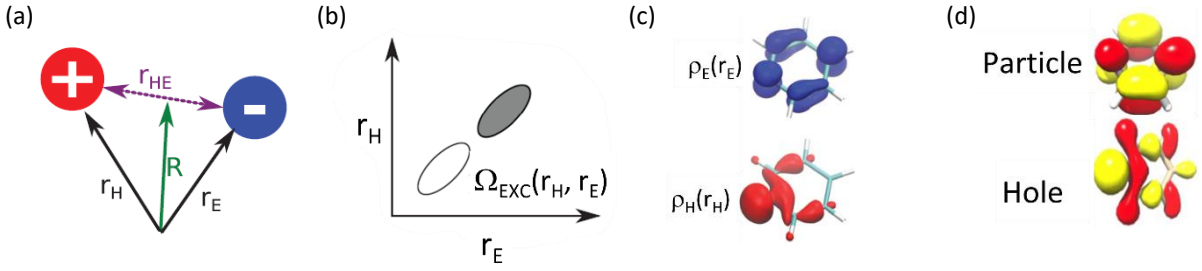

Figure 2.8 (a) The hole and electron coordinates $\mathbf{r}_H$ and $\mathbf{r}_E$, the center-of-mass coordinate R, and the separation $\mathbf{r}_{HE}$, and (b) an exemplary exciton wavefunction $\Omega(\mathbf{r}_h, \mathbf{r}_e)$ (c) Deconstruction of $\Omega(\mathbf{r}_h, \mathbf{r}_e)$ into separate hole $\rho_H(\mathbf{r}_H)$ and particle $\rho_E(\mathbf{r}_E)$ densities, using an $n\pi^*$ excited state (S1) in pyridine as example. (d) NTOs for the pyridine molecule for this excited state. Adapted from Ref.[194]

$\mathbf{T}$ can be diagonalized and a singular value decomposition (SVD) can be performed. However, since $\mathbf{T}$ is non-symmetric, a simple diagonalization is not possible. Instead, a temporary matrix for occupied $\mathbf{T}_{occ}$ and virtual $\mathbf{T}_{vir}$ orbitals are defined as follows:

$$\mathbf{T}_{occ} = \mathbf{T}\mathbf{T}^{\mathbf{T}}, \qquad \mathbf{T}_{vir} = \mathbf{T}^{\mathbf{T}}\mathbf{T} \tag{2.112}$$

where $\mathbf{T}^{\mathbf{T}}$ is the transpose of $\mathbf{T}$**.** Both $\mathbf{T}_{occ}$ and $\mathbf{T}_{vir}$ are square matrices with dimension $n_{occ} \times n_{vir}$, respectively, which are then diagonalized using unitary transformation matrices $\mathbf{U}_{occ}$ and $\mathbf{U}_{vir}$:

$$\mathbf{U}_{occ}^{-1}\mathbf{T}_{occ}\mathbf{U}_{occ} = \mathbf{\Lambda}_{occ} = (\lambda_1, \dots, \lambda\, n_{occ}) \tag{2.113}$$

$$\mathbf{U}_{vir}^{-1}\mathbf{T}_{vir}\mathbf{U}_{vir} = \mathbf{\Lambda}_{vir} = (\lambda'_1, \dots, \lambda' n_{vir}) \tag{2.114}$$

The produced diagonal terms $\mathbf{\Lambda}_{occ}$ and $\mathbf{\Lambda}_{vir}$ are eigenvalues of the occupied $\{\varphi_i\}_{i\in[1,n_{occ}]}$ and virtual NTOs $\left\{\varphi'_j\right\}_{j\in[1,n_{vir}]}$,respectively. If these eigenvalues are numbered in order of decreasing magnitude, then:

$$1 \geq \lambda_k \equiv \lambda'_k \geq 0 \;\forall\; k \in [1, n_{occ}] \text{ and } \quad \lambda'_k = 0 \;\forall\; k \in \left[n_{occ}+1, n_{vir}\right] \tag{2.115}$$

$$\sum_i \lambda_k = 1 \quad \forall\; k \in [1, n_{occ}] \tag{2.116}$$

To produce NTOs a unitary transformation is performed on the occupied $\{\Psi_i\}_{i\in[1,n_{occ}]}$ and virtual $\left\{\Psi'_j\right\}_{j\in[1,n_{vir}]}$ MOs, respectively:

$$(\varphi_1, \dots, \varphi_{n_{occ}}) = (\Psi_1, \dots \Psi_{n_{occ}})\mathbf{U}_{occ} \tag{2.117}$$

$$(\varphi'_1, \dots, \varphi'_{n_{vir}}) = (\Psi'_j, \dots \Psi'_{n_{vir}})\mathbf{U}_{vir} \tag{2.118}$$

$\mathbf{T}$ expressed in terms of NTOs[194] is diagonal and its (i,j) element is simply constructed as follows:

$$T_{ij} = \left|\left[\mathbf{U}_{occ}^{\mathbf{T}}\mathbf{T}\mathbf{U}_{vir}\right]_{ij}\right| = \sum \sqrt{\lambda_i}\,\langle\varphi_i|\varphi_j\rangle = \sqrt{\lambda_i}\delta_{ij}, \qquad \lambda'_k = 0 \;\forall\; \{i,j\} \in [1, n_{occ}] \tag{2.119}$$

Hence, the $n_{occ} \times n_{vir}$ dimension of $\mathbf{T}$**,** expressed in terms of MO excitations (2.110), has been reduced to n_{OCC} dimensions when $\mathbf{T}$ is expressed in terms of NTO excitations (2.119). Only one or very few number of orbital pairs have dominant contributions in the NTOs, which facilitates analysis when MOs fail to offer such compact description. The hole and particle densities of NTOs can be expressed as:

$$\rho_H(\mathbf{r}_H) = \sum\nolimits_i \lambda_i \left|\varphi_i(\mathbf{r}_H)\right|^2 \tag{2.120}$$

$$\rho_E(\mathbf{r}_E) = \sum\nolimits_i \lambda_i \left|\varphi'_i(\mathbf{r}_E)\right|^2 \tag{2.121}$$

The NTO pair shape (Figure 2.8D) can be built based on the hole and particle densities, and excitations can be categorized. The related eigenvalue λ_i of an NTO pair, which when multiplied by 100 is the percentage contribution of the NTO to the excitation, reflects the significance of each hole-particle excitation to the overall transition. Note that the eigenvalue λ_i can be slightly greater than 1, because de-excitations exist in TD-DFT that are ignored in $\mathbf{T}$. If the value is significantly higher than 1, then using TDA-LR-TDDFT (*c.f.* 2.4.4) is better alternative.

2.4.5.2 Convolution of modelled UV-Vis spectrum

TD-DFT can be used to generate a stick absorption spectrum where each stick corresponds to a distinct electronic transition. In contrast, a measured spectrum is characterized by a few broad absorption bands. Various approximations exist to connect a TD-DFT stick spectrum to an experimental spectrum.[199, 200] Consider an excitation between the singlet states S_i and $S_{j>i}$ that results from the absorption of a photon of luminous intensity, dI, by a thin layer of a homogeneous ideal gas with thickness dl as shown by the relation:[199, 200]

$$dI = -I\varepsilon(\omega)dl \qquad (2.122)$$

where the luminous intensity of the incident radiation is I and the absorption coefficient is $\varepsilon(\omega)$:

$$\int \varepsilon(\omega)d\omega = N_i B_{i\to j} h\bar{\omega} \qquad (2.123)$$

The number of atoms in state i per unit volume is denoted N_i. The average energy $\bar{\omega}$ is over all electronic transitions from state i to j. The Einstein absorption coefficient, $B_{i\to j}$, can be written as: [200]

$$B_{i\to j} = \frac{\pi e^2 f_{i\to j}}{hc^2 m_e \bar{\omega}} \qquad (2.124)$$

where the mass of an electron is m_e, the Planck constant is h, and the speed of light in vacuum is c.

The oscillator strength of the electron, $f_{i\to j}$, can be obtained by combining Eq. (2.123) and Eq. (2.124):[200]

$$f_{i\to j} = \frac{m_e c^2}{N_i \pi e^2}\int \varepsilon(\omega)d\omega \qquad (2.125)$$

Integrating the luminous intensity, Eq. (2.122), over the ideal gas layer of length l, yields:

$$\log\left(\frac{I}{I_0}\right) = -\varepsilon(\omega)l \qquad (2.126)$$

The measured absorbance (A) of a solution of concentration c_0, in a cuvette with width l, penetrated by a radiation of intensity I_0, is dictated by the Beer-Lambert law:[201]

$$\mathrm{A} = \log\left(\frac{I}{I_0}\right) = -\epsilon(\omega)c_0 l \qquad (2.127)$$

The TD-DFT $f_{i\to j}$ depends on the theoretical ε of the gas, and not the molar absorption coefficient ϵ of the solution. To relate ε and ϵ, Eq. (2.126) and Eq. (2.127) are combined to give:

$$\varepsilon(\omega) = \epsilon(\omega)c_{gas}\ln(10) \;\; , c_{gas} = \frac{1}{22.44} mol\ L^{-1} \qquad (2.128)$$

where c_{gas} is the concentration of the ideal gas. The TD-DFT $f_{i\to j}$ can then be reformulated in terms of a function of the experimental ϵ:

$$f_{i\to j} = \underbrace{\frac{m_e c^2 c_{gas}\ln(10)}{N_i \pi e^2}}_{4.32\times 10^{-9}\, mol\ cm\ L^{-1}} \int \epsilon(\omega)d\omega \qquad (2.129)$$

Therefore, the electron is like an oscillator with a characteristic frequency ω and can be excited from S_i to state $S_{j>i}$ by a radiation of the same frequency as the characteristic frequency.

Since several transitions may occur within a narrow frequency range, many studies deconvoluted measured absorption bands into different fitted bands that cumulatively combine to reproduce the measured band.[202-205] The shape of each fitted band $\mathfrak{B}$ depends on the electronic transitions and intensity of the transition:

$$\mathfrak{B} = \begin{cases} \omega_{i\to j} \\ \epsilon(\omega_{i\to i}) \end{cases} \qquad (2.130)$$

The energy of electronic transition from excited S_i to $S_{j>i}$ denoted as $\omega_{i\to j}$ dictates the position of the absorption maximum. The intensity associated with the transition is ϵ and it dictates the molar absorption coefficient at $\mathfrak{B}$. The area $\boldsymbol{\mathcal{A}}$ of $\mathfrak{B}$ is obtained by integrating over all ϵ under $\mathfrak{B}$:

$$\boldsymbol{\mathcal{A}} = \int \epsilon(\omega)\,\mathrm{d}\omega \qquad (2.131)$$

Statistically, $\mathfrak{B}$ can be simulated using a pseudo-Voigt function ($\mathfrak{B}_v$), with absorption coefficient (ϵ_v), produced by a weighted linear combination of Gaussian and Lorentzian function(s) with heights ϵ_{G} and ϵ_{L}, respectively:

$$\epsilon_v = L\epsilon_G(\omega) + (1-L)\epsilon_L(\omega)\,, \qquad L \in [0,1] \qquad (2.132)$$

In practice, $L \approx 1$, which allows ϵ_v to be:[206, 207]

$$\epsilon_v \approx \epsilon_G(\omega) \tag{2.133}$$

Following this approximation, each $\mathfrak{B}_v$ can represented as a normalized Gaussian function centered on $\omega_{i \to j}$:

$$\epsilon_v(\omega) = \boldsymbol{\mathcal{A}_v} g(\omega) \tag{2.134}$$

where $g(\omega)$ is a Gaussian function and $\boldsymbol{\mathcal{A}_v}$ is the area of the pseudo-Voigt function, with a half-bandwidth of γ and can be written as:

$$g(\omega) = \frac{1}{\sqrt{\pi}\gamma_{red}} e^{\left[-\left(\frac{\omega}{\gamma_{red}}\right)^2\right]} \quad , \qquad \gamma_{red} = \frac{\gamma}{2\sqrt{\ln(2)}} \tag{2.135}$$

$$\boldsymbol{\mathcal{A}_v} = \frac{\epsilon_0 \gamma}{2} \sqrt{\frac{\pi}{\ln(2)}} \tag{2.136}$$

By combining Eq. (*2.129*) and (*2.131*) the oscillator strength becomes:

$$f_v(\omega) = \underbrace{\left(\frac{m_e c^2 c_{gas} \ln(10)}{2 N_i \pi e^2} \sqrt{\frac{\pi}{\ln(2)}} \right)}_{4.60 \times 10^{-9}\ mol\ cm\ L^{-1}} \epsilon_0 \gamma \tag{2.137}$$

Hence, f_v is directly proportional to ϵ_0, which directly proportional to $\boldsymbol{\mathcal{A}_v}$, which implies that f_v of an absorption stick is directly proportional to $\boldsymbol{\mathcal{A}_v}$. This forms the theoretical basis by which chemistry software applications create Gaussian absorption bands centered on absorption sticks.

2.4.5.3 Deconvolution of experimental UV-Vis spectrum

A complex absorption spectrum may require the resolution of individual absorption bands to obtain specific information about their position, height, or width. Three parameters, namely position (wavelength or frequency corresponding to the absorption maximum), intensity (absorbance or molar absorptivity at the maximum), and width (typically the half-height bandwidth), are used to describe a symmetrical spectral band. The deconvolution of symmetrical spectral bands commonly employs the Gaussian function and the Lorentzian function. The Gaussian line shape can be mathematically represented as follows:[208]

$$A(v) = A_{max} exp\left[-(4\ln 2)\left(\frac{v - v_{max}}{\Delta v}\right)^2\right] \quad (2.138)$$

where A is an absorbance at a wavenumber v, and A_{max} and v_{max} are the maximum absorbance and wavenumber at maximum absorbance, and Δv is the half-width.

The Gaussian band equation can be simplified by re-formulating it in terms of an adjustable parameter σ, as follows:

$$A(v) = A_{max} exp\left[-\left(\frac{v - v_{max}}{\sigma}\right)^2\right] \quad (2.139)$$

Therefore, by employing a deconvolution procedure, the observed spectrum can be resolved into individual Gaussian bands, allowing for the extraction of position, height, and width information of each band. This procedure requires an estimation of the number of bands necessary to describe the spectrum, as well as initial values for parameters such as v_{max}, A_{max} and σ that approximate the band shape. The deconvolution process involves varying these parameters to minimize the sum of the squares of the differences between the observed and calculated absorbance. By achieving a reasonably good fit to the observed data points, the deconvolution procedure enables the resolution of the absorption spectrum into separate Gaussian bands and the extraction of specific band information.

2.5 Chemical solvent models

The theoretical framework presented in prior sections did not include solvent effects to model each chemical in a vacuum. However, the vast majority of experimental data are collected in the solvated phase, which leads to the necessity of incorporating solvent effects into the analysis of quantum chemical systems.

2.5.1 Solvent effect on DFT potential energy surface

Solvation free energy (ΔG°_{sol}) is the most important parameter in describing how a solute interacts with its surroundings.[77] It represents the change in free energy that occurs when molecule A moves from the gas phase into the condensed phase. This change depends on the

equilibrium constant that characterizes how species A is partitioned between the gaseous and condensed phases:

$$\Delta G^{\circ}_{sol} = \lim_{[A]_{sol} \to 0} \left\{ -RT \ln \left(\frac{[A]_{sol}}{[A]_{gas}}\Big|_{eq} \right) \right\} \qquad (2.140)$$

The limit ensures ideal solution behavior. The effects of solvation can be demonstrated using the solvated potential energy surface (PES) created by adding the free energy of solvation point by point to the gas-phase PES (Figure 2.9A). The gas-phase reaction joins two minima with almost equal energy, whereas the solvent-phase reaction from left to right is strongly exergonic. Hence, the gas-phase and solvent-phase equilibrium constants are different.[77] The development of models to efficiently compute solvation free energies and thus approximate solvent effect has been a high priority. [77]

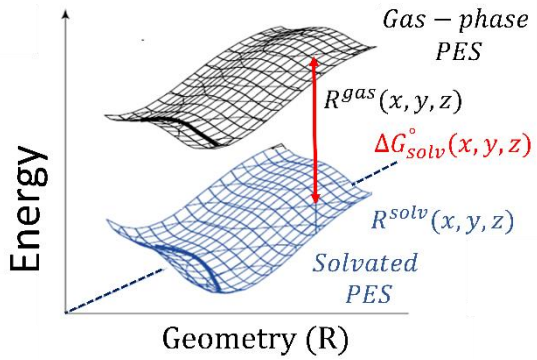

Figure 2.9 A three-dimensional gas-phase PES (black) and the PES derived from adding the free energy of solvation (blue). The chemical reaction proceed from one minimum-energy structure to another (thick line).

2.5.2 Explicit models

Explicit solvent models (Figure 2.10A) entail placing explicit solvent molecules in the chemical system before approximating the Schrödinger equation.[77] These models enables the analysis of specific solute-solvent interactions and exposes the structure of multiple solvation layers that surround the solute, which is useful for understanding solvation cages. However, in addition to increasing the computational effort due to the increase in system size, the number of degrees of freedom of the chemical system increases due to the extra solvent molecules. This results in an increase in the number of PES minima that substantially increases the computational effort needed to explore the PES.

2.5.3 Implicit models

Unlike explicit models, implicit solvent models, do not include solvent molecules directly.[166, 209] Instead, the solute is submerged in a quantum-mechanical (QM) reaction field, which polarizes the system and mimics the effects of the liquid solvent at a fixed temperature and pressure. The eigenvalue equation for the time-independent Schrödinger equation has the following structure:[166, 210, 211]

$$[\hat{\mathcal{H}} + \hat{V}_\tau]\Psi = \varepsilon_{sol}\Psi \qquad (2.141)$$

where the electronic Hamiltonian $\hat{\mathcal{H}}$ treating the solute in vacuo, while the extra operator $\hat{V}_\tau$ applies the QM reaction field to describe solute-solvent interactions and it is equal to the total potential minus the potential of the gas-phase solute. The energy of the solute in solution ε_{sol} is associated the wavefunction Ψ of the solute. Since the application of the reaction field operator typically depends on empirical equilibrium solvent parameters, these can be seen as equilibrium solvation models. The solute is placed in a solvent cavity that represents the solute-solvent boundary. Different implicit models exist, but regardless of the model, the solvation free energy can be universally expressed as:

$$\Delta G_{sol} = \Delta G_{cav} + \Delta G_{el} + \Delta G_{rep} + \Delta G_{dis} \qquad (2.142)$$

The cavitation free energy ΔG_{cav} is the free energy required to form the solvent cavity around the solute.[212] The repulsion free energy ΔG_{rep} accounts for Pauli repulsion.[213] The dispersion free energy ΔG_{dis} describes dispersion forces between solvent and solute.[213, 214] The electrostatic free energy ΔG_{el} models partial charge redistribution under the influence of the solvent. Unlike the other terms, ΔG_{el} is calculated during the SCF procedure.[77]

(a) (b)

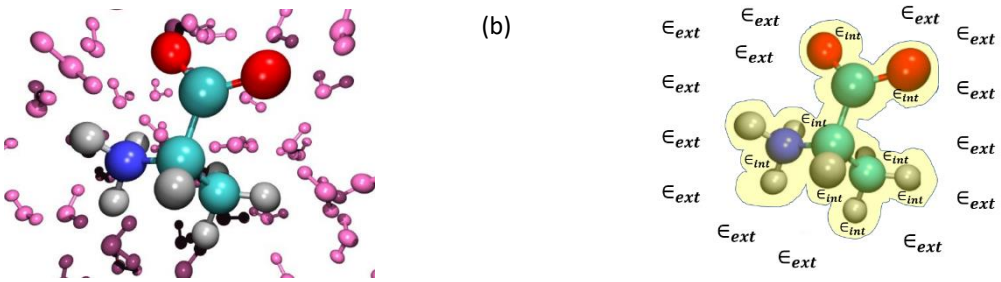

Figure 2.10 An acetonitrile molecule immersed in an explicit (a) solvated phase (pink) and implicit (b) solvated phase.

While implicit models reduce computational cost, they neglect specific solvent structure effects that are critical in strong and specific solvent-solute interactions in the first-solvation-shell, for example π-π stacking interactions or monatomic ions.[215, 216] Therefore, reliable calculations of solute-solvent interaction must account not only for LR electrostatic polarization effects but also SR polarization and non-electrostatic effects. Hybrid modelling approaches use an implicit solvent field and only include explicit solvent molecules for the first solvation shell.[217-220] Such a strategy is frequently used in the aqueous coordination sphere of a highly charged metal cation, where the electrostriction of the first shell causes the solvent molecules to behave more like a ligand than a solvent.

2.5.3.1 Polarizable Continuum Models vs Solvent Model based on Density

One type of widely used implicit models due to their adaptability and accuracy are the polarizable continuum models (PCMs)[166] such as the conductor-like PCM (C-PCM) or integral equation formalism PCM (IEF-PCM).[210, 221, 222] The interior of the PCM cavity experiences an isotropic dielectric field ϵ_{int}, which is different from the continuous anisotropic dielectric field ϵ_{ext} (Figure 2.10B) outside of the cavity. The volume and surface of this cavity is calculated using interlocked spheres with fixed atomic radii centered on each atom.[166] This introduces discontinuities at the intersection of two spheres, which can lead to SCF convergence issues.[223, 224] To circumvent this, Gaussian smoothing can be undertaken at the intersection of the cavity spheres.[225, 226] A critical problem in all implicit models is how the surface charge is constructed. A PCM cavity surface charge is represented by tesserae of charge elements $\mathrm{d}q$, calculated from the apparent charge distribution $\tau(\mathbf{r})$ and surface element area $\mathrm{d}S$:[210, 221]

$$\mathrm{d}q = \tau(\mathbf{r})\mathrm{d}S(\mathbf{r}) \qquad (2.143)$$

This distribution of electrostatic charges obeys the nonhomogeneous Poisson equation (NPE) of point charges:[227]

$$\nabla_{\mathbf{r}} \cdot [\epsilon \cdot \nabla_{\mathbf{r}} V_{\tau}(\mathbf{r})] = \begin{cases} -4\pi\rho(\mathbf{r}) & \Leftrightarrow \epsilon = \epsilon_{int} \\ 0 & \Leftrightarrow \epsilon = \epsilon_{ext} \end{cases} \qquad (2.144)$$

where ρ is the electronic density of the solute, ϵ is the relative permittivity and V_{τ} the QM reaction field.

The QM reaction field is obtained by solving the NPE within a specific PCM formalism (IEF-PCM or C-PCM etc.):

$$V_\tau(\mathbf{r}) = \int_S \frac{\tau(\mathbf{r}')}{|\mathbf{r} - \mathbf{r}'|} \mathrm{d}S(\mathbf{r}) \qquad (2.145)$$

The intrinsic Coulomb radii $\mathbf{r}'$ define the solvent accessible surface (SAS)[228] formed by integrating the apparent charge over the tesserae. The PCM solvation free energy can be decomposed:

$$\Delta G_{sol} = \Delta G_{ENP} + \Delta G^0_{conc} \qquad (2.146)$$

The first term ΔG_{ENP} is the electrostatic (E), nuclear (N) and polarization (P) bulk electrostatic contribution to ΔG_{sol}. The second term ΔG^0_{conc} accounts for the difference between the standard concentration of the gas and liquid phases. If the number of moles of reactant and products species are the same and if the gas phase and solvent phase geometry are assumed to be the same then ΔG^0_{conc} and the nuclear contribution are zero. [229] Hence, under these conditions the self-consistent reaction field (SCRF) calculation computes ΔG_{sol} as follows:[230]

$$\Delta G_{sol} = \Delta G_{EP} = \left\langle \Psi \middle| H^0 - \frac{e}{2} V_\tau \middle| \Psi \right\rangle + \frac{e}{2} \sum\nolimits_k Z_k \, v^k_\tau - \langle \Psi^0 | H^0 | \Psi^0 \rangle \qquad (2.147)$$

where e is the atomic unit charge, v^k_τ and Z_k are the reaction field and atomic charge, respectively, evaluated at atom k, H^0 and Ψ^0 are the solute electronic Hamiltonian and wavefunction, respectively, in the gas phase, and Ψ is the polarized solute wavefunction in solution. Although PCM includes the SR polarization and LR electrostatic effects, it does not explicitly define the SR electrostatic and non-electrostatic solute-solvent interactions, hence may poorly describe first-solvation shell effects.

In an attempt to improve the IEF-PCM models, the solvent model based on density (SMD) has been developed.[211] SMD was parametrized with training sets of solvation free energy data and is thus highly recommended specifically for calculation of free energy of solvation (2.148). SMD separately defines the short-range non-electrostatic contribution to ΔG_{sol}:

$$\Delta G_{sol} = \Delta G_{ENP} + \Delta G_{CDS} + \Delta G^0_{conc} \qquad (2.148)$$

The ENP and ΔG^0_{conc} contributions are identical to IEF-PCM (2.147).[231, 232] The cavity-dispersion solvent-structure (CDS) correction ΔG_{CDS} is newly introduced to approximates the SR non-electrostatic solute-solvent interactions such as both hydrogen bonding and exchange repulsion in the first solvation shell, [166, 209, 212] which are crucial to obtaining accurate ΔG_{sol}:

$$\Delta G_{CDS} = \sum_{k}^{atoms} \sigma_k A_k\left(\mathbf{R}, R_{VDW_k} + r_s\right) + \sigma^{[M]} \sum_{k}^{atoms} A_k\left(\mathbf{R}, R_{VDW_k} + r_s\right) \quad (2.149)$$

The atomic surface tension σ_k of atom k and the molecular surface tension $\sigma^{[M]}$, account for other nearby solvent molecules. The solvent-accessible surface area (SASA) A_k as a function of the geometry $\mathbf{R}$ is the area generated by the center of an implicit solvent molecule that is assumed to be spherical as it is rolling on the exposed van der Waals surface of the solute molecule. Unlike SMD, which uses the Coulomb radii to define the SASA, PCM SASA is computed using the Analytic Surface Area (ASA) algorithm,[233] which uses Bondi van der Waals radii[234] R_{VDW_k} or 2.0 Å if no Bondi radius is available, and the solvent radius r_s (usually 0.4 Å) is added to R_{VDW_k}. Although SMD explicitly defines the SR solute-solvent interaction in the CDS term, it does not guarantee improved performance over IEF-PCM because ΔG_{CDS} is not a state function, only ΔG_{sol}. Hence, the accuracy of SMD compared to IEF-PCM should not be assumed based on the formulation of ΔG_{sol}, but should be verified against the experimental observables.

2.5.4 Solvatochromism

The effect of solvent on electronic excitations is not only about the solvation of the PES of the GS, but also of the EES. The unequal solvation of the GS and EES PESs causes solvatochromism[77] (Figure 2.11). Consider EES and GS solvation during vertical absorption in an implicit solvent model (c.f. Section 2.5.3). Because the electronic transition speed is close to the speed of light, the solvent is only equilibrated to the electronic density of the GS solute at the point of absorption.

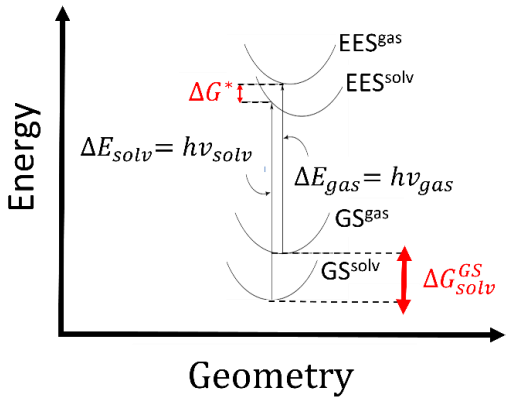

Figure 2.11 A two-dimensional gas-phase, solvated phase GS PESs and the corresponding EES PESs.

The nuclear motion of the solute is on the slower molecular vibration timescale, which is almost frozen on the absorption timescale, based on the Born Oppenheimer approximation. Hence, the solute and solvent do not fully equilibrate during excitation. As a result, the GS may be better solvated than the EES, with the GS equilibrium free energy of solvation ΔG_{solv}^{GS} being different to the EES non-equilibrium solvation free energy ΔG^*. The VTE (ΔE_{solv}) is then specified by Eq.(2.150), showing the effect of solvatochromism due to the differential solvation of the ESS:

$$\Delta E_{solv} = \Delta E_{gas} + \underbrace{\Delta G^* - \Delta G_{solv}^{GS}}_{solvatochromism} \tag{2.150}$$

In polar solvents, a blue shift will usually occur because ΔG_{solv}^{GS} is greater than ΔG^* due to better electrostatic solute-solvent interactions in the GS than the EES.[77] Non-polar solvents exhibit the opposite phenomenon, i.e. their absorption spectra are red-shifted. This appears to be a manifestation of better dispersion interactions between the solvent and the EES, as the EES is more polarizable than the GS due to highly excited electron(s) in the EES.

Chapter 3 Experimental details

3.1 General procedures and physical measurements

3.1.1 Synthesis of $Ru_2(\mu\text{-}O_2CCH_3)_3(2\text{-}Fap)I$

The $Ru_2(\mu\text{-}O_2CCH_3)_3(2\text{-}Fap)Cl$ complex was synthesized from a mixture of $Ru_2(\mu\text{-}O_2CCH_3)_4Cl$ and 2-Fap following the literature procedure.[47] $Ru_2(\mu\text{-}O_2CCH_3)(2\text{-}Fap)Cl$ (0.0245 mmol, 0.0139 g) and a 1.1 equivalent (0.0269 mmol, 0.00458 g) of $AgNO_3$ were dissolved in 2 mL dry methanol. The methanolic solution was stirred for 1h and white a precipitate of AgCl was filtered over paper using gravity filtration and subsequently further purification through celite to ensure the removal of any excess $AgNO_3$ and pump to dryness in a rotary evaporator giving a brown precipitate of 0.0167 g of $[Ru_2(\mu\text{-}O_2CCH_3)_3(2\text{-}Fap)]^+$ with a yield of 86%. The $[Ru_2(\mu\text{-}O_2CCH_3)(2\text{-}Fap)]^+$ (0.0294 mmol, 0.0167 g) compound was dissolved in 2 mL acetone and treated with a 1.2 equivalent (0.0294 mmol, 0.00529 g) of NaI and the solution was stirred for 24h giving a light brown solution, which filtered off, washed with acetone (2 × 30mL) and dried under vacuum generating the $Ru_2(\mu\text{-}O_2CCH_3)(2\text{-}Fap)_4I$ complex with a yield of 60%. The UV-Vis absorption spectra of chloride and iodide derivatives were characterized in DCM, DMSO and water.

3.2 Computational methods

3.2.1 General ground state calculations set up

The following is applicable to all DFT calculations unless otherwise stated. The initial coordinates for all the complexes were inferred from the corresponding crystallographic data.[18, 29, 43, 47] All DFT geometry optimizations and energy calculations were performed on unconstrained structures using the Gaussian 16 (Revision C.01) suite.[235] Unrestricted calculations were performed in every case for the open-shell complexes. Electrons of alpha and

beta spins are independently described which results in a set of orbital energies and molecular orbitals for electrons of alpha spin (alpha manifold) and beta spin (beta manifold).[236] Tight optimization (*Opt=tight*) criteria were used in all cases. Quadratically convergent SCF (*scf=xqc*) was used in some cases were SCF convergence failed with standard techniques. No symmetry constraints were used. An ultrafine integration grid was used for numerical integration by specifying the *int=ultrafine* keyword. This is the recommend integration grid quality for better accuracy and stability of the calculations, which invokes a very large number of points (99 radial shells and 590 angular points per shell for each atom) over which the *numerical integration* of the integrals in a given DFT functional is evaluated. All structures were fully optimized and harmonic frequency calculations (*freq*) were performed to establish the nature of the critical points. A quartet spin state was specified for all metal-containing complexes (see Figure 1.1). Some calculations of doublet states where done initially to confirm that the quartet state had a lower energy (see Figure 1.5). No symmetry constraints were used for the optimization. Where applicable, the default SDD ECP[143] basis set by Stuttgart-Dresden are applied to ruthenium and iodine. All calculations were run specifying 24 shared-memory cores with up to 40 Gb random access memory and 300 Gb disk space. The pop=full keyword was used to specify that the compositions of all MOs are written to the output.

3.2.2 Excited state calculations and UV-Vis spectra analysis

In general, the *TD(N states = 200, root = 1)* was specified for excited state calculations to obtain the UV-Vis absorption spectra of the complexes. The keyword *N states = 200* specifies that the lowest 200 singlet-singlet electronic transitions should be calculated, which was sufficient to cover the region from 100 nm to 1500 nm. The *root=1* keyword specifies that the first excited state should be used for calculating population analysis and electron density. The *guess=read* keyword specifies that the initial MO coefficients should be used as the first guess. The *geometry=allcheck* was specified so that the charge, spin multiplicity and molecule specification from a previous checkpoint file, specified using the *%oldchk* keyword, should be used.

The GaussView 6.06.16 program[237] was used to edit Gaussian input files. Molecular structures and surfaces were viewed and analyzed using Visual Molecular Dynamics 1.9 (VMD),[238] UCSF Chimera 1.15 software packages[239] or Chemissian 4.01[240]. The UV-vis spectra and NTOs were visualized using the Chemissian program, SpecDis 1.70.1,[241] GaussView 6.06.16 or VMD software programs. The predicted UV-Vis spectra were plotted using a Gaussian broadening model and half-bandwidths were taken to be equal to 0.16 eV. Mulliken charge contribution of fragments to the NTOs were obtained using the Chemissian *fragment contribution* functionality. A fragment was formed by grouping atoms according to their label number assigned to them in the generated Gaussian output files. Deconvolution of the experimental absorption spectra were conducted by fitting as many Gaussian curves as there are major excitations using the Solver[242] add-on in Microsoft Excel suite and the latter was also used for plotting of graphs. TD-DFT UV-Vis spectra curves were plotted with SpecDis without preforming any similarity factor as this was observed to produce poorer convolution of peaks than those obtained by only manually adjusting the half-bandwidths.

In order to test the effect increasing the basis set size from Def2-SVP to Def2-TZVP, geometry optimizations and subsequent frequency analysis calculations were performed in the gas phase at the B3LYP/Def2-SVP, B3LYP/Def2-TZVP levels of theory coupled to the SDD ECP on Ru and I atoms. In addition, geometry optimization and frequency calculations were performed using the B3LYP/LANL2DZ coupled to the LANL2-ECP on Cl, I and Ru atoms, to test the effect of changing from Def2-type to LANL2-type basis sets. The B3LYP/LANL2DZ level of theory coupled to the LANL2-ECP for Ru and I atoms but the D95 all-electron basis set for the Cl atom, was also employed to test the effect of not having a ECP on Cl. The gas-phase optimized ground state structures were used as input for gas-phase TD-DFT calculations at the same level of theory as the gas-phase geometry optimization. The energies and intensities of the lowest 200 singlet-singlet electronic transitions were calculated and the first excited state was used for printing population and electron density using the *Root=1* keyword. The gas-phase optimized structures were used as input for SPE solvent-phase TD-DFT calculations at the same level of theory.

To test the effect of implicit solvent on the geometry and the resultant calculated spectra, geometry re-optimizations and subsequent frequency analysis calculations in the solvent phase

(DCM, DMSO or water) were performed on the gas-phase structures at the same levels of theory as the gas-phase geometry optimization. The solvent-phase optimized structures were used as input for TD-DFT calculations at the same level.

For evaluating the performance of different DFT functionals, geometry optimizations and subsequent frequency analysis calculations were performed at the BP86/LANL2DZ, PBE/LANL2DZ, B3LYP/LANL2DZ, TPSSh/LANL2DZ, CAM-B3LYP/LANL2DZ, and LC-ωHPE/LANL2DZ, levels of theory in the IEF-PCM solvated phase(DCM, DMSO or water). The solvent-phase optimized structures obtained were used as input for TD-DFT calculations at the same level of theory.

3.2.3 Natural transition orbitals calculations and charge contributions

The TD-DFT checkpoint files outputted after TD calculations were used as input for NTO calculations.[195] Every excited state (*N*) with oscillator strength of 0.01 a.u or higher within the 400 nm-1500 nm range were analyzed. In addition, for the 200 nm-400 nm range, only one or two states having the highest oscillator strength in each band were analyzed with NTOs, due to the great number (in general more than a hundred) of excited states with high oscillator strengths below the 400 nm region. For every excited state (*N*), the *Pop=SaveNTO* keyword was used to write NTO information and *Density=(Check, Transitions=N)* was used to specify which excited state should be saved.

The percentage contribution of NTOs to an excited state were automatically derived using the Chemissan software package. To test whether the percentage contributions of canonical MOs to an excited state are similar to those of NTOs, the percent contribution of each MO was calculated on the basis of the transition amplitude yielded in the TD-DFT Gaussian output file, as follows:

$$\%MO_i = \frac{100 f_i^2}{\sum_{i=0}^{N} f_i^2}$$

where f_i is the oscillator strength associated with $\%MO_i$, which represents the i-th MO orbital contributing the excited state.

Chapter 4 Results and discussion

4.1 Strategy for choosing the best TD-DFT level of theory for predicting the UV-Vis-NIR electronic absorption spectra of diruthenium(II,III) complexes

TD-DFT is the most widely applied *ab initio* tool for modelling UV-Vis-NIR spectra[243, 244] and can be extended to incorporate environmental solvent effects.[162, 166-175] Most implementations of TDDFT utilize the A-LR-TDDFT approximation where, in the limit of an electron density slowly varying in time, GS DFT functionals are used in the calculation of the TD exchange-correlation kernel. Despite its successes and versatility, the quality of the results obtained with A-TD-DFT is profoundly functional-dependent and TD-DFT benchmarks studies deal almost exclusively with diamagnetic (closed shell) systems and small open-shell systems, only a few studies have been published on larger open-shell systems such as diruthenium complexes, probably because of the convergence difficulties usually associated with such calculations.[21, 63, 69, 245-251] One of the aims of this section is to validate the level of theory, including appropriate functionals and basis sets by benchmarking the results against experimental spectra. A second important aim is to use the validate previously assigned electronic transitions of some characteristic bands in the UV-Vis spectra of diruthenium complexes whose characterization have been ambiguous and/or contradictory. This validation is important because it serves as precursor to the first-time theoretical characterization of electronic transition in mono-ap diruthenium complexes.

4.1.1 Benchmarking LANL2- and Def2-type basis set in gas and solvated phase

To assess the advantages and disadvantages of a series of TD-DFT approaches one of the key aspects is the choice of basis set and solvation. While the family of Def2 basis sets is newer and popular, the Los Alamos National Laboratory basis with split-valence-double$-\zeta$ (LANL2DZ) is also renowned and has been widely used in for geometry and energy calculations[98] but most importantly it has also seen use in excited state calculations.[21, 149-152, 154, 155, 252] Applied to Ru_2

complexes, the Def2-type and LANL2-type basis sets have shown good performance in conjunction with the B3LYP functional.[21, 63]

Unlike previous studies that used either one of these basis sets based on prior knowledge, this investigation has opted to compare the performance of the Def2-type against LANL2-type basis sets. To do so, LANL2DZ has been selected,[142] which applies the D95 basis set[142] to all first-row atoms and the LANL2-ECPs and associated valence-region functions to all non-first row atoms (i.e., Cl, Br, I and Ru), LANL2DZ+D95, which employs the all-electron D95 basis set[142] also on the Cl atom and the LANL2-ECPs and valence functions on only Ru, Br and I atoms, against the Def2-SVP and Def2-TZVP basis sets, both which employ the Stuttgart (or SDD as abbreviated in Gaussian) ECPs on Ru, Br and I, and an all-electron basis set on Cl and first-row atoms.[145] Def2-QZVPP which was not tractable for TD-DFT calculations on the current system is not included, but the double- and triple-ζ counterparts represent good compromise between accuracy and performance.

The B3LYP functional and IEF-PCM solvation model have been employed for a reasonable comparison to the previous study[21] and the TDDFT calculations were conducted. Before evaluating the effect of the basis set, the effect of the including an implicit solvent on the accuracy of the predicted UV-Vis spectra is evaluated. Three relevant approaches for the analysis are selected: (i) predict the UV-Vis in the gas phase based on the GS molecular geometry optimized in vacuo, (ii) predict the UV-Vis in the solvated phase based on GS molecular geometry optimized in the gas phase or (iii) predict the UV-Vis in solvated phase based on GS molecular geometry optimized in solvated phase. Shown in Figure 4.1A-C is the UV-Vis spectra predicted in IEF-PCM acetonitrile (AN) for the $[Ru_2(O_2CCH_3)_3X_2]^-$ compounds. The approaches (i), (ii) and (iii) are denoted as B3LYP/LANL2DZ // B3LYP/LANL2DZ, B3LYP/LANL2DZ-IEFPCM(AN) // B3LYP/LANL2DZ and B3LYP/LANL2DZ-IEFPCM(AN) // B3LYP/LANL2DZ-IEFPCM(AN), respectively, against the experimentally obtained spectrum (Expt.).[21] There are three distinct bands in the experimental spectrum denoted band 1-3 that are made of two ultraviolet (UV) bands and one visible (Vis) band, whereas there are up to five bands, denoted band 1 - 5, in approach (i), (ii) and (iii), that consist of two UV bands, one Vis band and a Vis shoulder band, and one near-infrared (NIR) band as shown in Table 4.1.

(a)

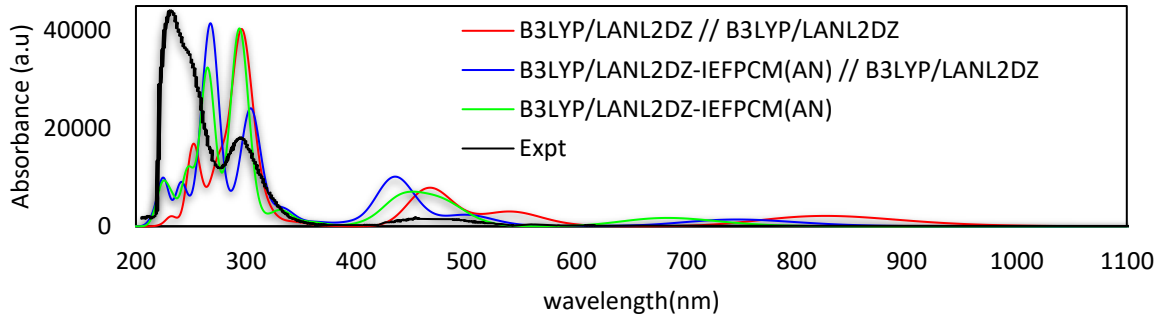

(b)

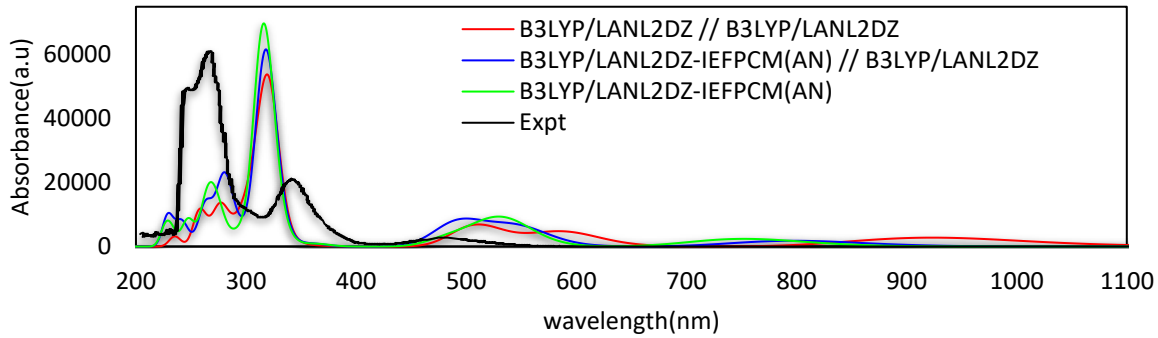

(c)

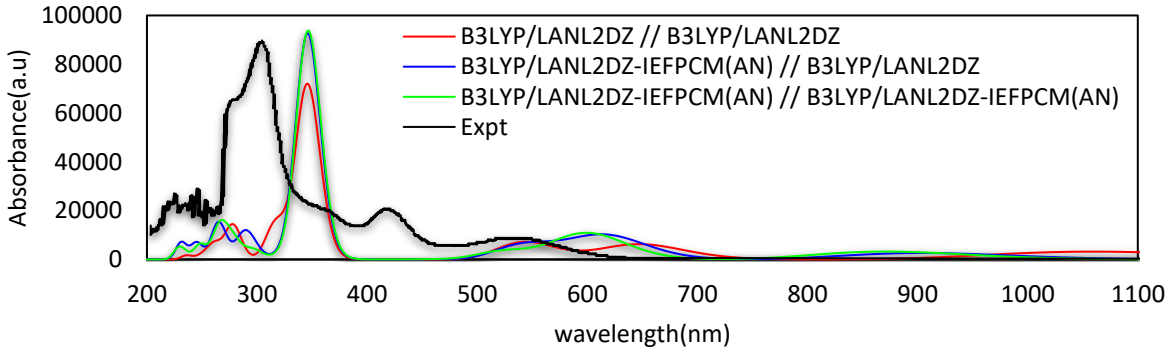

Figure 4.1 Comparison of experimental (Expt.) UV-Vis spectra of anionic $[Ru_2(O_2CCH_3)_4X_2]^-$ complexes, where X = Cl **(a)**, Br **(b)** or I **(c)**, recorded in acetonitrile (AN) and the corresponding TDDFT UV-Vis-NIR spectra predicted at B3LYP/LANL2DZ//B3LYP/LANL2DZ, B3LYP/LANL2DZ-IEFPCM(AN)//B3LYP/LANL2DZ and B3LYP/LANL2DZ-IEFPCM(AN)//B3LYP/LANL2DZ-IEFPCM(AN) levels of theory.

The two additional predicted bands, band 5 and 6, have previously been reported experimentally in acetonitrile at around 630 - 700 nm and 1150 nm, respectively, for the $[Ru_2(O_2CCH_2CH_2CH_3)_3)_3X_2]^-$ complex,[57] which occurred at slightly different wavelengths to those presented in Figure 4.1A-C. All the bands correspond to those previously discussed (c.f. section 1.2). Since band 3 or 4 may or may not be observable in the predicted spectra and either one could be a shoulder band depending on the relative intensity of the other, the convention that band 3 is the primary band (*viz.* the band with higher absorbance) is adopted, which is

compared to the experimental spectra, while band 4 (if present) is the shoulder band, irrespective of the wavelength.

Table 4.1 Comparison of environmental effect UV-Vis wavelength of maximum absorption (λ_{max}) of anionic $[Ru_2(O_2CCH_3)_4X_2]^-$ complexes, where X = Cl, Br, or I, recorded experimentally (Expt.) in acetonitrile (AN) and predicted using TDDFT UV-Vis-NIR (i − iii) at B3LYP/LANL2DZ//B3LYP/LANL2DZ, B3LYP/LANL2DZ-IEFPCM(AN)//B3LYP/LANL2DZ and B3LYP/LANL2DZ-IEFPCM(AN)//B3LYP/LANL2DZ-IEFPCM(AN) levels of theory.

Band	Expt. λ_{max} (nm)	B3LYP/LANL2DZ // B3LYP/LANL2DZ (*i*)		B3LYP/LANL2DZ-IEFPCM(AN) // B3LYP/LANL2DZ (*ii*)		B3LYP/LANL2DZ-IEFPCM(AN) // B3LYP/LANL2DZ-IEFPCM(AN) (*iii*)	
		λ_{max} (nm)	SE (nm)	λ_{max} (nm)	SE (nm)	λ_{max} (nm)	SE(nm)
				$[Ru_2(O_2CCH_3)_4Cl_2]^-$			
1	230	254	24	267	37	266	36
2	293	297	4	306	13	295	2
3	454	465	11	433	-21	449	-5
4		537		504		527	
5		829		741		680	
				$[Ru_2(O_2CCH_3)_4Br_2]^-$			
1	269	276	7	281	12	270	1
2	346	319	-27	317	-29	315	-31
3	476	510	34	505	29	525	49
4		585		530		483	
5		922		800		748	
				$[Ru_2(O_2CCH_3)_4I_2]^-$			
1	305	276	-25	293	-12	271	-34
2	418	319	-71	347	-71	347	-71
3	538	510	115	620	82	606	68
4		585		544		545	
5		922		908		865	
AD			35.3		34		33

sh = shoulder band. Signed error (SE) = $\lambda^{TD\text{-}DFT}$ - λ^{Expt}. Absolute deviation (AD): $\frac{1}{N}\sum|\Delta\lambda_{max}|$

This ensures that the experimental Vis band 3 is always compared to the primary band, which prevents ambiguous comparison of wavelengths of maximum absorption, and avoids the

acquired error due to subjective positioning of the poorly defined shoulder. In addition, it is a scientifically reasonable tactic since the most intense band predominantly influences the wavelength of maximum absorption.

Approach (iii) has an overall smaller deviation (SE) from experimental values than both approaches (i) and (ii) for band 2 - 3 of the $[Ru_2(O_2CCH_2CH_2CH_3)_3)_3Cl_2]^-$ and $[Ru_2(O_2CCH_2CH_2CH_3)_3)_3Br_2]^-$ species, and only band 2 of $[Ru_2(O_2CCH_2CH_2CH_3)_3)_3I_2]^-$. The net smaller deviation is more obviously reflected in the absolute deviation (AD) obtained, which equals to 35.3 nm, 34.0 nm and 33.0 nm in approach $(i), (ii)$ and (iii), respectively. This indicates that approach (iii), which involves the full geometry optimization in the solvated phase and coupling of the UV-Vis prediction to the solvated phase, outperforms full gas-phase prediction and solvated-phase prediction on the basis of gas-phase molecular geometry.

In addition, it also indicates that the molecular geometry is significantly affected by the presence of the solvent. Approach (ii) is the second-best option if approach (iii) is not tractable. Approach (i) being the least accurate suggests that solvation is ultimately crucial to the accuracy of the UV-Vis spectrum predicted.

Given that approach (iii) yielded the lowest AD and the best reproduced band shape, this approach is used to further evaluate the basis set effect on the accuracy of the computed spectra. Since the LANL2DZ and LANL2DZ+D95 basis sets yielded equivalent results (Figure 4.2) with only minor differences in the intensity, only the LANL2DZ result is shown in Table 4.2.

This similarity indicates that applying the D95 basis set on the chloride atom rather than an ECP, has a negligible effect on the computed spectra. In contrast, changing the basis set from LANL2DZ to Def2-SVP significantly lowers the excited state energies as evident in Table 4.2, which blue-shifts all the absorption bands 1 - 5. The blues-shift of band 1, 2, 3, 4 and 5 are within 17 - 38 nm, 34 - 38 nm, 43 - 105 nm, 153 nm and 110 - 180 nm, respectively, which suggests that the blue-shift due to the basis set change predominantly affects the low-energy infrared IR bands, followed by the Vis bands, whereas the UV bands are least affected. This might be an indication that the polarization functions included in the Def2-SVP basis set increases the energy gap between the bonding and anti-bonding MOs.

(a)

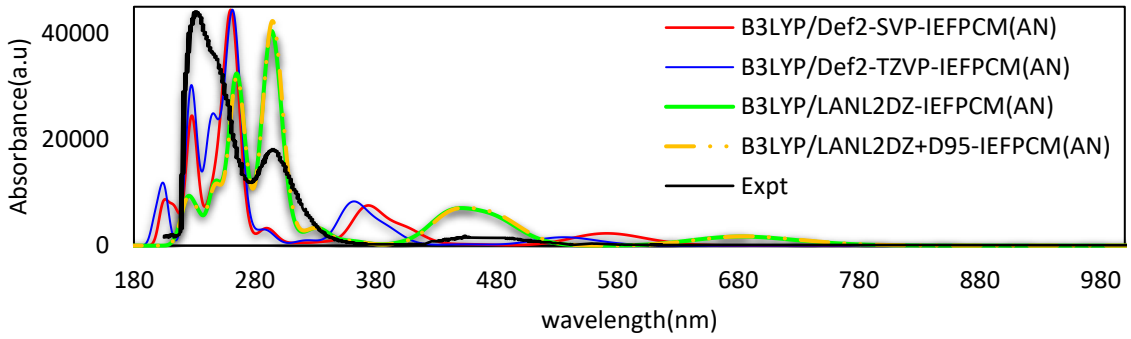

(b)

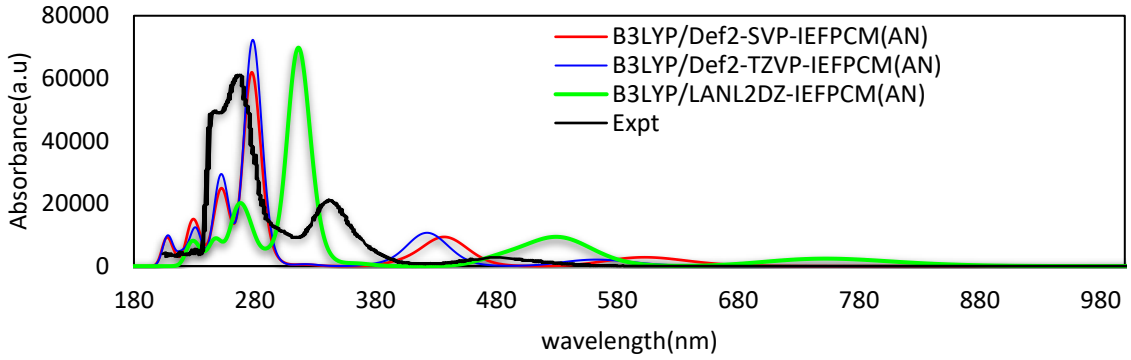

(c)

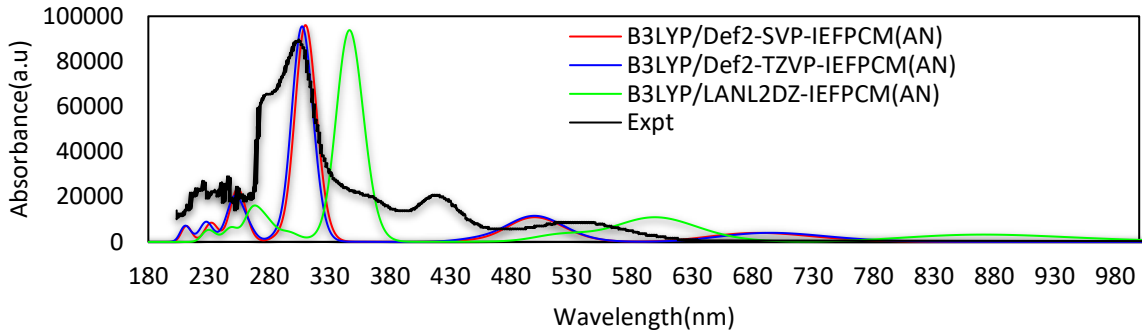

Figure 4.2 Comparison of experimental (Expt.) UV-Vis spectra of anionic $[Ru_2(O_2CCH_3)_4X_2]^-$ complexes, where X = Cl **(a)**, Br **(b)** or I **(c)**, recorded in acetonitrile (AN) and the corresponding TDDFT UV-Vis-NIR spectra predicted using Def-SVP-IEFPCM(AN), Def-TZVP-IEFPCM(AN), LANL2DZ-IEFPCM(AN) and LANL2DZ+D95-IEFPCM(AN) in conjunction with the B3LYP

The Def2-TZVP basis set gives a larger blue-shift in comparison to the Def2-SVP basis set, but does not qualitatively change the shape of the band. The trends in the signed errors (SEs) from experimental values (line at y = x) is graphically illustrated (Figure 4.3), where accuracy plots show the deviation of calculated TDDFT wavelengths of maximum absorption for band 1 - 3.

Table 4.2 Comparison of basis set effect on the UV-Vis wavelength of maximum absorption (λ_{max}) of anionic $[Ru_2(O_2CCH_3)_4X_2]^-$ complexes, where X = Cl, Br, or I, recorded experimentally (Expt.) in acetonitrile (AN) and predicted using TDDFT UV-Vis-NIR at the B3LYP/Def2-SVP-IEFPCM(AN), B3LYP/Def2-TZVP-IEFPCM(AN), and B3LYP/LANL2DZ-IEFPCM(AN) levels of theory.

Band	Expt. λ_{max} (nm)	B3LYP / LANL2DZ -IEFPCM		B3LYP / Def2-SVP -IEFPCM		B3LYP / Def2-TZVP-IEFPCM	
		λ_{max}(nm)	SE	λ_{max}(nm)	SE	λ_{max}(nm)	SE
				$[Ru_2(O_2CCH_3)_4Cl_2]^-$			
1	230	266	36	228	-2	223	-7
2	293	295	2	261	-32	261	-32
3	454	449	-5	406	-48	389	-65
4		527		374		361	
5		680		570		538	
				$[Ru_2(O_2CCH_3)_4Br_2]^-$			
1	269	270	1	253	-16	253	-16
2	346	315	-31	278	-68	279	-67
3	476	525	49	439	-37	420	-56
4							
5		748		600		559	
				$[Ru_2(O_2CCH_3)_4I_2]^-$			
1	305	271	-34	253	-52	254	-51
2	418	347	-71	309	-109	308	-110
3	538	606	68	501	-37	503	-35
4		545					
5		865		685		690	
AD			33		44.6		48.8

sh = shoulder band. Signed error(SE) = $\lambda^{TD\text{-}DFT} - \lambda^{Expt}$. Absolute deviation (AD): $\frac{1}{N}\sum|\Delta\lambda_{max}|$.
B3LYP/LANL2DZ+D95 is not show because it yielded similar result to B3LYP/LANL2DZ

The wavelengths yielded by LANL2DZ are generally more clustered near the y = x line, thus closer to the experimental values in comparison Def2-SVP and Def2-TZVP, which yielded similar trends. Indeed, the AD yielded with LANL2DZ, Def2-SVP and Def2-TZVP are equal to 33.0 nm, 44.6 nm, and 48.8 nm, respectively. This indicates that the smaller LANL2DZ basis set unexpectedly outperforms the Def2-type basis sets. In addition, increasing the number of basis functions in the Def2-type basis sets worsens the deviation, which implies that the Def2-QZVPP

basis set possibly would have produced equally bad or worse discrepancies. In light of this, the LANL2DZ basis set will be used for further analysis.

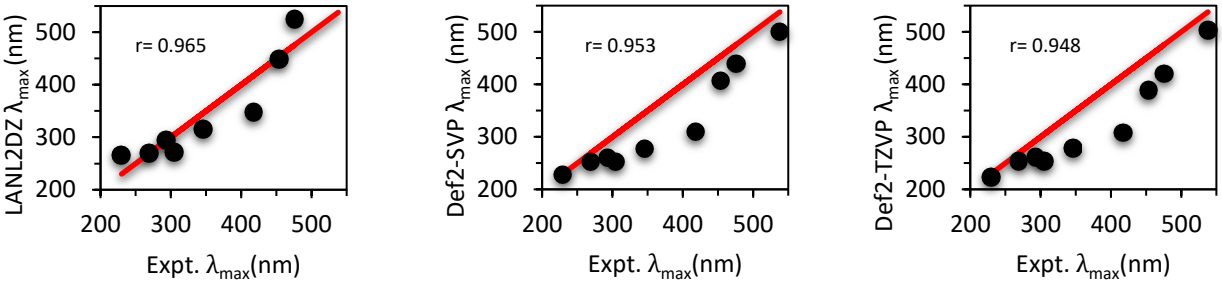

Figure 4.3 Accuracy plots for TD-DFT calculated wavelength of maximum absorption for (a) LAN2DZ (b) Def2-SVP and (c) Def2-TZVP in conjunction with B3LYP and IEF-PCM in Acetonitrile. Points above the line indicate positive errors while points below the line indicate negative errors.

4.1.2 Benchmarking GGA, hybrid GGA, hybrid meta-GGA and RSH functionals

In this section, a series of DFT functionals will be benchmarked. To do this, functionals that can be classified into the following four major categories have been selected: non-hybrid GGA, GH-GGA, GH-mGGA and RSH. The motivation behind this choice of functionals is that it would allow us to gauge the effect of introducing HF exact exchange (EX) when going from non-hybrid GGA to GH-GGA, the outcome of introducing kinetic energy density upon going from GH-GGA to GH-mGGA, and the consequence of splitting the interelectronic operator into a LR part and a SR part when going from GH-GGA to RSH. It would also enable us to assess the effect of different percentages (%) of EX included in the different GH functionals.

The test set of functionals consist of two popular[98] GGAs, namely empirically parameterized BP86[101, 111] and non-empirical PBE,[101] which are parameterized and theoretical GGA functionals, respectively. In addition, two popular[98] GH-GGAs (the amount of exact HF exchange is given in brackets) namely, B3LYP(20%)[117, 118] and PBE0(25%)[115, 116] were included, whereas one popular GH-mGGA namely TPSSh(28%) has been included.[120] The RSH functionals constitute the last category and use a growing fraction of exact exchange when the interelectronic distance increases: LC-ωHPBE ($\omega = 0.40$ au^{-1}, $\alpha = 0$, $\beta = 1$) and the well-known

CAM-B3LYP (ω = 0.33 au^{-1}, α = 0.19, β = 0.46). Calculations were done on all the $[Ru_2(O_2CCH_3)_4X_2]^-$ complexes.

Firstly, the performance within GGA functionals is compared. The BP86 and PBE functionals yielded similar band shapes and only a minor blue-shift of all the PBE bands (Figure 4.4).

(a)

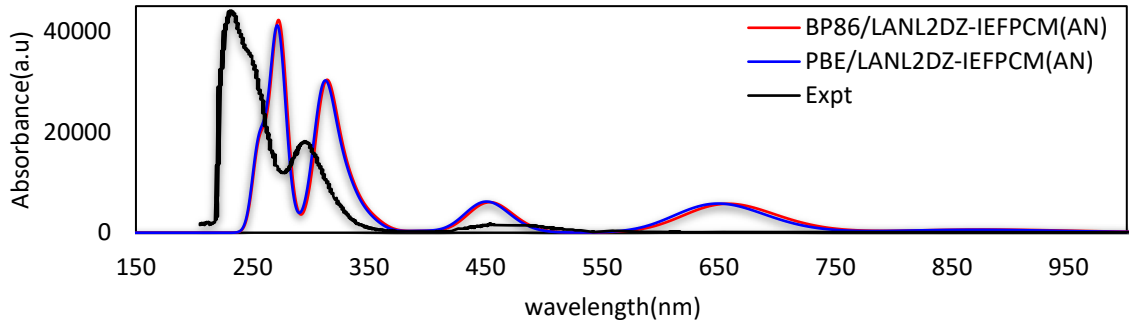

(b)

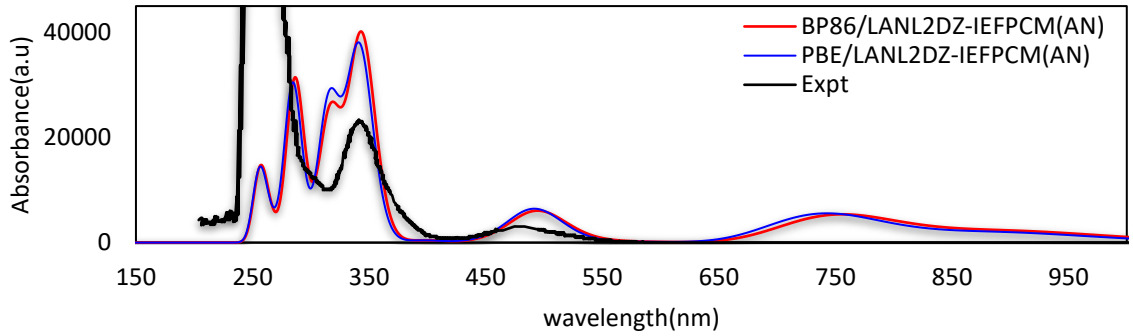

(c)

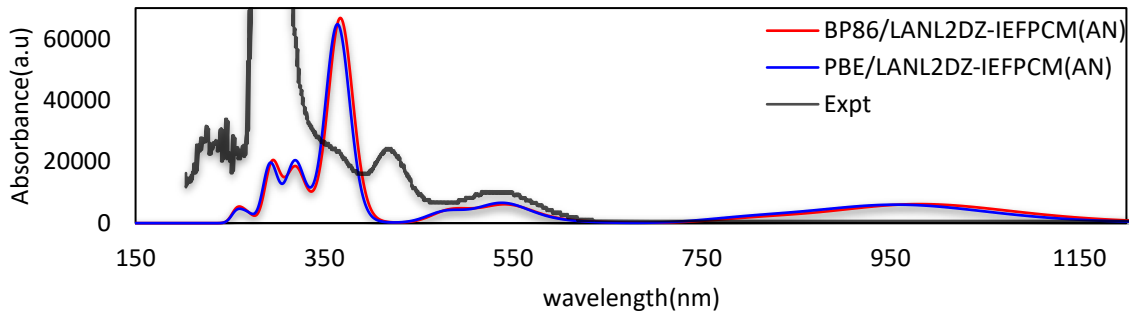

Figure 4.4 Comparison of experimental (Expt.) UV-Vis spectra of anionic $[Ru_2(O_2CCH_3)_4X_2]^-$ complexes, where X = Cl **(a)**, Br **(b)** or I **(c)**, recorded in acetonitrile (AN) and the corresponding TDDFT UV-Vis-NIR spectra predicted at the PBE/LANL2DZ-IEFPCM(AN) and BP86/LANL2DZ-IEFPCM(AN) levels of theory.

The blue-shift was measured to be 0 – 3 nm, 2 – 3 nm, 4 – 12 nm, 8 nm and 1 – 30 nm for bands 1, 2, 3, 4, and 5, respectively. The discrepancies may be attributable to the fact that PBE is a

non-empirical functional whereas BP86 includes the B88[111] exchange that has empirical parameters that have been fitted to the exchange energy of the noble gas atoms. The similarity in the band shape is ascribable to the fact that both are non-hybrid GGAs incorporating similar expressions for the LSDA part based on the uniform electron gas. The AD yielded by BP86 and PBE are 20.6 nm and 18.4 nm, respectively (Table 4.3).

Table 4.3 Comparison of DFT functional effect on the UV-Vis wavelength (nm) of maximum absorption (λ) of anionic $[Ru_2(O_2CCH_3)_4X_2]^-$ complexes, where X = Cl, Br, or I, recorded experimentally (Expt.) in acetonitrile (AN) and predicted using TDDFT UV-Vis-NIR the BP86, PBE, B3LYP, PBE0, TPSSH, CAM-B3LYP and LC-ωHPBE functionals in conjunction with the LANL2DZ basis set and IEFPCM(AN) solvation.

Band	Expt.	BP86		PBE		B3LYP		PBE0		TPSSH		LC-ωHPBE		CAM-B3LYP [b]	
	λ	λ	SE	λ	SE	λ	SE		SE	λ	SE	λ	SE	λ	SE
							$[Ru_2(O_2CCH_3)_4Cl_2]^-$								
1	230	273	43	270	40	266	36	247	17	266	36	263	33		
2	293	316	23	314	21	293	0	275	-18	307	14	336	43		
3	454	458	4	454	0	447	-7	404	-50	446	-8	506	52		
4						480		458							
5		658		657		684		637		641		855			
							$[Ru_2(O_2CCH_3)_4Br_2]^-$								
1	269	288	19	286	17	267	-2	255	-14	281	12	257	-12	284	15
2	346	345	-1	343	-3	317	-29	293	-53	329	-17	324	-22	419	73
3	476	501	25	489	13	532	56	487	11	488	12	500	24	512	36
4								449		492					
5		753		739		747		686		727					
							$[Ru_2(O_2CCH_3)_4I_2]^-$								
1	305	322	17	322	17	270	-35	258	-47	290	-15	282	-23	313	8
2	418	369	-49	366	-52	347	-71	321	-97	353	-65	366	-52	482	64
3	538	542	4	535	-3	607	69	556	18	533	-5	542	4	573	35
4		487		479		523		493							
5		980		950		876		767		853					
	AD		20.6		18.4		33.9		36.1		20.4		29.4		38.5

[a] Experimental spectra from Ref [21]. sh = shoulder band. Signed error (SE) = $\lambda^{TD\text{-}DFT} - \lambda^{Expt}$. Absolute deviation (AD): $\frac{1}{N}\sum|SE|$.

[b] The CAM-B3LYP data for X=Cl is not available in spectra **(a)** because the calculation failed to converge.

This indicates that the non-empirical GGA PBE outperforms the empirical GGA BP86 by an AD of only 2.2 nm in predicting the UV-Vis spectra of $[Ru_2(O_2CCH_3)_4X_2]^-$ complexes. Secondly, the

performance within the GH-GGAs functionals is considered. The band shapes change and there is a net blue-shift upon going from B3LYP to PBE0 (Figure 4.5).

(a)

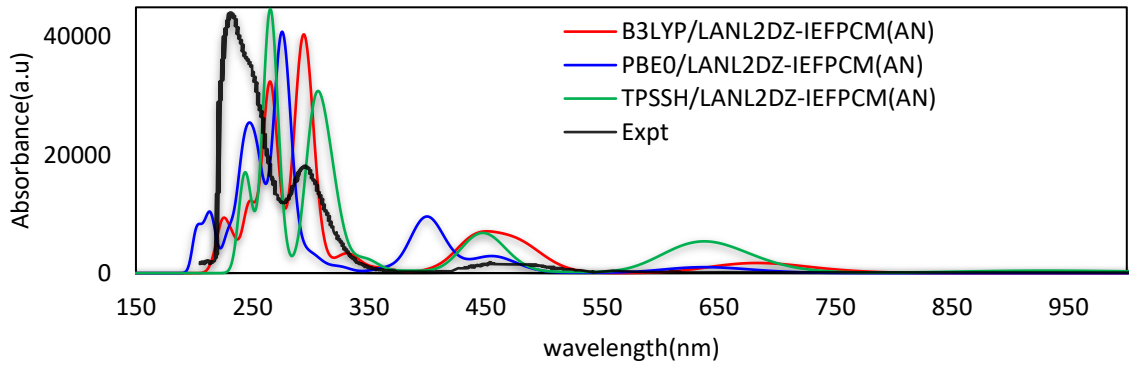

(b)

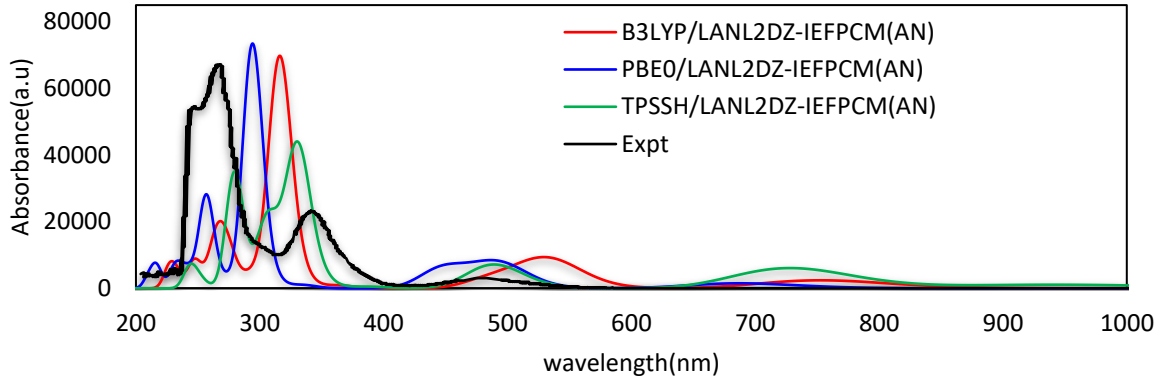

(c)

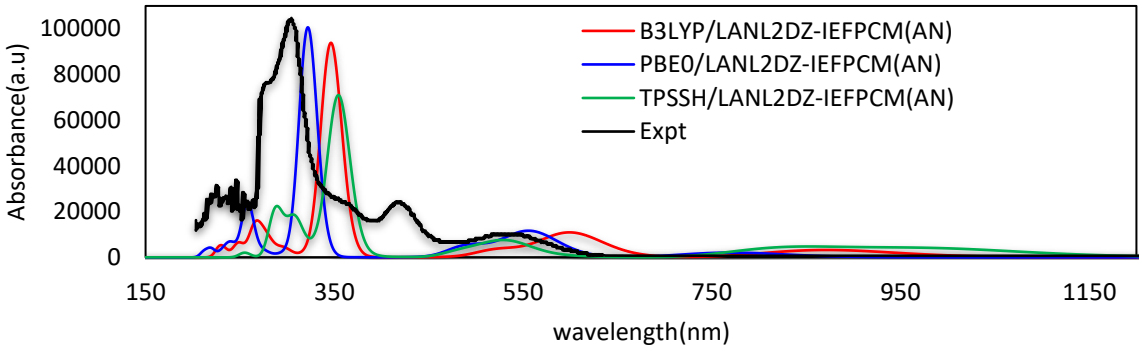

Figure 4.5 Comparison of experimental (Expt.) UV-Vis spectra of anionic $[Ru_2(O_2CCH_3)_4X_2]^-$ complexes, where X = Cl **(a)**, Br **(b)** or I **(c)**, recorded in acetonitrile (AN) and the corresponding TDDFT UV-Vis-NIR spectra predicted at the B3LYP/LANL2DZ-IEFPCM(AN), PBE0/LANL2DZ-IEFPCM(AN) and TPSSH/LANL2DZ-IEFPCM(AN) levels of theory.

The blue-shift was calculated to be within 12 - 19 nm, 18 - 26 nm, 43 - 51 nm, 22 - 51 nm and 47 - 109 nm, for band 1, 2, 3, 4 and 5, respectively. This results in ADs of 33.9 nm and 36.1 nm

for B3LYP and PBE0, respectively. This indicates that the increase in HF exchange from 20% to 25%, when going from the empirical GGA B3LYP to the non-empirical PBE0 causes an increase in AD, and that the popular B3LYP functional outperforms the PBE0 functional at predicting the UV-Vis by a difference in AD of 3.8 nm.

When comparing the best performing GH-GGA, namely B3LYP, against the GH-mGGA TPSSh, the bands shift inconsistently, i.e. some are blue-shift while others are red-shifted; however, the calculated ADs are 33.9 nm and 20.4 nm for B3LYP and TPSSh, respectively. This indicates that GH-mGGA TPSSh outperforms the empirical GH-GGA B3LYP at predicting the UV-Vis spectra by a lower AD of 13.5 nm. The better performance of TPSSh can therefore be attributed to the inclusion of kinetic energy density (τ) and the increase in HF exchange from 20% to 28% when going from B3LYP to TPSSH, which suggests that an increase in the percentage of HF exchange is not the only factor that improves the performance. The results obtained within the RSH functionals is then analyzed. The band shapes of the RSH functionals CAM-B3LYP and LC-ωHPBE are very different from those obtained with the GGA, GH-GGA and GH-mGGA functionals (Figure 4.6). The NIR bands are virtually non-existent, especially in the $[Ru_2(O_2CCH_3)_4Br_2]^-$and $[Ru_2(O_2CCH_3)_4I_2]^-$ complexes, while the primary Vis bands are very weak.

This indicates that while the RSHs have been optimized to describe the charge transfer transitions that predominantly occur at high energies (small wavelength), the low-energy (high wavelength) transitions are poorly described. It has been shown previously that several RSH lead to relatively poor geometries, so that performing geometry optimization and transition energy calculations with the same RSH may yield unsatisfactory results.[244, 253] This result from literature, together with the loss of resolution of the Vis and NIR bands seen here, suggests that the RSH methods are not suitable for qualitive description of the Vis and NIR bands in diruthenium complexes.

In addition, both methods were highly time-consuming and the geometry optimization of $[Ru_2(O_2CCH_3)_4Cl_2]^-$ did not successfully converge when using CAM-B3LYP. There is a net red-shift of all the bands when going from LC-ωHPBE to CAM-B3LYP, which is attributable to the different ω, α and β parameters used in LC-ωHPBE (ω = 0.40 au^{-1}, α = 0, β = 1) and CAM-B3LYP(ω = 0.33 au^{-1}, α = 0.19, β = 0.46) to describe the LR and SR interelectronic potential.

(a)

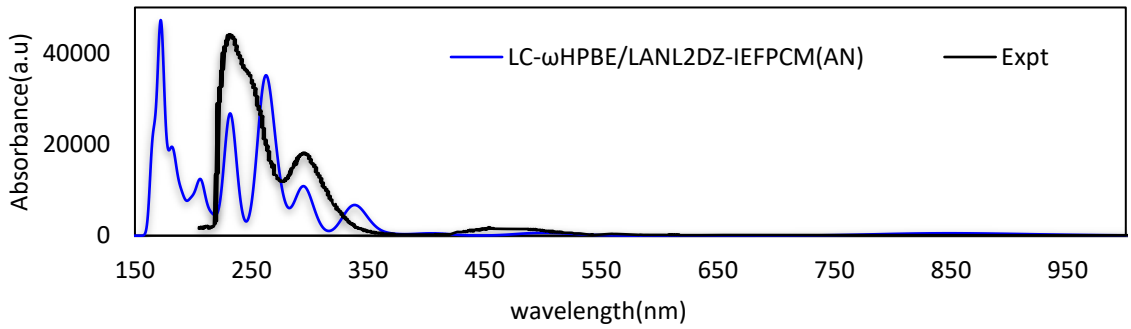

(b)

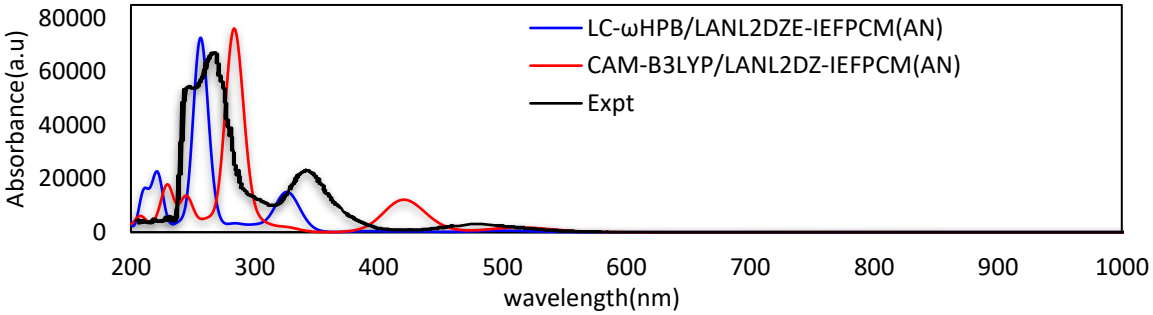

(c)

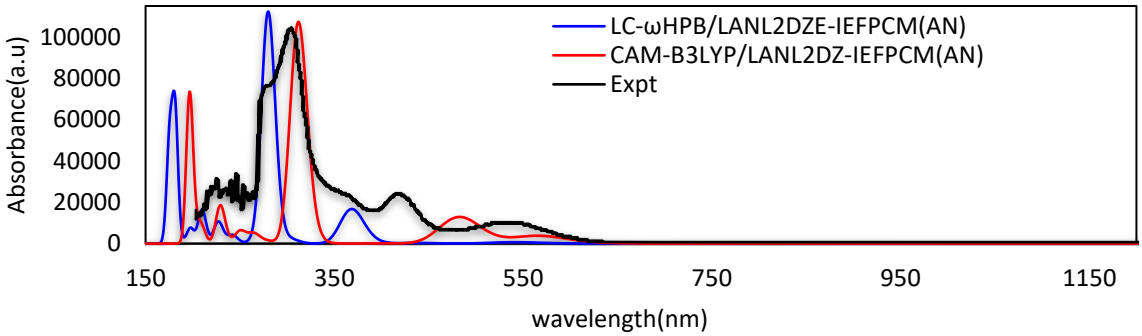

Figure 4.6 Comparison of experimental (Expt.) UV-Vis spectra of anionic $[Ru_2(O_2CCH_3)_4X_2]^-$ complex, where X = Cl **(a)**, Br **(b)** or I **(c)**, recorded in acetonitrile (AN) and the corresponding TDDFT UV-Vis-NIR spectra predicted at the B3LYP/LANL2DZ-IEFPCM(AN), PBE0/LANL2DZ-IEFPCM(AN) and TPSSH/LANL2DZ-IEFPCM(AN) levels of theory. The CAM-B3LYP data for X=Cl is not available in spectra **(a)** because the calculation failed to converge.

The resulting ADs are 29.4 nm and 38.5 nm for LC-ωHPBE and CAM-B3LYP, respectively. This indicates that LC-ωHPBE outperforms the CAM-B3LYP functional at predicting the UV-Vis spectrum by an AD difference of 9.1 nm. In summary (see Table 4.3), the ADs of the BP86, PBE, B3LYP, PBE0, TPSSH, LC-ωHPBE and CAM-B3LYP functionals are 20.6 nm, 18.4 nm, 33.9 nm, 36.1 nm, 20.4 nm, 29.4 nm and 38.5 nm, respectively. The order of functionals from best to

worst performing is thus PBE, TPSSH, BP86, LC-ωHPBE, B3LYP, PBE0, CAM-B3LYP. This is consistent with trends in SEs from experimental values that are graphically illustrated (Figure 4.7), where accuracy plots show the behavior, underestimation or overestimation, of various calculated TDDFT wavelengths of maximum absorption over all the bands.

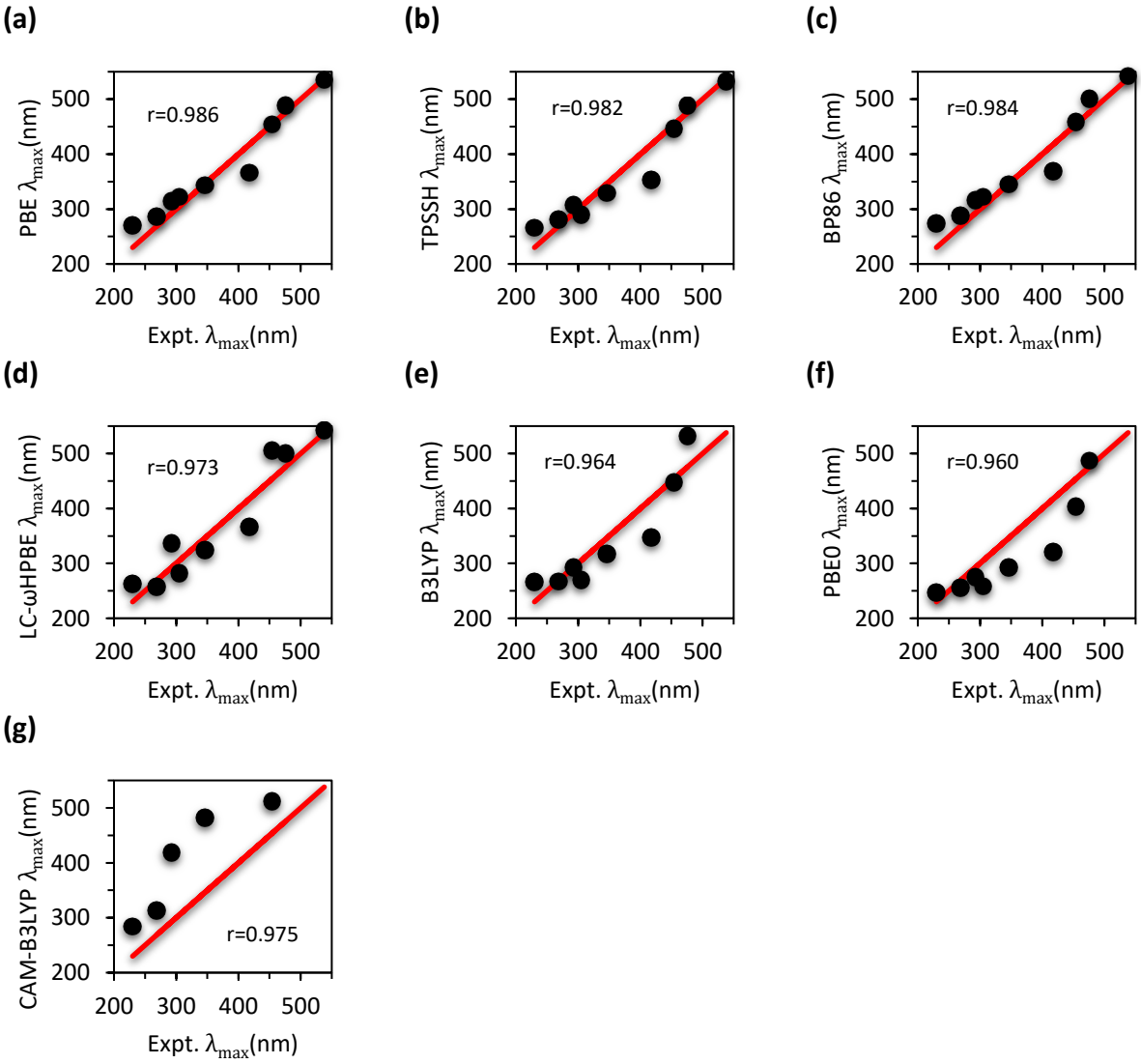

Figure 4.7 Accuracy plots for TD-DFT calculated wavelength of maximum absorption for (a) PBE (b) TPSSH (c) BP86 (d) LC-ωHPBE, (e) B3LYP, (f) PBE0, and (g) CAM-B3LYP, for the $[Ru_2(O_2CCH_3)_4X_2]^-$ complexes, where X =Cl, Br, I. The red line represents the y=x line. Points above and below the line indicate positive or negative errors, respectively.

The wavelengths yielded by the various TD-DFT methods diverges from the experimental values when going from Figure 4.7A to Figure 4.7G, which corresponds to the order of increasing AD.

While the PBE, TPSSh and BP86 functionals have most points clustered near the y = x line, the GH-GGAs and LC-ωHPBE functionals have a weaker correlation with sporadically larger errors, and the CAM-B3LYP functional shows the poorest correlation to experiment. This poor behavior for CAM-B3LYP has previously been reported for triplet states, where it performed the worst among LDA, GGA and GH-GGA functionals.[188, 254, 255] While Table 4.3 and Figure 4.7 shows the total AD and the trends in signed errors, Figure 4.8 provides insightful trends of the ADs of individual bands. The purple bar-graphs indicate that the AD of band 1 is almost constant across the various functionals, except in CAM-B3LYP which has the smallest AD for band 1.

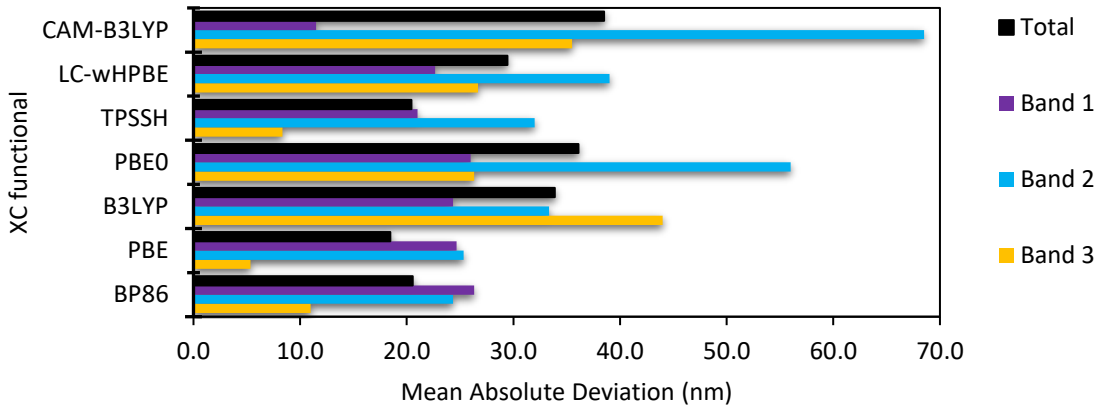

Figure 4.8 Comparison of density functional mean absolute deviations for UV-Vis absorption band 1, 2 and 3 of the $[Ru_2(O_2CCH_3)_4X_2]^-$ complexes, where X = Cl, Br, I. LANL2DZ and IEFPCM(Acetonitrile) was used in all cases.

The blue bar-graphs show that the AD of band 2 generally increases when going from non-hybrid GGA to GH-mGGA, to GH-GGA, to RSH functionals and is a dominant error in almost all the categories of functionals. While TPSSh produced the lowest AD for band 2, the accuracy of the CAM-B3LYP and PBE0 functionals greatly suffered due to the large deviation from the band. The yellow bar-graphs indicate that the GH-mGGA TPSSh and the non-hybrid GGAs PBE and BP86 a much lower AD for band 3, in comparison to the other functionals. As indicated by the black bar-graph, the PBE functional produced the lowest total AD, which is equal to 18.4 nm.

The best performing functional is therefore the GGA PBE, while the GH-mGGA TPSSh is the second-best and the third-best performing functional is BP86. In light of the unresolved geometry convergence of some of the RSH functionals and the poor band shapes yielded, the

GH-GGAs B3LYP, followed by PBE0 are the fourth and fifth best performing. RSH functionals are the worst performing, with LC-ωHPBE being the sixth best and the CAM-B3LYP functional performing the worst. For the diruthenium complexes, using either PBE or TPSSh is therefore recommended. PBE will be used for further analysis in section 4.2.

4.1.3 Comparing natural transition orbitals and canonical molecular orbitals

LR-TD-DFT calculations typically yield the vertical transition energies, the oscillator strengths and the MO compositions of each transition. The vertical transition energies (VTEs) are the splitting energies between the GS and the EES, the oscillator strength (f) can be related to experimental molar absorption coefficients (c.f. Eq. (2.137), and thus by the Beer-Lambert Law to the intensities of the measured absorption bands, whereas the MO compositions allow a chemical interpretation of the results by relating the EES to a transition between given MOs. The single-electron excitation can be described in terms of the concept of *hole* and *particle.* During the process an electron leaves a *hole* and goes to a *particle*. The *hole* and *electron* (particle) can be defined in different ways.[194, 195] There is no universal notation for representing the character of electronic transitions. Although the notation used for metal-metal electronic transitions is usually unambiguous, confusion arises when representing ligand-to-metal charge transfer (LMCT) with unexplained notations such as $\pi(\mathrm{Ru}-\mathrm{O}) \rightarrow \pi^*(\mathrm{Ru}_2)$ and $\sigma/\pi(\mathrm{Cl}) \rightarrow \sigma^*/\pi^*(\mathrm{Ru}_2)$. Unlike previous authors who have omitted pictures of LMCT MOs[21] or those who have presented graphical representations of EDD[63] and NTOs[248] without explaining their LMCT notations, the MO and NTO graphical representations will be presented and compared. Given an interest of this study in fully characterizing the electronic transitions in asymmetrical Ru_2 complexes and to correlate the spectroscopic behavior to the assigned characters, it is therefore crucial to ascertain previous characterization, to rectify some errors and to develop a notation for LMCT such that one can reconstruct transition orbital (TO) pictures from a provided written notation.

To validate previous assignment of the electronic transitions of $[Ru_2(O_2CCH_3)_4X_2]^-$ complexes, where X =Cl, Br, I (which were achieved using canonical Mos by Castro et al[21]), and to compare

them against the more sophisticated NTO representation, TD-DFT and subsequently NTO calculations for the complexes in the acetonitrile (AN) solvated phase based on geometries optimized in AN at the B3LYP/LANL2DZ-IEFPCM(AN) level of theory was performed. Although B3LYP was found to perform worse than PBE or TPSSh based on benchmarking (c.f. 4.1.2), B3LYP is used in this validation process because it was employed in the study by Castro *et al.*,[21] and the goal here is to reproduce their results. The MOs of representative excited states, *viz.* excited states with transition amplitudes $(\Omega) \geq 0.01$, and NTO calculations at the same level of theory, on the first 200 most intense singlet-singlet transitions, *viz.* transitions with oscillator strength $(f) \geq 0.01$ and percentage contribution $(\%\mathrm{NTO}) \geq 25\%$, were calculated. The most relevant NTO and MO transitions with their corresponding percentage are collected in Table 4.4. Both the NTO and canonical MO representations yielded seven significant electronic transitions within the 265.0 - 681.7 nm range of the spectrum, which are the representative transitions producing bands 1 - 5 previously noted in Table 4.3.

Table 4.4 Comparison of TD-DFT UV-Vis MO and NTO transitions for $[Ru_2(O_2CCH_3)_4Cl_2]^-$ complexes in acetonitrile (AN), calculated at the B3LYP/LANL2DZ-IEFPCM(AN) level of theory was used in all cases.

λ (nm)	f	MO1 → MO2		hole → particle		Assignment
		MO1	MO2	hole	particle	
Band 4						
681.7	0.016	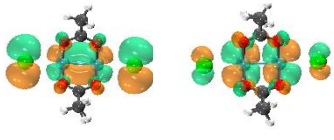		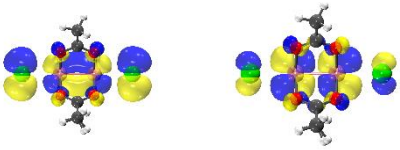		π(Cl,Ru₂) → π*(Cl,Ru₂)
		Major (60%)		Major (60%)		
		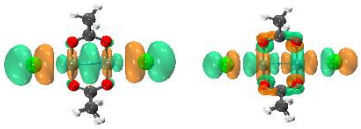		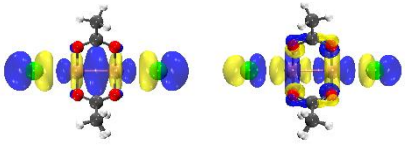		σ(Cl,Ru₂) → σ*(Cl,Ru₂)
		Minor (20%)		Minor (22%)		
		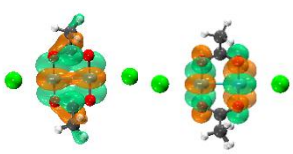		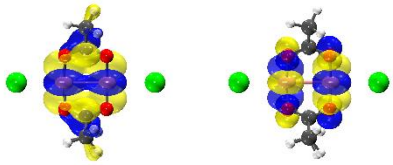		δ(C-O,Ru₂) → δ*(O,Ru₂)

		Minor (16%)	Minor (16%)	
Band 3				
476.5	0.043	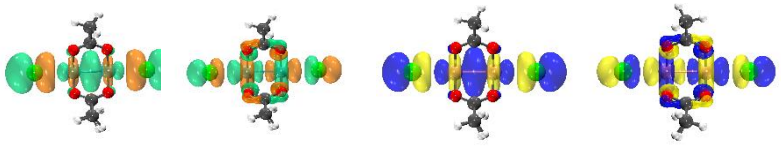		$\sigma(Cl,Ru_2) \rightarrow \sigma^*(Cl,Ru_2)$
		79%	83%	
440.3	0.060	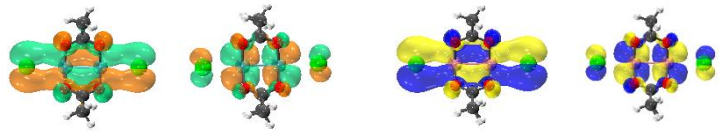		$\pi(Ru\text{-}Cl,O,Ru_2) \rightarrow \pi^*(Cl,Ru_2)$
		Major (74%)	Major (55%)	
		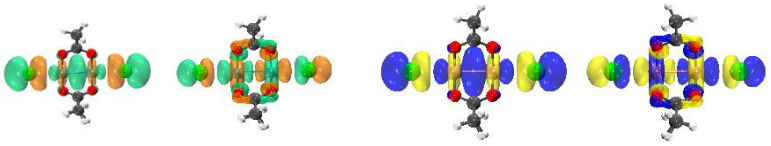		$\sigma(Cl,Ru_2) \rightarrow \sigma^*(Cl,Ru_2)$
		Minor (14%)	Minor (39%)	
Band 2				
332.6	0.015	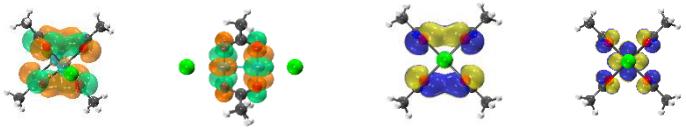		$\pi(O) \rightarrow \pi^*(O)/\delta^*(Ru_2)$
		97%	93%	
331.0	0.015	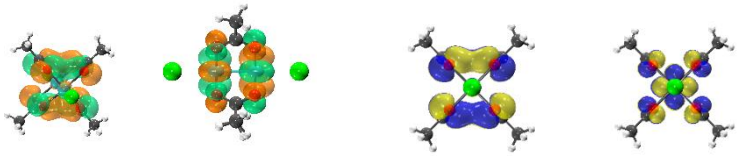		$\pi(O) \rightarrow \pi^*(O)/\delta^*(Ru_2)$
		97%	93%	
Band 1				
293.4	0.274	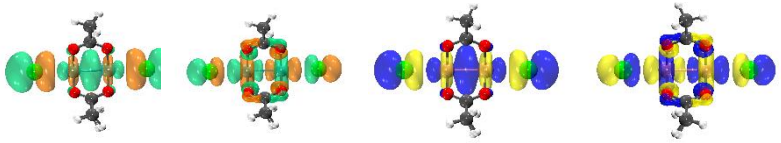		$\sigma(Cl,Ru_2) \rightarrow \sigma^*(Cl,Ru_2)$
		Minor(21%)	Minor(15%)	
		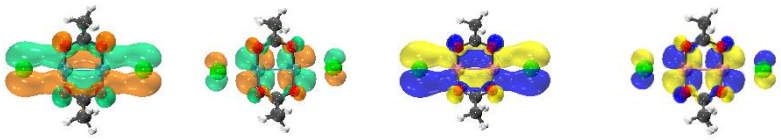		$\pi(Ru\text{-}Cl,O,Ru_2) \rightarrow \pi^*(Cl,Ru_2)$
		Major(53%)	Major(50%)	

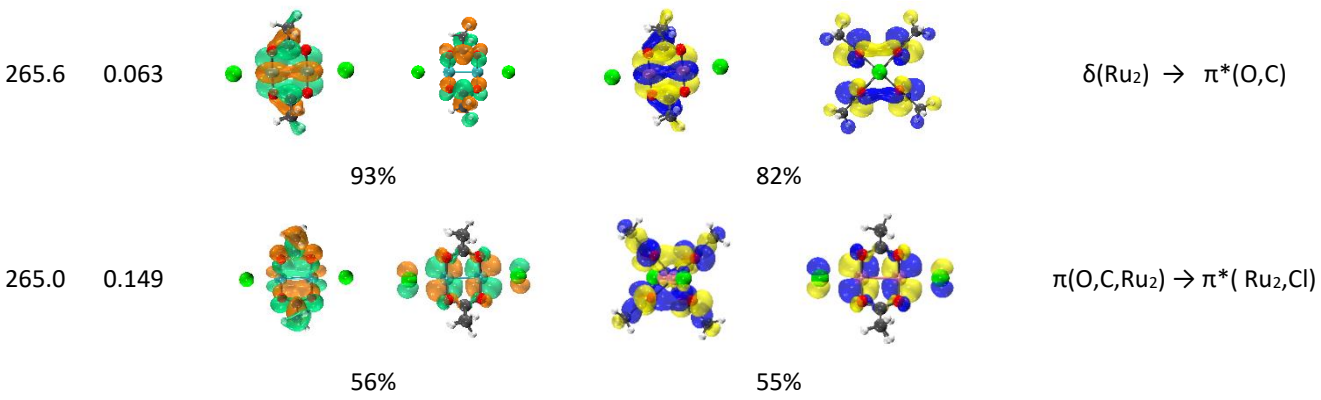

The MO and NTO graphical representations produced identical TO pictures, which suggests that the unitary transformation of occupied and virtual MOs to produce NTOs has little effect on the shape of the TOs. The percentage contributions of TOs to an excitation produced by the NTO and MO methods generally differ by 2 - 25%, although the relative contribution (*viz.* major/minor) of a particular TO is the same in all cases. While the similarity between MO and NTO representation is consistent with the fact that neither methods should in principle produce contradictory results, the differences can be ascribed to the unitary transformation of occupied and virtual MOs, as well as the consideration of de-excitations in NTOs that were neglected in the calculation of the percentage contribution of MOs. Note that the percentages do not necessarily add up to 100%, as insignificant transitions are neglected. Since the NTO percentage contributions were produced automatically by means of the trusted software code Chemissian,[240] and the NTO analysis is much quicker in comparison to analyzing several MOs, those results will be used in further analysis.

Symbols used to describe TOs are now defined. The notation $\sigma(X_2)$, $\pi(X_2)$ or $\delta(X_2)$, where X is an atom, defines TOs with predominantly σ(X - X), π(X - X) or δ(X - X) bonding character, respectively, and equivalently for Ru - Ru anti-bonding character. The symbolic representation σ(X) and π(X) describes a TO hole with principally a non-bonding p_z-orbital or non-bonding p_x-/p_y-orbital, respectively. σ*(Y) and π*(Y) are used for a TO particle. The σ(X,Y), π(X,Y) or δ(X,Y) notation is equivalent to the σ, π or δ notation on every atom X and Y.

The NTO method yielded eight representative excitations within the 268.45 - 843.44 nm range of the spectrum, which are pertinent to the transitions producing the groups of experimental

bands 1 - 3 in Figure 4.9.A and the band 4, which is not observed experimentally because it is optically forbidden, possibly due to the high molecular symmetry. [21] Band 1 and 2 correspond to the previously discussed higher and lower energy UV bands (c.f. table Table 1.1), while band 3 and 4 correspond to the Vis and NIR bands. The excitation produced at 681.7 nm (state 1) has three composite transitions.

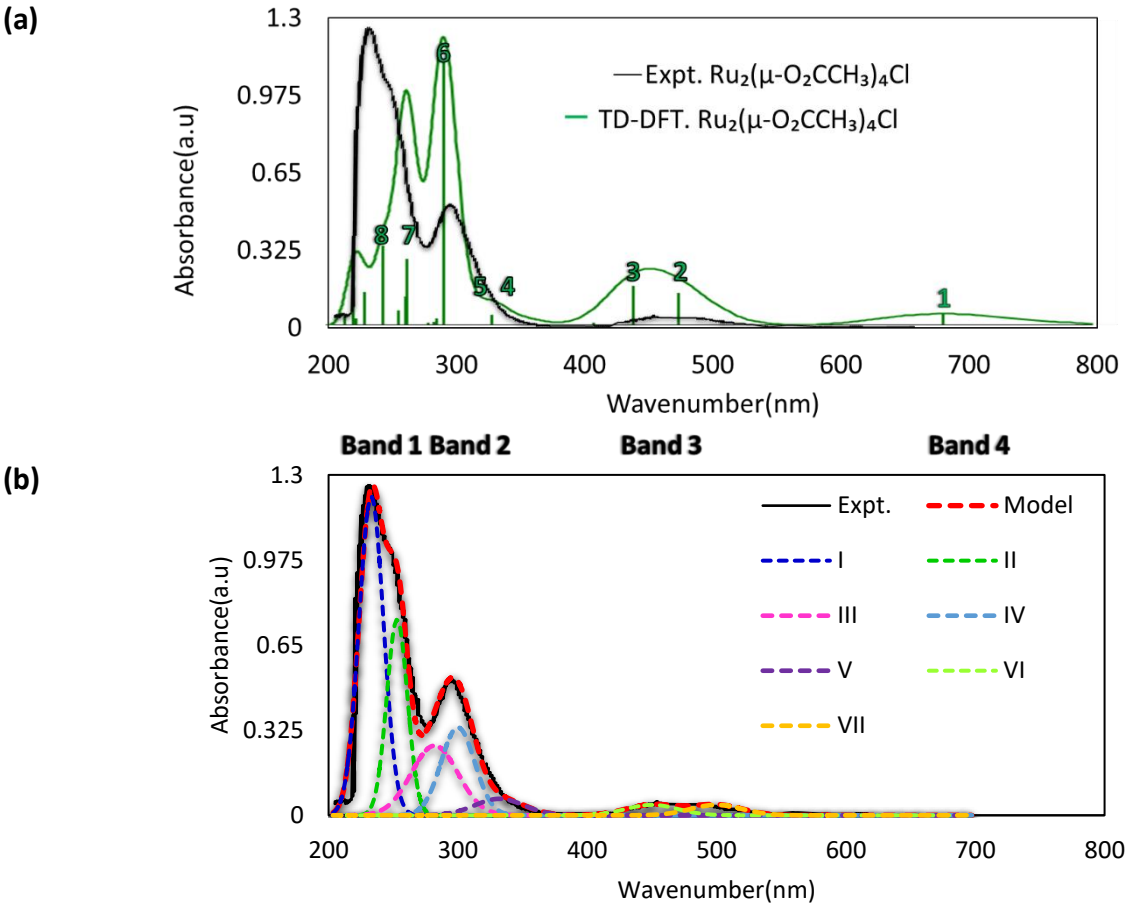

Figure 4.9 (a) Experimental curve (black), TD-DFT (green) of the electronic absorption spectrum of $[Ru_2(O_2CCH_3)_4Cl_2]^-$ in water. Numbers annotate the re-numbered excited states for clarity. (b)Experimental curve (data), fit peaks I - VII, cumulative fit curve (Model) obtained from Gaussian deconvolution of the electronic absorption spectrum of $[Ru_2(O_2CCH_3)_4Cl_2]^-$ in Acetonitrile.

The major one contributing 60%, includes two chloride atoms with significant non-bonding p_y-orbitals that are symmetric in hole and antisymmetric in particle, hence π(Cl) in hole and π*(Cl) in particle. In addition, there is π(Ru_2) character in the hole and π*(Ru_2) character in the particle. The combined assignment this major transition is therefore denoted

$\pi(Cl,Ru_2)\rightarrow\pi^*(Cl,Ru_2)$. The first minor contribution with 22% has two chloride atoms with significant p_z-orbitals that are symmetric in hole and antisymmetric in particle, hence $\sigma(Cl)$ in hole and $\sigma^*(Cl)$ in particle. In addition, there are $\pi(Ru_2)$ in hole and $\pi^*(Ru_2)$ in particle. The combined assignment is this minor transition is therefore $\sigma(Cl,Ru_2)\rightarrow\sigma^*(Cl,Ru_2)$. The second minor contribution of 16% has predominantly $\pi(C\text{-}O)/\delta(Ru_2)\rightarrow\pi(O)/\delta^*(Ru_2)$ character. Therefore, the net overall assignments of the 681.7 nm excitation would be a mixture of metal-metal excitation and LMCT denoted as $\sigma/\pi(Cl,Ru_2)/\pi(C\text{-}O)/\delta(Ru_2)\rightarrow\sigma^*/\pi^*(Cl,Ru_2)/\ \pi(O)/\delta^*(Ru_2)$. Although this excitation has significant oscillator strength, it is linked to the experimental non-observed band 4.

The experimental band 3 is associated with the excitations produced at 476.5 nm (state 2) and 440.3 nm (state 3). State 2 is characterized by a $\sigma(Cl,Ru_2)\rightarrow\sigma^*(Cl,Ru_2)$ transition, whereas state 3 has two composite transitions; the major one contributing 55% has two chloride atoms with significant bonding $\pi(Ru\text{-}Cl)$ character together with p_y-orbitals on the carboxylate oxygen atoms and $\pi(Ru_2)$ character in the hole. In addition, there is non-bonding p_y-orbitals character in the particle. It is important to note that the p_y-orbitals on the carboxylate oxygen atom in the hole are weakly interacting with the $\pi(Ru_2)$ bond but given that it is not $\pi(Ru\text{-}O)$ as previously reported,[21, 57] it is therefore reasonably characterized as $\pi(O)$. The combined assignment of the excitation is therefore denoted $\pi(Ru\text{-}Cl,O,Ru_2)\rightarrow\pi^*(Cl,Ru_2)$.

The excitation produced at 331.99 nm and 332.96 has one transition contributing 93%, which consists of significant symmetric p_y-orbitals on the two acetate oxygen atoms in the hole and non-bonding p_y-orbitals on the same atoms together with anti-bonding $\delta^*(Ru_2)$ character, in the particle. The p_y-orbitals in the hole are partially overlapping, which suggests only weak O---O interaction (non-bonding), reasonably denoted $\pi(O)$ and not $\pi(O\text{-}O)$. Based on the TOs, the combined assignment is therefore denoted $\pi(O)\rightarrow\ \pi^*(O)/\delta^*(Ru_2)$.

The excitation produced at 265.6 nm has one transition contributing 82%, which has significant bonding $\delta(Ru_2)$ character in the hole, and non-bonding anti-symmetric p_y-orbitals on the oxygen atoms and carbon atoms of acetate group in the particle, which also exhibit weak O---O interaction. Based on the TOs, the combined assignment is therefore denoted $\delta(Ru_2)\rightarrow\ \pi^*(O,C)$.

The excitation produced at 265.0 nm has one transition contributing 55%, which has significant bonding δ(Ru_2) character and non-bonding symmetric p_y-orbitals and p_x-orbitals on the oxygen and carbon atoms of the acetate group in the hole, which also exhibit weak O---O interaction, together with anti- symmetric p_y-orbitals on Cl and anti-bonding π*(Ru_2) characters. Based on the TOs, the combined assignment is therefore denoted π(O,C)/π(Ru_2) → π*(Cl,Ru_2). The remaining percentage contribution is distributed across multiple metal-metal transitions with very small percentages, and thus are not shown. The excitations that can be rationalized in a similar way to the abovementioned excitations, as they exhibit similar characteristic TOs, are left undiscussed.

The Gaussian deconvolution of the experimental UV-Vis spectrum into seven bands is shown in Figure 4.9B. The first two strong experimental bands within 209 nm - 360 nm can be represented with five Gaussian curves denoted I, II, III, IV, and V at 233 nm, 253 nm, 282 nm, 300 nm and 332 nm respectively. These bands can therefore be associated to the excitations calculated at 265.0 nm, 265.6 nm, 293.4 nm, 331.0 nm and 332.6 nm, respectively. The weak experimental band within the 400 nm - 550 nm range can be fitted with two Gaussian curves at 450 nm and 500 nm, denoted VI and VII, which can be associated with the calculated excitations at 440.3 nm and 476.5 nm, respectively. The results are summarized in Table 4.5 and compared with previously reported data.

The wavelength predicted in this work are generally within 1.7 nm of those previously reported by Castro *et al.*, while the oscillator strengths are generally within 0.002 a.u, except those at 293.9 nm and 266.2 nm, which are underestimated by 0.079 a.u and 0.067 a.u, respectively. The minor discrepancies could be due to a different implementation of TD-DFT or different default settings in the earlier Gaussian 03 version[256] in comparison to the Gaussian 16 used in this work[235]. Nonetheless, the good agreement in general suggests that the previously reported predictions have been well-reproduced in terms of wavelength and oscillator strengths. The percentage contributions of TOs are within 3 - 26% and 1-32% of those previously reported for the MO and NTO methods. The discrepancies in percentage contributions might be attributed to different implementations used in the Chemissian[240] (used in this work) and the (previously used) SWizard[257] programs.

Finally, new assignments for some transitions have been proposed. The πL→π*, σ→σ*, πRuO→π*, pO→π*, δ→pCO, and πRuCO→π* transitions have been reassigned as π(Cl,Ru_2)→π*(Cl,Ru_2), σ(Cl,Ru_2)→σ*(Cl,Ru_2), π(Ru-Cl,O,Ru_2)→π*(Cl,Ru_2), π(O)→π*(O)/δ*(Ru_2), δ(Ru_2)→π*(O,C), and π(O,C,Ru_2)→π*(Ru_2,Cl), respectively. The UV-Vis spectra of

Table 4.5 Comparison of TD-DFT UV-Vis wavelength (λ)of electronic transition (State) of the anionic $[Ru_2(O_2CCH_3)_4Cl_2]^-$ complex, and the experimentally recorded band maxima (Expt.) in acetonitrile (AN). The B3LYP/LANL2DZ-IEFPCM(AN) level of theory was used in all cases.

State	λ [a] (nm)	λ[b] (nm)	f [a]	f [b]	%[a]	%MO[b]	%NTO[b]	Assignment[a]	Assignment[b]
					Band 4				
1	680.0	681.7	0.015	0.016	52	60	60	πL → π*	π(Cl,Ru_2) → π*(Cl,Ru_2)
					33	20	22	σ → σ*	σ(Cl,Ru_2) → σ*(Cl,Ru_2)
					11	16	16	δ → δ*	π(C-O)/δ(Ru_2) → δ*(Ru_2)/π(O)
					Band 3				
2	475.0	476.5	0.042	0.043	99	79	83	σ → σ*	σ(Cl,Ru_2) → σ*(Cl,Ru_2)
3	439.2	440.3	0.062	0.060	70	74	55	πRuO → π*	π(Ru-Cl,O,Ru_2) → π*(Cl,Ru_2)
					17	14	39	σ → σ*	σ(Cl,Ru_2) → σ*(Cl,Ru_2)
					Band 2				
4	332.6	330.99	0.015	0.015	92	97	93	pO → π*	π(O) → π*(O)/δ*(Ru_2)
5	331.9	330.96	0.015	0.015	92	97	93	pO → π*	π(O) → π*(O)/δ*(Ru_2)
					Band 1				
6	293.9	293.4	0.353	0.274	47	21	15	σ → σ*	σ(Cl,Ru_2) → σ*(Cl,Ru_2)
7	266.2	265.6	0.130	0.063	52	60	60	δ → pCO	δ(Ru_2) → π*(O,C)
8	265.2	265.0	0.150	0.149	33	20	22	πRuCO → π*	π(O,C,Ru_2) → π*(Ru_2,Cl)

[a] From Ref[21] [b] From this work.

$[Ru_2(O_2CCH_3)X]^-$ (X=Cl, Br, I) has been successfully re-characterized and, unlike previous reports, the current assignment indicates that almost all excitations have significant mixed ligand and

metal characters, except the $\delta(Ru_2)\rightarrow\delta^*(Ru_2)$ transition that has predominant metal-metal character.

4.2 Analysis of UV-Vis-NIR electronic absorption spectra of $Ru_2(\mu\text{-}O_2CCH_3)_3(\mu\text{-}2\text{-}Fap)X$ (X=Cl, Br, I)

In Section 4.1.2, various basis sets and functionals were tested and the most suitable level of theory for TD-DFT calculations was determined to be PBE/LANL2DZ-IEFPCM. The NTO analysis was conducted, a convention for denoting TO characters was established and the characterization of the simpler system consisting of a symmetric $Ru_2(\mu\text{-}O_2CCH_3)_4X$ complexes, where X represents a Cl, Br, or I axial ligand, was conducted. The spectroscopic behaviours of $Ru_2(\mu\text{-}O_2CCH_3)_3(\mu\text{-}2\text{-}Fap)X$ complexes are concomitant with asymmetric structural features. Whilst already published computational data for the symmetric bimetallic ruthenium complexes in acetone is available, the characterization of more complex mixed-ligand systems, that are more soluble in various (non-)aqueous, cannot be inferred from this data. The $[Ru_2(\mu\text{-}O_2CCH_3)_3(\mu\text{-}2\text{-}Fap)(Solv)_{2-n}X_n]^{(1-n)+}$ series, where n = 0, 1 or 2, X = Cl, Br or I, and 2-Fap = 2-fluoroanilinopyridinate anion, in solvent (Solv = water, DCM or DMSO), will be used as models for mono-ap diruthenium complexes, as the chloride containing derivatives are well known be highly soluble in these three solvent, instead of the acetonitrile. This would enable us to corroborate our experimental and computational results with published experimental data. To date, no such theoretical analysis has been conducted on these complexes.

4.2.1 Characterization of absorption bands of $Ru_2(\mu\text{-}O_2CCH_3)_3(\mu\text{-}2\text{-}Fap)Cl$

The UV-vis spectrum of $Ru_2(\mu\text{-}O_2CCH_3)_3(\mu\text{-}2\text{-}Fap)Cl$ was measured in water, which was observed to exhibit the four characteristic bands, including the strong UV band (250-350 nm), the weak narrow visible band (400-450 nm), broad visible (480-770 nm) with shoulder (570-585 nm) and a weak NIR band (850-1100 nm). The measured spectrum is consistent with the previously

reported spectrum,[43] hence without further experimental characterization it can be concluded that the $Ru_2(\mu\text{-}O_2CCH_3)_3(\mu\text{-}2\text{-}Fap)Cl$ complex was formed.

Having concluded that the PBE/LANL2DZ-IEFPCM combination was the most suitable for spectrum calculation, geometry optimization of $Ru_2(\mu\text{-}O_2CCH_3)_3(\mu\text{-}2Fap)Cl$ was undertaken at this level of theory in the water solvent phase and the nature of the stationary point as a minimum was confirmed through a subsequent frequency calculation as no imaginary frequencies were found for the optimized structure. The Ru-Ru and Ru-Cl bond lengths of the optimized structure were 2.354 Å and 2.551 Å, respectively, whereas the experimentally measured values are 2.286 Å and 2.485 Å, respectively.[47] The Ru-Ru and Ru-Cl bond lengths were thus overestimated by 0.068 Å and 0.066 Å, respectively. The overestimation could be attributed to the disparity between the lower degrees of freedom of vibrations in the recorded crystal structure in comparison to the implicitly solvated molecule.

The highest occupied molecular orbitals of the α-manifold and β-manifold are δ^* and δ MOs, respectively, whereas the lowest unoccupied molecular orbitals of the α-manifold and β-manifold are δ and $\pi*$ MOs, respectively. The compound consists of three SOMOs (Figure 4.10), which is consistent with previous publications that measured a 3.94 μB magnetic moment value for $Ru_2(\mu\text{-}O_2CCH_3)_3(\mu\text{-}2\text{-}Fap)Cl$ and that assigned MOs as being of π* and δ* character.[47, 258] The MO diagram is consistent with the established $\sigma^2\pi^4\delta^2(\pi^*\delta^*)^3$ ground state configuration but it does not show the spin-paired ordering of the MOs.

The expected three SOMOs consist of two π* MOs and one δ* MO, where the latter is higher in energy than the former two, which is consistent with $\delta^* > \pi^*$ ordering (Figure 4.10) predicted in other Ru_2^{5+} complexes[9-11, 21, 63, 248, 259] and indicative of the expected Ru-Ru two and a half (2.5) bond order of Ru_2^{5+} complexes.[8, 12] The two π* SOMOs are 0.143 eV apart, while the δ* SOMO is 0.315 eV higher than the lesser stable π* SOMO. The discrepancy of the observed energy gap, which amounts to a considerably larger value compared to 0.026 eV and 0.0026 eV for $[Ru_2(\mu\text{-}O_2CCH_3)_4]^+$ and $[Ru_2(\mu\text{-}O_2CCH_3)_4Cl]^-$, respectively, as previously documented by Norman *et al.*,[38] might appear to contradict the anticipated state of degeneracy. However, the π* - δ* energy gap is anticipated to be wider in the N, N-donor Fap ligand due to stronger π-donation into the

δ*-SOMO (c.f. Figure 1.6) of the N-donor atoms. Indeed, the Fap fragment contributes substantially more to the δ*-SOMO, which is denoted 116α in Figure 4.10, than the fragment

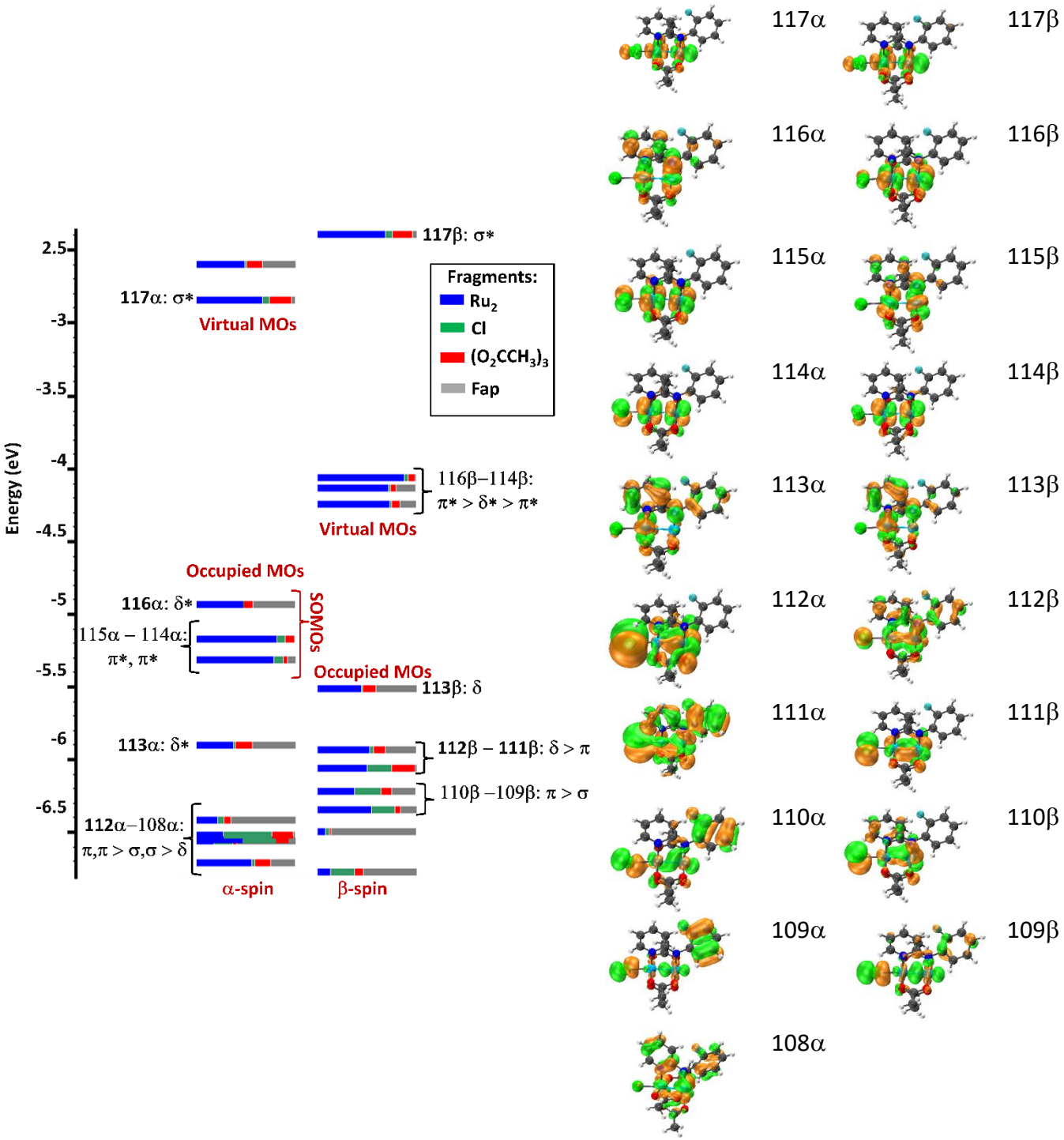

Figure 4.10 A portion (-2.35 eV to -7.00 eV) of spin unrestricted MOs of $Ru_2(\mu\text{-}O_2CCH_3)_3(\mu\text{-}2\text{-}Fap)Cl$, partitioned into percentage contributions from (blue) two Ru atoms, (green) one Cl atom, four acetate groups and one Fap group. Orbital pairing (blue dashed). Calculated using PBE/LANL2DZ-IEPCM in water

comprising all the acetate ligands. There is evident antibonding overlap between the Ru-based d_{xy} orbital and p_y(N) orbitals of the Fap bridging ligand at MO 116α, which is consistent with the destabilizing effect of the Fap ligand on the δ*-SOMO proposed before.[34, 38-41] Furthermore, considering that the corresponding unoccupied β-spin MOs are easily seen to be very close in enerfgy (Figure 4.10), with 0.044 eV separating the lesser stable π* and δ* MOs in the β-spin manifold.

Although the SOMOs are not strictly degenerate, their energies are very close and it is therefore reasonably anticipated that upon the interaction between matching α-spin SOMOs and β-spin unoccupied MOs, the resultant spin-restricted or "paired" SOMOs would be even closer than what is seen in the unrestricted SOMOs, which is consistent with the anticipated state of degeneracy of three SOMOs.

The α-spin density is higher than the β-spin density as there are more electrons with α-spin than with β-spin within the complex. The unpaired electrons are evenly delocalized on the Ru_2 core (Figure 4.11), which is consistent with the equivalence of the ruthenium atoms. This suggests that referring to dimer as Ru_2^{5+} is more appropriate than the mixed-valent designations of Ru^{2+}, Ru^{3+}, or Ru_2(II, III).

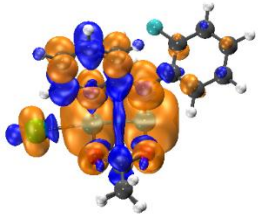

Figure 4.11 The difference between the α-spin (orange) and β-spin (blue) density in $Ru_2(\mu\text{-}O_2CCH_3)_3(\mu\text{-}2\text{-}Fap)Cl$. Obtained with PBE/LANL2DZ-IEFPCM.

There is more net spin density on the Ru atoms than on the ligands, which indicates that the three unpaired electrons have more metal than ligand character, which is consistent with the higher percentage contribution of the Ru atoms to the SOMOs (Figure 4.10). The non-zero contribution of spin density on the ligand is not necessarily a sign that the ligand has radical character, but may be a consequence of spin contamination due to the use of unrestricted KS computations. The chloride also possesses a higher α-spin than β-spin density, which is informative of the significant spin polarization on the chloride upon interacting with the

complex moiety. Indeed, the chloride predominantly contributes π-MOs (111α-112 α). In contrast to previous studies, which relied on comparing bands in analogous compounds such as $Ru_2(\mu\text{-}O_2CR)_4Cl$ or $Ru_2(\mu\text{-}ap)_4Cl$,[43, 47] the characterization of the UV-Vis spectrum of $Ru_2(\mu\text{-}O_2CCH_3)_3(\mu\text{-}2\text{-}Fap)Cl$ was performed using TD-DFT and NTO calculations. Specifically, the first 200 most intense singlet-singlet transitions were retrieved based on oscillator strength (*f*) values greater than or equal to 0.01 and percentage contribution (%NTO) greater than or equal to 25%, at the PBE/LANL2DZ IEFPCM level of theory in water, using geometries that had been fully optimized in water.

The most relevant calculated NTO transitions with their corresponding percentage contribution for the $Ru_2(\mu\text{-}O_2CCH_3)_3(\mu\text{-}2\text{-}Fap)Cl$ complex is collected in Table 4.6. C_a and N_a are used to differentiate the aniline carbon and nitrogen atoms from those of pyridine, which are denoted C_p and N_p.

Table 4.6 NTO transitions for $Ru_2(\mu\text{-}O_2CCH_3)_3(\mu\text{-}2\text{-}Fap)Cl$ complex in water, calculated at the PBE/LANL2DZ-IEFPCM(water) level of theory was used in all cases.

Excited state	λ (nm)	f	hole → particle		Assignment[a] and type[b]
			hole	particle	
			Band 4		
3	843.44	0.016	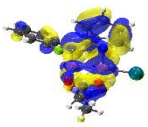	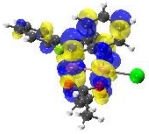	91% $\pi(Ru\text{-}N_p,C_p\text{-}N_a,C_p\text{-}C_p,C\text{-}O)/\delta(\mathbf{Ru_2}) \rightarrow \delta^*(\mathbf{Ru_2})/\pi^*(N_p,N_a,C_p,O)$ *type: MMCT*
			Band 3		
8	680.41	0.012	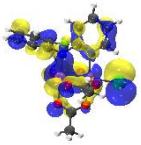	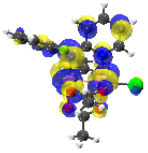	92% $\pi(\mathbf{Cl},F,C_p\text{-}N_p,Ru\text{-}N_a,C_a,O,\mathbf{Ru_2}) \rightarrow \delta^*(\mathbf{Ru_2},N_a,N_p,C_p)$ *type: LMCT and MMCT*
11	642.71	0.011	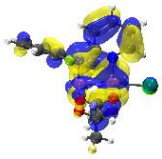	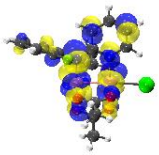	87% $\pi(Ru\text{-}N_a,C\text{-}O,C_p\text{-}C_p)/\delta(\mathbf{Ru_2}) \rightarrow \delta^*(\mathbf{Ru_2})$ *type: MMCT*

12	632.03	0.025	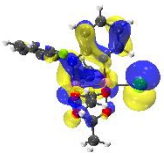	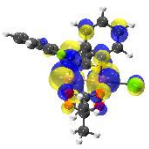	88% $\pi(\mathbf{Cl},C_p\text{-}N_p,Ru\text{-}N_a,C_p\text{-}C_p,\mathbf{Ru_2}) \rightarrow \pi^*(\mathbf{Ru_2})$ *type: LMCT and MMCT*
17	564.39	0.011	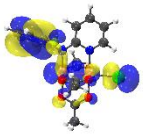	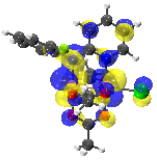	38% $\pi(Ru\text{-}N_a,\mathbf{F},\mathbf{C_a\text{-}C_a})/\sigma(Cl,Ru_2) \rightarrow \pi^*(\mathbf{Ru_2})$ *type: LMCT*
			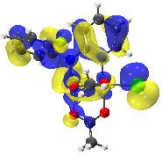	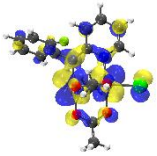	32% $\pi(\mathbf{Cl},F,Ru\text{-}N_a,C_a\text{-}C_a,C_p\text{-}C_p,C_p\text{-}N_p) \rightarrow \pi^*(\mathbf{Ru_2})$ *type: LMCT*
19	552.67	0.011	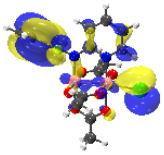	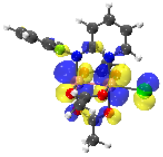	75% $\pi(\mathbf{Cl},\mathbf{F},\mathbf{C_a\text{-}C_a}) \rightarrow \pi^*(\mathbf{Ru_2})$ *type: LMCT*
			Band 2		
31	464.33	0.008	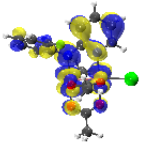	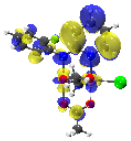	83% $\pi(\mathbf{C_a},\mathbf{N_a},C_p\text{-}C_p,C_p\text{-}N_p,O)/\delta^*(\mathbf{Ru_2}) \rightarrow \pi^*(\mathbf{C_p},\mathbf{N_p})$ *type: LLCT and MLCT*
52	378.67	0.010	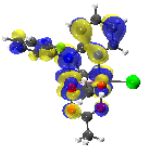	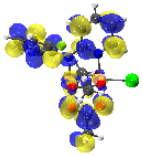	41% $\pi(\mathbf{C_a},\mathbf{N_a},C_p\text{-}C_p,C_p\text{-}N_p,O)/\delta^*(\mathbf{Ru_2}) \rightarrow \pi^*(C_a,C_p,\mathbf{O},\mathbf{C})$ *type: LLCT and MLCT*
			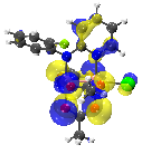	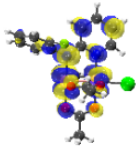	33% $\pi(C_p\text{-}C_p,N_p\text{-}C_p,\mathbf{O}) \rightarrow \pi^*(N_a,N_p,C_p,O)/\delta^*(\mathbf{Ru_2})$ *type: LMCT*
			Band 1		
87	333.26	0.024	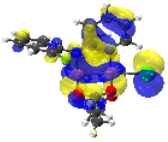	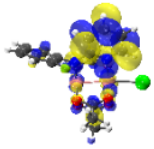	28% $\pi(Cl,O)/\delta(\mathbf{Ru_2}) \rightarrow \pi^*(\mathbf{N_p},\mathbf{C_p})$ *type: MLCT*
134	298.19	0.028	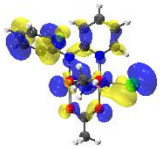	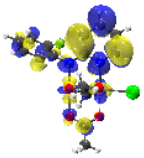	35% $\pi(\mathbf{Cl},F,C_a)/\sigma(Ru_2) \rightarrow \pi^*(\mathbf{C_p},\mathbf{N_p})$ *type: LLCT*

185	268.45	0.035	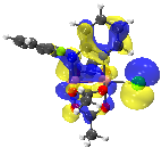	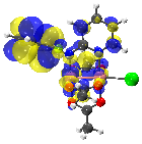	29% $\pi(\mathbf{Cl},N_p\text{-}Ru,Ru_2) \rightarrow \pi^*(\mathbf{C_a},O)$ *type: LLCT*

C_p and N_p denote carbon and nitrogen atoms of the pyridine moiety. C_a and N_a denote carbon and nitrogen atoms of the aniline moiety. C and O denote carbon and oxygen atoms of an acetate ligand. d(Ru) indicates a non-bonding d-type orbital on the Ru atom. [a] Only orbitals contributing more than 10% in Table 4.7 to the NTOs used in formulating the assignments. [b] The highlighted orbital are the most contributing (≤ 24% in Table 4.7) orbitals to the NTOs, used to determine the transition type.

The NTO method yielded eleven significant excitations within the 268.45 - 843.44 nm range of the spectrum, which are the representative transitions producing the groups of bands denoted 1 - 4 in Figure 4.12A. To ascertain the nature of transitions as metal-based and/or ligand-based charge transfer (CT), the orbital contributions from the ruthenium and chloride atoms, acetate and anilinopyridinate groups to the selected NTOs are quantified in Table 4.7. Guided by eleven significant excitations, the Gaussian deconvolution of the experimental UV-Vis spectrum into eleven curves is presented in Figure 4.12B.

Experimental absorption band 1 (250-350 nm) covers up to 162 excitations with several intense bands, which is consistent with the experimentally observed very intense absorption (reaching absorbance > 20000 a.u) band in this range. It would be too laborious to characterize every single one of them.

(a)

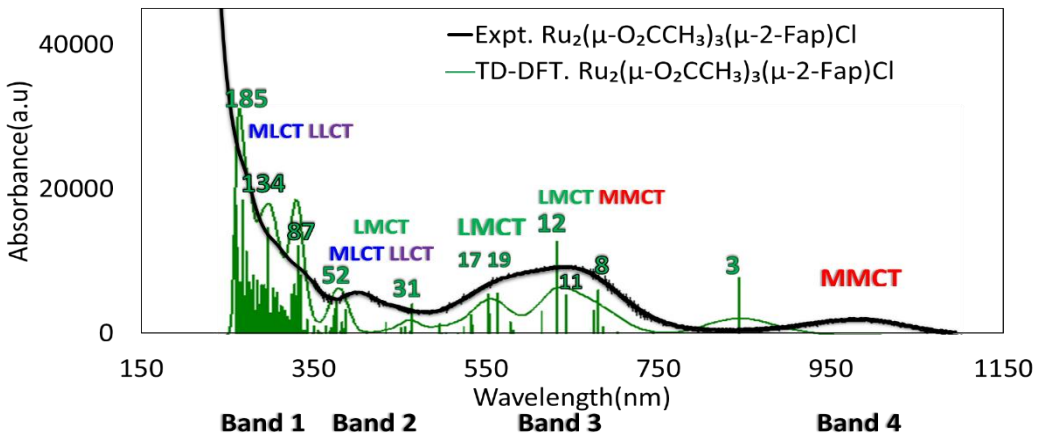

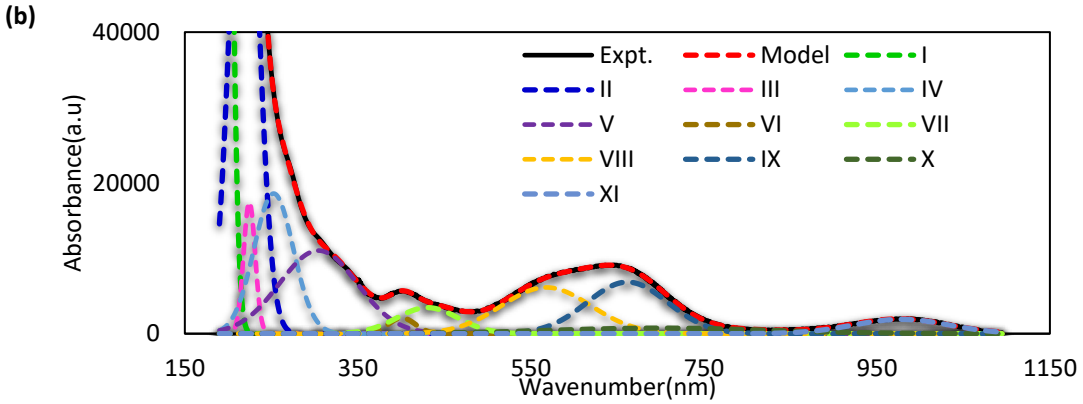

Figure 4.12 (a) Experimental curve (black), TD-DFT (green) of the electronic absorption spectrum of $Ru_2(\mu\text{-}O_2CCH_3)_3(\mu\text{-}2\text{-}Fap)Cl$ in water. (b) Experimental band (Expt), fit curves I - X, cumulative fitted curve (Model) obtained from Gaussian deconvolution of the electronic absorption spectrum of $Ru_2(\mu\text{-}O_2CCH_3)_3(\mu\text{-}2\text{-}Fap)Cl$ in Water. TD-DFT employed the PBE/LANL2DZ-IEFPCM (water) level of theory.

Since all those excitations converge into three maxima, only the three excitations, namely, excited states 87, 134, and 185, associated with those maximum points have been characterized.

The associated NTOs confirm the presence of a combination of one metal-to-ligand charge transfer (MLCT) and two ligand-to-ligand charge transfer (LLCT) characters with π(Cl, O)/δ(**Ru_2**) → π*(**N_p**, **C_p**), π(**Cl**, F, C_a)/σ(Ru_2) → π*(**C_p**, **N_p**) and π(**Cl**, N_p-Ru, Ru_2) → π*(**C_a**, O) characters, respectively. Based on the orbital contribution, the MLCT is predominantly a flow of electron charge from the Ru_2 unit to the pyridine moiety, while the LLCTs consist of electron charge flowing from the axial chloride ligand to the pyridine and aniline moiety. The dominant chloride character of the LLCT is consistent with the previously observed sensitivity of band 1 to the nature of the halogen in tetracarboxylates.[21] In addition, the predominant ligand character of these transitions is consistent with the high energy of band 1.

Table 4.7 Percentage contribution of fragmented Mulliken charges to the NTOs of $Ru_2(\mu\text{-}O_2CCH_3)(\mu\text{-}2\text{-}Fap)Cl$ calculated with PBE/LANL2DZ-IEFPCM in water.

State #	λ (nm)	NTO (%)	Fragment contribution to hole (%)						Fragment contribution to particle (%)					
			Ru		Cl	Fap		Acetate	Ru		Cl	Fap		Acetate
			1	2		Anil	Pyri		1	2		Anil	Pyri	
3	843.44	91	46	5	1	14	22	12	23	41	0	15	12	10
8	680.41	92	12	26	33	12	7	10	26	41	1	12	10	9
11	642.71	87	44	24	2	8	14	8	37	44	2	4	3	9
12	632.03	88	7	23	40	7	15	8	34	42	2	7	6	8
17	564.39	38	2	10	14	69	1	5	36	43	2	6	5	7

		32	7	24	30	14	17	8	32	43	2	9	7	7
19	552.67	75	2	5	24	64	4	1	45	45	4	2	1	3
31	464.33	83	18	27	0	25	20	10	2	3	0	4	85	6
52	378.67	41	18	27	0	25	20	10	1	3	0	13	23	60
		33	2	1	1	1	6	88	22	40	0	15	12	11
87	333.26	28	26	31	16	7	9	11	4	1	0	5	84	7
134	298.19	35	4	19	45	20	3	9	1	2	0	7	85	5
185	268.45	29	8	23	48	5	9	7	1	5	0	73	5	15

Ru1 (bonded to Cl) and Ru2 are denoted 1 and 2, respectively. The Fap is split into aniline (anil) and pyridine (pyri) fragments. Fap includes the F and N atoms.

Although there are numerous excitations in the UV region, the three characterized states sufficiently serve their purpose of detecting the presence of metal-based and/or ligand-based character. Furthermore, the UV-Vis band 1 can be fitted with five Gaussian curves, curves I, II, III, IV, and V located at 192.27 nm, 218.74 nm, 224.56 nm, 252.67 nm, and 394.35 nm. Curves III and IV are situated directly beneath curves I and II and are visibly less pronounced, whereas the maximum of curve V does not overlap with curves I and II. Therefore, curves I, II, and V represent the primary contributors to band 1, which aligns with the three maxima associated with excited states 87, 134, and 185 in this region. It is worth noting that band 1 has not been formerly characterized in the existing literature (Table 4.8).

Table 4.8 Summarized comparison of TD-DFT UV-Vis characterization in this study and previously reported assignments. TD-DFT employed the PBE/LANL2DZ-IEFPCM(water) level of theory.

Previous assignments	Current assignments
	Band 1
None	$\pi(Cl,O)/\delta(Ru_2) \rightarrow \pi^*(N_p,C_p)$ $\pi(Cl,C_a)/\sigma(Ru_2) \rightarrow \pi^*(C_p,N_p)$ $\pi(Cl,N_p\text{-}Ru,Ru_2) \rightarrow \pi^*(C_a,O)$
	Band 2
$\pi(\mathbf{N/aryl}) \rightarrow \sigma^*/\pi^*/\delta^*(Ru_2)$[b]	$\pi(\mathbf{C_a,N_a,C_p\text{-}C_p,C_p\text{-}N_p},O)/\delta^*(Ru_2) \rightarrow \pi^*(C_p,N_p)$
$\sigma/\pi/\delta(Ru_2) \rightarrow \delta^*(Ru_2)$[b]	$\pi(\mathbf{C_a,N_a,C_p\text{-}C_p,C_p\text{-}N_p},O)/\delta^*(Ru_2) \rightarrow \pi^*(C_a,C_p,O,C)$
$\pi(\mathbf{N/aryl}) \rightarrow \pi^*(Ru_2)$[a][b]	$\pi(\mathbf{C_p\text{-}C_p,N_p\text{-}C_p},O) \rightarrow \pi^*(N_a,N_p,C_p,O)/\delta^*(Ru_2)$
	Band 3
$\pi(\mathbf{Ru\text{-}O/N, Ru_2}) \rightarrow \pi^*(\mathbf{Ru_2})$[a][b]	$\pi(\mathbf{Cl},F,C_p\text{-}\mathbf{N_p,Ru\text{-}N_a},C_a,O,\mathbf{Ru_2}) \rightarrow \delta^*(Ru_2,N_a,N_p,C_p)$
$\delta(\mathbf{Ru_2})/\pi(\mathbf{N}) \rightarrow \pi^*(\mathbf{Ru_2})$[b]	$\pi(Ru\text{-}\mathbf{N_a},C\text{-}O,C_p\text{-}C_p)/\delta(\mathbf{Ru_2}) \rightarrow \delta^*(Ru_2)$
$\pi(\mathbf{X}) \rightarrow \pi^*(\mathbf{Ru_2})$[c]	$\pi(\mathbf{Cl},C_p\text{-}\mathbf{N_p},Ru\text{-}\mathbf{N_a},C_p\text{-}C_p,\mathbf{Ru_2}) \rightarrow \pi^*(\mathbf{Ru_2})$ $\pi(\mathbf{Ru\text{-}N_a},F,C_a\text{-}C_a)/\sigma(Cl,\mathbf{Ru_2}) \rightarrow \pi^*(\mathbf{Ru_2})$

	$\pi(\mathbf{Cl},F,\mathbf{Ru\text{-}N_a},C_a\text{-}C_a,C_p\text{-}C_p,C_p\text{-}\mathbf{N_p}) \rightarrow \pi^*(\mathbf{Ru_2})$ $\pi(\mathbf{Cl},F,C_a\text{-}C_a) \rightarrow \pi^*(\mathbf{Ru_2})$
Band 4	
$\delta(\mathbf{Ru_2}) \rightarrow \delta^*(\mathbf{Ru_2})$[a][b] $\delta(\mathbf{Ru_2}) \rightarrow \pi^*(\mathbf{Ru_2})$[c]	$\pi(Ru\text{-}N_p,C_p\text{-}N_a,C_p\text{-}C_p,C\text{-}O)/\delta(\mathbf{Ru_2}) \rightarrow \delta^*(\mathbf{Ru_2})/\pi^*(N_p,N_a,C_p,O)$

[a]From Ref.[43,21,63]. [b]From Ref.[63]. [c]From Ref.[47]. Highlighted are the characters matching those previously reported.

The experimental absorption band 2 (400-450 nm) overlaps with two predicted band maxima which are associated with the two most intense excitations, namely, states 31 and 52, which combined, are characterized by LMCT, MLCT and LLCT. State 31 consists of $\pi(\mathbf{C_a}, \mathbf{N_a}, C_p\text{-}C_p, C_p\text{-}N_p, O)/\delta^*(\mathbf{Ru_2}) \rightarrow \pi^*(\mathbf{C_p}, \mathbf{N_p})$, which based on the orbital contribution, predominantly qualifies as a mixture of LLCT and MLCT. State 52 has a major and minor transition denoted $\pi(\mathbf{C_a}, \mathbf{N_a}, C_p\text{-}C_p, C_p\text{-}N_p, O)/\delta^*(\mathbf{Ru_2}) \rightarrow \pi^*(C_a, C_p, \mathbf{O, C})$ and $\pi(C_p\text{-}C_p, N_p\text{-}C_p, \mathbf{O}) \rightarrow \pi^*(N_a, N_p, C_p, O)/\delta^*(\mathbf{Ru_2})$, which are of predominantly, LMCT plus MLCT and LMCT respectively. Neither state 31 nor state 51, exhibit chloride character, which is consistent with previously reported slight sensitivity of band 2 to the type of axial ligand. Deconvolution of the experimental band shows that band 2 can be fitted with only two Gaussian curves, namely, curves VI and VII at 400.76 nm and 430.42 nm, respectively, which is consistent with the two identified maxima at states 31 and 52. TD-DFT and deconvolution suggest that excitation 31 is essentially responsible for the high baseline of the local minima between band 1 and band 2 or between band 2 and band 3. Band 2 corresponds to the previously characterized experimental bands within 400 nm - 464 nm (c.f. band 2A and 2B in Table 1.2). Unlike the previous assignments,[47, 63] which were based on tetra-ap Ru_2, as indicated in Table 4.8, the current assignment has revealed that transitions of $\sigma(Ru_2) \rightarrow \sigma^*(Ru_2)$ and $\pi(N/aryl) \rightarrow \sigma^*(Ru_2)$ characters are not exhibited by the mono-ap $Ru_2(\mu\text{-}O_2CCH_3)_3(\mu\text{-}2\text{-}Fap)Cl$ complex. However, there is some overlap of the characters assigned to the hole TOs with previously reported TOs (Table 4.8). In addition, unlike the previous report, the current result reveals there are not only LMCT but also MMCT and MLCT at band 2.

Experimental band 3 overlaps two TD-DFT band maxima. The first maximum is associated with two intense excitations namely states 17 and 19, both consisting of mixed LMCT and MMCT. State 17 consists of a major $\pi(Ru\text{-}N_a, \mathbf{F}, \mathbf{C_a\text{-}C_a})/\sigma(Cl, Ru_2) \rightarrow \pi^*(\mathbf{Ru_2})$ LMCT from the aniline group

to the ruthenium atoms and a minor π(**Cl**, F, Ru-N_a, C_a-C_a, C_p-C_p, C_p-N_p) → π*(**Ru_2**) LMCT from the chloride to the ruthenium atoms, while state 19 only consist of a π(**Cl**, **F, C_a-C_a**) → π*(**Ru_2**) LMCT from the aniline and the chloride to the Ru_2 unit. The second maximum results from three predominant excitations namely states 8, 11, and 12, consisting of π(**Cl**, F, C_p-N_p, Ru-N_a, C_a, O, **Ru_2**) → δ*(**Ru_2**, N_a, N_p, C_p) mixed LMCT plus MMCT, π(Ru-N_a, C-O, C_p-C_p)/δ(**Ru_2**) → δ*(**Ru_2**) MMCT and π(**Cl**, C_p-N_p, Ru-N_a, C_p-C_p, **Ru_2**) → π*(**Ru_2**) mixed LMCT plus MMCT, respectively. Both predicted maxima at band 3 are characterized by significant halogen axial ligand character, which is consistent with a previously reported sensitivity of band 3 in tetracarboxylate to the type of axial ligand.[21] The Gaussian deconvolution reveals that band 3 can be fitted with two equally intense Gaussian curves namely VIII and X at 567.74 nm and 661.69 nm, respectively, which is consistent with the two identified TD-DFT maxima. Deconvolution also supports that band 3 is due to two independent bands, as evidenced by the curve VIII and IX. This forms the theoretical basis for the conspicuous shoulder band that is detectable experimentally in this region.

In agreement with the experimental shoulder band, the first maximum associated with states 17 and 19 are predicted to be less intense and have lower energy than the second maximum associated with excitations in states 8, 11 and 12, which reasonably give rise to the band 3 local maximum. Band 3 corresponds to bands 3A and 3B previously introduced (c.f. Table 1.2). Unlike previous assignments[63] by analogy to $Ru_2(\mu\text{-Rap})_4Cl$ (Table 4.8), the current result demonstrates that band 3 of $Ru_2(\mu\text{-}O_2CCH_3)_3(\mu\text{-}2\text{-Fap})Cl$ is not characterized as a δ(Ru_2) → π*(Ru_2) transition. Hence the previous δ(Ru_2) → π*(Ru_2) proposition from literature[63] is incorrect. Similarly, the previous assignment of Ru_2 tetracarboxylates[21] showed that band 3 had some π(Ru-O) → π*(Ru_2) transitions and was ambiguously characterized[43] for the mixed-ligand system, whereas the current assignment reveals that there are only π(Ru-N_a) → π*(Ru_2) transitions in the mixed-ligand $Ru_2(\mu\text{-}O_2CCH_3)_3(\mu\text{-}2\text{-Fap})Cl$ complex. Gaussian curve, X, which lies at 699.99 nm, has very weak intensity which could be the previously reported very weak excitation at ~700 nm of δ(Ru_2) → π*(Ru_2) character.[63] This implies that if the δ(Ru_2) → π*(Ru_2) excitation was present then it would have a very weak intensity. Unlike the carboxylate ligand, which possesses π(O) character where only one lobe of the p-orbital of the oxygen donor interacts

with a ruthenium orbital in the hole, the ap ligand predominantly possesses π(Ru-N) character (Figure 4.13) where both lobes of the p-orbital of the nitrogen donor atom interact with a ruthenium orbital in the hole. The difference in character can attributed to the geometrical differences between the predominantly sp^3 (with two lone pairs) and sp^2 (with one lone pair) hybridized oxygen atom and nitrogen donor atoms, respectively.

Figure 4.13 Comparison of π(O) and π(Ru-N) orbital character in (a) $Ru_2(OCCH_3)_4Cl$ and (b) $Ru_2(OCCH_3)_3(2\text{-}Fap)Cl$, respectively.

Lastly, the weaker band 4 is linked to state 3 characterized by the π(Ru-N_p, C_p-N_a, C_p-C_p, C-O)/δ(**Ru_2**) → δ*(**Ru_2**)/π*(N_p, N_a, C_p, O) transition, which the orbital contribution reveals to be predominantly MMCT. In contrast to the analogous band of $[Ru_2(\mu\text{-}O_2CCH_3)_3Cl_2]^-$, which possessed significant chloride character, $Ru_2(\mu\text{-}O_2CCH_3)_3(\mu\text{-}2\text{-}Fap)Cl$ does not exhibit axial ligand character, which suggests that band 4 in solution is expected to be virtually insensitive to the type of axial halogen ligand. Deconvolution supports that band 4 can be fitted with a single Gaussian curve, as evidenced by the curve at 978.09 nm, denoted curve XI, which is consistent with a single peak predicted at state 3. Unlike previous propositions in the literature[47] which suggested that there should be some δ(Ru_2) → π*(Ru_2) character in band 4, in the current work only the δ(Ru_2) → δ*(Ru_2) transition has been predicted. In agreement with the previous study, band 4 has been predicted at much higher energy than where it would occur experimentally (c.f. Table 1.1). This discrepancy was previously attributed to the substantial increase in π-donation due to four equatorial ap ligands (in $Ru_2(ap)_4Cl$), which preferentially destabilize the energy of the δ*(Ru_2) orbitals and thus increase the δ(Ru_2) - δ*(Ru_2) splitting energy.[63] However, given the current molecule possesses only a single ap ligand, the current results do not support the attribution of this disparity to the high π-donation. In addition, a similar deviation was observed for the TD-DFT result of $[Ru_2(\mu\text{-}O_2CCH_3)_4Cl_2]^-$ (c.f. Figure 4.9).

4.2.2 Comparison of neutral, cationic, and anionic species

The spectroscopic behaviour of the $Ru_2(\mu\text{-}O_2CCH_3)_3(\mu\text{-}Rap)Cl$ complexes has been a subject of discussion due to the ambiguous attribution of the splitting of band 3 (Table 4.8) into two components in aqueous solution to the association and dissociation of the axial ligand which could in principle result in a cationic $[Ru_2(\mu\text{-}O_2CCH_3)_3(\mu\text{-}Rap)(H_2O)_2]^+$ complex. In addition, the shoulder band is absent in excess amount of chloride ligands.[43, 71] To evaluate the validity of the proposed equilibrium on the UV-Vis spectrum and to ascertain whether the spectrum can be used to identify the species in solution, the UV-Vis spectra of the neutral, cationic and anionic complexes (Figure 4.14) are calculated in water, through TD-DFT calculations at the PBE/LANL2DZ-IEFPCM level of theory, and subsequently compared with the experimental UV-vis spectra measured in water.

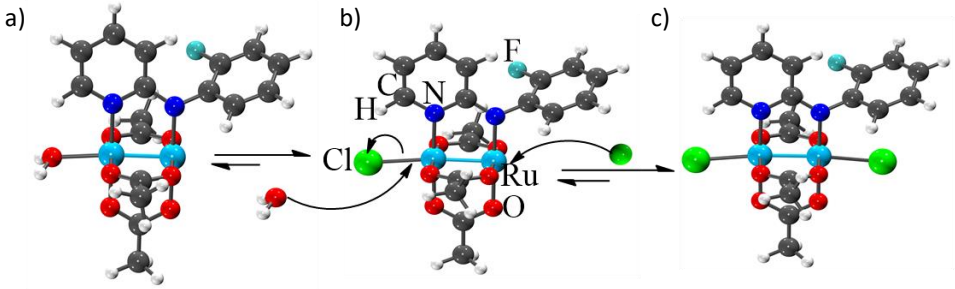

Figure 4.14 Neutral (a), cationic (b) and anionic (c) complexes used for the UV-Vis simulation

Like the neutral complex, the cationic counterpart (Figure 4.15A) is predicted to have two band maxima associated with states 7 and 12, which are characterized by a LMCT plus MMCT $\pi(C_p\text{-}N_p, C_p\text{-}C_p, F, \mathbf{Ru\text{-}N_a}, C_a, \mathbf{Ru_2}) \rightarrow \delta^*(\mathbf{Ru_2})/\pi^*(N_a, N_p, C_p)$ and a LMCT $\pi(\mathbf{F}, \mathbf{C_a\text{-}C_a}, \mathbf{Ru\text{-}N_a}, C_p\text{-}N_p, C_p\text{-}C_p, Ru_2) \rightarrow \delta^*(\mathbf{Ru_2})/\pi^*(N_a, N_p, C_p)$, respectively, as confirmed by the fragment charge contribution to the NTOs (Table 4.9) and the illustrated NTOs (c.f. Table 4.11).

It is important to note that state 12 contained significant aniline character that includes the fluoride ortho substituent, which is consistent with the sensitivity of absorption band 3 to the nature of the ortho substituent, elegantly demonstrated by Kadish *et al.* [47] on an extensive series of Rap (R represent various substituent) ligands. However, investigating this further in the current work due to time constraints is not intended.

The double maxima present in both the neutral and cationic complexes indicate that both species exhibit shoulder and primary bands at the experimental band 3, which are characterized by LMCT and MMCT. The result prohibits the attribution of the shoulder and primary bands to the cationic or anionic species exclusively. Consequently, the separate results do not support or revoke the existence of an equilibrium between the neutral and cationic species in an aqueous solution.

However, the experimentally observed band 3 is much better reproduced by a cumulatively fitted curve (Figure 4.15B) obtained from the 1:1 sum of the curves of the neutral and cationic species than from curves of the individual species separately. The resulting absorbance reflects the effect of a weighted linear combination of the corresponding oscillator strengths, which are directly proportional to the molar absorptivity of the presumed neutral and cationic species at equilibrium in solution.

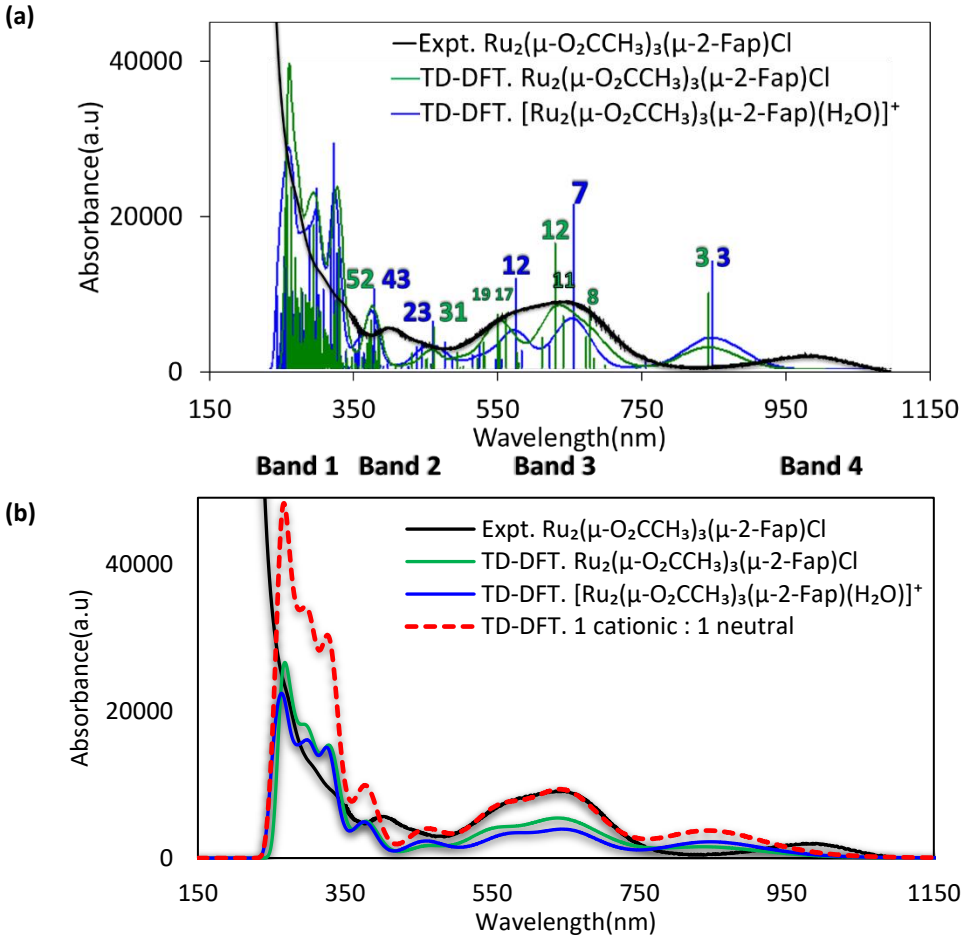

Figure 4.15 (a) Experimental curve (black), TD-DFT absorption curve of the neutral (green) $Ru_2(\mu\text{-}O_2CCH_3)_3(\mu\text{-}2\text{-}Fap)Cl$ and cationic (blue) $[Ru_2(\mu\text{-}O_2CCH_3)_3(\mu\text{-}2\text{-}Fap)(H_2O)]^+$ in water. (b) The

experimental curve (Black), and cumulative fit curve (Red) were obtained from the sum of green and blue fit curves. PBE/LANL2DZ-IEFPCM was used.

The good agreement between the cumulative fitted curve and the experimental curve at band 3, supports the presence of both the neutral and cationic complex in water, which provides some evidence to confirm the previously presumed equilibrium between the cationic and neutral species in aqueous solution.[43, 47, 71] A hypochromic red-shift is predicted for band 3 when going from the neutral to the cationic species, as demonstrated by the more intensive and red-shifted states 7 and 12 of the cationic species relative to states 12 and 17/19 of the neutral counterpart. The explicit water molecule does not significantly contribute to the excitations predicted at band 3 (Table 4.9) for the cationic species.

Table 4.9 Percentage contribution of fragmented Mulliken charges to the NTOs of $[Ru_2(\mu\text{-}O_2CCH_3)(\mu\text{-}2\text{-}Fap)(H_2O)]^+$ calculated with PBE/LANL2DZ-IEFPCM in water.

State #	λ (nm)	NTO (%)	Fragment contribution to hole (%)						Fragment contribution to particle (%)					
			Ru		H_2O	Fap		acetate	Ru		H_2O	Fap		acetate
			1	2		Anil	Pyri		1	2		Anil	Pyri	
3	849.62	93	46	3	0	15	23	13	23	38	0	16	13	10
7	657.16	92	9	26	0	42	12	10	22	38	0	17	13	10
12	578.12	93	13	9	0	44	23	10	24	39	0	16	12	10
23	463.95	41	24	37	14	12	2	11	45	47	1	2	2	3
		26	17	25	0	27	21	10	3	2	0	5	82	8
43	378.67	34	39	1	0	21	27	13	2	1	0	4	85	8
		24	46	24	0	2	7	23	2	2	0	4	68	24

Ru1 (bonded to H_2O) and Ru2 are denoted 1 and 2, respectively. The Fap is split into aniline (anil) and pyridine (pyri) fragments. Fap includes the F and N atoms.

The alteration of band 3 is thus due to the absence of the chloride-based transitions, 8, 17 and 19 (c.f. Table 4.11), in the cationic model, which is consistent with the reduced number of significant excited states when in the simulated spectrum of the cationic complex (Figure 4.15A). This result indicates that the excited states in the spectrum of the neutral complex, devoid of chloride-based transition density, viz. states 11 and 17 are transformed to states 7 and 12 and consequently red-shifted in the cationic complex. This qualitatively confirms that

the experimentally observed shoulder at band 3 in coordinating solvent, is due to a shift in the electronic transition energies of the cationic species relative to those of the neutral species.

Unlike previous studies, which presumed that the characteristic excitation of band 3 is the same in the neutral and cationic species, the obtained NTOs results (see Table 4.11), reveal that the dominant excitations causing band 3 differ between the neutral and cationic species. Although, both the cationic and neutral species exhibit a LCMT and a MMCT, the $\delta^*(Ru_2)$ character is absent in the states 12 and 17/19 of the neutral counterpart. Given that both cationic and neutral complexes are present in an aqueous solution, both $\pi(Ru_2) \rightarrow \pi^*(Ru_2)$ and $\pi(Ru_2) \rightarrow \delta^*(Ru_2)$ are therefore present in solution. Therefore, the $\pi(Ru_2) \rightarrow \delta^*(Ru_2)$ transition, previously detected in $Ru_2(\mu\text{-ap})_4Cl$ (Table 4.8), is promoted by the cationic complex in $[Ru_2(\mu\text{-}O_2CH_3)_3(\mu\text{-ap})]^+$, which suggest that the transition must be observable in species with a very weakly binding axial ligand.

In the anionic counterpart (Figure 4.16A), band 3 has been predicted to be caused by the three predominant excitations namely states 14, 15 and 20, which are linked to mixed LMCT and MMCT $\pi(\mathbf{Cl_a}, Cl_p, \mathbf{Ru_2}) \rightarrow \pi^*(\mathbf{Ru_2})$ with minor LMCT $\pi(\mathbf{Cl_a}\text{-Ru}, O, \mathbf{F}, \mathbf{C_a\text{-}C_a}, \text{Ru-}\mathbf{N_a}) \rightarrow \pi^*(N_a, N_p, \mathbf{Ru_2})$ contribution, LMCT $\pi(\mathbf{Cl_a\text{-}Ru}, \mathbf{Cl_p}, F, C_a\text{-}C_a, \text{Ru-}N_a) \rightarrow \pi^*(\mathbf{Ru_2})$, and LMCT $\pi(Cl_a, \mathbf{Ru\text{-}N_a}, F, C_a, \mathbf{C_p\text{-}C_p}, \mathbf{C_p\text{-}N_p}, \text{C-O})/\delta(\mathbf{Ru_2}) \rightarrow \delta^*(\mathbf{Ru_2})/\pi^*(N_a, N_p, C_p, O)$ with minor LMCT $\pi(\mathbf{Cl_p}, N_a, F, C_a\text{-}C_a) \rightarrow \pi^*(\mathbf{Ru_2})$ NTO excitations, respectively (Table 4.11 and Table 4.10).

(a)

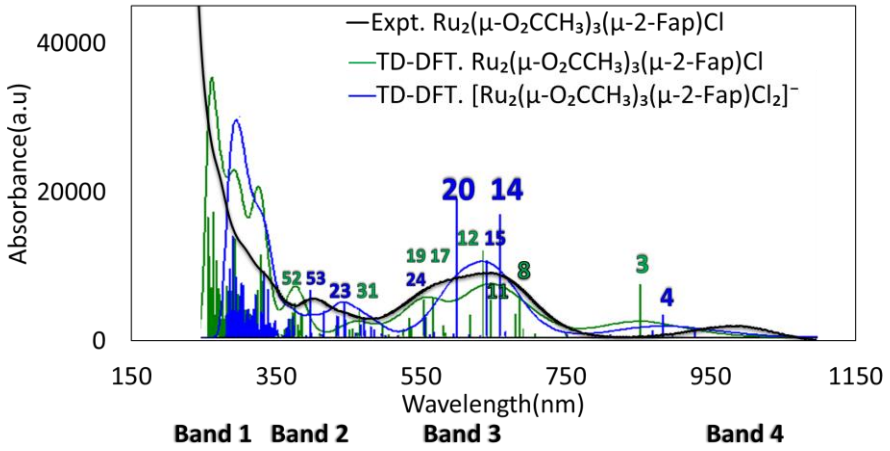

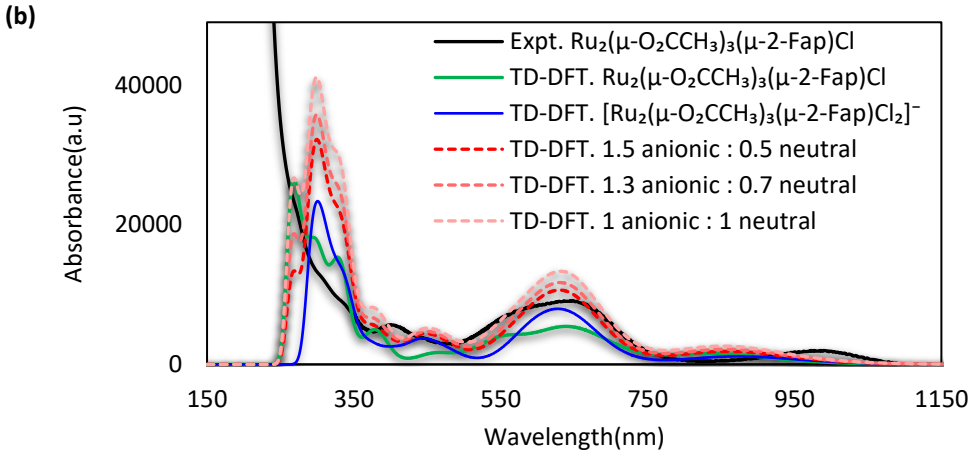

Figure 4.16 Experimental curve (black), TD-DFT absorption curve of the neutral (green) $Ru_2(\mu\text{-}O_2CCH_3)_3(\mu\text{-}2\text{-}Fap)Cl$ and anionic (blue) $[Ru_2(\mu\text{-}O_2CCH_3)_3(\mu\text{-}2\text{-}Fap)Cl_2]^-$ complexes in water. TD-DFT employed the PBE/LANL2DZ-IEFPCM(water) level of theory.

There is also state 24 which has a $\pi(Cl_a, \mathbf{Cl_p}) \rightarrow \pi^*(\mathbf{Ru_2})$ LCMT with minor $\pi(\mathbf{F, C_a\text{-}C_a})/\sigma(Ru_2, Cl_p\text{-}Ru) \rightarrow \pi^*(\mathbf{Ru_2})$ LMCT, but it is of relatively weaker intensity compared to state 14, 15 and 20. All these transitions possess significant contributions from the chlorides. This result is consistent with the substantial sensitivity of band 3 measured in excess chloride.[21, 43] In contrast to the neutral and cationic species, the anionic form exhibits a narrower band 3 with a single maximum. The reason for this can be identified when comparing states 15 and 24 to states 14 and 20. The former two states (15 and 24) possess significant contribution from the chloride adjacent to the pyridine (Cl_p) and are relatively weaker intensity compared to the latter two states (14 and 20), which possess significant contribution from the chloride adjacent to the aniline (Cl_a).

Table 4.10 Percentage contribution of fragmented Mulliken charges to the NTOs of $[Ru_2(\mu\text{-}O_2CCH_3)(\mu\text{-}2\text{-}Fap)(Cl_2)]$ calculated with PBE/LANL2DZ-IEFPCM in water.

State #	λ (nm)	NTO (%)	Fragment contribution to hole (%)							Fragment contribution to particle (%)						
			Ru		Cl		Fap		acet.	Ru		H_2O		Fap		acet.
			1	2			Anil	Pyri		1	2			Anil	Pyri	
4	873.98	78	40	10	5	8	10	17	10	29	40	0	0	11	10	10
14	654.89	38	20	20	19	32	0	1	8	45	43	3	3	0	0	6
		56	2	5	4	44	31	8	6	41	30	1	1	10	9	9

15	637.08	74	2	12	31	26	17	5	7	42	44	2	3	3	3	3
20	596.79	54	6	27	1	12	17	26	12	29	40	0	0	11	10	10
		24	3	5	3	67	12	6	4	42	43	2	3	1	1	7
24	554.50	52	3	3	73	15	0	0	6	45	43	3	3	0	0	6
		27	13	10	10	3	52	3	8	43	44	3	3	2	2	3
42	446.31	43	7	8	30	29	6	1	18	44	44	3	3	1	2	3
53	399.74	69	44	8	1	2	11	21	12	2	0	0	0	5	87	6

Ru1 (bonded to Cl1) and Ru2 (bonded to Cl2) are denoted 1 and 2 and are bonded to the pyridine and aniline groups respectively, respectively. The Fap is split into aniline (anil) and pyridine (pyri) fragments. Fap includes the F

This indicates that the previously reported absence of the shoulder band in excess chloride,[43] was due to a strong trans-effect of Cl_a in the cationic species which drops the intensity of some of the Cl_p-based LMCTs associated with the neutral species.

Similar to the neutral and cationic species, there is strong LMCT and MMCT associated with states 14 and 20, which suggests an overlap of two independent bands. However, a single maximum band is predicted due to the very low intensity of the anionic state 14 and the smaller separation in energy between the excitation energy of states 14 and 20, in comparison to the corresponding excitation energy gap in neutral and cationic species. This is evident in the increasing wavelength separation from 57.10 nm to 67.64 nm to 79.04 nm upon changing from the anionic (states 14 and 20) to neutral (states 12 and 17) to cationic (12 and 7) form.

Unlike the previous attribution[43] of the disappearance of the shoulder band in excess chloride solely to the formation of the anionic dichloro species based on previously reported formation of $[Ru_2(F_3ap)_4(H_2O)Cl_2]^-$ in excess chloride,[43] the current results (Figure 4.16B) demonstrates the existence of an equilibrium between the anionic and neutral species in varying excess chloride concentrations using cumulatively fitted curves. The shoulder band in these cumulatively fitted curves become more pronounced shoulder as the anionic to neutral proportion increases from 1:0 to 1:1.

Band 2 has chloride character in the TOs (Table 4.11) of both the two dominant anionic species namely states 42, This result is consistent with high sensitivity of band 2 when changing from the cationic and neutral form to the anionic complex and the previously observed[43] sensitivity of band 2 in solution upon addition of excess chloride. Furthermore, the TOs (Table 4.11)

associated with all the species do not possess fluoride character, which is consistent with the virtually non-existent shoulder at band 2 previously observed in the $Ru_2(\mu\text{-}O_2CCH_3)_3(\mu\text{-}2\text{-}Fap)Cl$ complex, in comparison to $Ru_2(\mu\text{-}O_2CCH_3)_3(\mu\text{-}F_5ap)Cl$ and $Ru_2(\mu\text{-}O_2CCH_3)_3(\mu\text{-}F_3ap)Cl$ which have more electronegative groups of atoms on the ap ligand and that displayed pronounced shoulder near band 2. [43]

It is important to note that all the species (neutral, cationic and anionic) do not contain chloride character in the states responsible for band 4. Indeed, the dominant MMCT $\pi(Ru\text{-}N_p, C_p\text{-}N_a, C_p\text{-}C_p, C\text{-}O)/\delta(\mathbf{Ru_2}) \rightarrow \delta^*(\mathbf{Ru_2})/\pi^*(N_p, N_a, C_p, O)$ character is preserved in all cases. This suggests that band 4 can be used to estimate and compare the $\delta(\mathbf{Ru_2}) \rightarrow \delta^*(\mathbf{Ru_2})$ energy gap in the different species.

Table 4.11 Comparison of NTO transitions neutral $Ru_2(\mu\text{-}O_2CCH_3)_3(\mu\text{-}2\text{-}Fap)Cl$, cationic $[Ru_2(\mu\text{-}O_2CCH_3)_3(\mu\text{-}2\text{-}Fap)]^+$ and anionic $[Ru_2(\mu\text{-}O_2CCH_3)_3(\mu\text{-}2\text{-}Fap)Cl_2]^-$ complexes in water, calculated at the PBE/LANL2DZ-IEFPCM(water) level of theory

$Ru_2(\mu\text{-}O_2CCH_3)_3(\mu\text{-}2\text{-}Fap)Cl$		$[Ru_2(\mu\text{-}O_2CCH_3)_3(\mu\text{-}2\text{-}Fap)]^+$		$[Ru_2(\mu\text{-}O_2CCH_3)_3(\mu\text{-}2\text{-}Fap)Cl_2]^-$	
hole → particle		hole → particle		hole → particle	
hole	particle	hole	particle	hole	particle
Band 4					
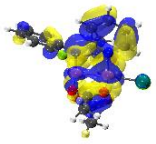	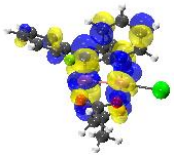	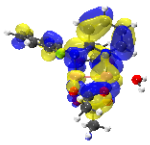	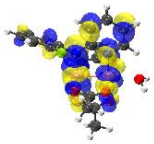	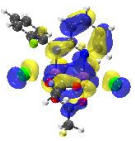	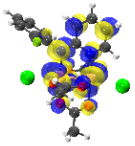
State 3 (843.44 nm, 0.015 a.u): $\pi(Ru\text{-}N_p,C_p\text{-}N_a,C_p\text{-}C_p,C\text{-}O)/\delta(\mathbf{Ru_2}) \rightarrow \delta^*(\mathbf{Ru_2})/\pi^*(N_p,N_a,C_p,O)$ (91%)		State 3 (849.640 nm, 0.021 a.u): $\pi(Ru\text{-}N_p,C_a,C_p\text{-}N_a,C_p\text{-}C_p,C\text{-}O)/\delta(\mathbf{Ru_2}) \rightarrow \delta^*(\mathbf{Ru_2})/\pi^*(C_p,N_p,N_a,C_a,O)$ (93%)		State 4 (873.98 nm, 0.006 a.u): $\pi(Ru\text{-}N_p,C_p\text{-}N_a,C_p\text{-}C_p,C\text{-}O)/\delta(\mathbf{Ru_2}) \rightarrow \delta^*(\mathbf{Ru_2})/\pi^*(N_p,N_a,C_p,O)$ (78%)	
Band 3					
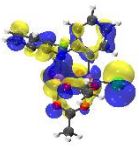	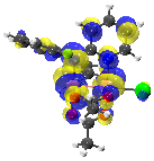			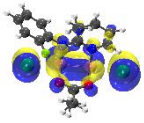	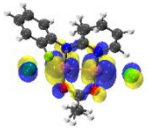
State 8 (680.41 nm, 0.012 a.u): $\pi(\mathbf{Cl},F,C_p\text{-}N_p,Ru\text{-}N_a,C_a,O,\mathbf{Ru_2})$				State 14 (654.89 nm, 0.035 a.u): $\pi(\mathbf{Cl_a},Cl_p,\mathbf{Ru_2}) \rightarrow \pi^*(\mathbf{Ru_2})$ (56%)	

→ δ*(**Ru_2**,N_a,N_p,C_p) (92%)

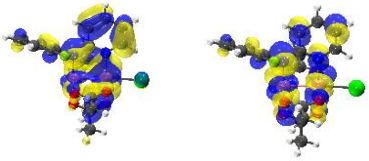

State 11 (642.71 nm, 0.011 a.u):
π(Ru-N_a,C-O,C_p-C_p)/δ(**Ru_2**)
→ δ*(**Ru_2**) (87%)

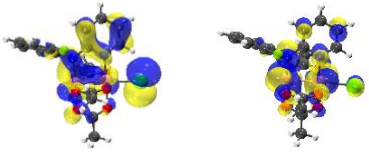

State 12 (632.03 nm, 0.025 a.u):
π(**Cl**,C_p-N_p,Ru-N_a,C_p-C_p,**Ru_2**)
→ π*(**Ru_2**) (88%)

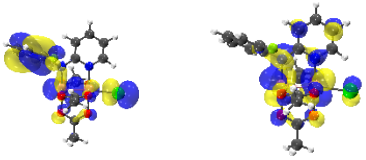

State 17 (564.39 nm, 0.011 a.u):
π(Ru-N_a,**F**,**C_a-C_a**)/σ(Cl,Ru_2)
→ π*(**Ru_2**) (38%)

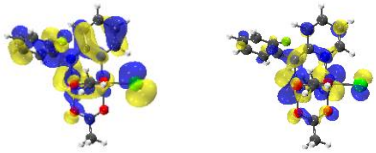

State 17 (564.39 nm, 0.011 a.u):
π(**Cl**,F,Ru-N_a,C_a-C_a,C_p-C_p,C_p-N_p)
→ π*(**Ru_2**) (32%)

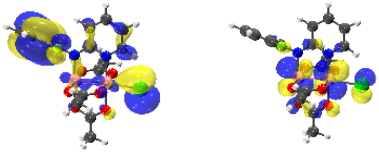

State 19 (552.67 nm, 0.011 a.u):
π(**Cl**,**F**,**C_a-C_a**) → π*(**Ru_2**) (75%)

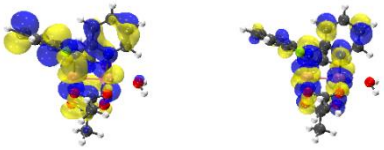

State 7 (657.160 nm, 0.032 a.u):
π(C_p-N_p,C_p-C_p,**F**,**Ru-N_a**,C_a,**Ru_2**)
→ δ*(**Ru_2**)/π*(N_a,N_p,C_p) (92%)

State 12 (578.12 nm, 0.0178 a.u):
π(**F**,**C_a-C_a**,**Ru-N_a**,C_p-N_p,C_p-C_p,Ru_2)
→ δ*(**Ru_2**)/π*(N_a,N_p,C_p) (93%)

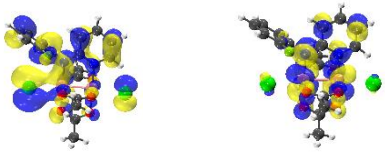

State 14 (654.89 nm, 0.035 a.u):
π(**Cl_a**-Ru,O,**F**,**C_a-C_a**,Ru-**N_a**)
→ π*(N_a,N_p,**Ru_2**) (38%)

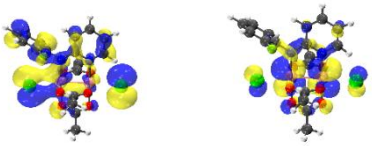

State 15 (637.08 nm, 0.022 a.u):
π(**Cl_a-Ru**,**Cl_p**,F,C_a-C_a,Ru-N_a) → π*(**Ru_2**)
(74%)

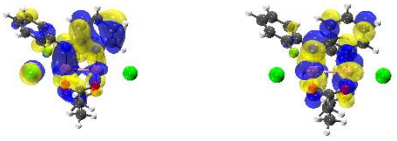

State 20 (596.79 nm, 0.039 a.u):
(Cl_a,**Ru-N_a**,F,C_a,**C_p-C_p**,**C_p-N_p**,C-O)/ δ(**Ru_2**)
→ δ*(**Ru_2**)/π*(N_a,N_p,C_p,O) (51%)

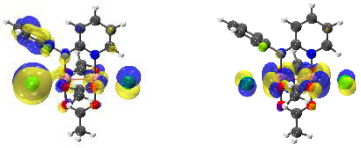

State 20 (596.79 nm, 0.039 a.u):
π(**Cl_a**,N_a,F,C_a-C_a) → π*(**Ru_2**) (24%)

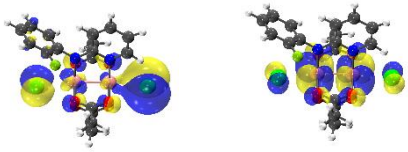

State 24 (554.50 nm, 0.007 a.u):
π(Cl_a,**Cl_p**) → π*(**Ru_2**) (52%)

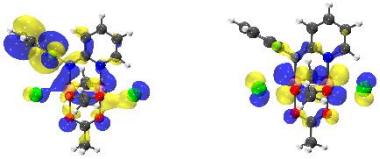

State 24 (554.50 nm, 0.007 a.u):
π(**F**,**C_a-C_a**)/σ(Ru_2,Cl_p-Ru) → π*(**Ru_2**)
(27%)

Band 2

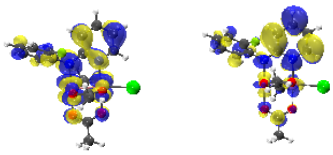

State 31 (464.33 nm, 0.008 a.u):
$\pi(\mathbf{C_a,N_a},C_p\text{-}C_p,C_p\text{-}N_p,O)/\delta^*(\mathbf{Ru_2})$
$\rightarrow \pi^*(\mathbf{C_p,N_p})$ (83%)

State 23 (463.95 nm, 0.0095 a.u):
$\pi(Cl_p,C_a\text{-}C_a)/\sigma(O_W,\mathbf{Ru_2})$
$\rightarrow \pi^*(\mathbf{Ru_2})$(41%)

State 42 (446.31 nm, 0.010 a.u):
$\pi(\mathbf{Cl_a,Cl_p},O)/\sigma(Cl\text{-}Ru) \rightarrow \pi^*(\mathbf{Ru_2})$ (43%)

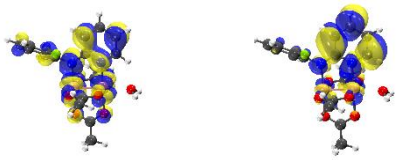

State 23 (463.95 nm, 0.0095 a.u):
$\pi(\mathbf{C_a,N_a},C_p,C_p\text{-}N_p)/\delta^*(\mathbf{Ru_2})$
$\rightarrow \pi(\mathbf{C_p,N_p},N_a,O)$ (26%)

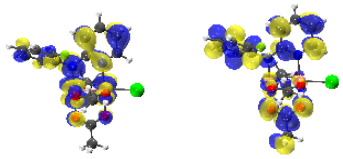

State 52 (378.67 nm, 0.010 a.u):
$\pi(\mathbf{C_a,N_a},C_p\text{-}C_p,C_p\text{-}N_p,O)/\delta^*(\mathbf{Ru_2})$
$\rightarrow \pi^*(C_a,C_p,\mathbf{O,C})$ (41%)

State 43 (378.672 nm, 0.01 a.u):
$\pi(N_a,Ru\text{-}N_p,\mathbf{C_p\text{-}C_p,C_p\text{-}N_p},O)/\delta^*(\mathbf{Ru_2})$
$\rightarrow \pi^*(\mathbf{N_p,C_p},O)$ (34%)

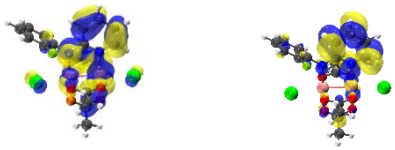

State 53 (399.74 nm, 0.013 a.u):
$\pi(Ru\text{-}N_p,C_p\text{-}C_p,N_a,C\text{-}O)/\delta(\mathbf{Ru_2})$
$\rightarrow \pi^*(\mathbf{N_p,C_p})$ (69%)

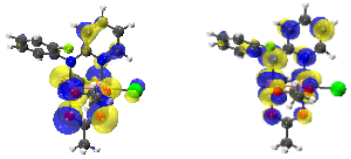

State 52 (378.67 nm, 0.010 a.u):
$\pi(C_p\text{-}C_p,N_p\text{-}C_p,\mathbf{O})$
$\rightarrow \pi^*(N_a,N_p,C_p,O)/\delta^*(\mathbf{Ru_2})$ (33%)

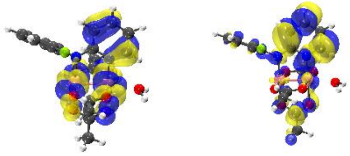

State 43 (378.672 nm, 0.01 a.u):
$\pi(Ru\text{-}N_p,C_p\text{-}C_p,C_p\text{-}N_p,O)/\pi^*(\mathbf{Ru_2})$
$\rightarrow \pi^*(\mathbf{N_p,C_p,O})$ (24%)

C_p and N_p denote carbon and nitrogen atoms of the pyridine moiety. C_a and N_a denote carbon and nitrogen atoms of the aniline moiety. C and O denote carbon and oxygen atoms of an acetate ligand. O_W denotes an oxygen atom of water. Cl_a and Cl_p are used to distinguish the chloride atoms on the aniline and pyridine sides respectively.
[a] The highlighted orbitals are the most contributing (≤ 24% in Table 4.7and Table 4.10 and Table 4.10) orbitals to the NTOs, used to determine the transition type.

The observed changes in electronic transitions and the resulting absorption spectrum shifts upon changing from the cationic to neutral to anionic complex can be rationalized in terms of the resulting variation in electronic structures. Consider the electronic structure calculations based on the first excited states of the neutral $Ru_2(\mu\text{-}O_2CCH_3)_3(\mu\text{-}2\text{-}Fap)Cl$, as well as its cationic and anionic derivatives as presented in an open-shell MO diagram (Figure 4.17).

The order of the α-manifold of the cationic and anionic species is essentially the same as what was discussed (c.f. section 4.2.1) for the neutral species. Given the possibility of obtaining a

doublet ground state in the cationic species (c.f. Figure 1.6 Comparison of the spin-restricted MO diagram and electronic configuration of (A) $[Ru_2(\mu\text{-}O_2CR)_4]^+$, (B) $[Ru_2(\mu\text{-}NOCR)_4]^+$ and (C) $[Ru_2(\mu\text{-}NN'CR)_4]^+$ complexes. Effect of bridging ligands indicated by the dashed lines.), electronic calculation on the quartet and doublet state of the cationic species yielded a total electronic energy of -1581.384495 Hartrees and -1581.374693 Hartrees for the quartet and doublet ground state, respectively.

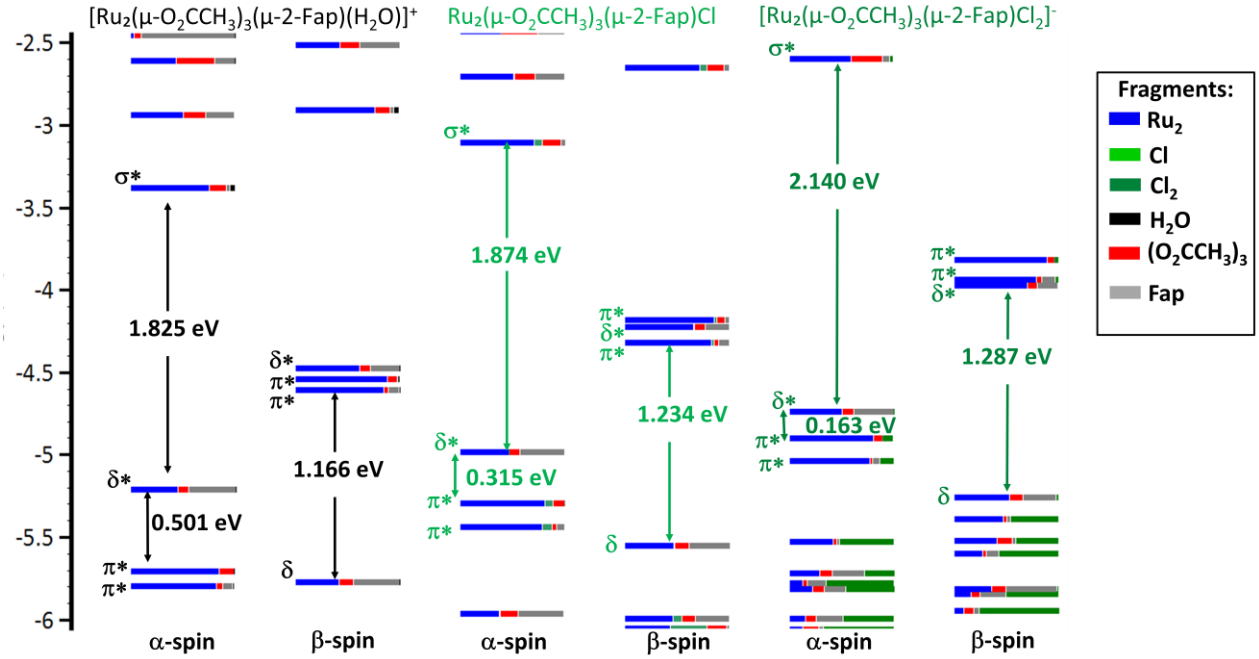

Figure 4.17 Electronic structure calculations of the cationic (black), neutral (green) and anionic (dark-green) complexes in water obtained at the PBE/LANL2DZ-IEFPCM level of theory.

Therefore, the quartet ground state is 0.009802 Hartree more stable than the doublet ground state and thus the electronic structure of the cationic species should contain three SOMOs like the neutral species (Figure 4.17). However, the order of the β-manifold, which accounts for most of the excitations on the spectrum, changes in the cationic and anionic species. Essentially, the order of the β-manifold LUMO, LUMO-1 and LUMO-2 changes from $\delta^*>\pi^*>\pi^*$ to $\pi^*>\delta^*>\pi^*$ to $\pi^*>\pi^*>\delta^*$ (see Figure 4.17) while moving from the cationic to the neutral to the anionic species, respectively. This change in the ordering of these MOs stems from the fact the fragment contribution of the axial ligands is significant to the π^* MOs but not the δ^* MO (see Figure 4.17) due to symmetry-aligned π^* overlap between a Ru-based d_{xz} (and d_{yz}) orbital and axial ligand p_x (and p_y) orbital at MO 114β (and 116β) (c.f. Figure 4.10). This axial ligand

fragment contribution to the π^* MOs is increasing while changing from cationic to neutral to anionic, which suggests an increasing π-donation to the Ru atom and increasing destabilization of the π^* MOs while the δ^* MO remains relatively unaffected. Hence, the change from $\delta^*>\pi^*>\pi^*$ to $\pi^*>\delta^*>\pi^*$ to $\pi^*>\pi^*>\delta^*$ arrangement.

While moving from cationic to neutral to anionic, the α- and β-spin HOMO-LUMO gap energies become larger and the π^*-δ^* gap energy of the α-manifold shrinks. The α-manifold δ^*-σ^* gap energy increases by 0.049 eV while moving from the cationic to the neutral complex, and further increases by 0.266 eV while moving from the neutral to the anionic species. The fragment contribution of the axial ligands is significant to the σ^* LUMO but not the δ^* HOMO (see Figure 4.17) of the α-manifold due to symmetry-aligned σ^* overlap between a Ru-based d_{z^2} orbital and axial ligand p_z orbital at MO 117α (c.f. Figure 4.10) and the axial ligand fragment contribution to the σ^* LUMO is increasing while changing from cationic to neutral to anionic, which is indicative of increasing σ-donation to the Ru atom in the same direction. Hence, the increasing HOMO-LUMO gap energy of the α-manifold is therefore a result of the destabilization of the σ^* LUMO with increasing σ-donation to the Ru_2 by the axial ligand. This is consistent with previously reported increasing HOMO-LUMO gap energy of the α-manifold while changing from I to Br to Cl axial ligand (X) of $[Ru_2(\mu\text{-}O_2CCH_3)_4X_2]^-$ complexes.[21] Similarly, there is fragment contribution by the axial ligands to the π^* MOs but not to the δ HOMO (see Figure 4.17) of the β-manifold due to symmetry-aligned π^* overlap between a Ru-based d_{xz} orbital and axial ligand p_x orbital at MO 114β (c.f. Figure 4.10) and the fragment axial ligand contribution to the π^* MOs is increasing while changing from cationic to neutral to anionic, which is indicative of increasing π-donation to the Ru atom in the same direction. Hence, the increasing HOMO-LUMO gap energy of the β-manifold is, therefore, a result of the destabilization of the π^* MOs with increasing π-donation to the Ru_2 by the axial ligand.

Contrary to the increase in HOMO-LUMO energy gaps discussed above, the decrease in π^*-δ^* gap energy of the SOMOs stems from the significant fragment contribution of the axial ligands to the π^* MOs but not the δ^* MO (see Figure 4.17) due to symmetry-aligned π^* overlap of a Ru-based d_{xz} (and d_{yz}) orbital with axial ligand p_x (and p_y) orbital at MO 114β (and 115β) (c.f.

Figure 4.10). The axial ligand fragment contribution to the π^* MOs is increasing while changing from cationic to neutral to anionic, which is indicative of increasing π-donation to the Ru atom in the same direction. Hence, the decreasing π^*-δ^* gap energy of the SOMO is, therefore, a result of the destabilization of the π^* MOs with increasing π-donation to the Ru_2 by the axial ligand. This decrease is consistent with what was discussed before (c.f. Figure 1.5).

The abovementioned differences are significant to understanding the different electronic spectra obtained. For instance, the simplest band, i.e. band 4, which the NTOs indicated is caused by $\delta(Ru_2) \rightarrow \delta^*(Ru_2)$ transitions predominantly associated with state 3 of the cationic or neutral complexes or state 4 of the anionic complex (see Table 4.11), comprises exclusively of β-manifold single-electron excitations (Figure 4.18).

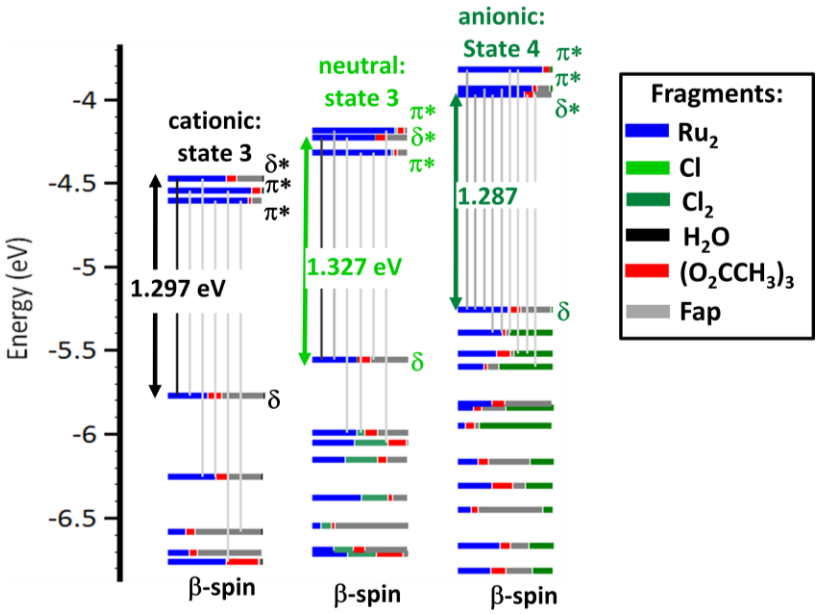

Figure 4.18 The single electron excitations and the δ-δ^* gap energies for band 4 of the cationic (black), neutral (green) and anionic (dark-green) complexes in water obtained at the PBE/LANL2DZ-IEFPCM level of theory.

The β-manifold δ-δ^* gap energy is 1.297 eV for the cationic species, 1.327 eV for the neutral species, and 1.287 eV for the anionic species. This increase in δ-δ^* gap energy while going from the cationic to the neutral species is consistent with the predicted blue shift of band 4 upon changing from the cationic to the neutral species (Figure 4.15). Similarly, the decrease in δ-δ^* gap energy upon changing from the neutral to the anionic species is consistent with the predicted red shift of band 4 upon changing from the neutral to anionic species (Figure 4.16).

Hence, a change in the electronic structure results in a different set of excitations, which are concomitant with spectroscopic shifts.

All the other manifested more complex changes in the absorption spectra can also be attributed to differences in the electronic structures of the different species that boil down to some changes in β-manifold MOs order, some changes in both the β-manifold and the α-manifold HOMO-LUMO gap energy and some changes in the π^*-δ^* gap energy.

4.2.3 Nature of halogen ligand

The solution UV-vis spectra for the $Ru_2(\mu\text{-}O_2CCH_3)_3(\mu\text{-}2\text{-}Fap)I$ species was measured in water, generated from the $Ru_2(\mu\text{-}O_2CCH_3)_3(\mu\text{-}2\text{-}Fap)Cl$ precursor. The measured spectra of $Ru_2(\mu\text{-}O_2CCH_3)_3(\mu\text{-}2\text{-}Fap)I$, the previously obtained $Ru_2(\mu\text{-}O_2CCH_3)_3(\mu\text{-}2\text{-}Fap)Cl$ complex in water as well as their simulated spectra in water using TD-DFT are shown in Figure 4.19. A strong red-shift of the absorption band 1 situated in the UV region from 195.00 nm - 368.99 nm to 199.00 nm - 395.65 nm can be easily observed upon changing from the chloride to the iodide complex, in agreement with the red-shift of the corresponding TD-DFT band predicted along the chloro - bromo - iodo series. Although the bromo derivative was not synthesized in the current work, a redshift of its band 1 relative to the chloride counterpart is expected based on the predicted shift.

Band 2 situated in the visible region is slightly red-shifted from 408.69 nm to 416.00 nm, which can be observed upon going from the chloride to the iodide complex, which is consistent with the corresponding TD-DFT curves virtually insensitive to the axial ligand.

The primary band of band 3 situated in the visible region is insensitive to the axial ligand, whereas its shoulder band is slightly red-shifted from 571.00 nm to 575.00 nm upon going from the chloride to the iodide compound, which is consistent with the two maxima predicted in the TD-DFT curve which are relatively unperturbed when changing from the chloro to the iodo derivative, in comparison to the bromo counterpart. On the basis based on the predicted substantial redshift of the curve of the bromo complexes, a redshift of its primary band relative to the chloride and iodide derivatives is expected. The NTOs (Table 4.12) reveal that the

maximum at states 17 and 19 of the chloride complex which is associated with the shoulder band is slightly red-shifted as the states are transformed into state 16 of the bromide complex and state 25 of the iodide complex, which is consistent with the slight red-shift of the shoulder band observed experimentally.

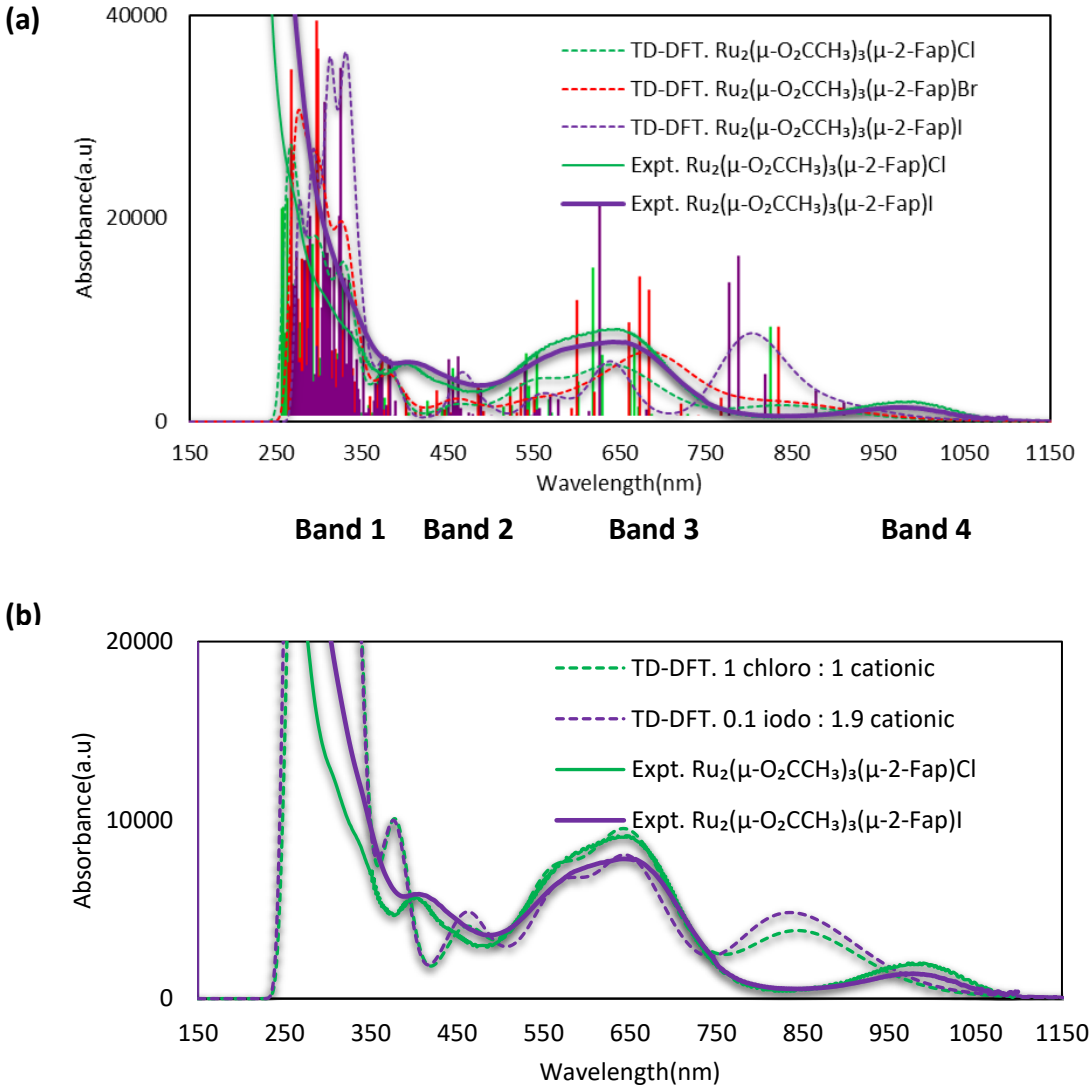

Figure 4.19 (a) Experimental (solid) and TD-DFT (dashed) curves of $Ru_2(\mu\text{-}O_2CCH_3)_3(\mu\text{-}2\text{-}Fap)X$ where X=Cl (green), Br(red) or I (purple) complexes in water. (b) Experimental (solid) and cumulative fit curves obtained from the sum of the TD-DFT curve of $[Ru_2(\mu\text{-}O_2CCH_3)_3(\mu\text{-}2\text{-}Fap)]^+$ with the TD-DFT curve of $Ru_2(\mu\text{-}O_2CCH_3)_3(\mu\text{-}2\text{-}Fap)Cl$ (green) or $Ru_2(\mu\text{-}O_2CCH_3)_3(\mu\text{-}2\text{-}Fap)I$ (purple). TD-DFT employed the PBE/LANL2DZ-IEFPCM(water) level of theory.

The primary band of band 3 is linked to the maximum at states 8, 11 and 12 of the chloride complex, which is substantially red-shifted as the states are transformed into the substantially red-shifted states 10, 12 and 13, respectively, of the bromide complexes, which are significantly distinct from the original states, whereas the maximum is relatively unaffected as the states are transformed into state 16 of the iodide complex, which is quite similar to the original state 11.

Table 4.12 Comparison of NTO transitions the neutral $Ru_2(\mu\text{-}O_2CCH_3)_3(\mu\text{-}2\text{-}Fap)X$ (X = Cl, Br and I) complexes in water, calculated at the PBE/LANL2DZ-IEFPCM(water) level of theory.

$Ru_2(\mu\text{-}O_2CCH_3)_3(\mu\text{-}2\text{-}Fap)Cl$		*$Ru_2(\mu\text{-}O_2CCH_3)_3(\mu\text{-}2\text{-}Fap)Br$*		*$Ru_2(\mu\text{-}O_2CCH_3)_3(\mu\text{-}2\text{-}Fap)I$*	
hole → particle		hole → particle		hole → particle	
hole	particle	hole	particle	hole	particle
Band 4					
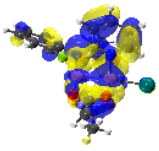	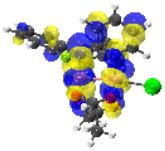	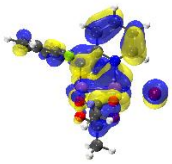	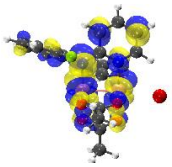	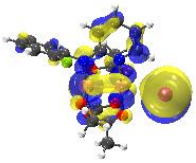	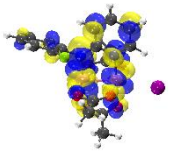
State 3 (843.44 nm, 0.015 a.u): $\pi(Ru\text{-}N_p,C_p\text{-}N_a,C_p\text{-}C_p,C\text{-}O)/\delta(Ru_2) \rightarrow \delta^*(Ru_2)/\pi^*(N_p,N_a,C_p,O)$ (91%)		State 3 (852.93 nm, 0.015 a.u): $\pi(Ru\text{-}N_p,C_p\text{-}N_a,C_p\text{-}C_p,C\text{-}O,Br)/\delta(Ru_2) \rightarrow \delta^*(Ru_2)/\pi^*(N_p,N_a,C_p,O)$ (88%)		State 5 (897.24 nm, 0.005 a.u): $\pi(C_p\text{-}C_p,C\text{-}O,I)/\delta(Ru_2) \rightarrow \delta^*(Ru_2)/\pi^*(N_p,N_a,C_p,O)$ (84%)	
				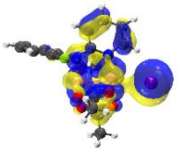	
				State 8 (836.06 nm, 0.007 a.u): $\pi(Ru\text{-}N_p,C_p\text{-}C_p,C\text{-}O,I)/\delta(Ru_2) \rightarrow \delta^*(Ru_2)/\pi^*(N_p,N_a,C_p,O)$ (83%)	
				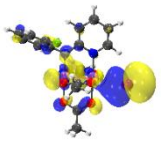	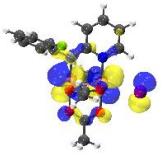
				State 9 (804.34 nm, 0.026 a.u): $\pi(Ru\text{-}N_a)/\sigma(I,Ru_2) \rightarrow \pi^*(Ru_2,I)$ (60%)	
				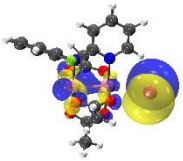	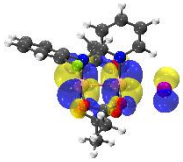
				State 9 (804.34 nm, 0.026 a.u): $\pi(I)/\sigma(Ru_2) \rightarrow \pi^*(Ru_2,I)$ (32%)	

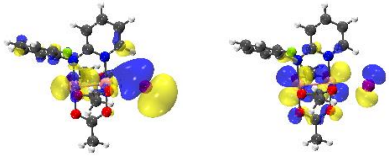

State 10 (794.04 nm, 0.022 a.u):
$\pi(I,Ru\text{-}N_a)/\sigma(I,Ru_2) \rightarrow \pi^*(Ru_2,I)$ (68%)

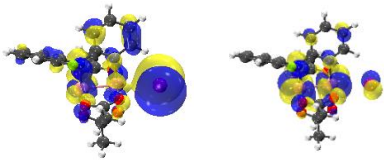

State 10 (794.04 nm, 0.022 a.u):
$\pi(I,Ru\text{-}N_a,Ru\text{-}N_p,C_p\text{-}C_p)/d(Ru_2)$
$\rightarrow \pi^*(Ru_2,I,N_a,N_p,C_p)$ (25%)

Band 3

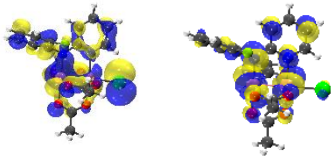

State 8 (680.41 nm, 0.012 a.u):
$\pi(Cl,F,C_p\text{-}N_p,Ru\text{-}N_a,C_p\text{-}C_p,C_a,Ru_2)$
$\rightarrow \delta^*(Ru_2,N_a,N_p,C_p)$ (92%)

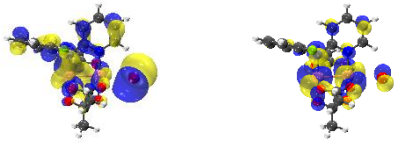

State 10 (697.98 nm, 0.021 a.u):
$\pi(Br,F,C_p\text{-}N_p,Ru\text{-}N_a,C_p\text{-}C_p,C_a)/\sigma(Ru_2)$
$\rightarrow \pi^*(Ru_2,N_a,N_p,C_p,Br)$ (37%)

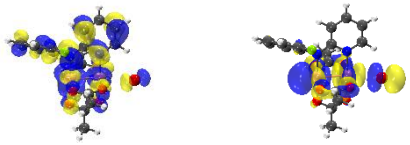

State 10 (697.98 nm, 0.021 a.u):
$\pi(N_p,N_a,C_p\text{-}C_p,C_a,O)/\delta^*(Ru_2)/\sigma(Br)$
$\rightarrow \sigma^*(Ru_2,Br)/\pi^*(O)$ (26%)

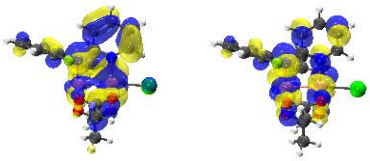

State 11 (642.71 nm, 0.011 a.u):
$\pi(Ru\text{-}N_a,C\text{-}O,C_p\text{-}C_p,C_a)/\delta(Ru_2)$
$\rightarrow \delta^*(Ru_2)/\pi^*(N,C_p,O)$ (87%)

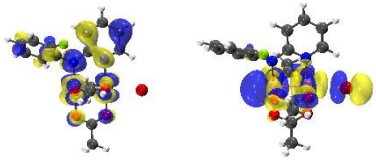

State 12 (687.47 nm, 0.023 a.u):
$\pi(N_p,N_a,C_p,C_a,O)/\delta^*(Ru_2)$
$\rightarrow \sigma^*(Ru_2,Br)/\pi^*(O)$ (49%)

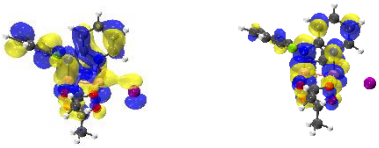

State 16 (640.05 nm, 0.034 a.u):
$\pi(I,Ru,C_p\text{-}N_p,Ru\text{-}N_a,C_p\text{-}C_p,C_a,Ru_2)$
$\rightarrow \delta^*(Ru_2)/\pi^*(N_p,N_a,C_p,O)$ (87%)

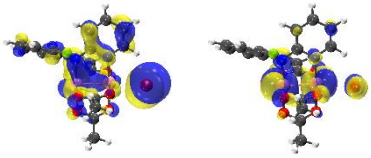

State 12 (687.47 nm, 0.023 a.u):
$\pi(Br,C_p\text{-}N_p,Ru\text{-}N_a,C_p\text{-}C_p,C_a)/\delta^*(Ru_2)$
$\rightarrow \pi^*(Ru_2,N_a,N_p,Br)$ (37%)

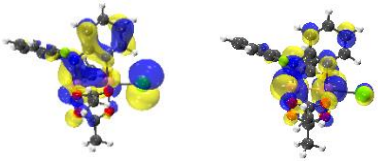

State 12 (632.03 nm, 0.025 a.u): $\pi(Cl,C_p\text{-}N_p,Ru\text{-}N_a,C_p\text{-}C_p,Ru_2) \rightarrow \pi^*(Ru_2,N_a,N_p,C_p,Cl)$ (88%)

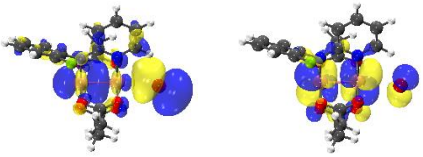

State 13 (675.01 nm, 0.016 a.u): $\sigma(Ru_2,Br) \rightarrow \pi^*(Ru_2,Br)$ (68%)

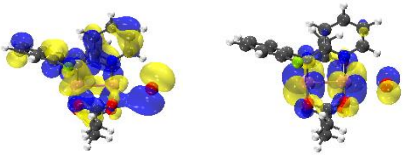

State 13 (675.01 nm, 0.016 a.u): $\pi(Br,F,C_p\text{-}N_p,Ru\text{-}N_a,C_p\text{-}C_p,C\text{-}O,C_a)/\delta^*(Ru_2) \rightarrow \pi^*(Ru_2,Br,O)$ (25%)

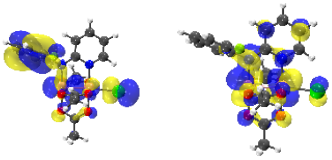

State 17 (564.39 nm, 0.011 a.u): $\pi(F,Ru\text{-}N_a,C_a\text{-}C_a)/\sigma(Cl,Ru_2) \rightarrow \pi^*(Ru_2,Cl,N_a,N_p,C_p)$ (38%)

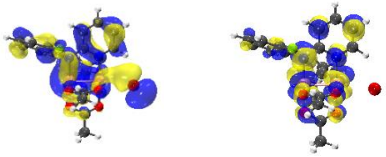

State 16 (612.76 nm, 0.019 a.u): $\pi(Br,F,C_p\text{-}N_p,Ru\text{-}N_a,C_p\text{-}C_p,C\text{-}O,C_a,Ru_2) \rightarrow \delta^*(Ru_2)/\pi^*(N_a,N_p,C_p,O)$ (74%)

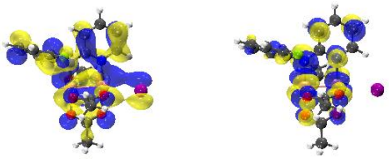

State 25 (550.83 nm, 0.009 a.u): $\pi(Ru\text{-}I,F,C_p\text{-}N_p,Ru\text{-}N_a,Ru\text{-}N_p,C_p\text{-}C_p,O,C_a,Ru_2) \rightarrow \delta^*(Ru_2)/\pi^*(N_a,N_p,C_p,O)$ (86%)

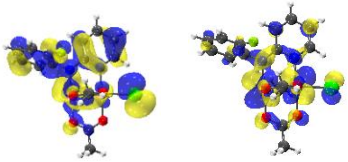

State 17 (564.39 nm, 0.011 a.u): $\pi(Cl,F,Ru\text{-}N_a,C_a\text{-}C_a,C_p\text{-}C_p,C_p\text{-}N_p)/d(Ru) \rightarrow \pi^*(Ru_2\ N_a,N_p,C_p,Cl)$ (32%)

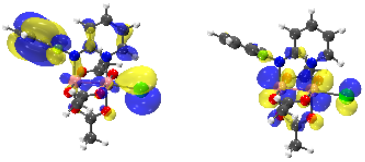

State 19 (552.67 nm, 0.011 a.u): $\pi(F,C_a\text{-}C_a)/\sigma(Ru_2,\ Cl\text{-}Ru) \rightarrow \pi^*(Ru_2,Cl,O)$(75%)

C_p and N_p denote carbon and nitrogen atoms of the pyridine moiety. C_a and N_a denote carbon and nitrogen atoms of the aniline moiety. C and O denote carbon and oxygen atoms of an acetate ligand. O_W denotes an oxygen atom of water. Cl_a and Cl_p are used to distinguish the chloride atoms on the aniline and pyridine sides respectively.

Band 4 situated in the near-infrared is blue-shifted from 993.00 nm to 986.00 nm upon changing from the chloride to the iodide complex, which is consistent with the predicted blue-shift of the iodide relative to chloride. Band 4 is predicted to be only slightly sensitive to the

bromide ligand. It is important to note that band 4 have been predicted at much lower energies than where it occurs experimentally, which is consistent with the previously reported deviation in Ru_2 tetracarboxylates and tetra-ap. [21, 63] In contrast to the previous study, the predicted band 4 is oddly very intense for this iodide complex. The NTOs (Table 4.12) reveal that the TOs of the state associated with band 4, namely state 3, remain intact when switching from the chloride to the bromide complex, with the only exception of the slightly substantial size of the bromide p-orbital in the hole, whereas state 3 is transformed into multiple intense states namely, state 5, 8, 9 and 10, which are all characterized by very bulky iodide p-orbitals and various metal-metal and LMCT characters. Notably states 9 and 10 contain $\pi(I)/\sigma(Ru_2) \rightarrow \pi^*(Ru_2, I)$ TOs at 804.34 nm and 794.04 nm which is consistent with the almost two-fold stronger intensity of these excitations and the blue-shift relative to state 3 of the chloride and bromide complex which occurs 843.44 nm and 852.93 nm, respectively.

Similar to the chloride complex (c.f. 4.2.1), the experimentally observed band 3 of the iodide complex is much better reproduced by the cumulative fit curve (Figure 4.19B) obtained from the sum of the curves of the neutral and cationic species. In addition, the intensity of the maximum associated with band 4 has dropped below that of band 3, which agrees well with the experimental spectrum. The better agreement between the theoretical and experimental curves at both bands 3 and 4 substantiate the existence of an equilibrium between the neutral $Ru_2(\mu\text{-}O_2CCH_3)_3(\mu\text{-}2\text{-}Fap)I$ form and the cationic $[Ru_2(\mu\text{-}O_2CCH_3)_3(\mu\text{-}2\text{-}Fap)]^+$ form. However, for the iodide complex 0.1:0.9 ratio of neutral to cationic is required to produce the best fit, implying that the equilibrium favours a higher ratio of the cationic form.

The observed changes in electronic transitions and the resulting absorption spectrum shifts upon changing the axial ligand from Cl to Br to I complex can be rationalized in terms of the resulting variation in electronic structures. Consider the electronic structure calculations based on the first excited states of the neutral $Ru_2(\mu\text{-}O_2CCH_3)_3(\mu\text{-}2\text{-}Fap)X$ (X=Cl, Br or I) as presented in an open-shell MO diagram (Figure 4.20). The order of the α-manifold of $Ru_2(\mu\text{-}O_2CCH_3)_3(\mu\text{-}2\text{-}Fap)Br$ and $Ru_2(\mu\text{-}O_2CCH_3)_3(\mu\text{-}2\text{-}Fap)I$ is essentially the same as what was discussed (c.f. section 4.2.1) for $Ru_2(\mu\text{-}O_2CCH_3)_3(\mu\text{-}2\text{-}Fap)Cl$ species. However, the order of the β-manifold, which accounts for most of the excitations on the spectrum, is different in the species containing an

iodide. Essentially, the order of the β-manifold LUMO, LUMO-1 and LUMO-2 changes from $\pi^*>\delta^*>\pi^*$ to $\delta^*>\pi^*>\pi^*$ (Figure 4.20) while moving from the chloride- or bromide-containing species to the iodide-containing derivative. This change in the ordering of these MOs stems from the fact the fragment contribution of the axial ligands is significant to the π^* MOs but not the δ^* MO (Figure 4.20) due to symmetry-aligned π^* overlap between a Ru-based d_{xz} (and d_{yz}) orbital and axial ligand p_x (and p_y) orbital at MO 114β (and 116β) (c.f. Figure 4.10). This axial ligand fragment contribution to the π^* MOs is decreasing while changing from chloride to bromide to the iodide species, which is indicative of decreasing π-donation to the Ru atom, decreasing destabilization of the π^* MOs while the δ^* MO remains relatively unaffected. This results in a change from $\pi^*>\delta^*>\pi^*$ to $\delta^*>\pi^*>\pi^*$ configuration order.

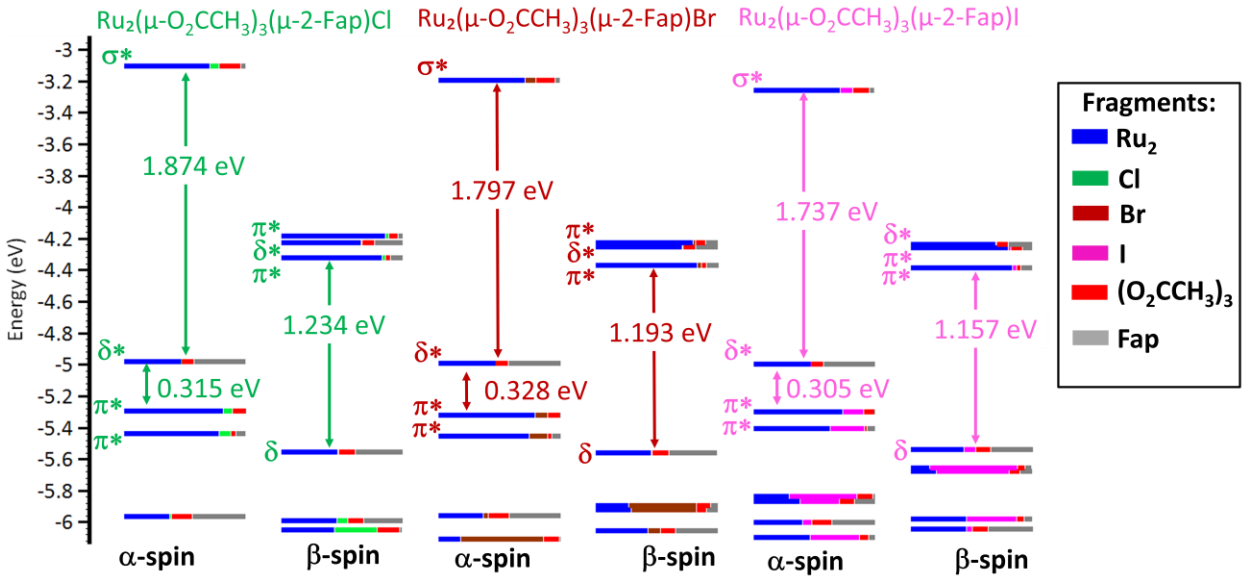

Figure 4.20 Electronic structure calculations of the $Ru_2(\mu\text{-}O_2CCH_3)_3(\mu\text{-}2\text{-}Fap)X$ where X is Cl (green), Br (brown) and I (pink) complexes in water obtained at the PBE/LANL2DZ-IEFPCM level of theory.

While moving from the chloride species to bromide or iodide neutral species, both the α- and β-spin HOMO-LUMO gap energies become smaller (Figure 4.20). Whilst it is anticipated that the α-manifold π^*-δ^* gap energy would become larger when changing from the chloride to the bromide to the iodide species, the data shows that the π^*-δ^* gap energy decreases when going from the chloride or bromide species to the iodide species. The α-manifold δ^*-σ^* gap energy decreases by 0.077 eV while moving from the chloride to the bromide species, and further decreases by 0.060 eV while moving from the bromide to the iodide species. The fragment

contribution of the axial ligands is significant to the σ^* LUMO but not the δ^* HOMO (Figure 4.20) of the α-manifold due to symmetry-aligned σ^* overlap between a Ru-based d_{z^2} orbital and axial ligand p_z orbital at MO 117α (c.f. Figure 4.10) and the σ-donation to the Ru atom is expected to decrease while changing from the chloride to the bromide to the iodide species.

Hence, the decreasing HOMO-LUMO gap energy of the α-manifold is a result of the stabilization of the σ^* LUMO with decreasing σ-donation to the Ru_2 by the axial ligand. This is consistent with previously reported decreasing HOMO-LUMO gap energy of the α-manifold while changing from Cl to Br to I axial ligand (X) of $[Ru_2(\mu\text{-}O_2CCH_3)_4X_2]^-$ complexes.[21] Similarly, there is fragment contribution by the axial ligands to the π^* MOs but not to the δ HOMO (Figure 4.20) of the β-manifold due to symmetry-aligned π^* overlap between a Ru-based d_{xz} orbital and axial ligand p_x orbital at MO 114β (c.f. Figure 4.10). The π-donation to the Ru atom decreases while changing from the chloride to the bromide to the iodide species as the bond length increases. Hence, the decreasing HOMO-LUMO gap energy of the β-manifold is a result of the stabilization of the π^* MOs with decreasing π-donation to the Ru_2 by the axial ligand.

Contrary to the decrease in the HOMO-LUMO energy gaps, the increase in π^*-δ^* gap energy of the SOMOs stems from the significant fragment contribution of the axial ligands to the π^* MOs but not the δ^* MO (Figure 4.20) due to the symmetry-aligned π^* overlap of a Ru-based d_{xz} (and d_{yz}) orbital with axial ligand p_x (and p_y) orbital at MO 114β (and 115β) (c.f. Figure 4.10). Although the axial ligand fragment contribution to the π^* MOs is increasing while changing from chloride to bromide to iodide, the π-donation should in principle decrease in the same direction due to the increasing bond length. Hence, the increasing π^*-δ^* gap energy of the SOMO when going from the chloride to the bromide species is a result of the stabilization of the π^* MOs with decreasing π-donation to the Ru_2 by the axial ligand. This decrease is consistent with what was discussed before (c.f. Figure 1.5). However, the decrease in the π^*-δ^* gap energy when changing from the chloride or bromide to iodide is peculiar, especially when considering that the corresponding electronic structure of the anionic $[Ru_2(\mu\text{-}O_2CCH_3)_3(\mu\text{-}2\text{-}Fap)I_2]^-$ species, which shows the expected increase the π^*-δ^* gap energy when changing from the chloride or bromide to iodide anionic species (Figure 4.21).

The electronic structure of the anionic species exhibits the expected energy gap trends (Figure 4.21) that were determined while varying from cationic to neutral to anionic (see Figure 4.17), such as the decrease in both the α-manifold and β-manifold HOMO-LUMO energy gap and the increase in the increase in the π^*-δ^* gap energy. In addition, in the anionic species, the order of the α-manifold also remains the same as what was discussed for the neutral and cationic, irrespective of the axial ligand.

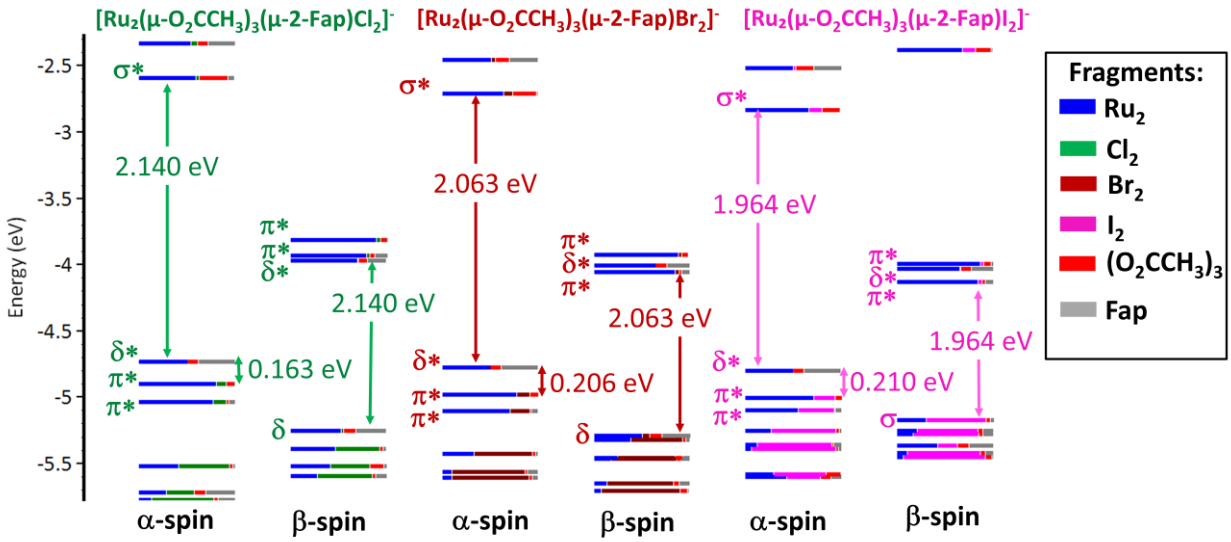

Figure 4.21 Electronic structure calculations of the $[Ru_2(\mu\text{-}O_2CCH_3)_3(\mu\text{-}2\text{-}Fap)X_2]^-$ where X is Cl (green), Br (brown) and I (pink) complexes in water obtained at the PBE/LANL2DZ-IEFPCM level of theory.

Furthermore, the order of the β-manifold LUMO, LUMO-1 and LUMO-2 changes from $\pi^*>\pi^*>\delta^*$ to $\pi^*>\delta^*>\pi^*$ (Figure 4.20) while moving from the chloride- to bromide- or iodide-containing species, which is consistent with the decreasing π-donation to the Ru atom and stabilization of the π^* MOs that was proposed for the neutral and cationic species to be responsible for the changing MOs order. A notable unique feature exhibited by the anionic species, $[Ru_2(\mu\text{-}O_2CCH_3)_3(\mu\text{-}2\text{-}Fap)I_2]^-$, is a σ HOMO of the β-manifold, instead of a δ HOMO that is present in the anionic bromide or chloride species as well as all the neutral and the cationic species. This σ HOMO has been reported before for the $[Ru_2(\mu\text{-}O_2CCH_3)_4X_2]^-$ (X=Cl, Br or I) analogue but not for mixed ligands.[21]

Monitoring the axial ligand substitution reactions of Ru_2 complexes spectroscopically by observing the changes in the wavelength of maximum absorption (Δ_{abs}) which are sensitive to

the nature of the axial ligand is a technique that is used in numerous studies to estimate and compare the thermodynamic axial ligand binding constant.[27, 28, 57, 58, 260-262] Given the interest of this study in correlating spectroscopic changes with specific molecular properties, the predicted excitation energy as a function of the type of axial ligand are considered.

The most intense LMCT found at band 1 and the charge transfer containing $\delta(Ru_2) \rightarrow \delta^*(Ru_2)$ transition at band 3, abbreviated MICT and $\delta \rightarrow \delta^*$ CT, respectively in Table 4.13, are red-shifted when going from chloride to bromide to iodide.

Table 4.13 The $\delta \rightarrow \delta^*$ charge transfer (CT) and the most intense CT (MICT) excitation wavelength of the $Ru_2(\mu\text{-}O_2CCH_3)_3(\mu\text{-}2\text{-}Fap)X$, $[Ru_2(\mu\text{-}O_2CCH_3)_3(\mu\text{-}2\text{-}Fap)X_2]^-$ and $[Ru_2(\mu\text{-}O_2CCH_3)_4X_2]^-$ complexes (X = Cl, Br, I) computed using the PBE/LANL2DZ-IEFPCM in water

Complex	$\delta \rightarrow \delta^*$ CT (nm)	MICT (nm)
$Ru_2(\mu\text{-}O_2CCH_3)_3(\mu\text{-}2\text{-}Fap)Cl$	843.44	268.45
$Ru_2(\mu\text{-}O_2CCH_3)_3(\mu\text{-}2\text{-}Fap)Br$	852.93	302.11
$Ru_2(\mu\text{-}O_2CCH_3)_3(\mu\text{-}2\text{-}Fap)I$	897.24	331.84
$[Ru_2(\mu\text{-}O_2CCH_3)_3(\mu\text{-}2\text{-}Fap)Cl_2]^-$	873.98	264.97
$[Ru_2(\mu\text{-}O_2CCH_3)_3(\mu\text{-}2\text{-}Fap)Br_2]^-$	896.72	316.11
$[Ru_2(\mu\text{-}O_2CCH_3)_3(\mu\text{-}2\text{-}Fap)I_2]^-$	954.45	346.58
$[Ru_2(\mu\text{-}O_2CCH_3)_4Cl_2]^-$	681.70	264.97
$[Ru_2(\mu\text{-}O_2CCH_3)_4Br_2]^-$	752.04	316.11
$[Ru_2(\mu\text{-}O_2CCH_3)_4I_2]^-$	871.24	346.58

The red-shift of the MICT is in agreement with the easily observable red-shift of band 1 in the measure spectra (Figure 4.19) when going from the chloride to the iodide complex, which suggests that changes in the λ_{max} of band 1 are indicative of altered axial coordination and the higher the wavelength λ_{max} of band 1 the longer the Ru-X bond length. Indeed, the clear red-shift of the $\delta \rightarrow \delta^*$ CT implies a decreasing δ-δ^* energy gap, which is concomitant with increasing π-δ^* energy gap and thus shift of $\delta \rightarrow \delta^*$ transitions to lower energy when going along the Cl - Br - I series. However, band 4 in the measured spectra is weakly sensitive to the axial ligand and it is not observable in some Ru_2 complexes such as the Ru_2 tetracarboxylates due to very weak intensity, band 4 is therefore not a suitable experimental diagnostic tool for

estimating the axial binding in this series but it has been reported to sensitivity to the nature bridging ligand.

Nonetheless, the δ → δ* CT character is predicted in all the complexes including the Ru_2 tetracarboxylates, with the red-shift trend still holding. This suggests that both MICT and δ → δ* CT can be used to theoretically estimate the relative axial coordination bond length. Indeed, a linear relationship between the wavelengths of MICT and δ → δ* CT is established (Figure 4.22), which shows that there is a good correlation between the MICT and δ → δ* CT and the Van der Waals radii (R_{VDW}) of the axial ligands.[263]

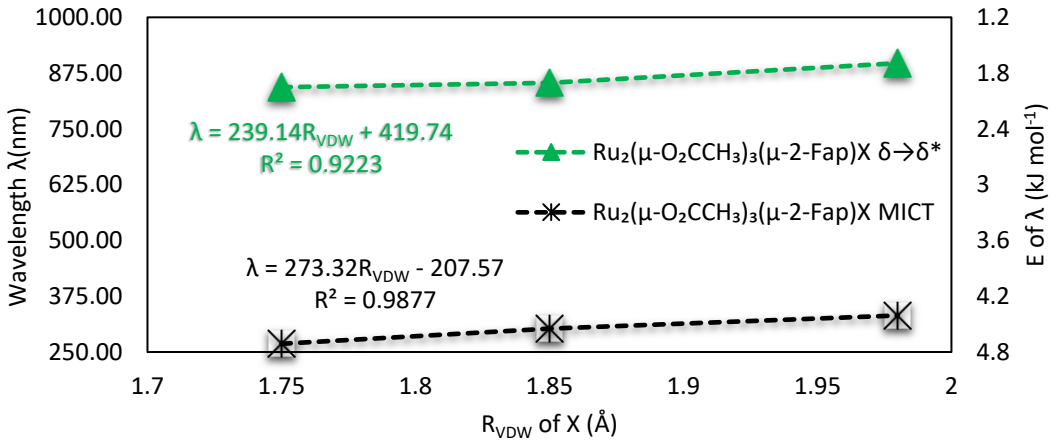

Figure 4.22 The δ → δ* charge(CT) and the most intense CT (MICT) excitation wavelength of the $Ru_2(\mu\text{-}O_2CCH_3)_3(\mu\text{-}2\text{-}Fap)X$, $[Ru_2(\mu\text{-}O_2CCH_3)_3(\mu\text{-}2\text{-}Fap)X_2]^-$ and $[Ru_2(\mu\text{-}O_2CCH_3)_4X_2]^-$ complexes (X = Cl, Br, I) computed using the PBE/LANL2DZ-IEFPCM in water, as a function of R_{VDW} of X.[263]

4.2.4 Solvatochromism

In the previous section, the solvent environment was kept constant while the nature of the axial ligand was allowed to vary, therefore the effect of the solvent was not explored. To investigate the solvent effect, the UV-Vis spectrum of the chlorinated complex $Ru_2(\mu\text{-}O_2CCH_3)_3(\mu\text{-}2\text{-}Fap)Cl$ was simulated in DCM, DMSO and water. When comparing the simulated spectra of the $Ru_2(\mu\text{-}O_2CCH_3)_3(\mu\text{-}2\text{-}Fap)Cl$ complex in water, DMSO and DCM (Figure 4.23), band 3 is the only band that is significantly shifted energetically, which is in agreement

with the reported[47] strong sensitivity of band 3 to the solvent and imply that the observed solvatochromic shift is partly a result of the changing bulk solvent polarity.

The hyperchromic red shift from 638.9 nm to 641.4 nm to 643.5 nm of the primary band at band 3 (λ_{max}) is predicted when switching from the solvation water to DMSO to DCM. Since $Ru_2(\mu\text{-}O_2CCH_3)_3(\mu\text{-}2\text{-}Fap)Cl$ is free of explicit solvent binding the predicted red-shift is directly the result of the bulk solvation polarity, which is dictated by its dielectric constant (ε).

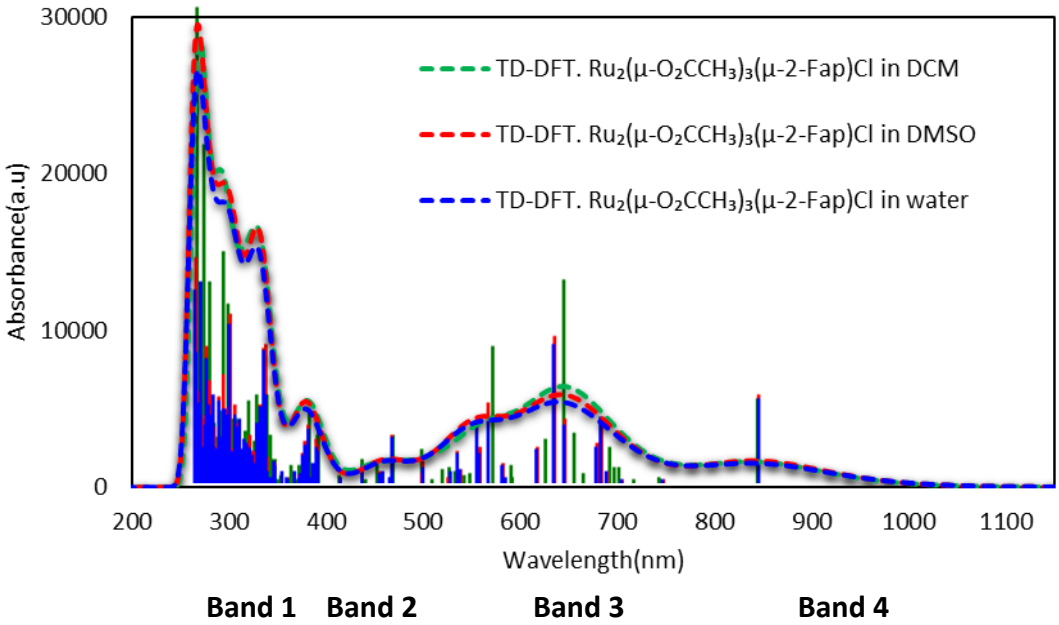

Figure 4.23 Comparison of the simulated (dashed) UV-Vis-NIR curves of $Ru_2(\mu\text{-}O_2CCH_3)_3(\mu\text{-}2\text{-}Fap)Cl$ obtained in DCM (green), DMSO (green) and water (red). Computed at the PBE/LANL2DZ-IEFPCM level of theory

Indeed, the redshift, which is a shift to lower energy, is concomitant with a decrease in the ε value when going from water (ε = 78.355) to DMSO (ε = 46.826) to DCM(ε = 8.930) as shown in the linear correlation obtained by a linear fit of the ε and λ_{max} (Figure 4.24), which indicates that there is a strong relationship between the shift in λ_{max} and the solvent polarity.

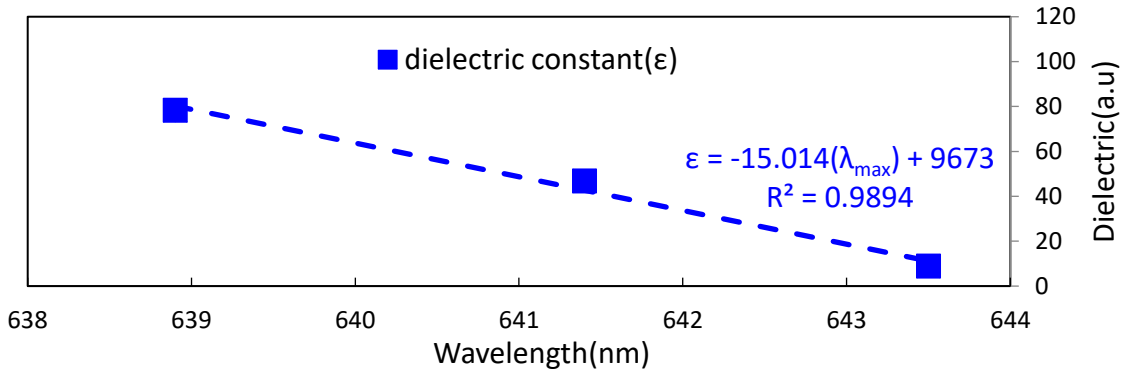

Figure 4.24 The solvent dielectric constant (ε) as a function of the simulated λ_{max}(nm) of band 3 of $Ru_2(\mu\text{-}O_2CCH_3)_3(\mu\text{-}2\text{-}Fap)Cl$.

The observed changes in electronic transitions and the resulting absorption spectrum shifts upon changing the implicit solvation medium from the DCM to DMSO to water can be interpreted in terms of the resulting variation in electronic structure. Consider the electronic structure calculations based on the first excited states of the neutral $Ru_2(\mu\text{-}O_2CCH_3)_3(\mu\text{-}2\text{-}Fap)Cl$ in DCM, DMSO or water, as presented in an open-shell MO diagram (Figure 4.25).

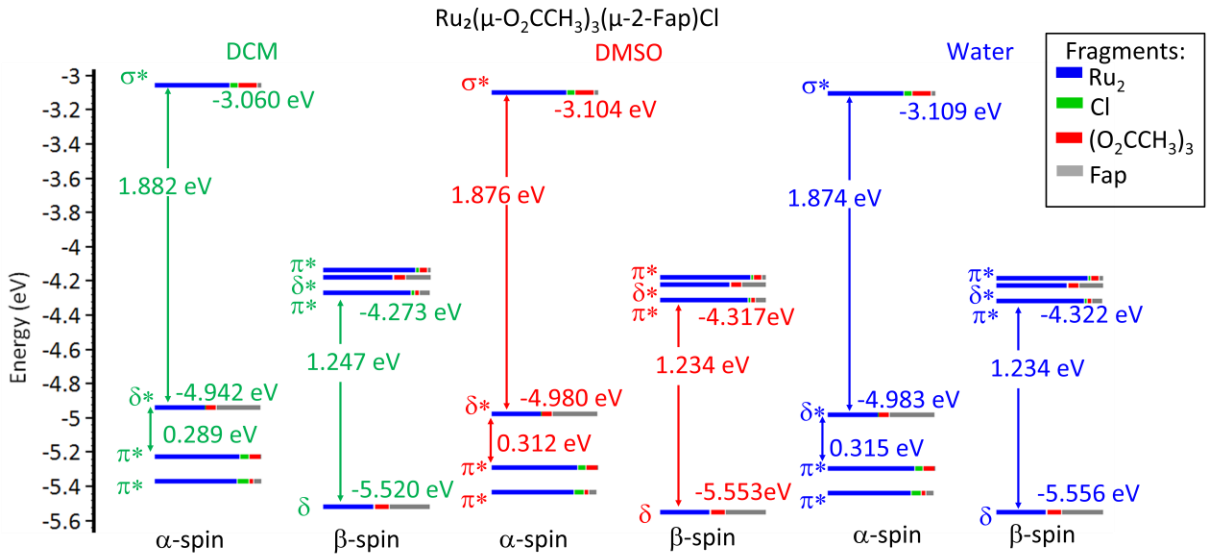

Figure 4.25 Electronic structure calculations of the neutral complex in the water, DCM and DMSO, obtained at the PBE/LANL2DZ-IEFPCM level of theory.

Changing the implicit solvent polarity does not change the order of both the α-manifold and the β-manifold, which was discussed (c.f. section 4.2.1), but MOs all shift towards lower energies

while maintaining their position relative to each other and the HOMO-LUMO and π^*-δ^* gap energies vary. For instance, the HOMO (or LUMO) of both the α-and β-manifold decreases by 0.044 eV (or 0.038 eV) while moving from DCM to DMSO, and decreases by 0.005 eV (or 0.003 eV) while moving from DMSO to water. The HOMO-LUMO gap energy of the α-manifold (or β-manifold) decreases by 0.006 eV (or 0.013 eV) while moving from DCM to DMSO, and decreases by 0.002 eV (or 0.00 eV) while moving from DMSO to water. Similarly, the π^*-δ^* gap energy in the SOMOs increases by 0.023 eV while moving from DCM to DMSO, and further increases by 0.003 eV while moving from DMSO to water.

Following the discussion above, it can be deduced that as the implicit solvent polarity increases the energy of all the MOs is lowered, and the HOMO-LUMO gap energy decreases, whereas the π^*-δ^* gap energy increases. Whilst the solvent dielectric constant presents some variation in the electronic structure, such variation are very small, roughly 1% or less of the gap energy. Hence, the predicted differences in the absorption spectra are minuscule, which is inconsistent with the large shifts observed experimentally while changing the solvents. It is therefore imperative to consider the role of an explicit coordinating solvent in the absorption spectrum. To this end, the UV-Vis spectra in Figure 4.26 illustrate the effect of solvent interaction, approximated as the difference between the $Ru_2(\mu\text{-}O_2CCH_3)_3(\mu\text{-}2\text{-}Fap)(Solv)Cl$ complex which has an explicitly interacting solvent molecule and the $Ru_2(\mu\text{-}O_2CCH_3)_3(\mu\text{-}2\text{-}Fap)Cl$ complex, in addition to the implicit solvation field.

(a)

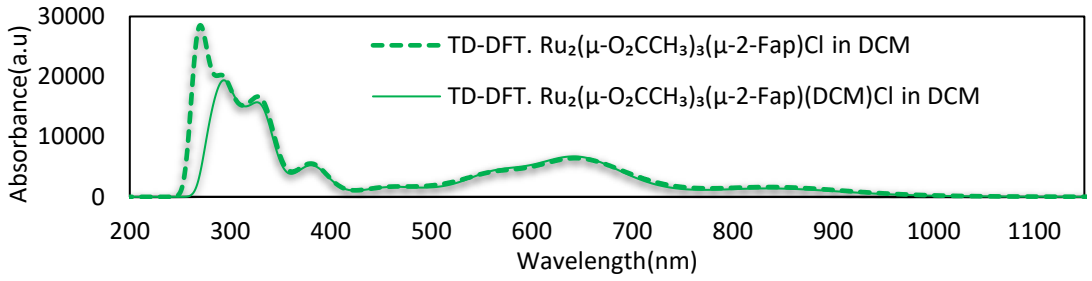

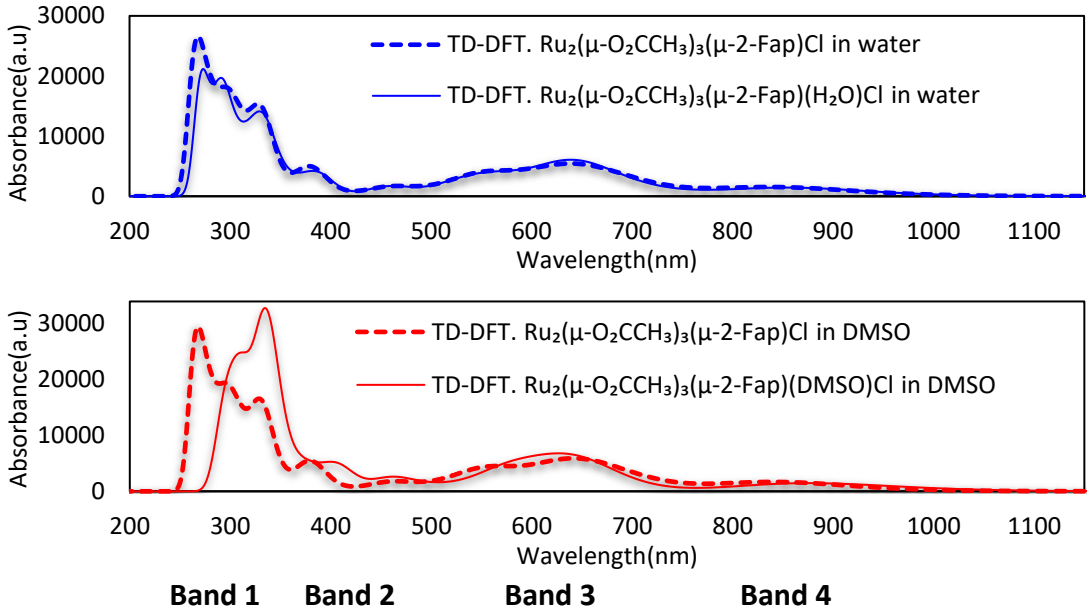

Figure 4.26 Comparison of TD-DFT absorption curve of the solvent-coordinated $Ru_2(\mu\text{-}O_2CCH_3)_3(\mu\text{-}2\text{-}Fap)(Solv)Cl$ (—) and non-coordinated $Ru_2(\mu\text{-}O_2CCH_3)_3(\mu\text{-}2\text{-}Fap)Cl$ (- - -) complexes in DCM (green), water (blue) and DMSO(red).

A strong red-shift of band 1 is predicted when going from $Ru_2(\mu\text{-}O_2CCH_3)_3(\mu\text{-}2\text{-}Fap)Cl$ to $Ru_2(\mu\text{-}O_2CCH_3)_3(\mu\text{-}2\text{-}Fap)(Solv)Cl$ for all the solvents but there is no clear trend concerning the nature of the solvent. Band 3 is also affected by explicit solute-solvent interaction, though to a lesser extent band 1. However, band 3 is blue-shifted in DMSO, red-shifted in DCM and relatively unaffected in water, when switching from $Ru_2(\mu\text{-}O_2CCH_3)_3(\mu\text{-}2\text{-}Fap)Cl$ to $Ru_2(\mu\text{-}O_2CCH_3)_3(\mu\text{-}2\text{-}Fap)(Solv)Cl$ model, which is consistent with the solvent donor number (DN).[264] Indeed, the simulated band 3 λ_{max} value decreases as the solvent DN increases from DCM (DN = 1.0) to water (DN = 18.0) to DMSO (DN =29.8) (Figure 4.27). Since, the DN is a measure of the Lewis basicity of the solvent, which dictates the coordinating strength of the solvent, the results substantiate that the previously reported [47] sensitivity of the band 3 λ_{max} in coordinating solvent partly attributed to solvent coordination at the axial site.

When comparing the simulated spectra of $Ru_2(\mu\text{-}O_2CCH_3)_3(\mu\text{-}2\text{-}Fap)Cl(Solv)$ (Figure 4.28) to those obtained for $Ru_2(\mu\text{-}O_2CCH_3)_3(\mu\text{-}2\text{-}Fap)Cl$ (Figure 4.23) in DCM, DMSO or water, it evident that combining an explicit solvent molecule (Solv) with an implicit solvent environment results in more visible shifts in the spectra as compared to the only having implicit solvent. These more pronounced spectral changes induced by an explicitly coordinating solvent are more consistent

experimental spectra that have been reported before for $Ru_2(\mu\text{-}O_2CCH_3)_3(\mu\text{-}2\text{-}Fap)Cl$, supporting the proposed hypothesis that the measured spectral shift while changing from DMSO to water was caused by coordinating solvents.[47]

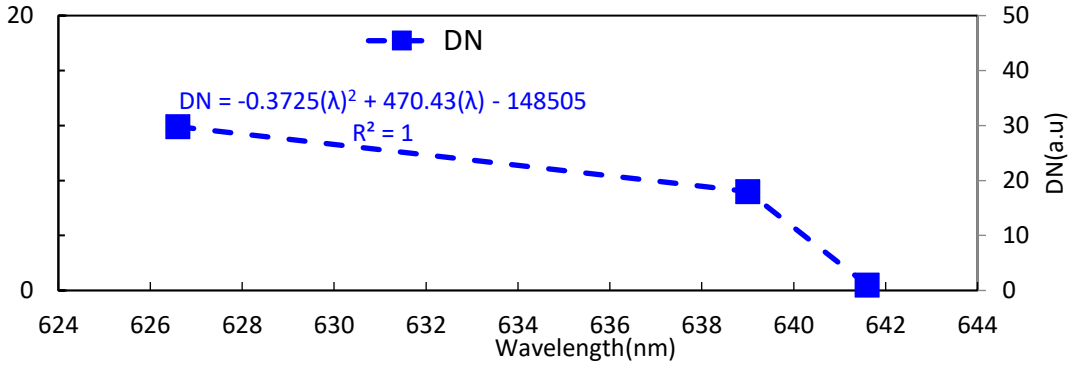

Figure 4.27 The solvent donor number (DN) as a function of the simulated λ_{max}(nm) of band 3 of $Ru_2(\mu\text{-}O_2CCH_3)_3(\mu\text{-}2\text{-}Fap)Cl$.

The evident changes in electronic transitions and the resulting absorption spectrum shifts upon changing the explicit solvent molecule and implicit solvent field from DCM to DMSO to water can be rationalized in terms of the resulting variation in electronic structures.

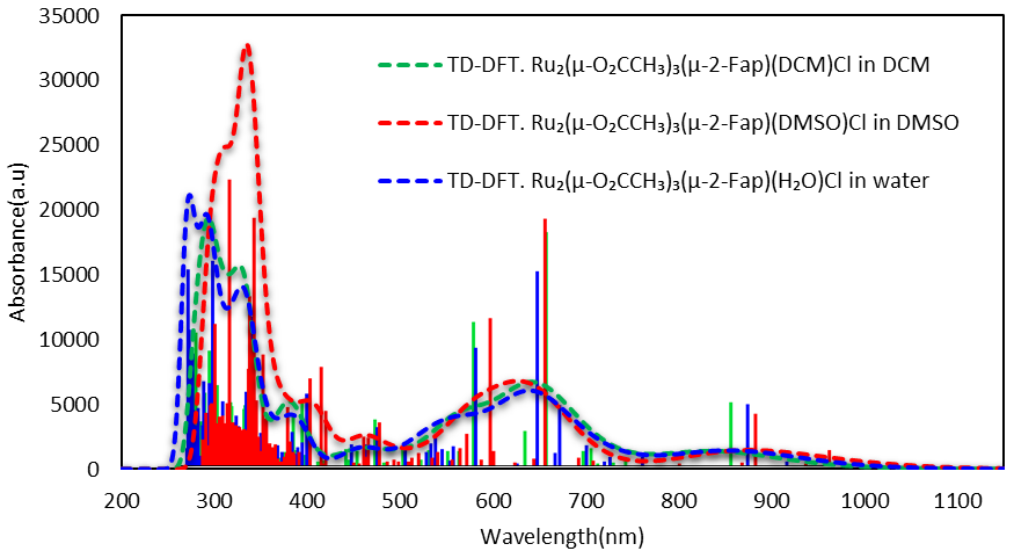

Figure 4.28 Comparison of the simulated (dashed) UV-Vis-NIR curves of $Ru_2(\mu\text{-}O_2CCH_3)_3(\mu\text{-}2\text{-}Fap)Cl$ obtained in DCM (green), DMSO (green) and water (red). Computed at the PBE/LANL2DZ-IEFPCM level of theory

Consider the electronic structure calculations based on the first excited states of the neutral $Ru_2(\mu\text{-}O_2CCH_3)_3(\mu\text{-}2\text{-}Fap)Cl(Solv)$ (Solv=DCM, DMSO or water) as presented in an open-shell MO

diagram (Figure 4.29). Interestingly, changing the explicit solvent molecule polarity does not change the order of both the α-manifold and the β-manifold that was discussed before (c.f. section 4.2.1). This invariability of MO order is similar to the intact MO order observed in Figure 4.25 while changing the implicit solvent only. In contrast to the lowering of all MOs energies with increasing implicit dielectric constant that was seen in Figure 4.25, tuning the DN of the explicitly interacting solvent molecule shifts all the MOs towards higher energies and the HOMO-LUMO and π^*-δ^* gap energies vary substantially.

For instance, the HOMO (or LUMO) of both the α-and β-manifold increases by 0.253 eV (or 0.019 eV) while moving from DCM to water, and increases further by 0.082 eV (or 0.173 eV) while moving from water to DMSO (Figure 4.29). The exhibited increase in the energy of the LUMOs of the α-manifold and β-manifold is due to increasing antibonding interaction between a Ru_2-based σ^* and π^* orbitals and a solvent-based p_z and p_y orbitals, respectively, while moving from DCM to water to DMSO, as evidenced by the more visible Ru-DMSO orbital overlap (Figure 4.29) in comparison to Ru-DCM or Ru-Water interaction. Unexpectedly, there are antibonding interaction at the HOMOs between a Ru_2-based δ^* and δ orbitals and a solvent-based p_x orbitals, respectively, that are not symmetry aligned but destabilization of the HOMOs.

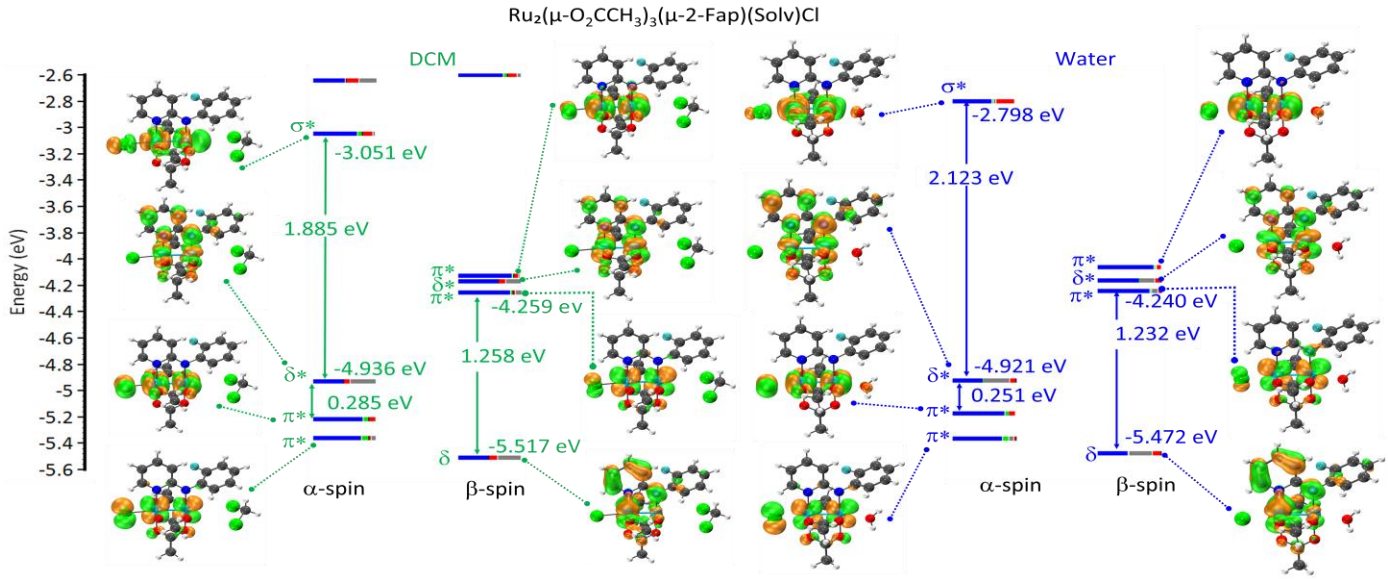

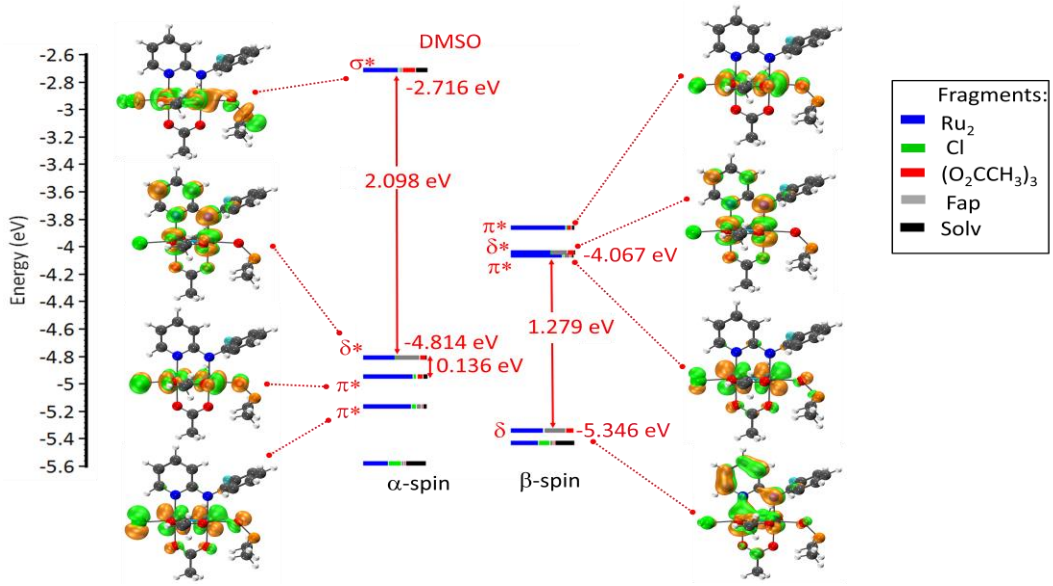

Figure 4.29 Electronic structure calculations of the neutral complex in explicitly bound water, DCM and DMSO solvent obtained at the PBE/LANL2DZ-IEFPCM level of theory.

The HOMO-LUMO gap energy of the α-manifold increases by 0.238 eV while moving from DCM to water, but decreases by 0.025eV while moving from water to DMSO (Figure 4.29). The HOMO-LUMO gap energy of the β-manifold decreases by 0.026 eV while moving from DCM to water, but increases by 0.047eV while moving from the water to DMSO (Figure 4.29). The π^*-δ^* gap energy in the SOMOs decreases by 0.034 eV while moving from DCM to water, and further decreases by 0.115 eV while moving from water to DMSO (Figure 4.29).

The exhibited decrease in the π^*-δ^* gap energy in the SOMOs is due to increasing antibonding interaction between a Ru_2-based π^* MOs and a solvent-based p_x and p_y orbitals, respectively, while moving from DCM to water to DMSO, as evidenced by the more visible Ru-DMSO orbital overlap (Figure 4.29) in comparison to Ru-DCM or Ru-Water interaction. This decrease in π^*-δ^* gap energy with increasing axial solvent donor number is consistent with the decreasing π^*-δ^* gap energy predicted while increasing the lability of the halide from Cl to Br to I.

Following the discussion above, it can be deduced that as the donor number of the explicitly interacting solvent molecule increases from DCM to water to DMSO, the energy of all the MOs increases, the π^*-δ^* gap energy decreases, whereas the HOMO-LUMO gap energy of both the α-manifold and the β-manifold may increase or decrease while the DN number increases.

Whilst the solvent dielectric constant presents a small variation in the electronic structure, the explicit solvent substantially changes the MO energies. Hence, the predicted differences in the absorption spectra are more visible due to an explicitly coordinating solvent, which is consistent with the large shifts observed experimentally while changing the solvents.

The UV-Vis spectra of $Ru_2(\mu\text{-}O_2CCH_3)_3(\mu\text{-}2\text{-}Fap)Cl(Solv)$ in DCM, DMSO and water obtained using TD-DFT together with the corresponding experimental spectra are presented in in Figure 4.30.

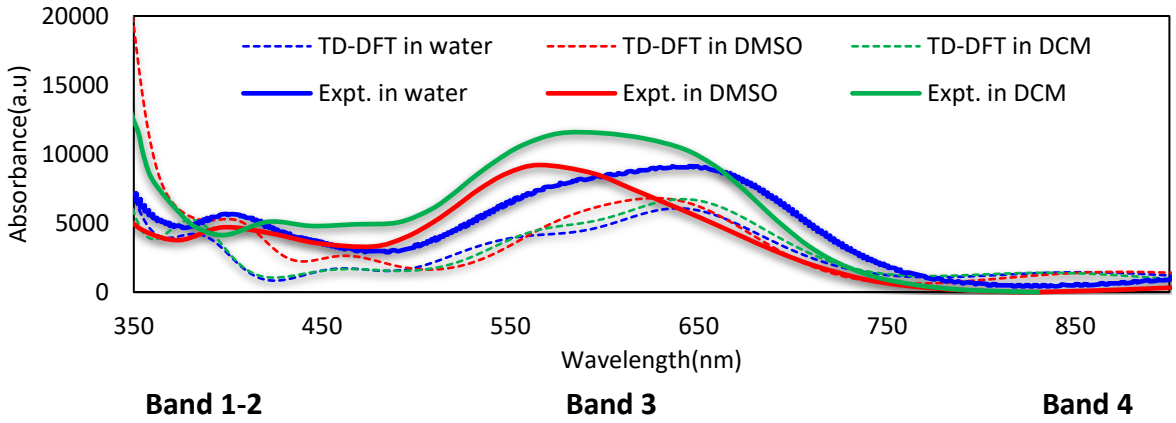

Figure 4.30 Comparison of the simulated (dashed) UV-Vis spectrum of $Ru_2(\mu\text{-}O_2CCH_3)_3(\mu\text{-}2\text{-}Fap)Cl(Solv)$ and experimentally obtained in DCM (green), DMSO (green) and water (red). Computed at the PBE/LANL2DZ. (See Figure 4.12 for Higher wavelengths band and peak)

There is a discrepancy between the predicted and experimental positioning of the shoulder band relative to the primary band of band 3 in both DCM and DMSO solutions. TD-DFT effectively predicted the position of the overall broad band, though not of the individual primary and shoulder band constituents. This deficiency could be due to the inability of TD-DFT calculations performed on solvated ground state to account for all possible solvent effects in real solution.

Chapter 5 Conclusions and future work

The full geometry optimization in the solvated phase and coupling of the UV-Vis prediction to the solvated phase, outperforms full gas-phase prediction and solvated-phase prediction on the basis of gas-phase molecular geometry. The smaller LANL2DZ unexpectedly outperforms the Def2-type basis sets. The best performing functional for TD-DFT analysis was the PBE. The TPSSH was the second-best. CAM-B3LYP had the worst performance. The UV-Vis spectra of $Ru_2(O_2CCH_3)X$ (X=Cl, Br, I) has been successfully re-characterized and the current assignment indicated that almost all excitations had significant mixed ligand and metal characters, except the $\delta(Ru_2) \rightarrow \delta^*(Ru_2)$ transition which only had predominant metal-metal character.

The interpretation of the UV-Vis spectrum of $Ru_2(\mu\text{-}O_2CCH_3)_3(\mu\text{-}2\text{-}Fap)X$ (X=Cl, Br, I) complexes was greatly facilitated by the remarkable agreement between the TD-DFT computational results and the experimental data obtained herein. Band 1 (250 - 350 nm) was characterized by two transitions namely $\delta(Ru_2) \rightarrow \pi^*(N_p,C)$, $\pi(Cl) \rightarrow \pi^*(C_p,N_p)$ and $\pi(Cl) \rightarrow \pi^*(C_a)$. Band 2 (400 - 450 nm) is attributed to $\pi(C_a,N_a)/\delta^*(Ru_2) \rightarrow \pi^*(C_p,N_p$. Band 3 (450 - 750 nm) was characterized by three excitations, which are $\pi(Cl,Ru_2) \rightarrow \delta^*(Ru_2)$, $\delta(Ru_2) \rightarrow \delta^*(Ru_2)$, $\pi(Cl,Ru_2) \rightarrow \pi^*(Ru_2)$, $\pi(F,C_a\text{-}C_a) \rightarrow \pi^*(Ru_2)$, $\pi(Cl) \rightarrow \pi^*(Ru_2)$ and $\pi(Cl,F,C_a\text{-}C_a) \rightarrow \pi^*(Ru_2)$. Band 4 (900 - 1000 nm) was characterized by a single excitation, namely, the $\delta(Ru_2) \rightarrow \delta^*(Ru_2)$ transition.

Deconvolutions of the experimental spectra was successfully performed. Both TD-DFT and deconvolution confirm that band 3 (450-550 nm region) was due to two independent bands. Both the neutral and cationic species possessed a characteristic shoulder and primary bands at band 3. Good agreement of the cumulative fit curve of $Ru_2(\mu\text{-}O_2CCH_3)_3(\mu\text{-}2\text{-}Fap)Cl$ and the experimental curve at band 3, supported the equilibrium between the cationic and neutral species in aqueous solution. The character of the dominant excitations causing band 3 was transformed when going from the neutral and cationic species. The anionic $[Ru_2(\mu\text{-}O_2CCH_3)_3(\mu\text{-}2\text{-}Fap)Cl_2]^-$ is predicted with a narrower band maxima and a single maximum at band 3 and the disappearance of shoulder band was attributed to reduced intensity and shift of vertical some transitions, which resulted in a narrower convoluted band. However, the

anionic species still presents a characteristic shoulder band, which is not observable experimentally under excess transition. Hence, the equilibrium between the anionic and neutral species in varying excess chloride solution was predicted to some extent with the additional information that the shoulder band might still be present but with lower intensity.

Band 1 and band 3 were significantly sensitive the axial ligand and can be used as theoretical basis for using band 1 or band 3 as to predict the Ru-X bond length, hence binding, of different types of axial ligands in a fixed solution. A red-shift of both the MICT at band 1 and the $\delta \rightarrow \delta^*$ CT at band 3 was predicted upon changing from chloride to bromide to iodide, and the good linear correlation between the wavelength of the MICT and $\delta \rightarrow \delta^*$ CT excitations, and the R_{VDW} value. A red-shift of band 1 or band 3 would therefore be indicative of weaker axial binding. Furthermore, band 1, band 2 and band 3 were predicted to be significantly sensitive to the nature of the solvent as evidenced by the predicted solvatochromic shift. The solvatochromic shift were attributed mainly to the solvent coordination at the axially site. Therefore, there is a balance between halide ligand and solvent coordination at the axial site and the nature of both of these species are important in attributing spectroscopic shift to axial ligand coordination.

In future, to assess the effect of such ligands and of varying the Rap substituent and the number of axial ligands on the UV-Vis spectrum, the TD-DFT simulation should be undertaken. Furthermore, a similar study to develop a theoretical framework for interpreting the electrochemical and vibrational spectroscopic behavior of these complexes should be carried out. Similar TD-DFT calculations can also be undertaken to evaluate the characteristics of a larger range of axial ligands including larger, non-halogen axial ligands such as potential biological or catalytic nucleophiles.

References

1. P. C. Bruijnincx and P. J. Sadler, *Curr. Opin. Chem. Biol.*, 2008, **12**, 197-206.
2. A. Terán, G. Ferraro, P. Imbimbo, A. E. Sánchez-Peláez, D. M. Monti, S. Herrero and A. Merlino, *Int. J. Biol. Macromol.*, 2023, **253**, 126666.
3. G. Gasser and N. Metzler-Nolte, *Curr. Opin. Chem. Biol.*, 2012, **16**, 84-91.
4. S. de Doncker, E. Fischer-Fodor, C. I. Vlad, P. Achimas-Cadariu, G. S. Smith and S. Ngubane, *Molecules*, 2023, **28**, 2671.
5. C. B. T. T. Medupe, N. Autar, S. Siangwata, J. Mutomb, G.A Venter, S. Prince and S. Ngubane., *J Biol Inorg Chem*, Unpublished.
6. T. T. M. N. Autar, S. Siangwata, J. Mutomb, G.A. Venter, S. Prince and S. Ngubane., *Dalton Trans.*, Unpublished.
7. J. G. Norman Jr, G. E. Renzoni and D. A. Case, *J. Am. Chem. Soc.*, 1979, **101**, 5256-5267.
8. F. A. Cotton, C. A. Murillo and R. A. Walton, *Multiple bonds between metal atoms*, Springer Science & Business Media, 2005.
9. J. G. Norman and H. J. Kolari, *J. Chem. Soc., Chem. Commun.*, 1975, 649-651.
10. J. G. Norman, H. J. Kolari, H. B. Gray and W. C. Trogler, *Inorg. Chem.*, 1977, **16**, 987-993.
11. J. G. Norman Jr and H. J. Kolari, *J. Am. Chem. Soc.*, 1978, **100**, 791-799.
12. T. A. Stephenson and G. Wilkinson, *Journal of Inorganic and Nuclear Chemistry*, 1966, **28**, 2285-2291.
13. T. E. Hopkins, A. Zalkin, D. H. Templeton and M. G. Adamson, *Inorg. Chem.*, 1966, **5**, 1427-1431.
14. K. M. Kadish, M. Nguyen, E. Van Caemelbecke and J. L. Bear, *Inorg. Chem.*, 2006, **45**, 5996-6003.
15. K. M. Kadish, T. D. Phan, L. Giribabu, E. Van Caemelbecke and J. L. Bear, *Inorg. Chem.*, 2003, **42**, 8663-8673.
16. J. L. Bear, Y. Li, B. Han, E. Van Caemelbecke and K. M. Kadish, *Inorg. Chem.*, 1997, **36**, 5449-5456.
17. S. Ngubane, K. M. Kadish, J. L. Bear, E. Van Caemelbecke, A. Thuriere and K. P. Ramirez, *Dalton Trans.*, 2013, **42**, 3571-3580.
18. M. J. Bennett, K. G. Caulton and F. A. Cotton, *Inorg. Chem.*, 1969, **8**, 1-6.
19. M. Mikuriya, D. Yoshioka and M. Handa, *Coord. Chem. Rev.*, 2006, **250**, 2194-2211.
20. M. A. Aquino, *Coord. Chem. Rev.*, 1998, **170**, 141-202.
21. M. A. Castro, A. E. Roitberg and F. D. Cukiernik, *Inorg. Chem.*, 2008, **47**, 4682-4690.
22. M. C. Barral, R. Gonzalez-Prieto, S. Herrero, R. Jimenez-Aparicio, J. L. Priego, M. R. Torres and F. A. Urbanos, *Polyhedron*, 2005, **24**, 239-247.
23. F. D. Cukiernik, D. Luneau, J.-C. Marchon and P. Maldivi, *Inorg. Chem.*, 1998, **37**, 3698-3704.
24. M. C. Barral, R. González-Prieto, R. Jiménez-Aparicio, J. L. Priego, M. R. Torres and Francisco A. Urbanos, *Eur. J. Inorg. Chem.*, 2003, **2003**, 2339-2347.
25. F. D. Cukiernik, M. Ibn-Elhaj, Z. D. Chaia, J.-C. Marchon, A.-M. Giroud-Godquin, D. Guillon, A. Skoulios and P. Maldivi, *Chem. Mater.*, 1998, **10**, 83-91.

26. A. Bino, F. A. Cotton and T. R. Felthouse, *Inorg. Chem.*, 1979, **18**, 2599-2604.
27. V. M. Miskowski, T. M. Loehr and H. B. Gray, *Inorg. Chem.*, 1987, **26**, 1098-1108.
28. D. S. Martin, R. A. Newman and L. M. Vlasnik, *Inorg. Chem.*, 1980, **19**, 3404-3407.
29. M. Barral, R. Jiménez-Aparicio, D. Pérez-Quintanilla, J. Priego, E. Royer, M. Torres and F. Urbanos, *Inorg. Chem.*, 2000, **39**, 65-70.
30. T. Togano, M. Mukaida and T. Nomura, *Bull. Chem. Soc. Jpn.*, 1980, **53**, 2085-2086.
31. B. K. Das and A. R. Chakravarty, *Polyhedron*, 1991, **10**, 491-494.
32. M. Abe, Y. Sasaki, T. Yamaguchi and T. Ito, *Bull. Chem. Soc. Jpn.*, 1992, **65**, 1585-1590.
33. M. McCann, A. Carvill, P. Guinan, P. Higgins, J. Campbell, H. Ryan, M. Walsh, G. Ferguson and J. Gallagher, *Polyhedron*, 1991, **10**, 2273-2281.
34. M. C. Barral, R. González-Prieto, R. Jiménez-Aparicio, J. L. Priego, M. R. Torres and F. A. Urbanos, *Eur. J. Inorg. Chem.*, 2004, **2004**, 4491-4501.
35. K. D. Drysdale, E. J. Beck, T. S. Cameron, K. N. Robertson and M. A. Aquino, *Inorg. Chim. Acta*, 1997, **256**, 243-252.
36. F. A. Cotton, Y. Kim and T. Ren, *Polyhedron*, 1993, **12**, 607-611.
37. F. A. Cotton and E. Pedersen, *Inorg. Chem.*, 1975, **14**, 388-391.
38. J. G. Norman, G. E. Renzoni and D. A. Case, *J. Am. Chem. Soc.*, 1979, **101**, 5256-5267.
39. G. M. Chiarella, F. A. Cotton, C. A. Murillo, K. Ventura, D. Villagrán and X. Wang, *J. Am. Chem. Soc.*, 2014, **136**, 9580-9589.
40. M. d. C. Barral, R. González-Prieto, S. Herrero, R. Jiménez-Aparicio, J. L. Priego, E. d. C. Royer, M. R. Torres, F. A. Urbanos and F. Zamora, *J. Cluster Sci.*, 2008, **19**, 219-230.
41. M. C. Barral, D. Casanova, S. Herrero, R. Jiménez-Aparicio, M. R. Torres and F. A. Urbanos, *Chem. Eur. J.*, 2010, **16**, 6203-6211.
42. T. Malinski, D. Chang, F. Feldmann, J. Bear and K. Kadish, *Inorg. Chem.*, 1983, **22**, 3225-3233.
43. K. M. Kadish, R. Garcia, T. Phan, J. Wellhoff, E. Van Caemelbecke and J. L. Bear, *Inorg. Chem.*, 2008, **47**, 11423-11428.
44. K. M. Kadish, L. L. Wang, A. Thuriere, E. Van Caemelbecke and J. L. Bear, *Inorg. Chem.*, 2003, **42**, 834-843.
45. A. R. Chakravarty, F. A. Cotton, D. A. Tocher and J. H. Tocher, *Organometallics*, 1985, **4**, 8-13.
46. F. Cotton and A. Yokochi, *Inorg. Chem.*, 1998, **37**, 2723-2728.
47. W. R. Osterloh, G. Galindo, M. J. Yates, E. Van Caemelbecke and K. M. Kadish, *Inorg. Chem.*, 2020, **59**, 584-594.
48. P. Angaridis, F. A. Cotton, C. A. Murillo, D. Villagrán and X. Wang, *Inorg. Chem.*, 2004, **43**, 8290-8300.
49. J. P. Collin, A. Jouaiti, J. P. Sauvage, W. C. Kaska, M. A. McLoughlin, N. L. Keder, W. T. Harrison and G. D. Stucky, *Inorg. Chem.*, 1990, **29**, 2238-2241.
50. M. Mintert and W. S. Sheldrick, *Inorg. Chim. Acta*, 1995, **236**, 13-20.
51. H. Miyasaka, C. Kachi-Terajima, T. Ishii and M. Yamashita, *J. Chem. Soc., Dalton Trans.*, 2001, 1929-1930.
52. H. Miyasaka, T. Izawa, K.-i. Sugiura and M. Yamashita, *Inorg. Chem.*, 2003, **42**, 7683-7690.

53. M. Ebihara, N. Nagaya, N. Kawashima and T. Kawamura, *Inorg. Chim. Acta*, 2003, **351**, 305-310.
54. F. A. Cotton, Y. Kim and T. Ren, *Inorg. Chem.*, 1992, **31**, 2723-2726.
55. C. Wilson and H. Taube, *Inorg. Chem.*, 1975, **14**, 2276-2279.
56. R. J. Clark and M. L. Franks, *J. Chem. Soc., Dalton Trans.*, 1976, 1825-1828.
57. V. M. Miskowski and H. B. Gray, *Inorg. Chem.*, 1988, **27**, 2501-2506.
58. R. J. Clark and L. T. Ferris, *Inorg. Chem.*, 1981, **20**, 2759-2766.
59. W. C. Trogler and H. B. Gray, *Acc. Chem. Res.*, 1978, **11**, 232-239.
60. J. C. Slater, *Phys. Rev.*, 1951, **81**, 385.
61. A. R. Chakravarty, F. A. Cotton and D. A. Tocher, *Inorg. Chem.*, 1985, **24**, 172-177.
62. A. R. Chakravarty and F. A. Cotton, *Inorg. Chim. Acta*, 1986, **113**, 19-26.
63. A. R. Corcos, M. D. Roy, M. M. Killian, S. Dillon, T. C. Brunold and J. F. Berry, *Inorg. Chem.*, 2017, **56**, 14662-14670.
64. T. Ren, *Organometallics*, 2002, **21**, 732-738.
65. G.-L. Xu, C.-Y. Wang, Y.-H. Ni, T. G. Goodson and T. Ren, *Organometallics*, 2005, **24**, 3247-3254.
66. S. P. Cummings, Z. Cao, C. W. Liskey, A. R. Geanes, P. E. Fanwick, K. M. Hassell and T. Ren, *Organometallics*, 2010, **29**, 2783-2788.
67. G. Zou, J. C. Alvarez and T. Ren, *J. Organomet. Chem.*, 2000, **596**, 152-158.
68. G. Xu and T. Ren, *Organometallics*, 2001, **20**, 2400-2404.
69. L. Zhang, B. Xi, I. Po-Chun Liu, M. Choudhuri, R. J. Crutchley, J. B. Updegraff, J. D. Protasiewicz and T. Ren, *Inorg. Chem.*, 2009, **48**, 5187-5194.
70. W. P. Forrest, M. M. Choudhuri, S. M. Kilyanek, S. N. Natoli, B. M. Prentice, P. E. Fanwick, R. J. Crutchley and T. Ren, *Inorg. Chem.*, 2015, **54**, 7645-7652.
71. M. Manowong, B. Han, T. R. McAloon, J. Shao, I. A. Guzei, S. Ngubane, E. Van Caemelbecke, J. L. Bear and K. M. Kadish, *Inorg. Chem.*, 2014, **53**, 7416-7428.
72. J. L. Bear, J. Wellhoff, G. Royal, E. V. Caemelbecke, S. Eapen and K. M. Kadish, *Inorg. Chem.*, 2001, **40**, 2282-2286.
73. T. Ren, *Coord. Chem. Rev.*, 1998, **175**, 43-58.
74. E. Schrödinger, *Phys. Rev.*, 1926, **28**, 1049-1070.
75. L. de Broglie, Migration - université en cours d'affectation, 1924.
76. A. Szabo and N. Ostlund, *Journal*, 1982.
77. C. J. Cramer, *Essentials of computational chemistry: theories and models*, John Wiley & Sons, 2013.
78. M. Born and R. Oppenheimer, *Annalen der Physik*, 1927, **389**, 457-484.
79. J. C. Slater, *Phys. Rev.*, 1929, **34**, 1293-1322.
80. F. Jensen, *Introduction to computational chemistry*, John wiley & sons, 2017.
81. W. Koch and M. C. Holthausen, *A chemist's guide to density functional theory*, John Wiley & Sons, 2015.
82. J. C. Slater, *Phys. Rev.*, 1951, **81**, 385-390.
83. J. P. Perdew and A. Zunger, *Phys. Rev. B*, 1981, **23**, 5048.
84. S. Kümmel and J. P. Perdew, *Mol. Phys.*, 2003, **101**, 1363-1368.
85. P. Hohenberg and W. Kohn, *Phys. Rev.*, 1964, **136**, B864-B871.
86. W. Kohn and L. J. Sham, *Phys. Rev.*, 1965, **140**, A1133-A1138.

87. J. Harris, *Phys. Rev. B*, 1985, **31**, 1770.
88. J. P. Perdew, A. Ruzsinszky, J. M. Tao, V. N. Staroverov, G. E. Scuseria and G. I. Csonka, *J. Chem. Phys.*, 2005, **123**.
89. J. P. Perdew and K. Schmidt, 2001.
90. P. A. Dirac, 1930.
91. D. M. Ceperley and B. J. Alder, *Phys. Rev. Lett.*, 1980, **45**, 566.
92. S. H. Vosko, L. Wilk and M. Nusair, *Can. J. Phys.*, 1980, **58**, 1200-1211.
93. J. Perdew, E. McMullen and A. Zunger, *Phys. Rev. A*, 1981, **23**, 2785.
94. J. P. Perdew and Y. Wang, *Phys. Rev. B*, 1992, **45**, 13244.
95. L. A. Eriksson, L. G. Pettersson, P. E. Siegbahn and U. Wahlgren, *J. Chem. Phys.*, 1995, **102**, 872-878.
96. C. Adamo, M. Ernzerhof and G. E. Scuseria, *J. Chem. Phys.*, 2000, **112**, 2643-2649.
97. S. Kurth, J. P. Perdew and P. Blaha, *Int. J. Quantum Chem.*, 1999, **75**, 889-909.
98. T. Sperger, I. A. Sanhueza, I. Kalvet and F. Schoenebeck, *Chem. Rev.*, 2015, **115**, 9532-9586.
99. T. Ziegler, *Chem. Rev.*, 1991, **91**, 651-667.
100. J. P. Perdew, *Phys. Rev. B*, 1986, **34**, 7406.
101. J. P. Perdew and W. Yue, *Phys. Rev. B*, 1986, **33**, 8800.
102. J. P. Perdew and Y. Wang, *Phys. Rev. B*, 1992, **45**, 13244-13249.
103. J. P. Perdew, K. Burke and M. Ernzerhof, *Phys. Rev. Lett.*, 1996, **77**, 3865-3868.
104. Y. Zhang and W. Yang, *Phys. Rev. Lett.*, 1998, **80**, 890.
105. J. P. Perdew, S. Kurth, A. Zupan and P. Blaha, *Phys. Rev. Lett.*, 1999, **82**, 2544.
106. J. P. Perdew, J. A. Chevary, S. H. Vosko, K. A. Jackson, M. R. Pederson, D. J. Singh and C. Fiolhais, *Phys. Rev. B*, 1992, **46**, 6671.
107. C. Bowen, G. Sugiyama and B. J. Alder, *Phys. Rev. B*, 1994, **50**, 14838-14848.
108. S. Moroni, D. M. Ceperley and G. Senatore, *Phys. Rev. Lett.*, 1995, **75**, 689-692.
109. E. H. Lieb and S. Oxford, *Int. J. Quantum Chem.*, 1981, **19**, 427-439.
110. F. Neese, T. Schwabe and S. Grimme, *J. Chem. Phys.*, 2007, **126**, 124115.
111. A. D. Becke, *Phys. Rev. A*, 1988, **38**, 3098.
112. C. v. Weizsäcker, *Z. Phys.*, 1935, **96**, 431-458.
113. J. Tao, J. P. Perdew, V. N. Staroverov and G. E. Scuseria, *Phys. Rev. Lett.*, 2003, **91**, 146401.
114. A. D. Becke, *J. Chem. Phys.*, 1993, **98**, 1372-1377.
115. C. Adamo and V. Barone, *J. Chem. Phys.*, 1999, **110**, 6158-6170.
116. M. Ernzerhof and G. E. Scuseria, *J. Chem. Phys.*, 1999, **110**, 5029-5036.
117. K. Kim and K. Jordan, *J. Phys. Chem.*, 1994, **98**, 10089-10094.
118. P. J. Stephens, F. J. Devlin, C. F. Chabalowski and M. J. Frisch, *J. Phys. Chem.*, 1994, **98**, 11623-11627.
119. V. N. Staroverov, G. E. Scuseria, J. Tao and J. P. Perdew, *J. Chem. Phys.*, 2003, **119**, 12129-12137.
120. Y. Zhao and D. G. Truhlar, *J. Phys. Chem. A*, 2005, **109**, 5656-5667.
121. H. Iikura, T. Tsuneda, T. Yanai and K. Hirao, *J. Chem. Phys.*, 2001, **115**, 3540-3544.
122. T. Yanai, D. P. Tew and N. C. Handy, *Chem. Phys. Lett.*, 2004, **393**, 51-57.
123. O. A. Vydrov and G. E. Scuseria, *J. Chem. Phys.*, 2006, **125**, 234109.

124. J.-D. Chai and M. Head-Gordon, *J. Chem. Phys.*, 2009, **131**, 174105.
125. S. Grimme, *J. Chem. Phys.*, 2006, **124**, 034108.
126. A. Tarnopolsky, A. Karton, R. Sertchook, D. Vuzman and J. M. Martin, *J. Phys. Chem. A*, 2008, **112**, 3-8.
127. Y. Zhang, X. Xu and W. A. Goddard III, *Proc. Natl. Acad. Sci.*, 2009, **106**, 4963-4968.
128. C. Møller and M. S. Plesset, *Phys. Rev.*, 1934, **46**, 618-622.
129. E. Brémond and C. Adamo, *J. Chem. Phys.*, 2011, **135**, 024106.
130. J. Toulouse, K. Sharkas, E. Brémond and C. Adamo, *J. Chem. Phys.*, 2011, **135**, 101102.
131. A. Görling and M. Levy, *Phys. Rev. B*, 1993, **47**, 13105.
132. I. Ema, J. Garcia De La Vega, G. Ramírez, R. López, J. Fernández Rico, H. Meissner and J. Paldus, *J. Comput. Chem.*, 2003, **24**, 859-868.
133. R. Ditchfield, W. J. Hehre and J. A. Pople, *J. Chem. Phys.*, 1971, **54**, 724-728.
134. J. S. Binkley, J. A. Pople and W. J. Hehre, *J. Am. Chem. Soc.*, 1980, **102**, 939-947.
135. M. J. Frisch, J. A. Pople and J. S. Binkley, *J. Chem. Phys.*, 1984, **80**, 3265-3269.
136. M. M. Francl, W. J. Pietro, W. J. Hehre, J. S. Binkley, M. S. Gordon, D. J. DeFrees and J. A. Pople, *J. Chem. Phys.*, 1982, **77**, 3654-3665.
137. P. Pyykko, *Chem. Rev.*, 1988, **88**, 563-594.
138. P. Pyykko and J. P. Desclaux, *Acc. Chem. Res.*, 1979, **12**, 276-281.
139. M. S. Gordon and T. R. Cundari, *Coord. Chem. Rev.*, 1996, **147**, 87-115.
140. M. J. Lopez, I. Cabria and J. A. Alonso, *J. Phys. Chem. C*, 2014, **118**, 5081-5090.
141. L. R. Kahn and W. A. Goddard III, *J. Chem. Phys.*, 1972, **56**, 2685-2701.
142. P. J. Hay and W. R. Wadt, *J. Chem. Phys.*, 1985, **82**, 299-310.
143. D. Andrae, U. Haeussermann, M. Dolg, H. Stoll and H. Preuss, *Theor. Chim. Acta*, 1990, **77**, 123-141.
144. R. Flores-Moreno, R. J. Alvarez-Mendez, A. Vela and A. M. Köster, *J. Comput. Chem.*, 2006, **27**, 1009-1019.
145. F. Weigend and R. Ahlrichs, *Phys. Chem. Chem. Phys.*, 2005, **7**, 3297-3305.
146. A. Schäfer, H. Horn and R. Ahlrichs, *J. Chem. Phys.*, 1992, **97**, 2571-2577.
147. J. I. Martinez, A. Castro, A. Rubio and J. Alonso, *J. Chem. Phys.*, 2006, **125**, 074311.
148. D. Kuter, G. A. Venter, K. J. Naidoo and T. J. Egan, *Inorg. Chem.*, 2012, **51**, 10233-10250.
149. I. Tavernelli, B. F. Curchod and U. Rothlisberger, *Chem. Phys.*, 2011, **391**, 101-109.
150. H. Li, T. T. Sun, C. Zhang, L. Liu, D. Zhao and Z. Yang, *Chin. J. Chem.*, 2017, **35**, 354-362.
151. O. V. Sizova, L. Skripnikov, A. Y. Sokolov and N. Ivanova, *Russ. J. Coord. Chem.*, 2007, **33**, 588-593.
152. M. A. Khan, J. Iqbal, M. Ilyas, A. R. Ayub, Y. Zhu and H. Li, *RSC Adv.*, 2022, **12**, 6336-6346.
153. R. Z. Khaliullin, A. T. Bell and M. Head-Gordon, *J. Chem. Phys.*, 2008, **128**, 184112.
154. J. Klein, H. Khartabil, J.-C. Boisson, J. Contreras-García, J.-P. Piquemal and E. Hénon, *J. Phys. Chem. A*, 2020, **124**, 1850-1860.
155. I. Tolbatov, T. Marzo, C. Coletti, D. La Mendola, L. Storchi, N. Re and A. Marrone, *J. Inorg. Biochem.*, 2021, **223**, 111533.
156. T. H. Dunning Jr and P. J. Hay, in *Methods of electronic structure theory*, Springer, 1977, pp. 1-27.
157. A. Dreuw and M. Head-Gordon, *Chem. Rev.*, 2005, **105**, 4009-4037.

158. L. Ordronneau, V. Aubert, V. Guerchais, A. Boucekkine, H. Le Bozec, A. Singh, I. Ledoux and D. Jacquemin, *Chem. Eur. J.*, 2013, **19**, 5845-5849.
159. S. Grimme, *J. Chem. Phys.*, 2013, **138**, 244104.
160. C. Van Caillie and R. D. Amos, *Chem. Phys. Lett.*, 1999, **308**, 249-255.
161. F. Furche and R. Ahlrichs, *J. Chem. Phys.*, 2002, **117**, 7433-7447.
162. G. Scalmani, M. J. Frisch, B. Mennucci, J. Tomasi, R. Cammi and V. Barone, *J. Chem. Phys.*, 2006, **124**, 094107.
163. F. Liu, Z. Gan, Y. Shao, C.-P. Hsu, A. Dreuw, M. Head-Gordon, B. T. Miller, B. R. Brooks, J.-G. Yu and T. R. Furlani, *Mol. Phys.*, 2010, **108**, 2791-2800.
164. J. Liu and W. Liang, *J. Chem. Phys.*, 2011, **135**, 184111.
165. D. Jacquemin, B. Mennucci and C. Adamo, *Phys. Chem. Chem. Phys.*, 2011, **13**, 16987-16998.
166. J. Tomasi, B. Mennucci and R. Cammi, *Chem. Rev.*, 2005, **105**, 2999-3094.
167. M. Cossi and V. Barone, *J. Chem. Phys.*, 2001, **115**, 4708-4717.
168. M. Caricato, B. Mennucci, J. Tomasi, F. Ingrosso, R. Cammi, S. Corni and G. Scalmani, *J. Chem. Phys.*, 2006, **124**, 124520.
169. J. Preat, P.-F. Loos, X. Assfeld, D. Jacquemin and E. A. Perpete, *J. Mol. Struct. (THEOCHEM)*, 2007, **808**, 85-91.
170. A.-N. Bondar, S. Fischer, J. C. Smith, M. Elstner and S. Suhai, *J. Am. Chem. Soc.*, 2004, **126**, 14668-14677.
171. D. Riccardi, P. Schaefer, Y. Yang, H. Yu, N. Ghosh, X. Prat-Resina, P. König, G. Li, D. Xu and H. Guo, *Journal*, 2006, **110**, 6458-6469.
172. G. D. Scholes, C. Curutchet, B. Mennucci, R. Cammi and J. Tomasi, *J. Phys. Chem. B*, 2007, **111**, 6978-6982.
173. P.-F. Loos, J. Preat, A. D. Laurent, C. Michaux, D. Jacquemin, E. A. Perpete and X. Assfeld, *J. Chem. Theory Comput.*, 2008, **4**, 637-645.
174. M. Wanko, M. Hoffmann, J. Frähmcke, T. Frauenheim and M. Elstner, *J. Phys. Chem. B*, 2008, **112**, 11468-11478.
175. D. Jacquemin, E. A. Perpète, A. D. Laurent, X. Assfeld and C. Adamo, *Phys. Chem. Chem. Phys.*, 2009, **11**, 1258-1262.
176. R. Lindh and L. González, *Quantum Chemistry and Dynamics of Excited States: Methods and Applications*, John Wiley & Sons, 2020.
177. M. A. Marques, C. A. Ullrich, F. Nogueira, A. Rubio, K. Burke and E. K. Gross, *Time-dependent density functional theory*, Springer Science & Business Media, 2006.
178. E. Runge and E. K. Gross, *Phys. Rev. Lett.*, 1984, **52**, 997.
179. R. Van Leeuwen, *Phys. Rev. Lett.*, 1998, **80**, 1280.
180. R. van Leeuwen, N. E. Dahlen, G. Stefanucci, C.-O. Almbladh and U. von Barth, *Introduction to the Keldysh formalism*, Springer, 2006.
181. J. Olsen and P. Jo/rgensen, *J. Chem. Phys.*, 1985, **82**, 3235-3264.
182. P. Sałek, O. Vahtras, T. Helgaker and H. Ågren, *J. Chem. Phys.*, 2002, **117**, 9630-9645.
183. Y. Shao, M. Head-Gordon and A. I. Krylov, *J. Chem. Phys.*, 2003, **118**, 4807-4818.
184. Z. Li and W. Liu, *J. Chem. Phys.*, 2010, **133**, 064106.
185. Z. Li, W. Liu, Y. Zhang and B. Suo, *J. Chem. Phys.*, 2011, **134**, 134101.

186. M. E. Casida, in *Recent Advances In Density Functional Methods: (Part I)*, World Scientific, 1995, pp. 155-192.
187. M. Petersilka, U. Gossmann and E. Gross, *Phys. Rev. Lett.*, 1996, **76**, 1212.
188. S. S. Leang, F. Zahariev and M. S. Gordon, *J. Chem. Phys.*, 2012, **136**, 104101.
189. M. E. Casida and M. Huix-Rotllant, *Density-Functional Methods for Excited States*, 2016, 1-60.
190. K. Burke, J. Werschnik and E. Gross, *J. Chem. Phys.*, 2005, **123**, 062206.
191. C. Adamo and D. Jacquemin, *Chem. Soc. Rev.*, 2013, **42**, 845-856.
192. D. Jacquemin, A. Planchat, C. Adamo and B. Mennucci, *J. Chem. Theory Comput.*, 2012, **8**, 2359-2372.
193. S. Hirata and M. Head-Gordon, *Chem. Phys. Lett.*, 1999, **314**, 291-299.
194. F. Plasser, M. Wormit and A. Dreuw, *J. Chem. Phys.*, 2014, **141**, 024106.
195. R. L. Martin, *J. Chem. Phys.*, 2003, **118**, 4775-4777.
196. S. A. Bäppler, F. Plasser, M. Wormit and A. Dreuw, *Phys. Rev. A*, 2014, **90**, 052521.
197. M. Rohlfing and S. G. Louie, *Phys. Rev. Lett.*, 1999, **82**, 1959.
198. J.-W. Van der Horst, P. A. Bobbert, M. Michels, G. Brocks and P. J. Kelly, *Phys. Rev. Lett.*, 1999, **83**, 4413.
199. J. J. Markham, *Rev. Mod. Phys.*, 1959, **31**, 956.
200. H.-H. Perkampus, in *UV-VIS Spectroscopy and Its Applications*, Springer, 1992, pp. 215-234.
201. D. F. Swinehart, *J. Chem. Educ.*, 1962, **39**, 333.
202. J. K. Kauppinen, D. J. Moffatt, H. H. Mantsch and D. G. Cameron, *Appl. Spectrosc.*, 1981, **35**, 271-276.
203. R. N. Jones and K. Shimokoshi, *Appl. Spectrosc.*, 1983, **37**, 59-67.
204. J. K. Kauppinen, D. J. Moffatt, M. Hollberg and H. Mantsch, *Appl. Spectrosc.*, 1991, **45**, 1516-1521.
205. D. B. Siano and D. E. Metzler, *J. Chem. Phys.*, 1969, **51**, 1856-1861.
206. L. Antonov and S. Stoyanov, *Appl. Spectrosc.*, 1993, **47**, 1030-1035.
207. C. K. Jørgensen, C.-H. de Verdier, J. Glomset and N. A. Sörensen, *Acta Chem. Scand.*, 1954, **8**, 1495-1501.
208. E. J. Billo, *Excel for chemists: a comprehensive guide*, John Wiley & Sons, 2004.
209. C. J. Cramer and D. G. Truhlar, *Chem. Rev.*, 1999, **99**, 2161-2200.
210. E. Cances, B. Mennucci and J. Tomasi, *J. Chem. Phys.*, 1997, **107**, 3032-3041.
211. A. V. Marenich, C. J. Cramer and D. G. Truhlar, *J. Phys. Chem. B*, 2009, **113**, 6378-6396.
212. J. Tomasi and M. Persico, *Chem. Rev.*, 1994, **94**, 2027-2094.
213. C. Amovilli and B. Mennucci, *J. Phys. Chem. B*, 1997, **101**, 1051-1057.
214. R. McWeeny, *Methods Comp. Mol. Phys.*, 1992, 3-17.
215. C. P. Kelly, C. J. Cramer and D. G. Truhlar, *J. Phys. Chem. B*, 2006, **110**, 16066-16081.
216. A. V. Marenich, R. M. Olson, A. C. Chamberlin, C. J. Cramer and D. G. Truhlar, *J. Chem. Theory Comput.*, 2007, **3**, 2055-2067.
217. M. S. Lee and M. A. Olson, *J. Phys. Chem. B*, 2005, **109**, 5223-5236.
218. J. R. Pliego Jr and J. M. Riveros, *WIREs Comput. Mol. Sci.*, 2020, **10**, e1440.
219. A. Okur and C. Simmerling, *Annu. Rep. Comp. Chem.*, 2006, **2**, 97-109.
220. S. Li and P. Bradley, *Proteins: Struct., Funct., Bioinf.*, 2013, **81**, 1318-1329.

221. E. Cancès and B. Mennucci, *J. Chem. Phys.*, 2001, **114**, 4744-4745.
222. A. Klamt, C. Moya and J. Palomar, *J. Chem. Theory Comput.*, 2015, **11**, 4220-4225.
223. A. W. Lange and J. M. Herbert, *J. Phys. Chem. Lett.*, 2010, **1**, 556-561.
224. D. Kosenkov and L. V. Slipchenko, *J. Phys. Chem. A*, 2011, **115**, 392-401.
225. G. Scalmani and M. J. Frisch, *J. Chem. Phys.*, 2010, **132**, 114110.
226. D. M. York and M. Karplus, *J. Phys. Chem. A*, 1999, **103**, 11060-11079.
227. R. K. Wangsness and R. K. Wangsness, *Electromagnetic fields*, Wiley New York, 1979.
228. L. C. Wrobel and M. Aliabadi, 2002.
229. A. Y. Ben-Naim, *Solvation thermodynamics*, Springer Science & Business Media, 2013.
230. M. R. Reddy and M. D. Erion, *Free energy calculations in rational drug design*, Springer Science & Business Media, 2001.
231. V. Barone and M. Cossi, *J. Phys. Chem. A*, 1998, **102**, 1995-2001.
232. M. Cossi, N. Rega, G. Scalmani and V. Barone, *J. Comput. Chem.*, 2003, **24**, 669-681.
233. D. A. Liotard, G. D. Hawkins, G. C. Lynch, C. J. Cramer and D. G. Truhlar, *J. Comput. Chem.*, 1995, **16**, 422-440.
234. A. v. Bondi, *J. Phys. Chem.*, 1964, **68**, 441-451.
235. M. J. Frisch, G. W. Trucks, H. B. Schlegel, G. E. Scuseria, M. A. Robb, J. R. Cheeseman, G. Scalmani, V. Barone, G. A. Petersson, H. Nakatsuji, X. Li, M. Caricato, A. V. Marenich, J. Bloino, B. G. Janesko, R. Gomperts, B. Mennucci, H. P. Hratchian, J. V. Ortiz, A. F. Izmaylov, J. L. Sonnenberg, Williams, F. Ding, F. Lipparini, F. Egidi, J. Goings, B. Peng, A. Petrone, T. Henderson, D. Ranasinghe, V. G. Zakrzewski, J. Gao, N. Rega, G. Zheng, W. Liang, M. Hada, M. Ehara, K. Toyota, R. Fukuda, J. Hasegawa, M. Ishida, T. Nakajima, Y. Honda, O. Kitao, H. Nakai, T. Vreven, K. Throssell, J. A. Montgomery Jr., J. E. Peralta, F. Ogliaro, M. J. Bearpark, J. J. Heyd, E. N. Brothers, K. N. Kudin, V. N. Staroverov, T. A. Keith, R. Kobayashi, J. Normand, K. Raghavachari, A. P. Rendell, J. C. Burant, S. S. Iyengar, J. Tomasi, M. Cossi, J. M. Millam, M. Klene, C. Adamo, R. Cammi, J. W. Ochterski, R. L. Martin, K. Morokuma, O. Farkas, J. B. Foresman and D. J. Fox, *Journal*, 2016.
236. A. Szabo and N. S. Ostlund, *Modern quantum chemistry: introduction to advanced electronic structure theory*, Courier Corporation, 2012.
237. R. Dennington, T. Keith and J. Millam, 2009.
238. W. Humphrey, A. Dalke and K. Schulten, *J. Mol. Graphics Modell.*, 1996, **14**, 33-38.
239. E. F. Pettersen, T. D. Goddard, C. C. Huang, G. S. Couch, D. M. Greenblatt, E. C. Meng and T. E. Ferrin, *J. Comput. Chem.*, 2004, **25**, 1605-1612.
240. L. Skripnikov, *Chemissian: software to analyze spectra, build density maps and molecular orbitals*, 2016.
241. T. Bruhn, A. Schaumlöffel, Y. Hemberger and G. Pescitelli, *Berlin, Germany*, 2017.
242. A. W. Muelleman and R. E. Glaser, *J. Chem. Educ.*, 2018, **95**, 476-481.
243. V. Barone and A. Polimeno, *Chem. Soc. Rev.*, 2007, **36**, 1724-1731.
244. D. Jacquemin, E. A. Perpete, I. Ciofini and C. Adamo, *Acc. Chem. Res.*, 2009, **42**, 326-334.
245. Z. Cao, B. Xi, D. S. Jodoin, L. Zhang, S. P. Cummings, Y. Gao, S. F. Tyler, P. E. Fanwick, R. J. Crutchley and T. Ren, *J. Am. Chem. Soc.*, 2014, **136**, 12174-12183.
246. Y. Kataoka, N. Imasaki, K. Arakawa, N. Yano, H. Sakiyama, T. Sugimori, M. Mitsumi and M. Handa, *Dalton Trans.*, 2019, **48**, 12421-12429.

247. Y. Kataoka, N. Imasaki, N. Yano, M. Mitsumi and M. Handa, *Dalton Trans.*, 2021, **50**, 9547-9553.
248. A. Raghavan and T. Ren, *Organometallics*, 2019, **38**, 3888-3896.
249. Y. Kataoka, S. Mikami, H. Sakiyama, M. Mitsumi, T. Kawamoto and M. Handa, *Polyhedron*, 2017, **136**, 87-92.
250. G.-L. Xu, R. J. Crutchley, M. C. DeRosa, Q.-J. Pan, H.-X. Zhang, X. Wang and T. Ren, *J. Am. Chem. Soc.*, 2005, **127**, 13354-13363.
251. A. Raghavan, F. Yuan and T. Ren, *Inorg. Chem.*, 2020, **59**, 8663-8666.
252. R. Z. Khaliullin, A. T. Bell and M. Head-Gordon, *J. Chem. Phys.*, 2008, **128**.
253. M. A. Rohrdanz and J. M. Herbert, *J. Chem. Phys.*, 2008, **129**, 034107.
254. G. Cui and W. Yang, *Mol. Phys.*, 2010, **108**, 2745-2750.
255. M. J. Peach, M. J. Williamson and D. J. Tozer, *J. Chem. Theory Comput.*, 2011, **7**, 3578-3585.
256. M. Frisch, *http://www. gaussian. com/*, 2004.
257. S. Gorelsky, *University of Ottawa, Ottawa, Canada*, 2010.
258. M. Cortijo, R. González-Prieto, S. Herrero, J. L. Priego and R. Jiménez-Aparicio, *Coord. Chem. Rev.*, 2019, **400**, 213040.
259. I. Tolbatov and A. Marrone, *Inorg. Chim. Acta*, 2022, **530**.
260. M. Spitzer, F. Gartig and R. Van Eldik, *Rev. Sci. Instrum.*, 1988, **59**, 2092-2093.
261. W. Le Noble and R. Schlott, *Rev. Sci. Instrum.*, 1976, **47**, 770-771.
262. G. Estiú, F. D. Cukiernik, P. Maldivi and O. Poizat, *Inorg. Chem.*, 1999, **38**, 3030-3039.
263. W. M. Haynes, *CRC handbook of chemistry and physics*, CRC press, 2016.
264. V. Gutmann, *Coord. Chem. Rev.*, 1976, **18**, 225-255.